Max-Planck-Institut für Kolloid- und Grenzflächenforschung

Abteilung Theorie

Charged Polymer-Macroion Complexes

Dissertation

zur Erlangung des akademischen Grades
"doctor rerum naturalium"
(Dr. rer. nat.)
in der Wissenschaftsdisziplin Theoretische Physik

eingereicht an der
Mathematisch–Naturwissenschaftlichen Fakultät
der Universität Potsdam

von

Hoda Boroudjerdi

Potsdam, im Oktober 2005

To my husband–Ali–,
my parents–Tayebeh and Abdolhadi–,
my siblings–Sarah, Fatima and Reza–,
and the memory of
my grandfathers

Contents

Abstract

This work explores the equilibrium structure and thermodynamic phase behavior of complexes formed by charged polymer chains (polyelectrolytes) and oppositely charged spheres (macroions). Polyelectrolyte-macroion complexes form a common pattern in soft-matter physics, chemistry and biology, and enter in numerous technological applications as well. From a fundamental point of view, such complexes are interesting in that they combine the subtle interplay between electrostatic interactions and elastic as well as entropic effects due to conformational changes of the polymer chain, giving rise to a wide range of structural properties. This forms the central theme of theoretical studies presented in this thesis, which concentrate on a number of different problems involving strongly coupled complexes, i.e. complexes that are characterized by a large adsorption energy and small chain fluctuations.

In the first part, a global analysis of the structural phase behavior of a single polyelectrolyte-macroion complex is presented based on a dimensionless representation, yielding results that cover a wide range of realistic system parameters. Emphasize is made on the interplay between the effects due to the polyelectrolytes chain length, salt concentration and the macroion charge as well as the mechanical chain persistence length. The results are summarized into generic phase diagrams characterizing the wrapping-dewrapping behavior of a polyelectrolyte chain on a macroion. A fully wrapped chain state is typically obtained at intermediate salt concentrations and chain lengths, where the amount of polyelectrolyte charge adsorbed on the macroion typically exceeds the bare macroion charge leading thus to a highly overcharged complex.

Perhaps the most striking features occur when a single long polyelectrolyte chain is complexed with many oppositely charged spheres. In biology, such complexes form between DNA (which carries the cell's genetic information) and small oppositely charged histone proteins serving as an efficient mechanism for packing a huge amount of DNA into the micron-size cell nucleus in eucaryotic cells. The resultant complex fiber, known as the chromatin fiber, appears with a diameter of 30 nm under physiological conditions. Recent experiments indicate a zig-zag spatial arrangement for individual DNA-histone complexes (nucleosome core particles) along the chromatin fiber. A numerical method is introduced in this thesis based on a simple generic chain-sphere cell model that enables one to investigate the mechanism of fiber formation on a systematic level by incorporating electrostatic and elastic contributions. As will be shown, stable complex fibers exhibit an impressive variety of structures including zig-zag, solenoidal and beads-on-a-string patterns, depending on system parameters such as salt concentration, sphere charge as well as the chain contour length (per sphere). The present results predict fibers of compact zig-zag structure within the physiologically relevant regime with a diameter of about 30 nm, when DNA-histone parameters are adopted.

In the next part, a numerical method is developed in order to investigate the role of thermal fluctuations on the structure and thermodynamic phase behavior of polyelectrolyte-

macroion complexes. This is based on a saddle-point approximation, which allows to describe the experimentally observed reaction (or complexation) equilibrium in a dilute solution of polyelectrolytes and macroions on a systematic level. This equilibrium is determined by the entropy loss a single polyelectrolyte chain suffers as it binds to an oppositely charged macroion. This latter quantity can be calculated from the spectrum of polyelectrolyte fluctuations around a macroion, which is determined by means of a normal-mode analysis. Thereby, a stability phase diagram is obtained, which exhibits qualitative agreement with experimental findings.

At elevated complex concentrations, one needs to account for the inter-complex interactions as well. It will be shown that at small separations, complexes undergo structural changes in such a way that positive patches from one complex match up with negative patches on the other. Furthermore, one of the polyelectrolyte chains may bridge between the two complexes. These mechanisms lead to a strong inter-complex attraction. As a result, the second virial coefficient associated with the inter-complex interaction becomes negative at intermediate salt concentrations in qualitative agreement with recent experiments on solutions of nucleosome core particles.

Zusammenfassung

In dieser Arbeit werden Gleichgewichtsstrukturen und die thermodynamischen Phasen von Komplexen aus geladenen Polymeren (Polyelektrolyten) und entgegengesetzt geladenen Kugeln (Makroionen) untersucht. Polyelektrolyt-Makroion-Komplexe bilden ein grundlegendes und wiederkehrendes Prinzip in der Physik weicher Materie sowie in Chemie und Biologie. In zahlreichen technologischen Prozessen finden sich ebenfalls Anwendungsbeispiele für derartige Komplexe. Zusätzlich zu ihrem häufigen Auftreten sind sie aufgrund ihrer Vielfalt von strukturellen Eigenschaften von grundlegendem Interesse. Diese Vielfalt wird durch ein Zusammenspiel von elektrostatischen Wechselwirkungen sowie elastischen und entropischen Effekten aufgrund von Konformationsänderungen in der Polymerkette bedingt und bildet das zentrale Thema der theoretischen Studien, die mit dieser Arbeit vorgelegt werden. Verschiedene Strukturen und Prozesse, die stark gekoppelte Komplexe beinhalten – das sind solche, für die eine hohe Adsorptionsenergie und geringe Fluktuationen in den Polymerketten charakteristisch sind –, bilden das Hauptthema der Arbeit.

Basierend auf einer dimensionslosen Darstellung wird im ersten Teil der Arbeit in einer umfassenden Analyse das strukturelle Phasenverhalten einzelner Polyelektrolyt-Makroion-Komplexe behandelt. Der Schwerpunkt wird hier auf das Wechselspiel zwischen Effekten aufgrund der Polyelektrolytkettenlänge, ihrer mechanischen Persistenzlänge, der Salzkonzentration und der Ladung des Makroions gelegt. Die Ergebnisse werden in allgemeinen Phasendiagrammen zusammengestellt, das das Aufwickeln-Abwickeln-Verhalten der Polyelektrolytkette auf einem Makroion beschreibt. Ein Zustand mit komplett aufgewickelter Kette tritt typischerweise bei mittleren Salzkonzentrationen und Kettenlängen auf; häufig ist hier die auf dem Makroion adsorbierte Gesamtladung des Polyelektrolyts größer als die Ladung des nackten Makroions, d.h. es findet in hohem Grad Ladungsinversion statt.

Äußerst bemerkenswerte Eigenschaften treten auf, wenn eine einzelne lange Polyelektrolytkette viele, ihr entgegengesetzt geladene Kugeln komplexiert. In biologischen Systemen findet man solche Komplexe zwischen DNS, die die genetische Information einer Zelle trägt, und kleinen, entgegengesetzt geladenen Histonproteinen. Diese Komplexe dienen als effizienter Mechanismus, die große Menge an DNS im Mikrometer-großen Zellkern eukaryotischer Zellen zu komprimieren. Die dadurch erhaltene komplexe Faser, eine Chromatinfaser, hat unter physiologischen Bedingungen einen Durchmesser von nur etwa 30 nm. Neue Experimente haben gezeigt, dass eine räumliche Zickzack-Anordnung einzelner DNA-Histon-Komplexe entlang der Chromatinfaser vorliegt. In der hier vorgelegten Arbeit wird eine numerische Methode vorgestellt, die auf einem einfachen Ketten-Kugel-Zell-Modell basiert und die die systematische Untersuchung des Mechanismus zur Faserbildung ermöglicht, wobei sowohl elektrostatische als auch elastische Wechselwirkungen berücksichtigt werden. Es wird gezeigt, dass stabile Komplexfasern in Abhängigkeit von der Salzkonzentration, der Kugelladung und der Kettenkonturlänge eine Vielfalt von Strukturen aufweisen, darunter Zickzack-, Solenoid-

und Perlenkettenformen. Für physiologisch relevante Bedingungen werden mit dieser Methode für DNA-Histon-Komplexe Fasern kompakter Zickzack-Struktur mit einem Durchmesser von etwa 30 nm erhalten.

Im folgenden Teil wird eine numerische Methode entwickelt, um den Einfluss thermischer Fluktuationen auf Struktur und thermodynamisches Phasenverhalten der Polyelektrolyt-Makroion-Komplexe zu untersuchen. Basierend auf der Sattelpunktsnäherung werden die experimentell beobachteten Reaktionsgleichgewichte in verdünnten Lösungen von Polyelektrolyten und Makroionen systematisch beschrieben. Das Gleichgewicht ist durch einen Verlust an Entropie für die einzelne Polyelektrolytkette durch die Bindung an das entgegengesetzt geladene Makroion gekennzeichnet. Diese Größe wurde aus dem Spektrum der Polyelektrolytfluktuationen um das Makroion erhalten und mittels einer Analyse der Normalmoden berechnet. Hierüber wird ein Phasendiagramm zur Stabilität der Komplexe erhalten, das qualitativ gute Übereinstimmungen mit experimentellen Ergebnissen aufweist.

Bei höheren Komplexkonzentrationen müssen auch die Wechselwirkungen zwischen den Komplexen berücksichtigt werden. Es wird gezeigt, dass sich die Struktur der Komplexe bei kleinen Abständen so ändert, dass positiv geladene Bereiche eines Komplexes mit negativ geladenen auf einem Nachbarkomplex räumlich korrelieren. Weiterhin können einzelne Polyelektrolytketten als verbrückendes Element zwischen zwei Komplexen dienen. Dieser Mechanismus führt zu starker effektiver Anziehung zwischen den Komplexen. In Übereinstimmung mit kürzlich durchgeführten Experimenten ist als Folge davon der zweite Virialkoeffizient der Wechselwirkung zwischen Komplexen bei mittleren Salzkonzentrationen negativ.

Chapter 1

Introduction

Complexes formed between charged polymers (polyelectrolytes) and oppositely charged macro-ions have attracted much attention in recent years due to their vast technological applications and challenging fundamental aspects.

Perhaps the most striking example of polyelectrolyte-macroion complexes occurs in biology and in the packaging process of DNA in eucaryotic cells, where large lengths of DNA–a highly negatively charged biopolymer–is stored inside the micron-size cell nucleus. There is substantial evidence that electrostatic effects play a prominent role determining various structural and thermodynamic properties of such complexes. From a theoretical point of view, electrostatic interactions make polyelectrolyte-macroion complexes a challenging subject for fundamental research, and on the other hand, give rise to generic properties that are closely related with several other interesting problems in soft-matter physics. In this chapter, I briefly discuss some of different aspects of polyelectrolyte-macroion complexes and, in particular, review biological relevance of these complexes. I will then outline the studies presented in this thesis, which are centered around the generic electrostatic aspects of these complexes.

1.1 Charged soft-matter: polymers and colloids

Electric charges and electrostatic interactions are ubiquitous in soft-matter and biological systems. Most of soft materials, such as polymers, colloids and proteins acquire surface charges (often due to dissociation of surface chemical groups) when dissolved in a polar solvent such as water. Because soft materials are easily deformed or re-arranged by potentials comparable to thermal energy, electrostatic interactions caused by permanent (or even induced) charges, that are typically of long-range and large strength, constitute a prominent factor determining the behavior and properties of these materials. This makes charged materials central to many technological applications.

Colloids and polymers are common ingredients of charged soft-matter systems. Smoke, fog, milk, paint and ink are only a few examples of colloidal systems. Polymers are encountered in many everyday-life examples such as chewing gum, dough, or egg white. Colloids comprise tiny solid or liquid particles that are suspended in another medium such as air or another liquid. An important factor, which makes colloidal solutions in many ways different from molecular or simple electrolyte solutions (such as sugar or salt solution), is the large asymmetry in size and mass between the colloidal particles and solvent molecules (or microscopic ions): Colloids are *mesoscopic* objects with sizes in the range of a few nanometers to

microns, and are thus characterized by a large total area (i.e. a large fraction of atoms) in contact with solvent. Therefore, colloidal physics is dominated by surface properties [4].

Polymers, which form another closely related macromolecular system, consist of many repeating subunits (monomers) that are chemically connected to form a flexible chain. Flexible polymers are distinguished by their many degrees of freedom associated with conformational arrangement of monomers that are easily excited by thermal energy at room temperature. This gives rise to a diverse phase behavior [185]: Polymer chains can have large extensions in the solution and be strongly entangled, or even collapse into a compact globular state (and thus form a colloidal system as it is, for instance, realized in proteins). Depending on their chemical structure, polymer chains can have a large mechanical stiffness as well, in which case they behave like rigid rods at length scales smaller than a characteristic persistence length. Several famous examples of stiff polymers are provided by Nature: actin filaments and microtubules that are known by their important role in biological processes occurring in the cell [1].

In recent years, charged polymers, or the so-called *polyelectrolytes*, and their synthesis have attracted a lot of attention because of their significant role in the production of cheap, non-toxic and environmentally friendly materials [10]. In contrast to water-insoluble hydrocarbon chains, polyelectrolytes typically show high affinity for water and heavy metal ions, which makes them useful in applications such as super-absorbing diapers, waste water purifiers and washing detergents and their additives.

Charged systems are typically associated with many-body features: *Macroions*, such as charged colloids or polymers, are always surround by neutralizing oppositely charged microscopic ions, called *counterions*, and also in general by *coions*. These particles form loosely bound ionic clouds around macroions and tend to screen their charges. In particular, counterions, that are attracted towards macroion surfaces, predominantly determine static or dynamic properties of macroionic solutions in many instances. Understanding the interactions between macroions across an ionic medium and their thermodynamic properties requires an understanding of the ionic clouds first [7].

1.1.1 polyelectrolyte-macroion complexes

In aqueous solutions, polyelectrolyte chains strongly interact with other charged mesoscopic objects and, in particular, tend to associate with oppositely charged colloids or other globular macroions. Depending on surrounding conditions (such as salt and macroion/polyelectrolyte concentration), a fraction of polyelectrolytes and macroions may "react"and form complexes comprising one or more macroions and polyelectrolyte chains. Examples are furnished by the complexation of synthetic polyelectrolytes with charged proteins [17, 26], charged plastic beads [18], gold particles [30, 31], charged micelles [22, 27, 24, 23] or dendrimers [20]. Note that these complexes are differentiated by the size of the spherical objects, which varies over several orders of magnitude. Repeated adsorption of anionic and cationic polyelectrolytes on a macroion can lead to well-characterized multilayers [19].

polyelectrolyte-macroion complexes have numerous applications ranging from fabrication of polymeric hollow shells [19] and calcium-incrustation-inhibition during the washing process [21]. An interesting feature is that adsorbed polyelectrolytes can act both as stabilizing and destabilizing agents in charged colloidal suspensions depending on the effective interactions mediated by the adsorbed polyelectrolyte layer between the resulting polyelectrolyte-macroion complexes.

From a fundamental point of view, polyelectroyte-macroion complexes are interesting in that they combine the subtle interplay between electrostatic interactions and elastic as well as entropic effects due to conformational changes of the polymer chain, which gives rise to a wide range of structural properties. One can distinguish a few limiting cases: Strongly coupled complexes are characterized by a large polyelectrolyte adsorption energy and small fluctuations effects, while weakly coupled complexes exhibit weak adsorption and thus dominant chain fluctuations. In the former case, which may be realized by highly charged and stiff polymers, one deals with a flat adsorbed polyelectrolyte layer with pronounced lateral order due to mutual electrostatic repulsions of the polyelectrolyte segments [40, 48, 49, 64, 66, 67, 68, 69, 43, 44]. In the weak coupling regime, strong fluctuations give rise to a *diffuse* adsorbed polymer layer [208, 58, 59, 46, 43, 44]. The studies presented in this thesis primarily focus on strongly coupled complexes.

Due to strong adsorption effects, strongly coupled complexes exhibit striking properties such as large overcharging (i.e. adsorption of polyelectrolyte charges more than necessary to neutralize the macroion charge) [37, 45, 48, 49, 64, 65, 66, 67, 68, 69, 47] and like-charge attraction [41, 42, 206, 207, 208, 209, 210, 211, 47], which results from structural correlations (or polyelectrolyte bridging) between highly overcharged complexes. This latter case is closely related to the like-charge attraction induced by structural correlations due to multivalent counterions [199, 197, 198, 202, 204, 205]. These aspects will be discussed in more detail in the forthcoming chapters.

1.2 Biological aspects

In biology, charged polymers and electrostatic effects emerge in many striking examples [9]. Almost all proteins, as well as the DNA and the RNA, are charged polymers. DNA, for instance, is a long biomolecule with a total length of about two meters in every human cell which is highly negatively charged: It bears one elementary charge per 1.7Å, which for human DNA adds up to 10^{10} elementary charges overall. Yet the DNA is densely packed inside the cell nucleus with a diameter of about few microns. In eucaryotic cells, this storage process involves a hierarchical structure, which serves a highly efficient packing mechanism. The main task here is to compact DNA molecules in such a way that they would be able to efficiently perform their biological functions in the cell. For this purpose, many portions of DNA must be accessible to a large variety of proteins such as gene regulatory proteins, RNA polymerases, transcription factors, etc [1, 2].

On the lowest level of DNA packaging, short segments (about 50 nm) of DNA are tightly wrapped around positively charged histone proteins with a diameter of about 5 nm. The resultant complexes are known as *nucleosome core particles*, which are linked together via a linker DNA. DNA-histone complexation within the core particles leads to nearly a 7-fold reduction in the linear size of the DNA molecule. On the next level, the string of nucleosome core particles fold into a thicker and denser structure, known as the *chromatin fiber*, which appears with a diameter of about 30 nm in physiological conditions. This 30 nm fiber undergoes a series of higher-order foldings ending up at the highly condensed *chromosomes* (see the illustration in Figure 1.1). The linear extension of the chromosome is about 10^4 times smaller than the contour length of the original DNA molecule. This large packing ratio occurs at metaphase stage of mitosis (nucleus division), that is before the cell division occurs. In the interphase stage (i.e. the long stage between one mitosis and the next in the cell cycle), the
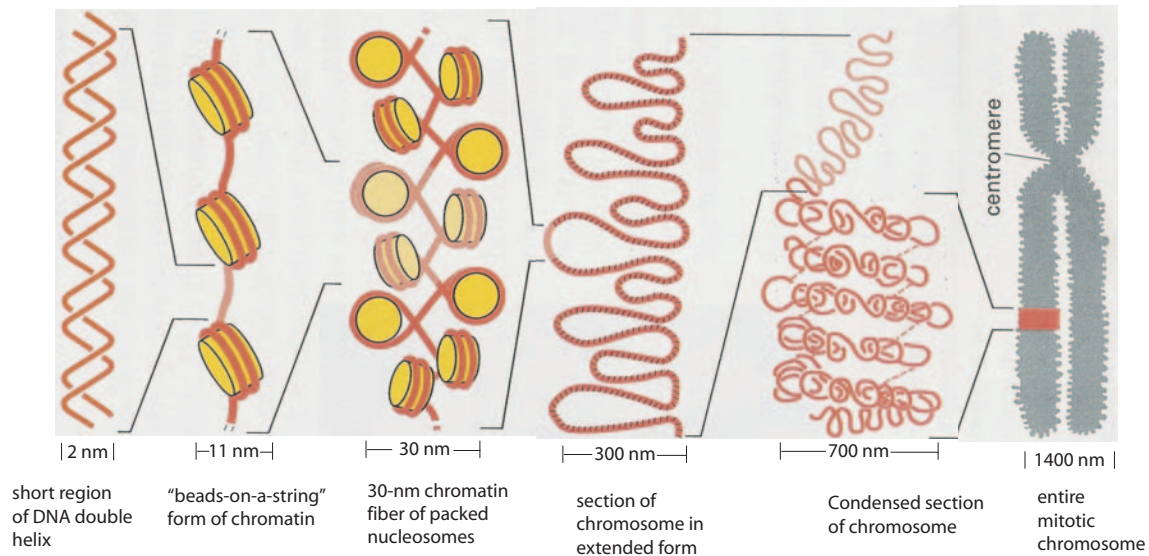
Figure 1.1: DNA packaging in the nucleus of eucaryotic cells involves a hierarchical structure on the lowest level of which DNA is complexed with histone protein forming nucleosome core particles. A jointed string of nucleosome forms the chromatin fiber that folds into a 30 nm thick fiber in physiological conditions. Chromatin folds into higher-order structures that eventually end up at the highly condensed *chromosome*, whose linear extension is much smaller than the contour length of the original chain (Figure after Ref. [1]).

packaging ratio will be less (about 250 [2]) and chromosomes are overall less condensed.

There is now mounting experimental evidence which shows that packaging of DNA and its organization within the cell nucleus play a central role in regulating its functions [2, 145, 146, 147]. Experimental techniques such as electron microscopy and x-ray crystallography have proved quite successful in defining the detailed structure of nucloesome and to some extent that of the chromatin fiber [2, 148, 152], although the structure of higher-order folding levels remains largely unknown and are yet to be elucidated. Recent experimental findings have triggered a growing theoretical interest in DNA complexes and chromatin structure, which aim to model the structure and physical properties of these system (see Ref. [50] for a recent review). The complexation of DNA with histone proteins is believed to be highly influenced by electrostatic interactions although a variety of other factors of specific origin are also present and play important roles. Some of these features are briefly reviewed in the following sections.

1.2.1   DNA

Biochemistry

"All living cells on Earth, without any known exception, store their hereditary information in the form of double-stranded molecules of DNA [Deoxyribonucleic acid]–long unbranched paired polymer chains, formed always of the same four types of monomers–A, T, C, G"[1]. Each DNA monomer (nucleotide) consists of two main parts: a sugar (deoxyribose) with a phosphate group attached to it, and an aromatic base, which may be one of the four
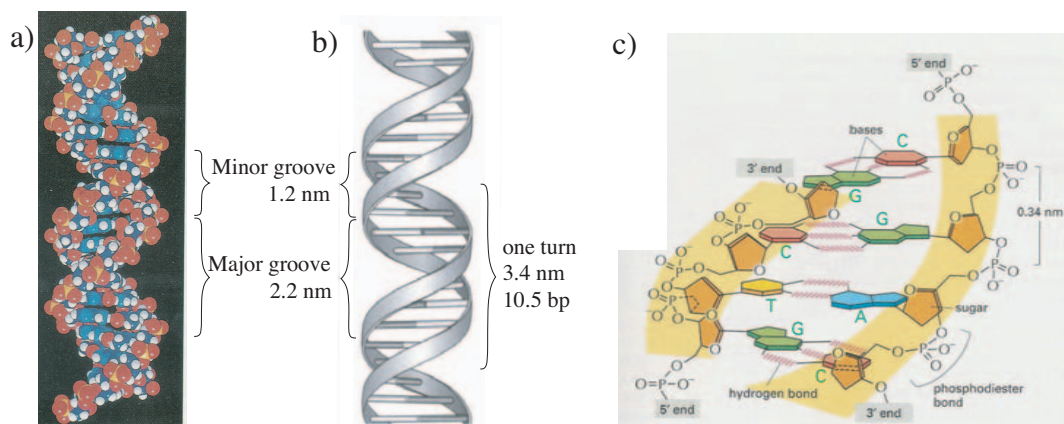
Figure 1.2: a) Space filling [1] and b) basic structure [2] of the DNA. Each turn of DNA is made up of 10.5 nucleotide pairs amounting to a pitch size of 3.4 nm. The coiling of the two strands around each other creates two grooves in the double helix as indicated in the figure. c) A short section of the double helix viewed from its side, showing four base pairs. The nucleotides are linked together covalently by phosphodiester bonds. The bases (A, C, G and T) zip two strands of DNA to each other via hydrogen bonds Ref. [1].

distinct bases adenine (A), guanine (G), cytosine (C) or thymine (T) that encode the genetic information.

A *single* strand of DNA (polynucleotide chain) consists of nucleotides joined together by covalent chemical bonds through the sugars and phosphates, which thus form a *backbone* of alternating sugar-phosphate-sugar-phosphate (Figure 1.2). To each sugar, one of the four bases is covalently bound. A normal DNA molecule is constructed from two such complementary strands which are bound together in the following manner: To each adenine binds a thymine (and vice versa) with two hydrogen bonds, and to each guanine binds a cytosine (and vice versa) with three hydrogen bonds, thereby resulting in a chain with two backbones which are linked together by complementary A-T and C-G *base pairs* (bp).

The DNA molecule forms a three-dimensional right-handed double-helical structure in which the two strands twist around each other such that all the bases are on the inside of the double helix, and the sugar-phosphate backbones are on the outside (Figure 1.2). This double helical structure is stabilized by hydrogen bonds between the complementary bases (and the stacking of base pairs), which are rather weak (as compared with typical covalent bonds) allowing the two strands to be pulled apart without breakage of their backbones. This makes the copying of genetic information (e.g., transcription and DNA replication) possible in living cells [1, 2]. Because each strand of DNA contains a sequence of nucleotides that is exactly complementary to the nucleotide sequence of its partner strand, each strand can act as a template for the synthesis of a new complementary strand when presented to an environment in which all kinds of nucleotides are present.

Physical parameters

Each DNA base pair is of a same width of 0.34 nm (equal to the center-to-center distance between adjacent nucleotide pairs). The backbones are held an equal distance apart along

the double helix, which has a diameter of about 2 nm. The planes of base pairs are almost perpendicular to the helix axis and the twist angle, that is rotation per residue, is 34.3°. Therefore, one helical turn is made up of 10.5 nucleotide pairs leading to a pitch size of 3.4 nm. The coiling of the two strands around each other creates two grooves in the double helix referred to as major groove (of 2.2 nm size) and minor groove (of 1.2 nm size) as indicated in Figure 1.2. The aromatic bases are planar and can easily be stacked, a process caused by hydrophobic and van-der-Waals interactions (which amount to about 4-15 kcal per mole of dinucleotide). On the other hand, each hydrogen bond between bases accounts for about 2-3 kcal/mol [1, 2, 50]. The double helical structure is destabilized at temperatures between 70 °C and 80 °C [2] or by externally applied stress [2, 162, 163, 164, 165, 167].

Any bending or twist of the double helix results in a distortion of the equilibrium conformation of stacked bases and the backbone, which costs energy and reflects the *mechanical* elastic properties of DNA. The bending rigidity of DNA is one of the key factors that will be taken into account in the investigations presented in this thesis. There is yet another contribution enhancing the bending rigidity of DNA, which stems from electrostatic interaction between charges on the backbone.

At physiological condition (aqueous solution of pH around 6.5-7.0), a hydrogen atom is dissociated from each phosphate group of the backbone resulting in two negative elementary charges per base pair of DNA. This amounts to a very high linear charge density of 5.88 e/nm, which has a huge impact on various physical properties of DNA. In particular, electrostatic repulsion between charges along the backbone leads to electrostatic stiffening of DNA chain, because they favor a straight conformation for the chain. Unlike intra-helix hydrogen bonds and van-der-Waals interactions, electrostatic interactions vary with the additional salt in solvent medium. In physiological conditions, one typically deals with a monovalent salt concentration of about 100 mM. Coions and counterions generated by dissociation of salt molecules lead to an effective screening of Coulomb interactions (e.g., in physiological condition, Coulomb interactions decay exponentially beyond a small screening length scale of about 1 nm–see Chapter 2 and Appendix B).

The bending properties may be quantified effectively by a length scale, referred to as the *persistence length*, which will be defined later on a systematic level (see section 2.1.1). Intuitively, this quantity corresponds to a length scale along the polymer backbone within which the polymer chain maintains an almost rod-like shape. Beyond this distance, thermal fluctuation are able to disorient chain segments independently of each other, and thereby, the overall chain conformation looks like a random coil. For DNA in physiological condition, the persistence length is about 50 nm [166, 167, 168] (corresponding to about 147 base pairs). This value decreases with increasing salt concentration down to a purely mechanical value of 30 nm for infinite salt [158, 159, 160, 189].

1.2.2 Proteins

Most of the dry mass of the cell is made from proteins, which execute almost all cell functions. They play an impressive variety of roles in the cell: Enzymes, for instance, are proteins that catalyze various chemical reactions within the cell. Proteins embedded in the cell membrane form channels and pumps that control the exchange of small molecules between interior and exterior of the cell. Other proteins, such as actin, tubulin, or motor proteins, act as message carriers between cells or signal integrators within a cell [1]. Specific examples are DNA polymerase, an enzyme which synthesizes DNA by joining nucleotides together (using a DNA
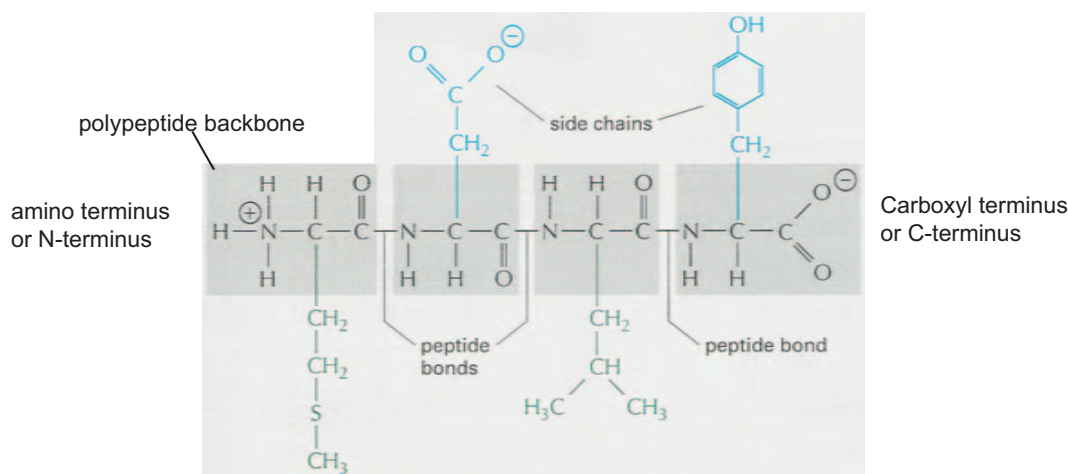
Figure 1.3: Proteins consist of a polypeptide backbone with attached side chains. The two ends of the polypeptide chain are chemically different: the end carrying the free amino group (NH_3^+) is known as the amino terminal or the N-terminal, and the one carrying the free carboxyl group (COO^-) is known as the carboxyl terminal or the C-terminal (Figure after Ref. [1]).

template as guide), and DNA nuclease, an enzyme which cleaves DNA.

A protein molecule (or polypeptide) is a polymer made from a long chain of amino acids (of twenty different types), each linked to its neighbors by a covalent peptide bond–see Figure 1.3. Attached to the polypeptide backbone are those parts of amino acids that are not involved in the peptide bond, the so-called side chains, which give each amino acid its unique chemical properties.

Proteins are by far the most structurally complex molecules known. The long polypeptide chain folds into a unique three-dimensional structure due to a variety of non-covalent intramolecular forces (such as van-der-Waals, ionic or hydrogen bonds) as well as intermolecular forces (such as hydrophobic interactions) that act between the side chains of polypeptides and the solvent medium (usually water) [1]. This folding process gives rise to globular proteins that have a compact shape with a typically rough surface. Enzymes tend to be globular as well as histone proteins that will be discussed further below. There are also proteins with simple elongated structure (fibrous proteins) [1]. Some proteins may assemble to form long filaments, such as actin filaments (made from the protein actin), which plays a significant role in biological processes occurring in the cell.

Histone proteins

The proteins that bind to the nuclear DNA of eucaryotic cells are traditionally categorized as *histones* and *non-histones*. Histones are present in large quantities within the cell (with total mass about equal to that of the DNA or almost half of the mass of proteins in the nucleus). These are in fact the proteins that are responsible for the most basic level of chromosome organization, the so-called *nucleosome*, in which DNA is wrapped around a histone core (section 1.2.3 below).

The histone core in the nucleosome is an *octamer* consisting of eight histone proteins,
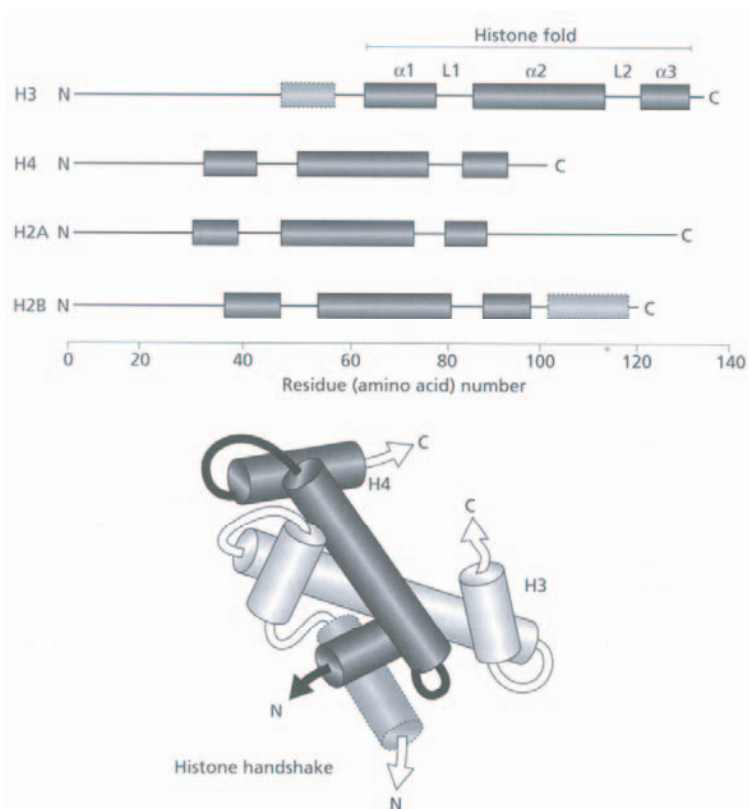
Figure 1.4: The central, globular domains of all four core histones have a set of three α-helical regions (dark shaded boxes labeled $\alpha1$, $\alpha2$ and $\alpha3$) that form a characteristic structure known as the histone fold (top). L1 and L2 are non-helical loops between the helices. The broken line, light shaded boxes represent α-helical regions not forming part of the histone fold. The fold domains of H3 and H4 interact in the core particle to form the histone handshake (bottom). The fold domains of H2A and H2B interact in the same way. The long N-terminals extends out from the core, making the histone tails (the arrows in the handshake) (Figure after Ref. [2]).

namely, two molecules from each of histones H2A, H2B, H3 and H4. These are relatively small proteins (with 102-135 amino acids) and each contains an N-terminal (or amino terminal) "tail"and a tertiary structure known as the *histone fold* (see Figure 1.4). The histone fold is typically formed from three α helices, one long and two short, connected by two nonhelical "loops". In nucleosome core assembly, the histone folds first bind to each other through an interaction known as "handshake", forming dimers of H3-H4 and H2A-H2B. The H3-H4 dimers combine to form tetramers, which then combine with two H2A-H2B dimers to complete the octamer core. The high resolution x-ray crystallographic analysis (Figure 1.6) reveals that the histone core is shaped roughly like a cylinder (or disk), 7 nm in diameter and 5.5 nm height [1, 2, 154]. There is also an axis of two-fold symmetry, the dyad axis, as shown diagrammatically in Figure 1.6d.

The histone proteins are highly basic, being rich in lysine and arginine amino acids that are positively charged at about neutral pH. The total number of lysine and arginine amino acids in a particular complete histone octamer is 216 [32], which is due to 13 lysine and 12 arginine residues in H2A, 20 lysine and 8 arginine in H2B, 12 lysine and 18 arginine in H3

and 11 lysine and 14 arginine in H4. There are also negatively charged amino acids (aspartate or glutamate), namely, 9 in H2A, 10 in H2B, 11 in H3 and 7 in H4. Finally, the number of acetylation (phosphorylation) sites are 1 (1) in H2A, 4 (1) in H2B, 4 (2) in H3 and 4 (1) in H4 (acetylation or phosphorylation refers to neutralization of a positive charge or addition of a negative charge, respectively). This amounts to an overall net charge of $+106e$ for the histone octamer. Such a high positive charge makes histones excellent DNA-binding proteins as the DNA is highly negatively charged. However, charge regulation effects may reduce the net charge of the octamer (note that lysine and arginine are rather weak bases and repulsion between neighboring positive charges as well as the image charge effects may suppress their complete dissociation in neutral pH). On the other hand, surrounding conditions such as salt concentration influence Coulomb interactions in such a way that one indeed has to account for the *effective* charge of the histone core as will be made clear later on. The histone core has a rough surface with grooves, ridges and relatively specific binding sites that introduce additional interactions with the nucleosomal DNA (see below).

The long N-terminal tail of each core histone is a quite flexible chain, which can extend out from the core region of the nucleosome. These tails contain roughly 50% of the basic amino acids of the octamer [2, 148, 150, 151], carrying therefore a large amount of positive charge which can be strongly attracted by DNA or other proteins. It is worth mentioning that, most of the acetylation and phosphorylation sites of the histone octamer is positioned in the histone tails, where they are exposed to the enzymes enhancing such modification *in vivo* [2, 145, 146, 147]. These modifications are conserved through evolution, and are believed to play significant role in regulating chromatin function [2]. Although the precise function of histone tails is yet to be elucidated, experimental results already indicate that they play a significant role in compaction of the chromatin structure (section 1.2.4 below).

The histone proteins are among the most highly conserved eucaryotic proteins (with virtually identical primary structures, i.e. amino acid sequence, from one organism to another), and it seems that even small changes in their structure leads to lethal effects for their function in the cell [2, 155].

1.2.3   DNA-protein complexes: Nucleosome core particle

Nucleosome is the basic building block of the chromosome, which may be isolated from unfolded chromatin (obtained, e.g., by exposure of chromatin to reduced salt concentration) using digestion with particular enzymes, known as nucleases, that cleave the DNA between the nucleosomes (see Figure 1.5). Each nucleosome contains about 200 base pairs of DNA and consists of two parts: the *chromatosome*, a unit of approximately 165 base pairs of DNA complexed with histone proteins, and the so-called *linker DNA* connecting consecutive chromatosomes to each other. The linker DNA is readily digested by nucleases and its length may vary depending on the organism or due to processes such as nucleosome repositioning or chromatin remodeling [2, 92, 93, 94, 95, 96, 97, 98, 50].

A schematic view of the chromatosome is shown in Figure 1.6e. It involves a *linker* H1 histone protein (or its variant H5), which is believed to occupy a position outside the core octamer, close to the entry-exit region of the DNA strand wrapped around the histone core. H1 is positively charged in neutral pH and has a globular core with two relatively long N- and C-terminal (amino and Carboxyl terminal respectively) tails capable of interacting with both linker and core DNA. The exact structural relationship between H1 and the nucleosome is still not clear, but its influence on the overall structure of the chromatin has been examined
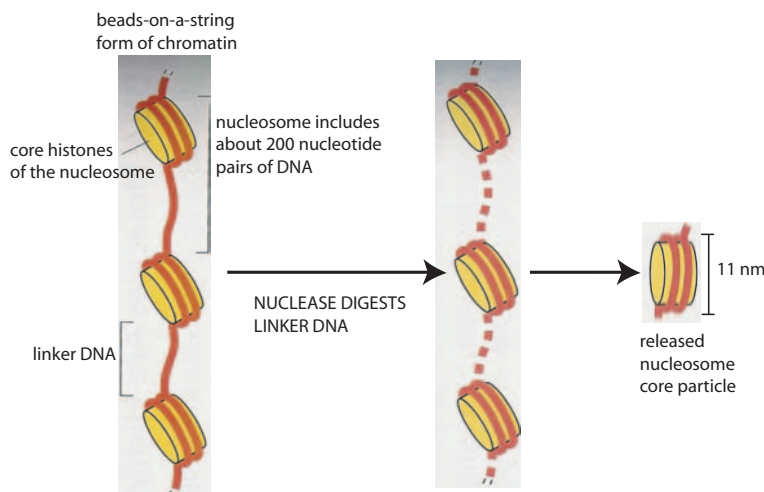
Figure 1.5: The nucleosome core particle is released from chromatin by digestion of the linker DNA with nuclease, an enzyme that cleaves DNA but leaves the core DNA intact. After dissociation of the isolated nucleosome into its protein core and DNA, one ends up with the nucleosome core particle consisting of a length of 146 nucleotide pairs wrapped around the histone core (Figure after Ref. [1]).

in various experiments [116, 123, 142] (see section 1.2.4 below).

Further digestion of chromatosome leads to depletion of the H1 histone and consequently, about 10 base pairs from each end of the DNA is digested leaving intact the so-called *nucleosome core particle* (or the core particle)-see Figures 1.5 and 1.6d and e. The detailed structure of the nucleosome core particle (NCP) has been resolved with high resolution x-ray crystallography at 2.8Å [148] (see Figure 1.6a and b), and recently at 1.9Å [149]. Within each nucleosome core particle, a length of 146 base pairs of DNA is wrapped around the histone octamer in a left-handed helical ramp of about 1-and-3/4 turns with a pitch size of about 2.8 nm. The nucleosome core particle is shaped like a flattened cylinder with a diameter of 11 nm (combined diameter of the core histone octamer and that of the DNA) and a height of 5.5 nm [2, 148, 149, 151] (Figure 1.6d and e). The nucleosome core particles are highly conserved in structure and identical for all eucaryotic cells.

DNA-histone interactions

The path followed by the DNA across the surface of the histone octamer is not smooth and in some regions is more sharply bent than others and as a result, the DNA's double helix structure is distorted in the nucleosome core particle. The double helix may be locally over-wound due to a small increase (up to 0.5 base pairs per turn) in its local twist. It is important to note that the exact path of the DNA on the histone octamer and its local properties are highly specific and may vary depending on specific properties of the core histones and the sequence of the DNA, and thus may differ from one nucleosome to another [2, 106]. (For instance, note that the A-T-rich sequences in the minor grooves are easier to compress than G-C-rich sequences, and therefore, each histone octamer tends to position itself on the DNA so as to maximize A-T-rich minor grooves on the inside of the DNA strand.)

There are 14 regions where the wrapped DNA contacts the histone octamer surface [2, 106,
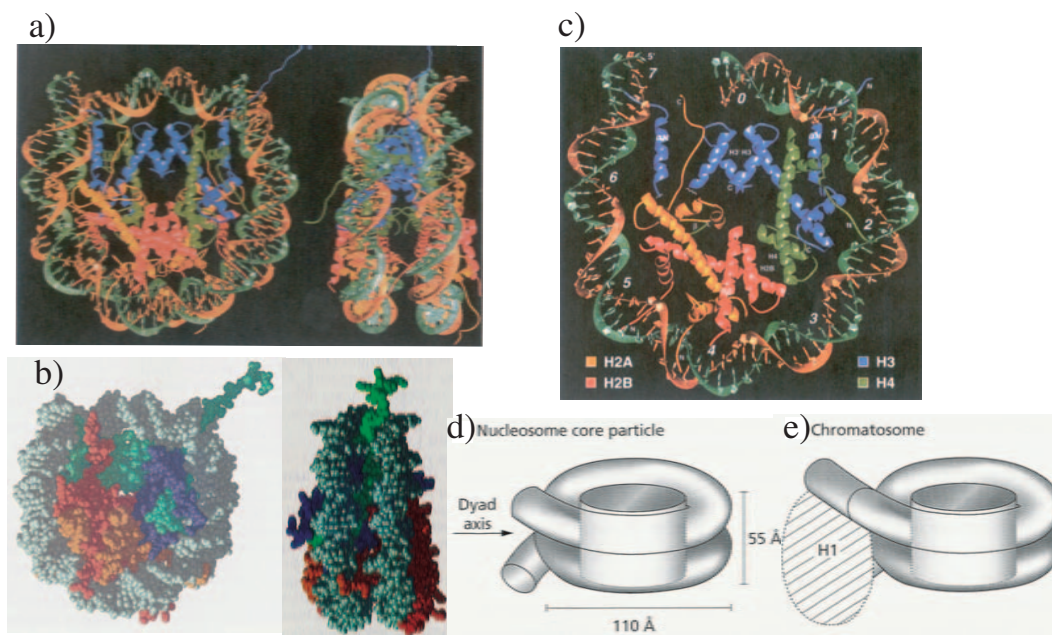
Figure 1.6: a) Computer-generated ribbon diagram [148, 2] and b) space filling diagram [148, 1] showing two different views of the structure of the nucleosome core particle based on X-ray crystallographic analysis at 2.8 $\mathring{A}$ resolution [148]. c) Computer-generated ribbon diagram [149, 2] showing the path of a single turn of the DNA helix around the histone core and histones arrangement within the core. One complete molecule of each histone is shown, together with parts of the second histone H3 molecule. The histone handshake motif, by which H2A interacts with H2B and H3 with H4, is clearly seen. Note the variable curvature of DNA as it folds around the histone core. d) A schematic picture of the nucleosome core particle [2]. The location of dyad axis and dimensions of the nucleosome core particle are given. e) Schematic view of the chromatosome [2], where possible location of histone H1 is demonstrated. Histone H1 adsorbs 19 base-pairs of DNA, and as a result, chromatosomal DNA amounts to 165 base-pairs.

148, 149]. These contacts are located where the minor grooves face the octamer surface and may involve specific bindings and hydrophobic interactions besides the overall electrostatic attraction between positive charges of histones and negative charges on the DNA backbone. In particular, at some contact regions there are several direct hydrogen bonds [148]. Though a reliable quantitative estimate of the binding energies due to contact sites is not yet available, an indirect method of estimating the mean binding energy (based on competitive protein binding to nucleosomal DNA [74, 75, 76]) suggests a value of about few $k_{\mathrm{B}}T$ per contact site [74, 75, 76, 50], which is nearly balanced by the energy cost due to the bending of the DNA around the histone core [50]. An estimate of the binding energy including only electrostatic and bending effects (i.e. electrostatic self-energy and bending of DNA as well as its electrostatic attraction with the histone core neglecting other specific effects) leads to a much larger binding energy of about $\sim 85k_{\mathrm{B}}T$ (measured with respect to an uncomplexed reference state) for a weak effective histone charge of $+20e$ in physiological salt concentration (100 mM NaCl) [48, 49, 210]. This huge binding energy suggests a dominant electrostatic stabilization of the nucleosome core particle. But, strikingly, at low salt (and also at high salt), the interplay between bending and electrostatic effects reproduces the low-salt expanded

(or unwrapped) DNA state [40, 48, 49] as observed also in experiments [83, 86, 84, 87, 88, 89, 90, 103, 104, 82] (see below).

A host of different experiments have been performed in oder to understand the mechanisms that control the structural stability of the nucleosome core particle. One class of experiments include investigation of the response of chromatin or subunits thereof to an external mechanical stress [107, 108], that gives insight into DNA-histone interactions (see also theoretical investigations in Refs. [77, 49, 97, 124, 139]). Interestingly, markedly different stretching responses are found at low and high salt concentration [107, 108] Another class of experiments [143, 145, 147, 146, 152, 153, 155, 151] involve chemical modification of the histones or DNA sequence, which provide insight into the specificity of interactions and allow to precise alteration of histone core charges (for instance, by acetylation and phosphorylation of amino acid residues of the histones). This again reflects the relevance of electrostatic interactions, which is confirmed by a third class of experiments that focus on the salt-induced behavior of the nucleosome core particles as will be briefly mentioned below.

Salt-induced behavior

The influence of salt concentration on the stability of nucleosome core particles has been considered experimentally using a variety of methods such as sedimentation studies [81, 84, 142], flow birefringence [82], neutron scattering [113], fluorescence [85, 86, 87, 88, 89, 90, 91], electrophoresis [103], x-ray scattering [212], and osmometry [212]. Some of these results have been summarized in Ref. [104] giving the following general trends: i) the native structure of nucleosome core particle remains stable in the range of salt (NaCl) concentrations between 2 mM and 750 mM (including in particular the physiological regime of 100 mM), which represents a *wrapped state* for DNA within the core particle; ii) below 1 mM, DNA is partially unwrapped forming the so-called low-salt *expanded state* of the nucleosome; iii) at very small salt concentrations (about 0.2 mM NaCl) an irreversible transition occurs which involves dissociation of the histone core and the DNA; iv) at salt concentrations beyond 0.75 M, dissociation of the histone core (including, e.g., dissociation of H2A-H2B dimers from (H3-H4)$_2$ tetramer) and also histone oligomers from DNA has been observed [85, 91, 104, 105]; beyond 1.5 M, the core particle is completely dissociated into histone oligomers and free DNA.

The strong dependence of the stability of the nucleosome core particles on salt concentration suggests an electrostatic origin for the predominant interactions, because electrostatic forces are highly influenced (due to a screening mechanism that will be explained later) by the presence of mobile co- and counterions introduced through the salt. Theoretical studies [48, 49, 72] have already shown that the experimental findings regarding the salt-induced wrapping-dewrapping behavior of the nucleosome core particle can be captured within a simple chain-sphere model that accommodates basic electrostatic and bending factors [48, 49, 72] (see the overview in Chapter 2). A generalization of these results for a generic charged polymer-macroion complex is presented later in this thesis (Chapter 3).

In addition, the experimental stability diagram [104] exhibits an association (or complexation) equilibrium between nucleosome core particles with free DNA and free histones in solution at moderate core particle and salt concentrations [104]. This signifies the role of thermal fluctuations in the complex formation process at intermediate concentrations, which is the subject of investigations in Chapter 5 [72].

Overcharging

On the theoretical side, an interesting aspect of the nucleosome core particle structure is that the total charge of DNA wrapped around the histone is more than the net charge of the histone core itself. The total charge of DNA (of 146 base pairs length) is -292e, while the net charge of the histone core is about +100e as discussed before. Neglecting other effects such as charge regulation (which can lower the effective histone charge), one ends up with about -190e overall charge for the core particle complex. Therefore, despite what one might naively expect, more DNA is adsorbed on the histone core than is necessary to neutralize its charge. Clearly, the self-repulsion of charged units on the DNA (as well as DNA bending rigidity) work against its electrostatic attraction to the histone core. Although the adsorption of DNA on the histone core may be aided by additional specific binding effects (such are hydrogen bounds [148]), recent theoretical studies exhibit that the *overcharging* of a charged sphere by a semiflexible charged chain such as DNA may be driven solely by peculiar electrostatic effects [45, 37, 65, 66, 67, 68, 69, 48, 49].

The overcharging has indeed emerged as a generic electrostatic mechanism that appears in a variety of problems such as DNA-lipid complexes and polyelectrolyte multilayer formation [69]. For the problem of DNA-histone complexation, several overcharging mechanisms have been introduced in literature including *counterion release* [45, 54, 55] and *structural correlations* [69]. In the former case, the free energy of complexation of a polyelectrolyte chain with macroion is dominated by the entropy of counterions released upon polyelectrolyte adsorption. (Note that counterions may be highly condensed around the polyelectrolyte or the macroion depending on their charge and surrounding conditions–see Chapter 2.) This mechanism may be particularly relevant at low salt concentrations and has been discussed in detail in Ref. [50]. On the other hand, structural correlations arise as a result of the coupling between electrostatic interactions and conformational changes of the polyelectrolyte chain as it adsorbs on an oppositely charged macroion [64, 69, 70, 49, 210, 40, 37, 45]. These effects can lead to an enormous overcharging particularly at high salt concentrations that will be considered in more detail in the following chapters.

1.2.4   Chromatin

Though a great deal of information has emerged from recent studies of the nucleosome, much less is known about the higher-order structures to which it gives rise. On the next level of DNA compaction, nucleosome core particles are linked to each other to form the so-called *chromatin fiber*, which has been subject of intense experimental [116, 118, 119, 121, 122, 123, 124, 125, 126, 128, 130] and theoretical [135, 136, 137, 138, 139, 140] works in recent years. One of the main issues is that how nucleosome core particles are arranged along the chromatin fiber and what are the underlying mechanisms stabilizing the fiber?

Under controlled treatment (e.g., exposure to low salt concentration), the chromatin fiber exhibits a stretched swollen or expanded structure resembling a *beads-on-a-string* structure (see Figure 1.7b). The string is DNA and the beads are individual nucleosome core particles as described before. This structure is also known as the "10 nm fiber" due to the diameter of about 10 nm of its beads. As the salt concentration increases, the fiber becomes gradually more folded and compact [116, 123, 105], and eventually at the physiological condition, it exhibits a thick and dense fiber of diameter about 30 nm, the so-called "30 nm fiber" (Figure 1.7a).

a)

b)
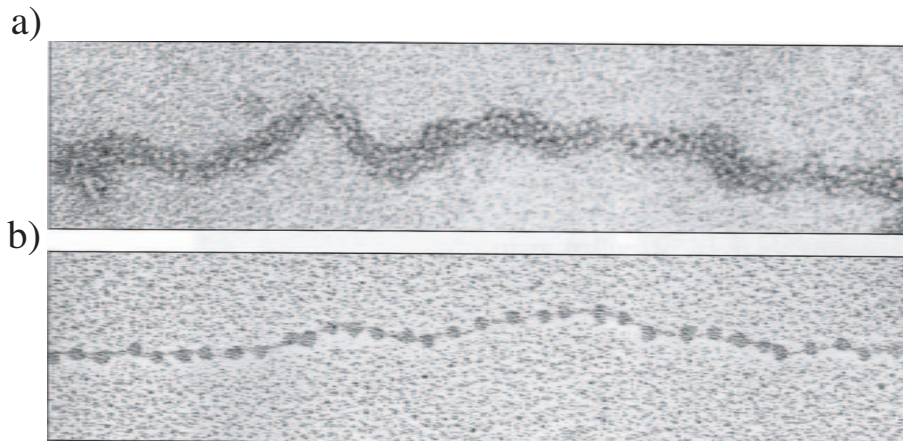
Figure 1.7: a) Chromatin isolated directly form cell nucleus appears in the electron micrograph as a 30 nm thick fiber. b) The experimentally unpacked, or swollen, chromatin (10 nm fiber) displays a beads-on-a-string pattern consisting of linked nucleosomes (Figures after Ref. [1]).

The precise structure of the 30 nm fiber has been subject of much debate in the past and several different models have been proposed for the arrangement of nucleosomes within this fiber (see the review in Ref. [50]). These include *solenoidal models* [2, 50], in which the string of nucleosomes form a solenoidal structure with the linker DNA bent in between consecutive nucleosomes, and helical *zig-zag* or *crossed-linker models* [2, 50, 122], in which straight DNA linkers connect consecutive nucleosomes that are located on the opposite sides of the fiber. In other words, in solenoidal model consecutive nucleosomes (linked by a single linker DNA) remain side by side (as nearest neighbors), while in zig-zag structure they take up positions on opposite sides of the fiber helix and the linker DNA joining them bridges the helical core. These models are constructed mainly based on geometrical considerations and the available evidence from experiments. Naively speaking, the solenoidal model may appear energetically unfavorable since the linker DNA in that case must bend sharply between adjacent nucleosomes. On a systematic level, however, one should account for geometrical factors as well as the interactions between various components in the system (e.g., histone core, DNA wrapped around the histones, linker DNA) in order to determine the energetically optimized form of the fiber (see Chapter 4 of this thesis).

Although existing experimental results on the 30 nm fiber can not yet completely exclude one of the two models mentioned above in favor of the other [2, 123, 133], substantial evidence is available which indicates a zig-zag structure at physiological conditions. Images obtained by electron cryomicroscopy [123, 122, 116] show a zig-zag motif at reduced salt concentrations and that this zig-zag structure is preserved and becomes more and more compact as the salt concentration is increased up to the physiological value [123] (see Figures 1.8a-c). A similar picture is obtained from force microscopy measurements [127, 128, 129]. In this respect, recent experiments in which single fibers can be stretched using micromanipulation techniques provide further insight into the detailed organization of the chromatin fiber [108]. Computer simulations [124, 136, 138, 140] and analytical models [137, 139], when compared with experiments, appear to support the zig-zag model. One of the models used for the 30 nm fiber is the so-called two-angle model [122], which is purely geometrical and yields a variety of
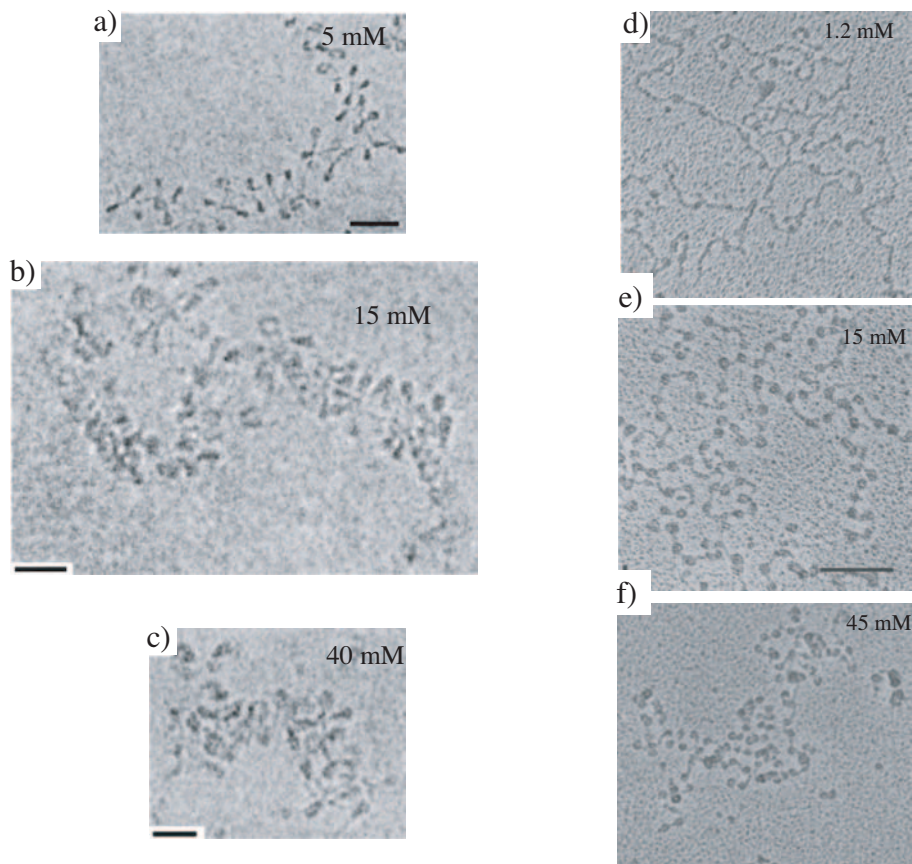
Figure 1.8: Electron cryomicroscopy of the chromatin extracted from different organisms in ionic strength of about 5 mM (a), 15 mM (b) and 40 mM (c) of monovalent salt respectively [123]. d), e) and f) demonstrate the ionic strength dependence of the structure of H1-depleted chromatin for monovalent salt concentration of about 1.2 mM , 15 mM and 45 mM respectively [116].

zig-zag conformations depending on two independent variables, namely, the entry-exit angle of DNA strand wrapped around the histone core and a rotational (dihedral) angle between axis of consecutive histone octamers along the fiber. This model has also been used to study mechanical properties of the fiber [137] as well as the influence of short-ranged nucleosome-nucleosome interactions within the fiber on these properties [137, 139].

The salt-induced swelling of the chromatin indicates that electrostatic interactions play a crucial role in organization of the fiber [50, 119, 120]. Furthermore, the linker histone H1 (or H5) [116, 117] as well as N-tails of the core histones [1, 144], which both carry considerable positive charges, appear to influence the conformation of the fiber, which reflects their possible interactions with the negatively charged DNA. As mentioned before, the linker histone is located outside the core particle and "glues" together the entering and exiting strands of the DNA along a short section giving rise to a "stem-like" structure (see Figures 1.8 and 1.9). This is believed to be important in the compaction of the chromatin fiber at elevated salt; in the absence of the linker histone, entering and exiting DNA strands are diverged and displaced with respect to each other, and as a result, the fiber exhibits an open and loose structure (see Figure 1.8 d, e and f) [116]. The electrostatic repulsion between the DNA strands in
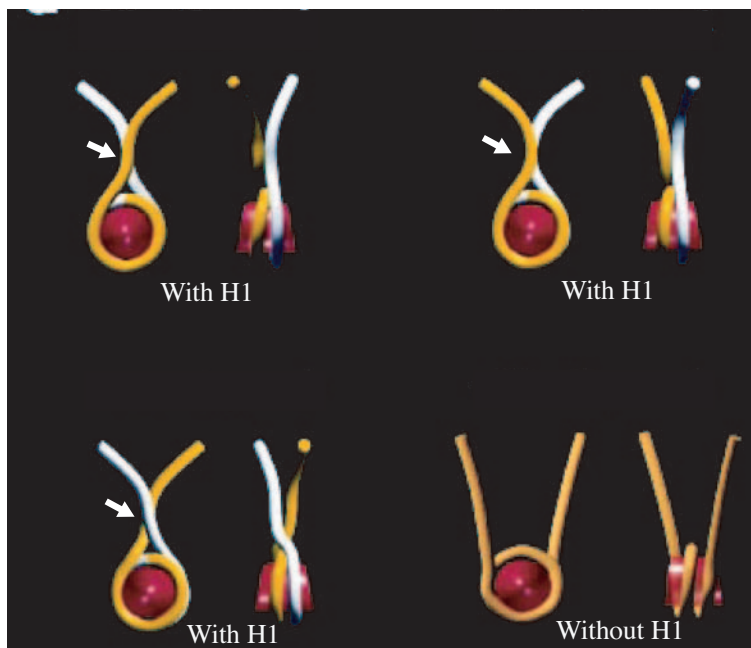
Figure 1.9: A schematic view of the nucleosome structure in chromatin with and without linker histone as indicated in the graph. As shown, the presence of linker histone glues the two stands of linker DNA together, giving rise to a stem like structure (shown by arrows). Three different ways of bringing two DNA linker strands together is demonstrated [123].

the presence of H1 linker is highly screened for increasing salt and, as a result, the entry-exit angle is expected to reduce, which can explain the compaction of the chromatin fiber with increasing salt concentration [139]. On the other hand, the cationic histone tails can interact and complex with the linker DNA, screening their bare electrostatic repulsion, and thus can aid the compaction of the fiber as well [139] (they can even mediate attractive interactions between neighboring nucleosomes [1, 157]). The precise role of these various factors has however remained largely elusive.

1.3   Overview of this work

The central goal in this thesis is to establish unambiguous results based on simple well-defined models for those aspects of charged polymer-macroion complexes that are mainly associated with electrostatic effects. I therefore adopt a series of well-defined approximations that incorporate electrostatic interactions but also account for elastic contributions and conformational changes of the polymer chains within a simple chain-sphere scheme.

In Chapter 2, I present the details of the chain-sphere model and discuss the approximations and theoretical methods involved in the studies presented in the forthcoming chapters. In particular, I will discuss the so-called ground-state approximation used to investigate strongly coupled complexes, i.e. complexes characterized by a large polyelectrolyte adsorption energy and small chain fluctuations. I will explain how ground-state configuration of a single complex can be classified based on its symmetric properties.

Chapter 3 concentrates on the structural properties of a single strongly coupled polyelectrolyte-macroion complex. Here I present a global analysis based on a rescaled (dimensionless) representation of the chain-sphere model. This leads to a generic (universal) phase diagram characterizing the wrapping-dewrapping transition of a polyelectrolyte chain on an oppositely charged macroion in a wide range of realistic system parameters. This chapter therefore generalizes previous studies that concentrate on the structural properties of a complex with parameters chosen appropriate for the DNA-histone system [40, 48, 49]. Emphasize is made on the interplay between the effects due to the PE chain length, salt concentration, the macroion charge as well as the mechanical chain persistence length and special attention is paid to chains with zero mechanical bending rigidity.

In Chapter 4, I consider complex fiber that are formed by a single long polyelectrolyte chain complexed with *many* oppositely charged spherical macroions. I develop a numerical method based on a chain-sphere cell model, which enables one to investigate the mechanism and stability of complex fibers within the ground-state approximation. The ultimate goal of this approach would be to model the structure of the chromatin fiber. In the present work, however, I will concentrate on a simple generic model in which some of the specific structural details of the chromatin (such as linker histones and histone tails) are neglected.

In Chapter 5, I investigate the thermodynamic stability of complexes formed by one semiflexible charged polymer wrapped around an oppositely charged sphere by incorporating thermal fluctuations around the ground-state configuration. Choosing parameters suitable for DNA-histone system, I determine all conformational eigen-modes and the corresponding eigen-value spectrum of the complexed chain fluctuations on the sphere, from which the free energy of complexation (binding) is obtained. This free energy includes the adsorption energy of the chain as well as the entropy loss chain suffers upon binding to the sphere. Using this I determine the so-called reaction constant corresponding to the complex formation process in a solution of charged polymers and macroions. Hence a global complexation phase diagram as a function of salt and DNA/histone concentration is obtained, which exhibits qualitative agreement with experimental results.

In Chapter 6, I investigate the effective interaction between two polyelectrolyte-macroion complexes within the ground-state approximation. It will be shown that at small distances, the complexes become highly correlated due to structural changes of the polyelectrolyte chains which leads to an asymmetric binding state (where positively charged patches on one complex match up with negatively charged patches on the other complex) or a bridging state (where one polyelectrolyte chains bridges between the two complexes). This gives rise to a strong attraction between complexes and thus a negative second virial coefficient associated with the inter-complex interaction at intermediate salt concentrations within the range where stable complexes are formed. These findings agree qualitatively with recent experiments on nucleosome core particles. I shall demonstrate that a simple screened monopole-dipole model reproduces these results.

Chapter 2

Chain-Sphere Model: An overview

This chapter provides an overview of the chain-sphere model and the theoretical methods that will be used to study polyelectrolyte-macroion complexes in the forthcoming chapters. In particular, I will discuss the so-called ground-state approximation used to investigate strongly coupled complexes and explain how ground-state configuration of a single complex can be classified based on its symmetry properties.

Designing a theoretical model that can account for the characteristic features of polyelectrolyte-macroion complexes requires a number of approximations concerning the structural details and interactions of polyelectrolyte (PE) chains and macroions. The *chain-sphere model* [39, 48, 49] has emerged as a first-step model for nucleosome core particles (NCPs) capturing the main features responsible for the salt-dependent behavior of NCPs as observed in recent experiments [86, 81, 84, 87, 88, 89, 90, 91, 102]. This model, as I shall review in what follows, combines the basic electrostatic and elastic aspects of PE-macroion complexes by adopting a number of simplifications. Yet given those simplifications, establishing a full theoretical analysis of the complexation process within this model appears to be a challenging problem. A rigorous analytical theory is still missing, and numerical results have emerged recently [14, 52, 41, 42, 44, 43, 48, 49, 72, 210].

The main advantage of the chain-sphere model is that it provides a well-defined theoretical framework allowing to identify those aspects of PE-macroion complexes, which are governed by electrostatics. It serves as a generic model and can in principle be adapted for charged chain-sphere complexes other than nucleosome core particles as long as other specific structural or interaction effects, which can be included later on as corrections, are not dominant.

The details of the chain-sphere model and the involved approximations will be reviewed in Section 2.1. In Section 2.2, I will briefly describe the regime of parameters corresponding to *strongly coupled* PE-macroion complexes that are of primary interest in this thesis. I will then discuss the ground-state-dominance approximation that will be used in Chapters 3, 4 and 6, and then explain how small-amplitude chain fluctuations around the ground-state may be taken into account as will be addressed in detail later in Chapter 5. Most of the studies in this thesis make use of numerical methods due to the complexity of the problem at hand. Here I will give a detailed review of the numerical minimization methods used to obtain the ground state of a complex (Section 2.3). Finally, I provide a brief review of characterization (or classification) methods for ground-state phases of a PE-macroion complex [39, 48, 49, 210, 72], which will be discussed separately in Chapter 3.

a)

$l_{\mathrm{p}} \ll L$

b)

$l_{\mathrm{p}} \approx L$

c)

$l_{\mathrm{p}} \gg L$

d)

$s = 0$ $\mathbf{T}(s)$

$s = L$

$\mathbf{T}(s')$

$$\langle \mathbf{T}(s) \cdot \mathbf{T}(s') \rangle \sim \exp(-|s\text{-}s'|/l_{\mathrm{p}})$$
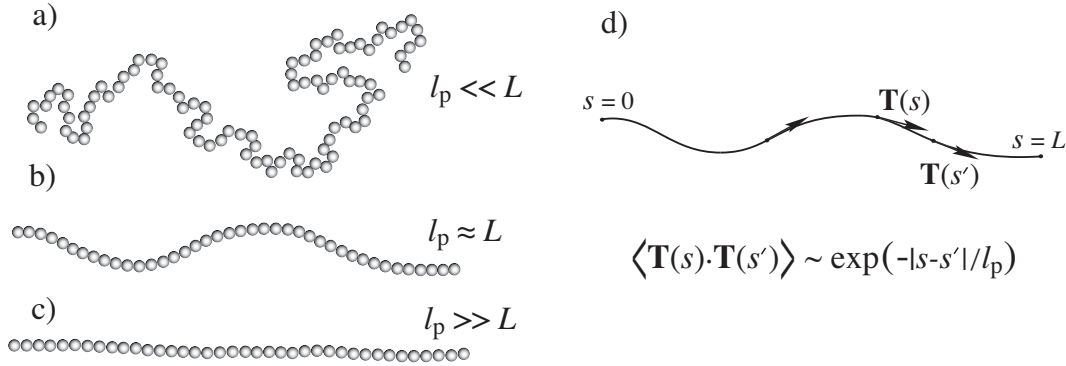
Figure 2.1: Schematic representation of *neutral* polymer chains with different stiffness properties. They may be classified as a) flexible ($\ell_{\mathrm{p}}/L \ll 1$), b) semiflexible ($\ell_{\mathrm{p}}/L \sim 1$) and c) rigid chains ($\ell_{\mathrm{p}}/L \gg 1$) depending on the ratio between chain (bare) *mechanical* persistence length, ℓ_{p}, and its contour length, L. For a charged chain, the same criterion may be applied by making use of the *effective* persistence, which is the *mechanical* persistence length plus an additional contribution from electrostatic self-repulsion of charged monomers (see the text and footnote 1). d) The mechanical persistence length, ℓ_{p}, of a neutral chain may be defined as the distance along the chain contour over which the tangent vectors, $\mathbf{T}(s)$, of the chain loose correlation ($0 \leq s \leq L$ is the contour parameter). One thus expects $\langle \mathbf{T}(s) \cdot \mathbf{T}(s') \rangle \sim \exp(-|s - s'|/\ell_{\mathrm{p}})$ when averaged over equilibrium configurations [6]. This concept can be generalized for charged chains as well.

2.1 Models and approximations

2.1.1 Polyelectrolyte chain

I describe the polyelectrolyte by an inextensible charged polymer chain of contour length L that may or may not have an intrinsic (mechanical) bending rigidity. I will conventionally assume that the PE chain is negatively charged with a uniform charge distribution of linear density $-\tau e$, where e is the elementary charge. For double-stranded DNA, I will adopt the *bare* value $\tau = 5.88$ nm^{-1} corresponding to maximum dissociation of phosphate groups that gives rise to two elementary charges per base pair of 0.34 nm length. In reality, however, the actual charge may be reduced from its bare value due to charge renormalization and charge regulation effects in an ionic solution that will be discussed briefly later in this chapter.

The PE chain may exhibit a range of stiffness properties depending on its chemical properties, linear charge density and the surrounding conditions such as the salt concentration. In general, the stiffness of the chain contains charge-independent and charge-dependent contributions. The former is due to the energy associated with the deformation of chemical bonds in the polymer backbone (in the case of double-helical DNA, one deals with deformation of hydrogen bonds that stabilize the double helix). This contribution is incorporated within a semiflexible (or worm-like) chain model using a finite *mechanical* bending stiffness or equivalently, a *mechanical* or *bare* persistence length ℓ_{p} (see the illustration in Figure 2.1).

The charge-dependent contribution to the chain stiffness stems from the fact that the charged monomers along the polymer backbone repel each other and tend to maximize their mutual distances leading to electrostatic stiffening of the PE chain [174, 175, 176, 177, 185]. Clearly, this electrostatic contribution is maximum in the absence of salt screening effects, where charged monomers interact with long-ranged Coulomb interaction. In the presence of

salt, these interaction are effectively screened (e.g., according to the Debye-Hückel mechanism [12] as will be discussed later) leading to a smaller electrostatic contribution to the chain stiffness [174, 175]. In the limit of infinite salt concentration, electrostatic effects diminish and one is left with the bare persistence length ℓ_p. One can in general define a salt-dependent *effective* persistence length, which can be calculated using a variety of methods and approximations [174, 175].[1] In the present analysis, however, I shall include the electrostatic contribution to the chain stiffness on a systematic level by explicitly including the electrostatic self-energy of the PE chain (see below).

For DNA, the mechanical persistence length has been determined in experiments as $\ell_p = 30$ nm [166, 167, 168]. I will not include the twist degrees of freedom explicitly when treating DNA complexes as, for instance, the ends of the DNA chain within nucleosome core particles are free to rotate. A possible coupling between twist and bending degrees of freedom would influence the effective mechanical stiffness of the chain. But these effects are included in the experimentally determined value for the persistence length that will be used here.
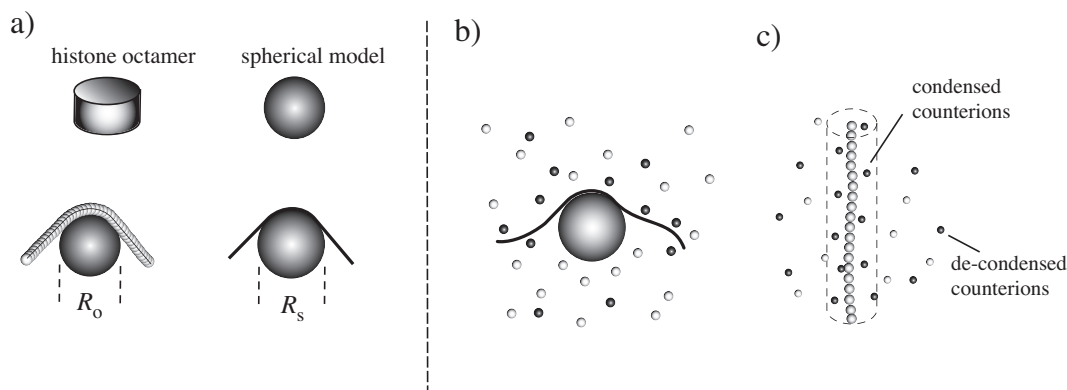
Figure 2.2: a) Macroions such as histone ocatmers are modeled as uniformaly charged sphere (top) with bare radius R_0. The chain diameter (bottom) is taken into account using a closest approach distance R_s (or the effective sphere radius). b) The presence of the mobile counterions of the PE chain and the macroion (shown by black and gray small spheres) lead to a complex many-body problem, which is treated using approximate methods. In particular, counterions lead to charge renormalization effects as they strongly condense around highly charged chains (as well as spheres). For PE chains (c), these non-linear effects can be treated using a two-fluid model [71] as explained in Section 2.1.4.

2.1.2 Macroion

The macroion is modeled as a sphere of radius R_0 with a uniform positive surface charge density. The charge valency of the macroion is taken as $+Z$. This is obviously a rough approximation as the macroion structure in reality may be more complex, e.g., being non-spherical in geometry and with rough surface structure [1]. The realistic charge pattern may be non-uniform and discrete as well. For the specific case of histone octamers in NCPs,

---

[1] A Debye-Hückel approximation analysis of the bending rigidity of an isolated and infinite PE chain (using Eq. (2.4)) yields the effective persistence length of $\ell_p^{\text{eff}} \simeq \ell_p + \tau^2 \ell_B/(4\kappa^2)$ [174, 175]. The first term represents the bare value while the second term stems from electrostatic self-energy with κ and ℓ_B being the inverse Debye screening length and the Bjerrum length as defined in the text. Thus even for a mechanically flexible chain ($\ell_p = 0$), one may have a large bending rigidity at small κ (small salt concentration).

experiments have revealed a cylinder-like structure for the histone core, which is 7 nm in diameter and 5.5 nm height (there are moreover additional flexible histone tails attached to this core). The histone surface possesses regions, which provide specific binding sites with the nucleosomal DNA (see Chapter 1 for details) that are neglected within the chain-sphere model. In actual calculations, I will take the radius of the macroion sphere such that it accounts for the finite radius of the PE chain as well, i.e. it yields the minimal distance of the sphere center and the monomer centers, which is denoted by R_s. For the DNA-histone system, I adopt the value $R_s = 5$ nm (corresponding to a mean histone radius of about $R_0 = 4$ nm and DNA radius of 1 nm)–see the illustration in Figure 2.2. The macroion sphere may be assumed to be rigid (hard core) [48, 49] or semi-rigid (soft core) [210, 72]. Throughout this work, I will adopt a semi-rigid sphere which excludes the PE chain but still allows small penetration of monomers into the sphere as will be discussed later.

   Note that any conformational changes of the macroion structure, which in proteins such as histones may occur for very small (e.g., below 0.2 mM) or very large salt concentrations (e.g., above 0.75 M) [141, 142, 113], are neglected. The most interesting experimental cases occur however within the intermediate salt regime (including, in particular, the physiological concentration of 100 mM monovalent salt), where the histone structure remains stable.

2.1.3   Interaction potentials

The following interaction potentials are included within the chain-sphere model considered in the present work: i) electrostatic interactions between PE chain monomers and the macroion as well as the electrostatic self-energy of the PE chain, ii) mechanical bending elastic energy of the PE chain (which is set to zero for mechanically flexible chains), and iii) a soft-core excluded-volume potential acting only between monomers and the macroion sphere.

Electrostatics

Electrostatic interactions typically result in a challenging many-body problem which can be tackled only within certain approximations. The complication arises due to the long-range nature of Coulomb interactions and the fact that the PE chain and the macroion are always surround by small mobile ions known as counterions and coions. This leads to a coupling between the degrees of freedom associated with the chain and the degrees of freedom associated with small ions, which is hard to account for on a systematic level. One thus commonly employs a number of well-established approximations. Insofar as the strongly coupled PE-macroion complexes are concerned, one can employ a ground-state-dominance approximation to describe the PE chain configuration, because chain fluctuations are relatively small due, for instance, to large effective persistence of the PE chain (see Section 2.2 below and Chapter 5). In contrast, the fluctuations due to the surrounding ionic atmosphere are quite important and have to be taken into account. In prticular, they can modify the bare Coulomb interaction between fixed charges in the system.

   On the mean-field level, that is as long as the correlation effects induced by mobile charges are negligible, one can describe the ionic cloud using the so-called non-linear Poisson-Boltzmann (PB) theory [11] (see Appendix B). The mean-field description holds for low valency ions and not too large charges on the macroions and the PE chain. For the DNA system, for instance, one can safely use it with monovalent salt as verified in experiments [8, 71] and simulations (see [187] and Refs. therein). While the non-linear PB theory can

be applied to a variety of relevant problems, for the purpose of the present study (which is calculation of the optimal path of a PE chain on a spherical macroion), it is at present not feasible even within numerical approaches, due to the coupling between chain fluctuations and ionic profile around the chain-sphere complex [15]. I will thus use the linearized form of the PB theory, the so-called Debye-Hückel (DH) approximation [12], to calculate electrostatic interactions. The DH approximation becomes progressively more accurate for increasing salt concentration. A discussion of non-linear electrostatic effects that are not captured within the DH theory is postponed to Section 2.1.4 below.

The main aspect of the DH theory is that the electrostatic interaction between fixed charges in solution is screened due to the presence of mobile salt (co- and counter-) ions taking an exponentially decaying form. In the absence of these effects, the Coulomb interaction (per $k_{\mathrm{B}}T$) reads

$$v(\mathbf{r}) = \frac{\ell_{\mathrm{B}}}{|\mathbf{r}|}, \tag{2.1}$$

between two elementary charges fixed at separation $\mathbf{r}$, where $\ell_{\mathrm{B}} = e^2/(4\pi\varepsilon\varepsilon_0 k_{\mathrm{B}}T)$ is referred to as the *Bjerrum length* [13] (representing the distance at which two elementary charges interact with thermal energy $k_{\mathrm{B}}T$ in a continuum medium of dielectric constant ε). In the presence of fluctuating salt ions, one obtains the interaction between two fixed elementary charges at separation $\mathbf{r}$ as

$$v_{\mathrm{DH}}(\mathbf{r}) = \ell_{\mathrm{B}} \frac{e^{-\kappa|\mathbf{r}|}}{|\mathbf{r}|}, \tag{2.2}$$

where $\kappa^2 = 4\pi\ell_{\mathrm{B}} \sum_i z_i^2 c_i$ is referred to as the *inverse Debye screening length*. Here c_i is the concentration of the ionic species i of valency z_i. For monovalent salt ($z_i = 1$) of concentration C_s as considered in this work, one has $\kappa^2 = 8\pi\ell_{\mathrm{B}}C_s$. In water and under physiological condition (100 mM monovalent salt, e.g., NaCl, at room temperature), one has $\ell_{\mathrm{B}} \simeq 0.7$ nm and $\kappa^{-1} \simeq 1$ nm.

Effective Hamiltonian

In order to construct the full Hamiltonian of the chain-sphere model within the Debye-Hückel approximation, I first parametrize the polymer configuration by the vector field $\mathbf{r}(s)$ with $0 \leq s \leq L$ being the contour parameter and choosing the sphere center as the origin. The effective Hamiltonian (in units of $k_{\mathrm{B}}T$) may be written as the combination of two terms

$$\mathcal{H}[\mathbf{r}(s)] = \mathcal{H}_p[\mathbf{r}(s)] + \mathcal{H}_{pm}[\mathbf{r}(s)], \tag{2.3}$$

in which

$$\mathcal{H}_p[\mathbf{r}(s)] = \frac{\ell_{\mathrm{p}}}{2} \int_0^L \mathrm{d}s \, [\ddot{\mathbf{r}}(s)]^2 + \tau^2 \ell_{\mathrm{B}} \int_0^L \mathrm{d}s \int_s^L \mathrm{d}s' \, \frac{e^{-\kappa|\mathbf{r}(s)-\mathbf{r}(s')|}}{|\mathbf{r}(s) - \mathbf{r}(s')|} \tag{2.4}$$

is the self-energy of the chain comprising the mechanical bending rigidity (first term) [6, 185]and the electrostatic self-energy (second term) in units of $k_{\mathrm{B}}T$ (note that the mechanical contribution depends on the chain local curvature $\ddot{\mathbf{r}}(s) = \mathrm{d}^2\mathbf{r}(s)/\mathrm{d}s^2$). Here I implicitly assume that the PE chain is inextensible, i.e. $|\dot{\mathbf{r}}(s)| = 1$. The other contribution comes from the PE-macroion interaction energy, that is

$$\mathcal{H}_{pm}[\mathbf{r}(s)] = -\frac{Z\tau\ell_{\mathrm{B}}}{1 + \kappa R_{\mathrm{s}}} \int_0^L \mathrm{d}s \left[\frac{e^{-\kappa(|\mathbf{r}(s)|-R_{\mathrm{s}})}}{|\mathbf{r}(s)|} - A\, e^{-(|\mathbf{r}(s)|-R_{\mathrm{s}})/\alpha} \right], \tag{2.5}$$

where the first term represents the electrostatic PE-macroion attraction within the DH theory (see Appendix B), and the second term represents the soft-core repulsion term characterized by two parameters A and α for the strength and the range of repulsion respectively.[2] I typically choose $A \ll 1/R_{\mathrm{s}}$ and $\alpha < \kappa^{-1}$, which gives an equilibrium sphere-monomer separation about the sphere radius R_{s} and guarantee the impenetrability of the sphere.

Note that the self-energy of the PE chain, $\mathcal{H}_p$, tends to straighten the PE chain. In the absence of the macroion, the minimal energy state of the PE chain is given by a straight line. While the mechanical bending rigidity term (first term in Eq. (2.4)) is independent of the salt concentration, the electrostatic self-energy (second term in Eq. (2.4)) becomes smaller upon increasing the salt concentration. At the same time, the PE-macroion attraction, which works against the two former contributions and tends to wrap the PE chain around the macroion, becomes weaker for increasing salt concentration. This transpires that the interplay between several factors including salt concentration, macroion charge and bare persistence length, determines the complexation behavior of the PE chain in a complicated manner as will be demonstrated in detail in Chapter 3.

The foregoing description of interactions involves several other assumptions that are worth-mentioning here. One is that the presence of solvent is introduced through a homogeneous dielectric constant (which in the case of water at room temperature is $\varepsilon \simeq 80$). Therefore image charge effects due to mismatch of the dielectric constant at boundaries are neglected. Within the present model, the interaction between PE charges is not influenced by the presence of the salt-excluded region introduced by the sphere. This effect modifies the interactions on the DH level at most by a factor of two [38, 40, 39]. I have also neglected possible excluded-volume interactions between chain monomers. Additional effects such as van-der-Waals forces, hydrogen bonds, solvent-induced interactions [4] and sequence specific binding effects [106, 93] and structural defects that might occur for the case of DNA [80] are neglected as well.

2.1.4 Non-linear effects: Counterion condensation

The DH interaction potential used in Eq. (2.3)-(2.5) neglects the non-linear electrostatic effects introduced by the ionic atmosphere around charged objects. On the mean-field level, these effects are fully incorporated within the non-linear Poisson-Boltzmann theory and may be introduced on the linear DH level using the approximate charge renormalization scheme [71]. The difference in geometry of the (linear) PE chain and the (spherical) macroion leads to qualitatively different behavior for surrounding counterions. For charged cylinders (or line of charges), Manning [71] and Oosawa [8] introduced an approximation scheme to the full non-linear problem, which is based on the concept of counterion condensation (see Appendix B for details).

In brief, one finds that in the presence of an infinite charged cylinder, counterions undergo a condensation transition, which is regulated by the dimensionless Manning parameter $\xi = z\tau\ell_{\mathrm{B}}$ [71], where z is the counterion valency taken as $z = +1$ for monovalent salt. For weakly charged cylinders $\xi < 1$, counterions dilute away from the vicinity of the cylinder due to dominant entropic factors. For highly charged cylinders $\xi > 1$, energetic attraction toward the cylinder wins and a fraction $1 - 1/\xi$ of counterions condense around the cylinder and partially renormalize its bare linear charge density $-\tau$. The counterions are therefore treated as a two-fluid system of condensed and de-condensed counterions at equilibrium with each

---

[2]Taking a soft potential is crucial when investigating thermal fluctuations of the PE chain adsorbed on the sphere (see Chapter 5 and Appendix E).

other (see Figure 2.2) [71, 8]. According to Manning [71], one can employ the DH theory in both regimes of ξ provided that one uses the renormalized charge, $-\tau^*$, of the cylinder as a boundary condition, that is

$$
\tau^* = \begin{cases} \tau & \xi < 1, \\[2mm] \tau/\xi = 1/\ell_{\mathrm{B}} & \xi > 1, \end{cases} \tag{2.6}
$$

for monovalent counterions. Note that the renormalized linear charge density is *independent* of the bare charge density. For DNA with the linear charge density of about $\tau = 5.88$ nm^{-1}, one obtains the Manning parameter of $\xi = 4.2$ and thus the renormalized linear charge density of $\tau^* \simeq 1.4$ nm^{-1} at room temperature and for monovalent salt. Naively, one may state that nearly 75% of the DNA charge is compensated by monovalent counterions. It turns out however that the assumption that condensed counterion "neutralize"the bare PE charge (i.e. counterions condense into a narrow region around the chain [71]) gives only a crude picture of the way counterions are distributed around the PE chain, which agrees more closely with a smooth density profile [187]. Yet, the preceding phenomenological counterion-condensation scheme can be put on a more rigorous basis using the non-linear PB theory [188].

In brief, the non-linear charge renormalization due to *counterion condensation* at charged polymers can be accounted for approximately within the DH approach by adopting the Manning charge-renormaliztion scheme [71, 189, 49]. For the purpose of the present work, the following remarks are in order.

First, the counterion-condensation effects become highly suppressed at elevated salt, i.e. for finite Debye screening length, κ^{-1}. In fact, the renormalized charge given by Eq. (2.6) is obtained in the strict limit of vanishing salt $\kappa \to 0$ and represents a *lower bound* for the effective renormalized charge of a charged line or cylinder. Secondly, this result is valid for an infinite cylinder, where end effects are absent. For a short cylinder or charged polymer, the counterion condensation is again suppressed because near the end-points (or at sufficiently large distances comparable to the polymer length) the form of the electrostatic potential attracting counterions changes toward that of a spherical object.[3] In this case, entropic effects become relevant and drive counterions away from the charge polymer (see Appendix B). Finally, in the problem of PE-macroion complexation, counterions are driven away from the PE chain due to the presence of the macroion. This bring into play the *counterion release* effects that have been considered extensively in other works [54, 55, 56, 46, 45].

One expects that for the experimentally relevant case of short chains and finite salt, the actual values for the PE charge fall into the range defined by the bare charge, τ (as the upper bound) and the renormalized Manning value (as the lower bound) as long as the mean-field theory holds. In the present work, I will employ the DH potentials but make use of these two limiting values for the PE charge in order to obtain an estimate of possible counterion-condensation effects present in actual systems. A previous single complex study [48, 49] has already shown that the structural phase diagram of the DNA-histon complexes remain qualitatively the same when these effects are included.

---

[3]Note that a charged sphere can not bind or condense its counterions in the absence of outer boundaries or salt screening, because entropy gain upon de-condenstion of counterions to infinity grows much faster ($\sim \ln r$) than the energy loss ($\sim 1/r$) at large distances, r, from the sphere.

2.2 Strongly coupled complexes

The investigations presented in the forthcoming sections of this thesis primarily concentrate on *strongly coupled* polyelectrolyte-macroion complexes, which have attracted a lot of attention in recent years [37, 40, 41, 42, 43, 44, 45, 46, 47, 48, 49, 51, 52]. This is mainly motivated by the fact that from an electrostatic point of view, the DNA-histone complexes occurring in the cell nucleus represent a strongly coupled system.

Qualitatively, one deals with a strongly coupled PE-macroion complex, when, for instance, the PE chain is strongly charged (or effectively rather stiff) and the macroion is highly charged, so that the PE chain forms a flat adsorbed layer on the sphere with pronounced lateral order due to mutual electrostatic repulsions of the PE segments. In other words, the PE segments become strongly correlated. Electrostatic correlations can trigger a number of striking properties such as *overcharging* [37, 65, 66, 67, 68, 69] and inter-complex *attractive* interactions [41, 42, 206, 207, 208, 209, 210] that will be discussed within the chain-sphere model later in the following chapters. The electrostatic adsorption energy of the PE chain on the macroion is typically quite large, and consequently the thermal fluctuations of the PE chain are relatively small. Thus strongly coupled complexes fall formally within the *low-temperature regime*, where the configuration of the PE is predominantly given by its *ground-state* or *optimal* configuration [45, 48, 49, 61, 62, 66, 67, 68, 69, 60] (see the illustration in Figure 2.3).

Note that by contrast in the converse limit of weak coupling (that is at high-temperatures and for flexible, weakly charged chains and macroions with the adsorption energy being comparable to the thermal energy), fluctuation effects are dominant giving rise to a *diffuse* adsorbed polymer layer on the sphere [208, 58, 59, 46, 43, 44]. This regime can be described using mean-field-like approaches including, e.g., variational and self-consistent techniques [56] and will not be considered in the present work.

There is another regime of PE-macroion complexes, which is known as *rosette* regime, that have been studied extensively in the past [61, 62] and observed also within Monte-Carlo simulations [63]. They consist of chain configurations which have multiple point contacts with the macroion sphere and exhibit large low-curvature loops connecting them. These structures are typically obtained for large persistence lengths (as compared with the sphere radius) and large chain lengths, but for relatively small adsorption energy, which is not large enough to bring the whole chain into contact with the sphere. This regime will not be considered in the present work (see Ref. [50] for a recent review).

2.2.1 Ground-state dominance

To demonstrate the strong coupling regime on a more systematic level, I consider the full partition function of a single PE-macroion complex, which, within the DH chain-sphere model, reads

$$\mathcal{Z}_c = \int \mathcal{D}\mathbf{r}(s) \; e^{-\mathcal{H}[\mathbf{r}(s)]}, \tag{2.7}$$

with the effective Hamiltonian $\mathcal{H}[\mathbf{r}(s)]$ being defined in Eqs. (2.3)-(2.5). The above expression incorporates a functional integral over all possible paths of the PE chain in the presence of an oppositely charge macroion which are weighted by the so-called Boltzmann weight of each configuration.

A full analysis of the complexation process based on the full partition function (2.7) is not

strong coupling   weak coupling
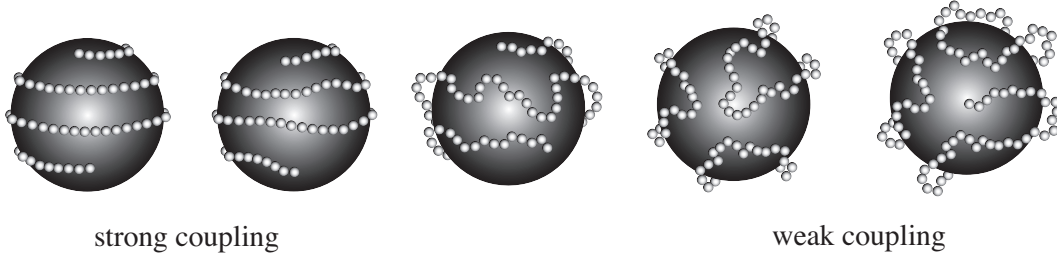
Figure 2.3: Schematic representation of various coupling regimes for PE-macroion complexes. In the strong-coupling regime, due to strong adsorption, the PE chain adopts its ground-state (minimal energy) configuration. Small fluctuations around the ground-state can be accounted for using a saddle-point approximation as discussed in the text and in Chapter 5. In the weak-coupling regime, on the contrary, the PE chain is weakly adsorbed and forms a diffuse layer around the macroion due to dominant fluctuation effects. The crossover between the two regimes may be controlled by the mechanical persistence length, chain linear charge density or macroion charge. This trend has been explicitly observed in recent simulations [43, 44].

yet available. In order to introduce an approximate method applicable in the strong-coupling regime, one may begin with the DH effective Hamiltonian, $\mathcal{H}[\mathbf{r}(s)]$, and rescale the spatial coordinates with a given length λ as $\mathbf{r} \rightarrow \tilde{\mathbf{r}} \equiv \mathbf{r}/\lambda$ and $s \rightarrow \tilde{s} \equiv s/\lambda$. One thus ends up with the rescaled effective Hamiltonian

$$
\begin{aligned}
\mathcal{H}[\tilde{\mathbf{r}}(\tilde{s})] &= \frac{\ell_{\mathrm{p}}}{2\lambda} \int_0^{\tilde{L}} \mathrm{d}\tilde{s}\, [\ddot{\tilde{\mathbf{r}}}(\tilde{s})]^2 + \lambda \tau^2 \ell_{\mathrm{B}} \int_0^{\tilde{L}} \mathrm{d}\tilde{s} \int_{\tilde{s}}^{\tilde{L}} \mathrm{d}\tilde{s}'\, \frac{e^{-\tilde{\kappa}|\tilde{\mathbf{r}}(\tilde{s})-\tilde{\mathbf{r}}(\tilde{s}')|}}{|\tilde{\mathbf{r}}(\tilde{s}) - \tilde{\mathbf{r}}(\tilde{s}')|} \\
&\quad - \frac{Z\tau\ell_{\mathrm{B}}}{1+\tilde{\kappa}\tilde{R}_{\mathrm{s}}} \int_0^{\tilde{L}} \mathrm{d}\tilde{s} \left[\frac{e^{-\tilde{\kappa}(|\tilde{\mathbf{r}}(\tilde{s})|-\tilde{R}_{\mathrm{s}})}}{|\tilde{\mathbf{r}}(\tilde{s})|} - \tilde{A}\, e^{-(|\tilde{\mathbf{r}}(\tilde{s})|-\tilde{R}_{\mathrm{s}})/\tilde{\alpha}} \right],
\end{aligned}
\tag{2.8}
$$

where other rescaled parameters are defined as $\tilde{R}_{\mathrm{s}} = R_{\mathrm{s}}/\lambda$, $\tilde{L} = L/\lambda$, $\tilde{\kappa} = \kappa\lambda$, $\tilde{\alpha} = \alpha/\lambda$ and $\tilde{A} = \lambda A$. The length scale λ may be arbitrarily chosen to be the chain contour length L, the sphere radius R_{s}, the inverse screening length κ^{-1}, or a combination of other factors that yields a quantity of length dimensionality.

The strong coupling regime for a PE-macroion complex may be defined as a regime of parameters where the dimensionless prefactors of the self-energy terms, $\ell_{\mathrm{p}}/\lambda$ and $\lambda\tau^2\ell_{\mathrm{B}}$, in the rescaled Hamiltonian (2.8) become sufficiently large, i.e. $\ell_{\mathrm{p}}/\lambda > 1$ and $\lambda\tau^2\ell_{\mathrm{B}} > 1$ for a physically relevant choice of λ. Choosing $\lambda = R_{\mathrm{s}}$, these conditions amount to a large *effective* (electrostatic plus mechanical) persistence length (incorporated via the self-energy terms) of the PE chain as compared with the sphere radius. While choosing $\lambda = L$ yields a more stringent condition as compared with the former case, with a large effective persistence length as compared with the chain contour length L.

For the nucleosome core particles, the DNA strand length is about 50 nm (corresponding to 146 base pairs) and the histone diameter is about 5 nm, while the bare mechanical persistence length of the DNA has been determined as 30 nm [158, 166, 167, 168]. Clearly, the preceding strong coupling conditions are satisfied for this system given the relatively large persistence length and linear charge density of DNA.

Optimal chain configuration

When system parameters satisfy the strong-coupling conditions, the integrand involved in the functional integral in Eq. (2.7) becomes dominated by the saddle-point of the effective Hamiltonian (2.3). The *saddle-point solution*, $\mathbf{r}_*(s)$, may be obtained in *actual units* using the Euler-Lagrange equation

$$\frac{\delta \mathcal{H}[\mathbf{r}(s)]}{\delta \mathbf{r}(s)}\bigg|_{\mathbf{r}_*(s)} = 0. \tag{2.9}$$

This equation can be used to determine the *optimal* or *ground-state* path of the PE chain on a sphere corresponding to the minimal value for energy or effective Hamiltonian. The optimal solution $\mathbf{r}_*(s)$ can be calculated numerically using a discretization procedure [48, 49, 210, 72], which will be discussed in Section 2.3 below.

Gaussian chain fluctuations

Small fluctuations of the chain around its optimal configuration may be accounted for using a saddle-point approximation, i.e. by expanding the Hamiltonian up to the second order around $\mathbf{r}_*(s)$ as

$$\mathcal{H}[\mathbf{r}(s)] \simeq \mathcal{H}[\mathbf{r}_*(s)] + \frac{1}{2} \int_0^L \mathrm{d}s\,\mathrm{d}s'\,(\mathbf{r}(s) - \mathbf{r}_*(s))^t \frac{\delta^2 \mathcal{H}}{\delta \mathbf{r}(s)\delta \mathbf{r}(s')}\bigg|_{\mathbf{r}_*(s)} (\mathbf{r}(s') - \mathbf{r}_*(s')), \tag{2.10}$$

which gives the so-called Gaussian-fluctuations contribution around the ground state. Inserting this into Eq. (2.7), one ends up with the partition function of a complex within the saddle-point approximation as

$$\mathcal{Z}_c \simeq \sqrt{\frac{(2\pi)^3}{\det \mathbf{H}}}\; e^{-\mathcal{H}[\mathbf{r}_*(s)]}, \tag{2.11}$$

which requires evaluation of determinant of the Hessian matrix

$$\mathbf{H} = \frac{\delta^2 \mathcal{H}[\mathbf{r}_*(s)]}{\delta \mathbf{r}_*(s)\delta \mathbf{r}_*(s')}. \tag{2.12}$$

The above procedure allows one to include the effects of thermal fluctuations on the complexation behavior of PEs and macroions in the strong-coupling regime, which is of key importance in the *thermodynamics* of complexation process in dilute solutions [103, 104, 72]. This can be addressed using numerical methods as will be discussed in detail in Chapter 5.

2.3   Numerical minimization method

Analytical minimization of the Hamiltonian (2.3) is difficult in three dimensions, while in two dimensions only perturbative results are available [40] and no closed-form expression can be given for the ground-state or optimal chain configuration. Numerical minimization techniques, however, have been used successfully in the past to study the problem of a single DNA-histone complex [48, 49]. In this work, I will use a similar numerical minimization method with a few technical improvements as compared with the previous applications [48, 49]. Previous methods employ a constrained minimization scheme since the sphere was assumed to be hard-core, which excludes the DNA chain from a spherical region in space. Here I adopt a soft-core repulsion (second term in Eq. (2.5)) which can be conveniently adjusted and allows a minimization method without an additional constraint.
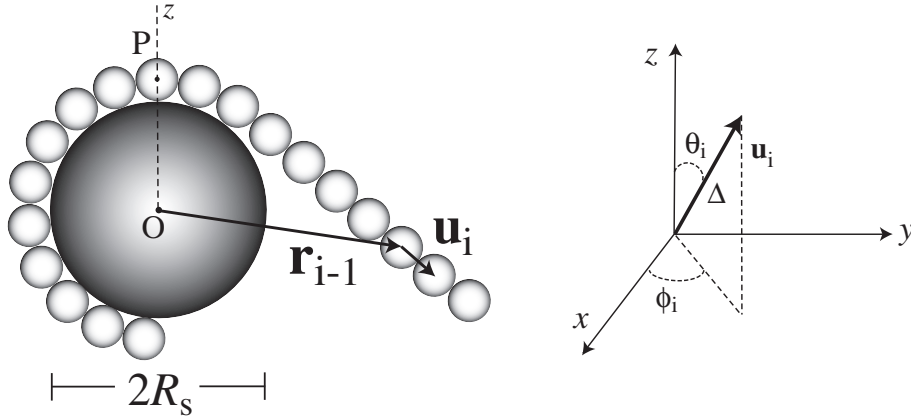
Figure 2.4: Schematic representation of the discrete model used for numerical study of the chain-sphere model (see the text). For the sake of representation, the apparent size of the point-like chain discretization beads (small gray spheres) is enhanced.

2.3.1 Discretization scheme

For the purpose of numerical computations, one needs to use the Hamiltonian (2.3) in a discretized form. The discretization scheme is shown in Figure 2.4. I discretize the PE chain of length L using $N+1$ *beads* or discretization points (labeled by $i = 0, \ldots, N$). This defines N rigid subunits described by a set of vectors $\{\mathbf{u}_i\}$, where the so-called *bond vectors* $\mathbf{u}_i = \mathbf{r}_i - \mathbf{r}_{i-1}$ have a fixed length, $|\mathbf{u}_i| = \Delta$, and are specified by their polar and azimuthal angles θ_i and ϕ_i. (Note that these subunits have no relation with physical monomers of the PE chain.) In addition to these $2N$ parameters, the position $\mathbf{r}_P$ of one bead, say the middle bead with $i = P = N/2$, has to be given in order to completely specify the location and conformation of the PE chain in the presence of the macroion. (I choose the frame of coordinates such that the origin, O, lies at the sphere center.) This leads to $2N + 3$ varaibles. However, due to the isotropic potential of the sphere, one can fix the O-P line as the z-axis (i.e. by setting to zero the $x - y$ cartesian coordinates of the reference point P as $r_P^x = r_P^y = 0$), which reduces the number of independent variables to $2N + 1$ (see Figure 2.4). Note that the rotation of the chain around the P-O axis does not change the effective Hamiltonian. This symmetry introduces Goldeston modes and slows down the numerical minimization procedure, which may be resolved by fixing the azimuthal angle of the middle bead, ϕ_P. One thus ends up with a minimal set of only $2N$ independent variables for the PE-macroion system, namely the set of N polar angles $\{\theta_i\}$, $N - 1$ azimuthal angles $\{\phi_i\}$ for $i \neq P$, and the z component of the reference point P of the chain from the center of the sphere, r_P.

Given $\mathbf{r}_P$ and $\{\mathbf{u}_i\}$, one can calculate the position of the i-th bead, $\mathbf{r}_i$, as follows

$$
\mathbf{r}_i = \begin{cases} \mathbf{r}_P - \sum_{j=1}^{P-i} \mathbf{u}_{P-j+1} & i < P, \\[2mm] \mathbf{r}_P + \sum_{j=P+1}^{i} \mathbf{u}_j & i > P. \end{cases} \tag{2.13}
$$

Inserting this discretized representation of $\mathbf{r}_i$ back into Eqs. (2.3)-(2.5), one obtains the

following expression for the self-energy of a single PE chain in the units of $k_B T$, i.e.

$$
\begin{aligned}
\mathcal{H}_p[\{\mathbf{r}_i\}] &= \frac{\ell_p}{\Delta} \sum_{i=2}^{N} \left\{ 1 - \cos(\theta_i - \theta_{i-1}) + \sin\theta_i \sin\theta_{i-1}\Big(1 - \cos(\phi_i - \phi_{i-1}) \Big) \right\} \\
&\quad + q^2 \ell_B \sum_{i=0}^{N-1} \sum_{j=i+1}^{N} \frac{e^{-\kappa|\mathbf{r}_i - \mathbf{r}_j|}}{|\mathbf{r}_i - \mathbf{r}_j|},
\end{aligned}
\tag{2.14}
$$

and for the chain-sphere interaction, one has

$$
\mathcal{H}_{pm}[\{\mathbf{r}_i\}] = -\frac{Z q \ell_B}{1 + \kappa R_s} \sum_{i=0}^{N} \left[\frac{e^{-\kappa(|\mathbf{r}_i| - R_s)}}{|\mathbf{r}_i|} - A\, e^{-(|\mathbf{r}_i| - R_s)/\alpha} \right],
\tag{2.15}
$$

in which $q = \tau L/(N+1)$ is the charge of each bead, and $\Delta = L/N$ is the distance between each two neighboring beads. The total effective Hamiltonian of the chain-sphere system is therefore given by

$$
\mathcal{H}[\{\mathbf{r}_i\}] = \mathcal{H}_{pm}[\{\mathbf{r}_i\}] + \mathcal{H}_p[\{\mathbf{r}_i\}].
\tag{2.16}
$$

2.3.2 Minimization scheme

To obtain the optimal set of variables $\{\theta_i, \phi_{i \neq P}, r_P\}$ which minimizes the effective Hamiltonian (2.16), I employ the quasi-Newton numerical minimization algorithm [3], which is designed to find the minima of functions in a multi-dimensional space of variables. This method requires evaluating the gradient vector of the Hamiltonian since at a minimum, the first-order variation of the Hamiltonian vanishes, i.e.

$$
\delta\mathcal{H} = \sum_{i=1}^{N} \frac{\mathrm{d}\mathcal{H}}{\mathrm{d}\theta_i} \delta\theta_i + \sum_{i=1, i\neq P}^{N} \frac{\mathrm{d}\mathcal{H}}{\mathrm{d}\phi_i} \delta\phi_i + \frac{\mathrm{d}\mathcal{H}}{\mathrm{d}r_P} \delta r_P = 0.
\tag{2.17}
$$

Numerically, the minimization procedure starts from an initial point in the space of variables and takes successive discrete steps in the opposite direction of the gradient in order to reduce the value of the Hamiltonian as well as the size of its gradient vector till it reaches to a local minimum. The explicit form of the first-order derivatives of the effective Hamiltonian that are used in the minimization algorithm are derived in Appendix A.1.

In most cases (especially for a single complex), the symmetries of the optimal (ground-state) configuration already indicate whether the result corresponds to the global minimum of the Hamiltonian as will be demonstrated explicitly later. Further checks must be done to ensure the global stability of the numerically determined structure, especially near the so-called discontinuous transition points (where several optimal states of the same energy coexist, Section 2.4), due to the appearance of meta-stable states (local minima). In general, the meta stable state solution can be resolved using a combination of parameter quenching and stochastic perturbation methods.

For most of the studies presented in this work, I fix the discretization degree to the optimal value $N = 250$, which is a good compromise between accuracy and efficiency. A discussion of discretization effects is given in Appendix D (see also Ref. [49]).

Rotational Symmetry: $\eta = 0$,
Mirror Symmetry: $\sigma = 0$

Broken Rotational Symmetry: $\eta \neq 0$,
Mirror Symmetry: $\sigma = 0$

Broken Rotational Symmetry: $\eta \neq 0$,
Broken Mirror Symmetry: $\sigma \neq 0$

Rotational Symmetry: $\eta \neq 0$,
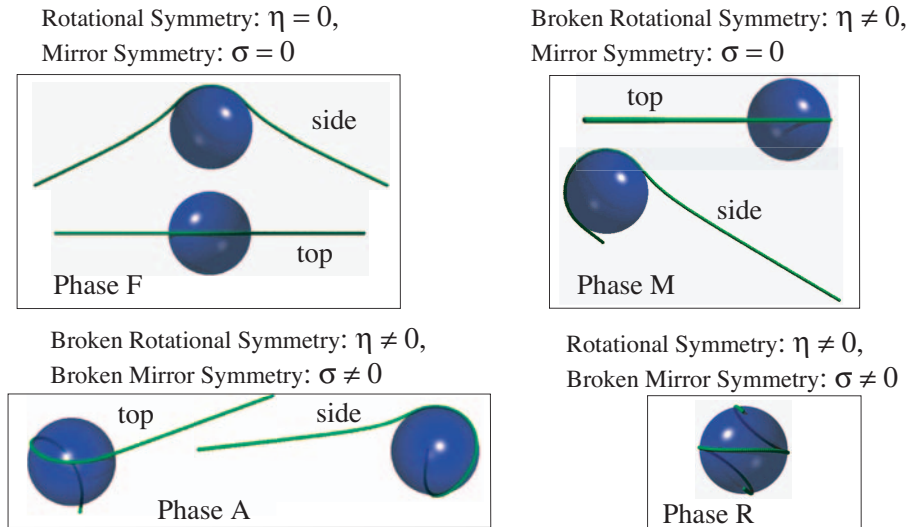Broken Mirror Symmetry: $\sigma \neq 0$

Figure 2.5: Numerically calculated ground-state configurations of a PE-macroion complex obtained for $Z = 40$ and $\kappa = 0$ (fully symmetric phase F), 0.1 (mirror symmetric phase M), 0.2 (asymmetric phase A) and 0.5nm^{-1} (rotational symmetry phase R) as indicated on the graph. Other parameters are chosen consistent with the DNA-histone system (see the text).

2.4 Characterization method: Ground-state symmetries

One generally expects that the ground state of a Hamiltonian system represents a highly *symmetric* state. (Symmetries are defined as operations on degrees of freedom which leave the Hamiltonian of the system unchanged.) This is in fact the case for the chain-sphere model [48, 49], whose ground state is determined by minimization of the effective Hamiltonian (2.3).

The optimal PE configuration (ground state) for a given set of parameters (such as sphere charge, Z, and Debye screening length, κ^{-1}) can be classified by two spatial symmetries namely, the *mirror symmetry* and a *two-fold rotational symmetry*. For a mirror-symmetric state, the chain configuration lies in a single plane being thus invariant upon reflection with respect to this plane (structures which conserve this symmetry and are not planar do not occur for the ground state as explicitly checked [49]) For a single complex, the rotational symmetry of the ground state occurs with respect to the axis connecting the chain mid-point to the sphere center. Typical examples of the two symmetric states are shown in Figure 2.5. The figure shows the numerically determined ground-state configurations of the Hamiltonian (2.3) for parameters appropriate for the DNA-histone system, e.g., chain persistence length $\ell_\mathrm{p} = 30$ nm, linear charge density $\tau = 5.88$ nm^{-1} and contour length $L = 49.69$ nm (146 DNA base pairs), and choosing the sphere charge as $Z = 40$. Symmetries of the ground state change according to the salt concentration as indicated in the figure caption. As seen, either of these symmetries may be broken or conserved independently by changing the salt concentration, leading, for the chosen values of system parameters, to a total of four distinct *ground-state phases* or symmetry classes (see below). A full analysis of the salt-dependent behavior of the DNA-histone model system is given in Refs. [48, 49]. A generalized approach for a generic PE-macroion complex will be given in the forthcoming Chapter 3. Here I will only focus on the method of classification of the ground state.

2.4.1 Order parameters

In order to identify the configurational symmetries, two independent order parameters were defined in Ref. [48, 49], which can reflect the rotational symmetry around an axis and the mirror symmetry of the chain configuration $\mathbf{r}(s)$. The rotational symmetry may be quantified by

$$\eta = \frac{\mathbf{r}^2(0) - \mathbf{r}^2(L)}{L^2}. \tag{2.18}$$

This quantity vanishes if an axis through the origin can be found, around which the chain configuration has two-fold rotational symmetry. While, in general, $\eta = 0$ does not necessarily imply two-fold rotational symmetry, for the set of optimal configurations it actually gives a measure of two-fold rotational symmetry, as has been explicitly checked [49].

The mirror symmetry can be quantified by a different *order parameter*, σ, that measures the deviations of the chain configuration from a planar (two-dimensional) structure. It is defined as

$$\sigma = \frac{1}{L} \int_0^L \mathrm{d}s\, \omega(s), \tag{2.19}$$

where $\omega(s) = \dot{\mathbf{N}}(s) \cdot \mathbf{B}(s)$ is the so-called torsion associated with the chain curve, $\mathbf{r}(s)$, with the vectors $\mathbf{N}(s)$ and $\mathbf{B}(s)$ being defined using the tangent vector $\mathbf{T}(s) = \dot{\mathbf{r}}(s)$ as

$$\mathbf{N}(s) = \frac{\dot{\mathbf{T}}(s)}{|\dot{\mathbf{T}}(s)|}, \quad \mathbf{B}(s) = \mathbf{T}(s) \times \mathbf{N}(s), \tag{2.20}$$

for non-vanishing curvature $|\ddot{\mathbf{r}}(s)|$ (note also that $|\dot{\mathbf{r}}(s)| = 1$ is assumed within the present model). If $\omega(s) = 0$ for all s, the curve is planar and lies in the plane of mirror symmetry. For a non-planar (three-dimensional) *ground-state* curve, $\omega(s) \neq 0$ for some s [49]. Again there exist three dimensional PE configurations ($\sigma \neq 0$) which possess mirror symmetry but they are not found as the ground state of the complex [49].

2.4.2 Symmetry classes

Using the two order parameters, η and σ, one can unambiguously distinguish the symmetries of the ground state configuration for a PE-macroion complex. As mentioned before, there are four distinct symmetry classes (ground-state phases) that are visualized in Figure 2.5 for a typical set of parameters. These phases are

- **Fully symmetric phase F**, where the chain conformation possesses both mirror symmetry and the two-fold rotational symmetry around the axis connecting the chain midpoint to the sphere center. It is thus referred to as the *fully symmetric phase* (corresponding to order parameters values $\eta = 0$ and $\sigma = 0$). In this phase, the chain exhibits an expanded conformation with two open arms; hence phase F is also known as *expanded phase*. This phase typically occurs when the self-energy of the PE chain (via its mechanical bending rigidity and electrostatic self-repulsion) overcomes the PE-macroion attraction [48, 49, 72], e.g., for small salt concentration (small screening effects) or small macroion charge (see Chapter 3).

- **Rotational symmetry phase R**, in which the chain conformation only has the two-fold rotational symmetry and the mirror symmetry is broken (i.e. $\eta = 0$ and $\sigma \neq$

0). The symmetry breaking is spontaneous and may occur, e.g., by changing the salt concentration resulting in a *wrapped* state. Physically, the wrapped state occurs at intermediate salt concentrations or sufficiently large macroion charge [48, 49, 43, 44, 45, 51, 52, 41, 42] as also observed in recent experiments [17, 18, 19, 20, 21, 103, 104].

– **Mirror-symmetric phase M**, where the two-fold rotational symmetry is broken and the chain conformation exhibits a *mirror-symmetric* planar shape (i.e. $\eta \neq 0$ and $\sigma = 0$).

– **Asymmetric phase A** with an *asymmetric* chain conformation with both symmetries being broken (i.e. $\eta \neq 0$ and $\sigma \neq 0$).

Note that M and A typically represent intermediate phases and in the phase diagram, they occur between phases F and R as will be shown in Chapter 3 (see also Refs. [48, 49, 72]).

Chapter 3

Strongly Coupled Complexes: Exploring the global phase diagram

A global analysis of the structural phase behavior of a single strongly coupled polyelectrolyte-macroion complex is presented based on a rescaled (dimensionless) representation of the chain-sphere model. This representation yields generic (universal) results that cover a wide range of realistic system parameters. Emphasize is made on the interplay between the effects due to the PE chain length and the salt concentration as well as those arising from the interplay between the PE chain length and the macroion charge that will be summarized in global phase diagrams. I will also discuss the effects of changing the mechanical chain persistence length with special attention to chains with zero mechanical bending rigidity.

In this chapter, I will focus on a *single* polyelectrolyte-macroion complex and examine structural properties of the complex for a wide range of system parameters such as persistence length of the polyelectrolyte (PE) chain, chain contour length and linear charge density, salt concentration of the medium as well as the macroion charge and radius. The main objective here is to establish *generic* (or universal) results that can be applied to a whole range of system parameters within the standard chain-sphere model. To this end, I will employ a rescaled description which allows for spanning the space of parameters using only a few independent *dimensionless* parameters, which are obtained by combining the actual system parameters mentioned above. The present study generalizes the previous results [48, 49] obtained for parameters consistent with the DNA-histone complexes, and may in general be applied to a variety of other polyelectrolyte-macroion complexes as well by identifying the corresponding relevant dimensionless parameters. This includes, for instance, complexes formed by mechanically *flexible* chains with various ratios of chain contour length to macroion radius, which can be realized, e.g., by synthetic PEs complexed with charged globular objects of different sizes such as micelles [22, 27, 24, 23], dendrimers [20], plastic beads [18], colloids [19, 26], latex particles [29] and nanoscopic gold particles [30, 31].

In this chapter, I will primarily focus on *strongly coupled* complexes and use the ground state analysis as described in Section 2.2 (I shall return to the effects of thermal fluctuations in Chapter 5). Special attention will be given here to a system with a mechanically flexible chain, which has not been considered in previous works [48, 49]. In this case, the chain stiffness is provided only by electrostatic self-repulsion of chain segments (electrostatic bending stiffness), therefore the ground-state approximation is still valid for sufficiently highly charged systems. In this case, the macroion overcharging by the PE chain appears to be more pronounced as

compared with a typical DNA-histone system [49, 45].

3.1 Dimensionless representation

The Hamiltonian of the idealized chain-sphere model (Section 2.1) for a chain configuration curve parameterized by $\mathbf{r}(s)$ (with $0 \leq s \leq L$) at an oppositely charged sphere of valency Z and radius R_s may be rewritten (in units of $k_\mathrm{B}T$) as

$$
\begin{aligned}
\mathcal{H}[\mathbf{r}(s)] \;=\; & \frac{\ell_\mathrm{p}}{2} \int_0^L \mathrm{d}s \; [\ddot{\mathbf{r}}(s)]^2 + \tau^2 \ell_\mathrm{B} \int_0^L \mathrm{d}s \int_s^L \mathrm{d}s' \; \frac{e^{-\kappa|\mathbf{r}(s)-\mathbf{r}(s')|}}{|\mathbf{r}(s) - \mathbf{r}(s')|} \\
& - \frac{Z\tau\ell_\mathrm{B}}{1 + \kappa R_\mathrm{s}} \int_0^L \mathrm{d}s \left[\frac{e^{-\kappa(|\mathbf{r}(s)|-R_\mathrm{s})}}{|\mathbf{r}(s)|} - A\, e^{-(|\mathbf{r}(s)|-R_\mathrm{s})/\alpha} \right].
\end{aligned}
\tag{3.1}
$$

As explained before (see Eq. (2.3)), the first term takes into account the *mechanical* bending contribution of the chain with bare mechanical persistence length of ℓ_p, the second term represents the electrostatic self-energy of the chain, the third and forth terms are chain-sphere electrostatic attraction and soft-core excluded-volume repulsion. The above expression for the Hamiltonian introduces several different parameters which all may affect the structure of a complex. However, since the number of basic units (or physical dimensionalities such as length, mass and charge) is finite, one may expect that the space of parameters can be spanned only by a few dimensionless parameters. This is actually the case for a chain-sphere model as will be explicitly shown below (see also the discussion in Section 2.2).

In order to establish dimensionless representation, I rescale the coordinates with a given length scale in the system, which is chosen here to be the sphere radius R_s, i.e. I define

$$
\tilde{\mathbf{r}} = \frac{\mathbf{r}}{R_\mathrm{s}}, \quad \tilde{s} = \frac{s}{R_\mathrm{s}}.
\tag{3.2}
$$

Employing the above rescaling scheme, we end up with the following rescaled representation for the Hamiltonian, that is

$$
\begin{aligned}
\tilde{\mathcal{H}}[\tilde{\mathbf{r}}(\tilde{s})] \;=\; & \frac{\tilde{\ell}_\mathrm{p}}{2} \int_0^{\tilde{L}} \mathrm{d}\tilde{s} \; [\ddot{\tilde{\mathbf{r}}}(\tilde{s})]^2 + \int_0^{\tilde{L}} \mathrm{d}\tilde{s} \int_{\tilde{s}}^{\tilde{L}} \mathrm{d}\tilde{s}' \; \frac{e^{-\tilde{\kappa}|\tilde{\mathbf{r}}(\tilde{s})-\tilde{\mathbf{r}}(\tilde{s}')|}}{|\tilde{\mathbf{r}}(\tilde{s}) - \tilde{\mathbf{r}}(\tilde{s}')|} \\
& - \frac{\tilde{Z}}{1 + \tilde{\kappa}} \int_0^{\tilde{L}} \mathrm{d}\tilde{s} \left[\frac{e^{-\tilde{\kappa}(|\tilde{\mathbf{r}}(\tilde{s})|-1)}}{|\tilde{\mathbf{r}}(\tilde{s})|} - \tilde{A}\, e^{-(|\tilde{\mathbf{r}}(\tilde{s})|-1)/\tilde{\alpha}} \right],
\end{aligned}
\tag{3.3}
$$

where $\tilde{\mathcal{H}} = \mathcal{H}/(\tau^2 R_\mathrm{s} \ell_\mathrm{B} k_\mathrm{B}T)$, and the key dimensionless parameters are defined as

$$
\tilde{\ell}_\mathrm{p} = \frac{\ell_\mathrm{p}}{\tau^2 R_\mathrm{s}^2 \ell_\mathrm{B}}, \quad \tilde{Z} = \frac{Z}{\tau R_\mathrm{s}}, \quad \tilde{\kappa} = \kappa R_\mathrm{s}, \quad \tilde{L} = \frac{L}{R_\mathrm{s}},
\tag{3.4}
$$

representing the rescaled bare persistence length, the rescaled sphere charge, the rescaled inverse screening length and the rescaled chain contour length respectively. (The soft-repulsion parameters are rescaled as $\tilde{\alpha} = \alpha/R_\mathrm{s}$ and $\tilde{A} = AR_\mathrm{s}$, which are fixed to some appropriate values and will not be considered as control parameters–see Appendix E).

In order to examine the ground-state properties of a complex defined by the Hamiltonian (3.3), I employ the numerical minimization method described in detail in Section 2.3, which makes use of a discretization model as depicted in Figure 2.4. Different ground-state symmetry classes (configurational phases) are specified using the order parameters associated with the two-fold rotational symmetry and the mirror symmetry as discussed in Section 2.4.1.
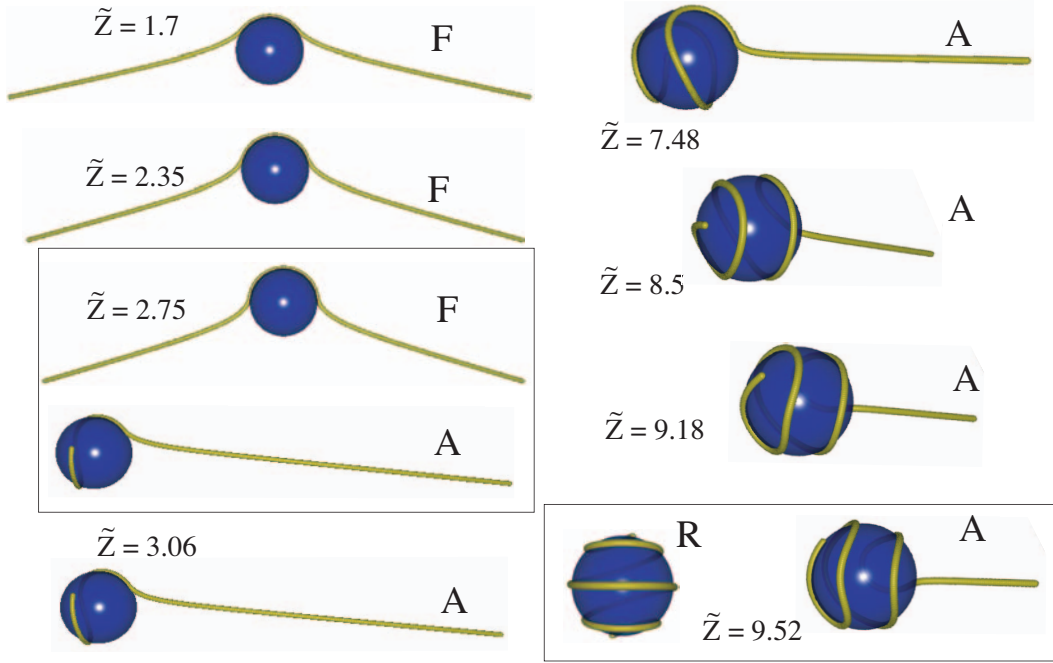
Figure 3.1: Optimal configurations obtained for a mechanically flexible chain ($\tilde{\ell}_{\mathrm{p}} = 0$) with contour length $\tilde{L} = 16.32$ in the absence of salt ($\tilde{\kappa} = 0$) and for various rescaled sphere charges $\tilde{Z}$. The coexisting states at $\tilde{Z} = 2.754$ (phases F and A) and 9.54 (phases A and R) are shown together in a closed box.

3.2 Phase behavior of a complex: Zero-salt limit

In this section, I first display the real space configuration of a PE-macroion complex for zero salt concentration with varying sphere charge and describe how the transition between different ground-state configurational phases occur. This serves as an illustration of how the generic phase behavior of the PE-macroion complexes are deduced from conformational changes of the PE chain. I will return to the effects of salt in the next section.

3.2.1 Effects of changing the rescaled sphere charge

In Figure 3.1, I show the PE chain configurations as obtained by minimizing the Hamiltonian (3.3) for various rescaled sphere charge $\tilde{Z}$ and at fixed rescaled chain length of $\tilde{L} = 16.32$ and rescaled inverse screening length $\tilde{\kappa} = 0$. Here I set the mechanical chain stiffness equal to zero, i.e. $\tilde{\ell}_{\mathrm{p}} = 0$. Note that for a sphere diameter of $R_{\mathrm{s}} = 5$ nm, the present case corresponds to a chain contour length of $L = 81.6$ nm (equivalent to 240 DNA base pairs).

For small non-zero sphere charge (e.g., $\tilde{Z} = 1.7$), the PE chain displays a finite bending around the sphere due to attraction between opposite charges on the chain and on the sphere. In other words, the continuous rotational symmetry associated with the ground-state of a free chain (which is a straight line) is broken and reduces to a two-fold rotational symmetry in the presence of the external potential of the sphere. The chain conformation thus appears to be fully symmetric (i.e. with both two-fold rotational symmetry and the mirror symmetry) representing thus the fully symmetric phase F. In this phase, the long-range self-repulsion of
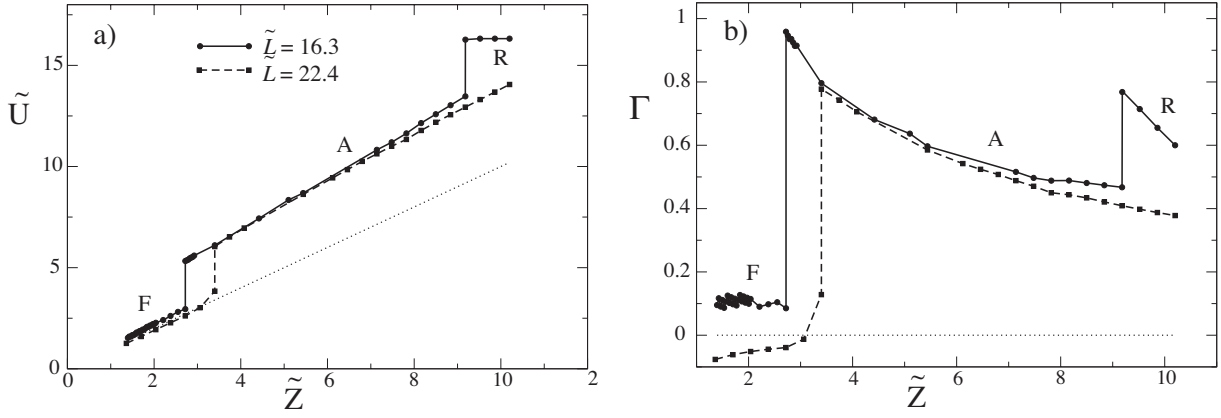
Figure 3.2: Overcharging of the PE-macroion complex represented by a) the adsorbed (or wrapped) PE charge $\tilde{U}$ (see the text) and b) the overcharging degree Γ as a function of the sphere charge $\tilde{Z}$ in the absence of salt ($\tilde{\kappa} = 0$) and for $\tilde{L} = 16.32$ and 22.4 as indicated on the graph. The thin dotted line shows the isoelectric line, where $\tilde{U} = \tilde{Z}$, i.e. the effective (net) charge of the complex is zero.

chain segments is still dominant and preserves even at $\tilde{Z} = 2.35$ (Figure 3.1). At rescaled sphere charge $\tilde{Z} = 2.754$, however, the sphere-chain attraction becomes strong enough to break both rotational and mirror symmetries: at this point, the expanded configuration (phase F) coexists with an asymmetric three-dimensional configuration (phase A), i.e. both these states appear as optimal states with the same ground-state energies. This value of the sphere charge therefore represents the locus of a discontinuous transition, at which both order parameters η and σ jump from zero in phase F to non-vanishing values in phase A (Section 2.4.1). (The transition point can precisely be localized using the order parameters and the energy difference as will be made clear later on.) In fact, the simultaneous breaking of the two symmetries is specific to the salt-free conditions [49], which can be de-coupled to a sequence of individual symmetry-breakings by introducing salt screening effects as will be shown later. Note that the transition value $\tilde{Z} = 2.754$ can be achieved by a combination of parameters, e.g., with a sphere diameter of $R_s = 5$ nm and $\tau = 5.88$ nm^{-1} (corresponding to histone and DNA parameters), and using the actual sphere charge $Z = 81$.

By further increasing the sphere charge, the PE chain is continuously pulled onto the sphere and becomes increasingly more wrapped. At $\tilde{Z} = 8.5$, the chain wraps about two turns around the sphere, but it still displays an extended arm. A second transition occurs at $\tilde{Z} = 9.52$, where the PE-macroion attraction becomes large enough to completely wrap the chain around the sphere, which as seen in the figure, displays nearly three complete turns. This transition is symmetry-restoring and gives rise to a completely wrapped state R with a two-fold rotational symmetry. This later transition is a discontinuous transition as the two states A and R coexist at this point (note that the non-vanishing order parameter, η, in phase A jumps back to zero in phase R–see Figure 3.8). For higher rescaled sphere charge, the chain configuration changes very little and retains the symmetry class R.

The wrapping transition at large $\tilde{Z}$ gives rise to a highly overcharged PE-macroion complex: at about $\tilde{Z} \simeq 10$, the total PE charge, τL (in units of the elementary charge e) which is wrapped around the sphere is larger than the sphere charge, Z, by a factor of about 1.75,
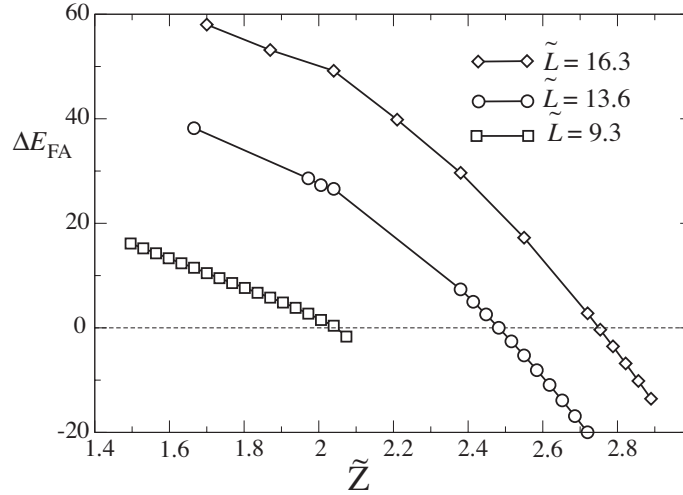
Figure 3.3: The energy difference between conformational phases F and A, $\Delta E_{\mathrm{FA}} = E_{\mathrm{A}} - E_{\mathrm{F}}$, as a function of $\tilde{Z}$ for zero salt and various rescaled contour lengths $\tilde{L} = 16.3$ (diamonds) $\tilde{L} = 13.6$ (spheres) and $\tilde{L} = 9.3$ (squares).

i.e. $\tau L/Z = 1.75$. Therefore, the overcharging degree defined as

$$\Gamma = \frac{\tilde{U}}{\tilde{Z}} - 1, \qquad (3.5)$$

with $\tilde{U}$ being in general the amount of PE charge wrapped around the macroion in rescaled units,[1] appears to be about $\Gamma = 0.75$. In Figure 3.2, I show the results obtained for $\tilde{U}$ and Γ at various rescaled sphere charges and for $\tilde{L} = 16.32$ and zero salt concentration (solid line). The location of the transitions occurring between phases F and A and between A and R is clearly reflected by the discontinuous jumps in both quantities $\tilde{U}$ and Γ. It is remarkable that the wrapped PE charge, $\tilde{U}$, shows a linear dependence on the sphere charge in phase F and A, which indicates that the wrapping of the PE arm(s) occurs locally and continuously in each phase, ensuring an almost constant rescaled *effective charge*, $\tilde{U} - \tilde{Z}$, for the complex. In phase R, the wrapped PE charge can not increase because the whole chain is adsorbed on the sphere. For a longer chain (e.g., $\tilde{L} = 22.4$ shown by dashed line in the figure), the full wrapping occurs at a larger sphere charge. These results indicate that the location of the transitions depend on the length of the PE chain as well, which will be considered separately in Section 3.2.3. As seen, in the present case with salt, the overcharging degree Γ is smaller than unity. Salt effects can indeed lead to quite large overcharging degrees ($\Gamma \gg 1$) as will be shown later.

3.2.2 Discontinuous transitions and meta-stable states

It is important to note that discontinuous transitions are typically associated with meta-stable states that represent the local minima of the Hamiltonian. As the system crosses a

---

[1]Note that U may be written as $U = \tau L_{\mathrm{w}}$, where L_{w} is the chain lengths wrapped around the sphere. In rescaled units $\tilde{U} \equiv \tau L_{\mathrm{w}}/\tau R_{\mathrm{s}} = \tilde{L}_{\mathrm{w}}$. Here I define a chain bead as wrapped or adsorbed on the sphere if its distance from the sphere center, r, fulfills $r < 1.02 R_{\mathrm{s}}$.

a) $\tilde{L}$=16.3 , $\tilde{\kappa}$ = 0, $\tilde{Z}$ = 8.5   b) $\tilde{L}$=16.3 , $\tilde{\kappa}$ = 0, $\tilde{Z}$ = 10.2

front   back   back   front

ground state   ground state

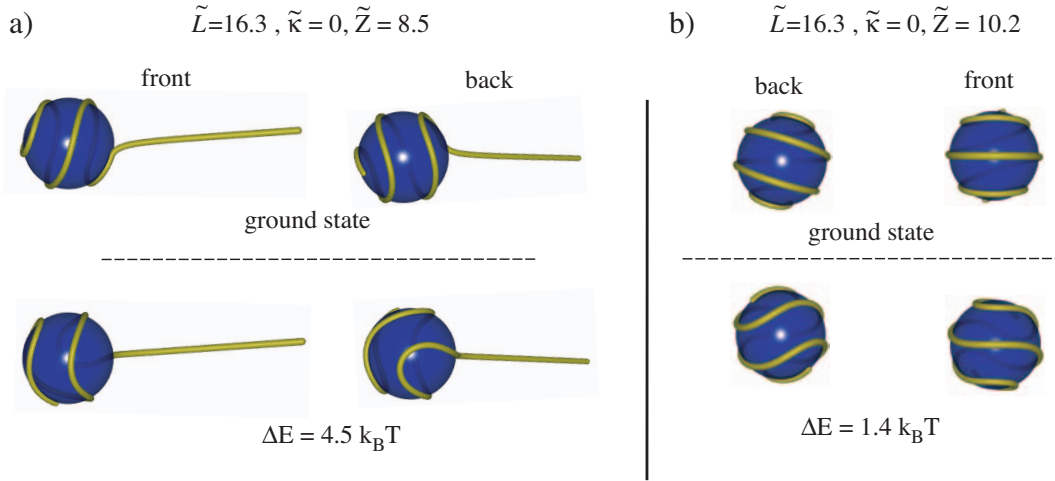$\Delta E = 4.5\ k_B T$ $\Delta E = 1.4\ k_B T$

Figure 3.4: Typical meta-stable states (bottom) belonging to the symmetry classes a) A and b) R shown along with the corresponding ground state configurations (top). The energy difference of these meta-stable states and the ground states, ΔE, is also given on the graph.

discontinuous transition point (by changing a relevant control parameter), one of the two global minima of the Hamiltonian, which correspond to two coexisting states at the transition point, is shifted and becomes a local minimum (meta-stable state) (this local minimum becomes eventually unstable and disappears). For instance, in Figure 3.1, phase F indeed persists as a meta-stable state when the sphere charge increases beyond the discontinuous transition point at $\tilde{Z} = 2.754$. Denoting the energy of state F with E_F and that of the state A with E_A (referring to the minimal value of the Hamiltonian $\mathcal{H}$, Eq. (3.3)), one can identify the locus of the discontinuous transition using the energy difference $\Delta E_{FA} \equiv E_A - E_F$. The results are shown in Figure 3.3 (open diamonds) for zero salt concentration $\tilde{\kappa} = 0$ and for the chain contour length $\tilde{L} = 16.3$ (corresponding to the configurations shown in Figure 3.1). As seen, at the transition point ($Z = 2.754$), ΔE_{FA} vanishes and the two phases coexist; below this point phase F is stable, i.e. $\Delta E_{FA} > 0$, and above that phase A is stable, i.e. $\Delta E_{FA} < 0$. In fact, in the range of the rescaled sphere charges $\tilde{Z}$ shown in the graph, both phases F and A exist; for very small (very large) $\tilde{Z}$, the meta-stable phase A (phase F) disappears.

The location of the transition point varies also with other parameters of the system such as salt concentration and the chain contour length. The effects of salt concentration for a fixed chain length has been considered in previous works [48, 49] and is briefly reviewed in Section 2.4 (complementary results will be given later in this chapter). In Figure 3.3, I show the energy difference for the same set of parameters but with two other smaller rescaled contour lengths (open circles and open squares). Clearly, the transition point between phases F and A shifts to smaller sphere charges as the rescaled chain length decreases, meaning that for shorter chains phase A becomes stable in a wider range of rescaled sphere charges. However, at sufficiently small contour length (comparable to about $L \simeq 2\pi R_s$), the asymmetric phase A completely disappears and the fully symmetric phase, F, turns out to be the only solution for the ground-state configuration. By scanning various values for $\tilde{L}$ and $\tilde{Z}$ (at fixed $\kappa = 0$), one will be able to sketch a global phase diagram (see below).

At this point, it is useful to note that in addition to the meta-stable states induced by
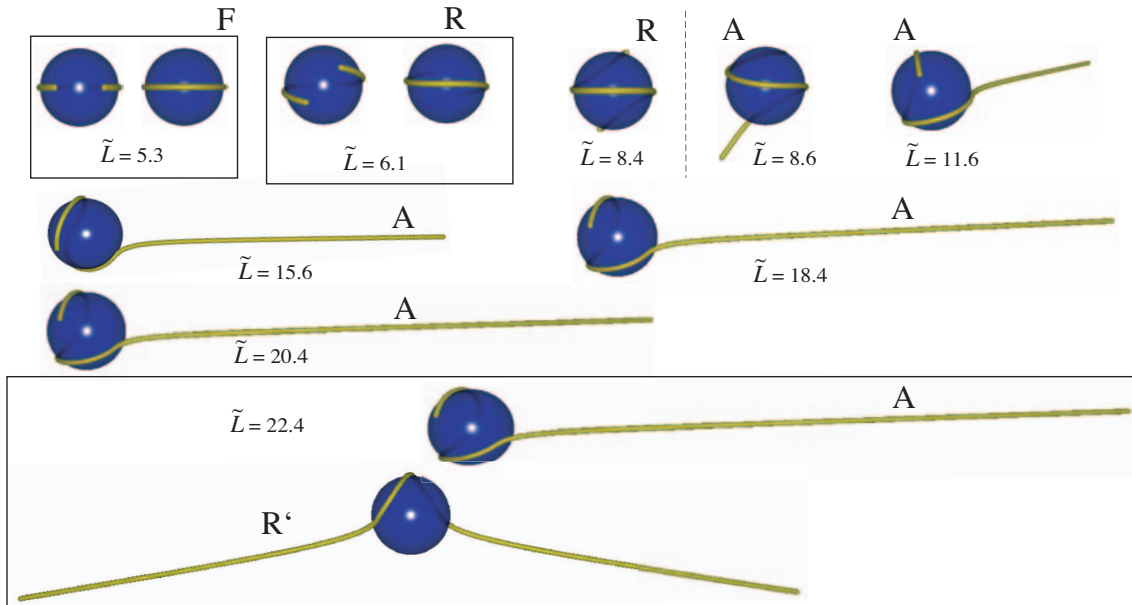
Figure 3.5: Configurations obtained for a fixed sphere charge $\tilde{Z} = 3.4$ and vanishing salt ($\tilde{\kappa} = 0$) for various rescaled PE contour length $\tilde{L}$.

discontinuous transitions, there are additional meta-stable states that may or may not belong to the four ground-state symmetry classes described in Section 2.4.2 [48, 49]. They correspond to local minima of the Hamiltonian. Some of these states may be energetically very close to the ground state suggesting that the role of thermal fluctuations may become important in those regions of the phase space inducing transitions between these locally stable states (see Chapter 5). In fact, the meta-stable states show typically more enhanced chain modulation on the sphere as compared with the ground state. In Figure 3.4, I show two such meta-stable states (bottom) belonging to symmetry classes A and R that are compared with the corresponding ground-state configurations (top). In each case, the energy difference, ΔE (in units of $k_\mathrm{B}T$) with respect to the ground-state configuration is shown as well, which, for the example shown for phase R (at $\tilde{Z} = 10.2$, $\kappa = 0$ and $\tilde{L} = 16.3$), amounts to only about $1.4 k_\mathrm{B}T$. This signifies the importance of employing various methods to check for the global stability of configurations obtained from numerical minimizations (Section 2.3.2) as performed routinely within the present study.

3.2.3 Effects of the rescaled chain contour length

For very small chain length, one can argue that the chain must be completely adsorbed on the sphere and adopt a fully symmetric configuration (phase F). In this case, the chain contour length forms a circular arc which ensures maximum distances between charged segments of the chain, and hence minimum self-repulsion. This situation is visualized in Figure 3.5 for a fixed rescaled sphere charge of $\tilde{Z} = 3.4$ and zero salt concentration $\kappa = 0$, when the rescaled chain length is $\tilde{L} = 5.3$. Restoring actual units, this length corresponds to $L = 5.3 R_\mathrm{s}$, i.e. somewhat smaller than the circumference of the great circle $2\pi R_\mathrm{s}$. For the present set of parameters, the end-point effects come into play for larger chain length (see, e.g., $\tilde{L} = 6.1$ or
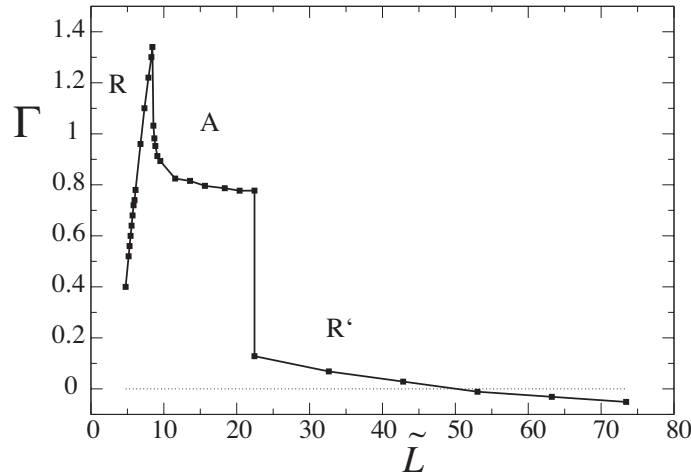
Figure 3.6: Overcharging degree Γ, Eq. (3.5), as a function of $\tilde{L}$ for $\tilde{Z} = 3.4$, $\tilde{\ell}_p = 0$ and zero salt ($\tilde{\kappa} = 0$).

in actual units $L \simeq 2\pi R_s$) including deflection of the end segments resulting thus in phase R, where the mirror symmetry (or two-dimensional geometry of the chain conformation) is broken but the two-fold rotational symmetry still holds.

By further increasing the chain length, a sequence of phase changes is found in which the chain is eventually *dewrapped*. This is because the self-repulsion between chain segments grows with the contour length and can not be overcome by the chain-sphere attraction. This is shown in Figure 3.5, where I obtain partially wrapped configurations corresponding to the asymmetric configurations A for intermediate $\tilde{L}$, and expanded configurations at large $\tilde{L}$, which (unlike the standard expanded state F) possesses only a two-fold rotational symmetry. The symmetry class of this latter phase coincides with that of phase R, but in contrast, here the chain is only partially wrapped around the sphere. For this reason, I will refer to this symmetry class as R'. In the figure, I show two coexisting states of A and R' at $\tilde{L} = 22.4$. For even larger chain contour length, the Coulombic self-repulsion contribution becomes the dominant factor, and hence, the sequence of phases terminates in the expanded-chain state F (not shown).

In Figure 3.6, the overcharging degree, Γ (Eq. (3.5)), is shown for the same set of parameters as in Figure 3.5 and for various $\tilde{L}$. As seen, Γ shows pronounced variations in different regions, and in particular, the following features are evident: in phases F and R, Γ increase rapidly and in a linear fashion with $\tilde{L}$ reaching a sharp peak (maximum wrapping) at about $\tilde{L} \simeq 8.5$ ($L = 42.5$ nm for a sphere radius of $R_s = 5$ nm) within phase R, where an overcharging degree of 1.4 is obtained. In fact, the peak at about $\tilde{L} \simeq 8.5$ coincides with the transition point between phases R and A. In phase A, Γ exhibits a plateau-like behavior with a value of about $\Gamma = 0.8$. When the transition to phase R' sets in ($\tilde{L} \simeq 22.4$), Γ suddenly jumps to a smaller value, and thereafter, slowly decreases due to the dewrapping of the chain from the sphere.
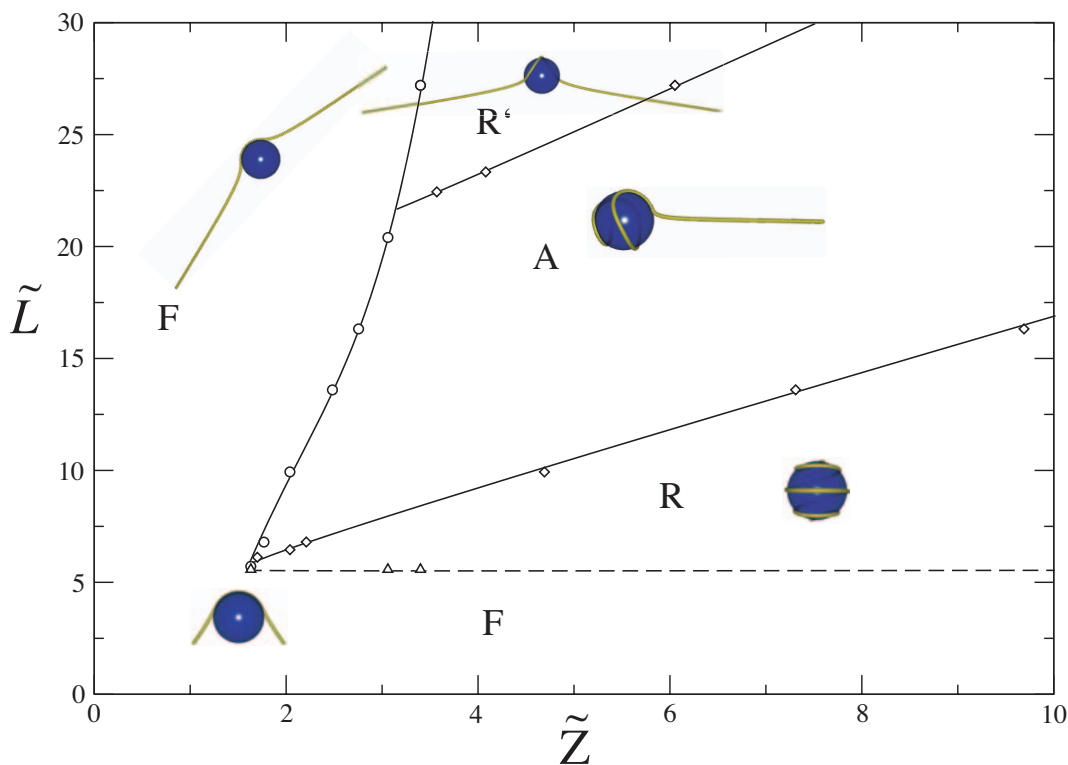
Figure 3.7: Phase diagram in terms of the rescaled parameters $\tilde{Z}$ and $\tilde{L}$ in the absence of salt ($\tilde{\kappa} = 0$) and for a mechanically flexible chain ($\tilde{\ell}_p = 0$).

3.2.4 sphere charge–chain length phase diagram

In the preceding sections, I focused on conformational changes of a strongly coupled complex in the absence of salt ($\kappa = 0$) and for a mechanically flexible chain ($\ell_p = 0$). I illustrated how transitions between various symmetry classes may be controlled by the rescaled sphere charge, $\tilde{Z}$, and the rescaled chain contour length, $\tilde{L}$. In order to obtain extensive information regarding the effects of $\tilde{Z}$ and $\tilde{L}$, I fix other parameters as $\kappa = 0$ and $\ell_p = 0$, and consider various scans of the space of parameters by changing either of $\tilde{Z}$ and $\tilde{L}$.

The result is a global phase diagram in terms of the rescaled sphere charge and the rescaled chain contour length, which is shown in Figure 3.7. Various configurational phases are indicated in the figure, where the symbols show the transition points and the intrapolating lines represent the phase boundaries. Note that the graph spans actual chain lengths up to $L = 150$ nm and actual sphere charges up to $Z = 300$ when DNA-histone parameter are chosen, i.e. $R_s = 5$ nm and $\tau = 5.88$ nm^{-1}.

As seen, both at sufficiently small chain length and at small sphere charge, the ground-state configuration is given by the fully symmetric phase F as required to minimize the self-repulsion of chain segments. Short chains in phase F (i.e. for $\tilde{L} < 5.57$) are highly adsorbed, while long chains take an expanded conformation with two open arms. The asymmetric phase A is obtained for intermediate to large chain lengths, while the fully wrapped phase R is obtained at small to intermediate values of chain length. Both phases appear only for sufficiently large
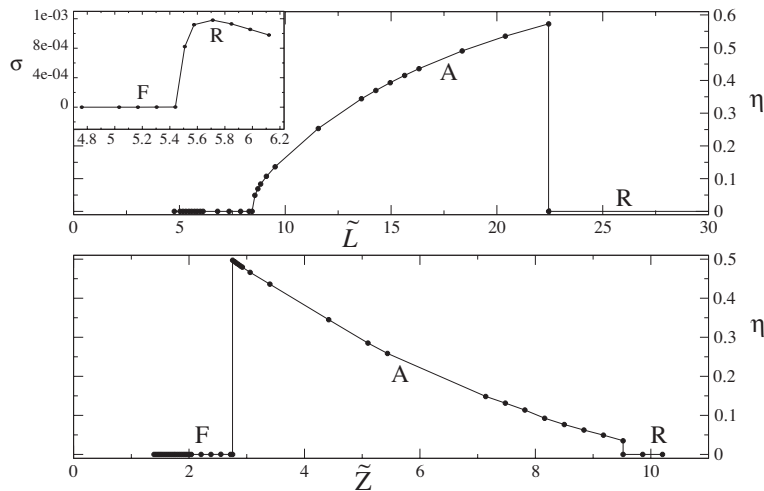
Figure 3.8: The single-complex order parameters. a) shows η as a function of $\tilde{L}$ for $\tilde{Z} = 3.4$ and zero charge. The inset shows order parameter σ as a function of $\tilde{L}$ for the same parameters. b) shows η as a function of $\tilde{Z}$ for $\tilde{L} = 16.3$ and zero salt.

sphere charge, that is for $\tilde{Z} > 1.63$ (corresponding to $Z > 48$ for the DNA-histone system). The highest degree of overcharging as discussed in Section 3.2.3 occurs at intermediate values of chain length and sphere charge, i.e. at the transition line between phases R and A. This region is also accessible experimentally.

The transition line between phases F and R at small $\tilde{L}$ (the dashed horizontal line $\tilde{L} = 5.57$) represents a *continuous* transition, i.e. the order parameters vary continuously (see Figure 3.8) and there are no coexisting states at the transition points. Other transition lines are, however, associated with *discontinuous* changes of the order parameters, as shown in Figure 3.8. The phase boundary between R and A at intermediate chain lengths, $\tilde{L}_{\mathrm{RA}}(\tilde{Z})$, and the phase boundary between A and R′ at large chain lengths, $\tilde{L}_{\mathrm{AR}'}(\tilde{Z})$, where the two-fold rotational symmetry is spontaneously broken (restored), shows linear dependence on the sphere charge, $\tilde{Z}$. An important point to be noted here is that the mirror symmetry phase M (Section 2.4.2) is not observed in the present phase diagram. As mentioned previously, this is because in the absence of salt, the mirror symmetry and the two-fold rotational symmetry of the ground state are broken simultaneously, and they may be decoupled only by introducing a finite Debye screening length, as observed also in previous studies [49].

In the following section, I turn to the influence of the salt concentration and mechanical bending rigidity.

3.3   Phase behavior: Salt effects

In Figure 3.9, I show configurations that are obtained as ground states at fixed rescaled sphere charge $\tilde{Z} = 1$ and rescaled chain length $\tilde{L} = 20.4$ but for various salt concentrations. The previously examined zero-salt limit is depicted as well exhibiting expectedly the expanded state F. As the salt concentration increases, the chain deflection grows but the geometrical symmetries remain intact until $\tilde{\kappa} = 0.5$, where a continuous transition to the mirror symmetry phase M occurs as a result of the two-fold rotational symmetry breaking. In phase M, one of
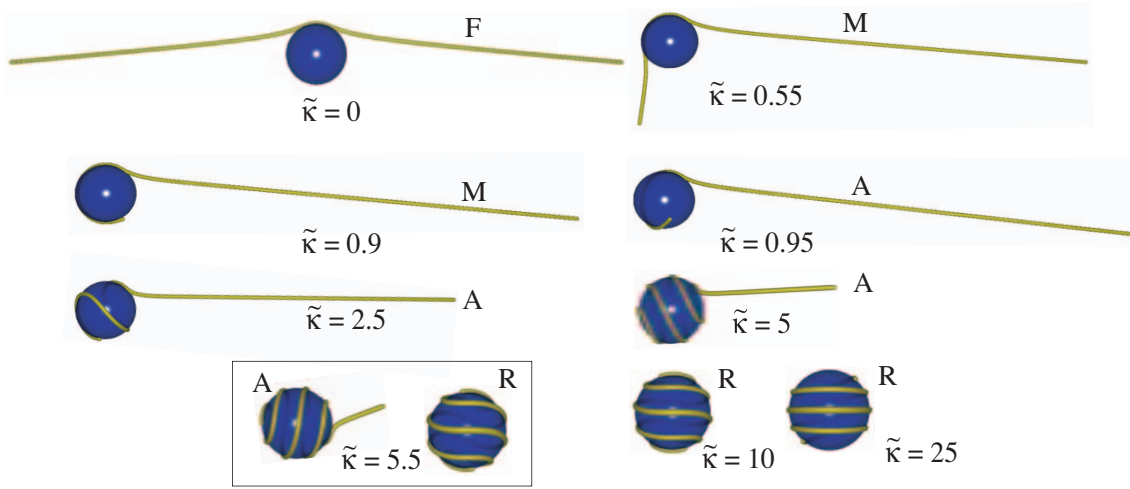
Figure 3.9: Optimal configurations obtained for various salt concentrations by fixing macroion charge at $\tilde{Z} = 1$ and choosing a mechanically flexible ($\ell_{\mathrm{p}} = 0$) PE chain with contour length $\tilde{L} = 20.4$.

the arms grows in length at the expense of the length of the other arm, a process that clearly diminishes the electrostatic repulsion between the two arms. Further increase in the salt concentration triggers wrapping of the PE chain around the sphere from one end (generating an asymmetric state A). Note that at large salt concentration the Debye screening length becomes quite small, e.g., at $\tilde{\kappa} = 5$, one has a screening length of $\kappa^{-1} = R_{\mathrm{s}}/5$ that is 20% of the sphere radius, which allows the chain segments to get closer to each other. Hence the free end is pulled upon the sphere and a highly wrapped conformation is formed from the other end. As seen, the number of turns increases as long as there are enough free segments to be adsorbed. Eventually, a highly *ordered* helical structure is formed in the fully wrapped state R. At $\tilde{\kappa} = 5.5$ (which for $R_{\mathrm{s}} = 5$ nm corresponds to $\kappa = 1.1$ nm^{-1}), phases A and R coexist as shown in the figure. This regime coincides with the physiologically relevant salt regime of about 100 mM monovalent salt, where highly wrapped states have been observed in complexes of DNA and histones in recent experiments as discussed elsewhere [103, 48, 49]. For a mechanically flexible chain with $\ell_{\mathrm{p}} = 0$, phase R remains intact with increasing salt as the bending rigidity which can induce dewrapping of the chain at high salt is missing (see Section 3.3.1 below).[2]

An interesting feature is that the lateral spacing between two successive turns decreases and the helical structure of the wrapped chain becomes more compact with increasing salt [38, 40, 39, 50]. Hence the compact chain wrapping can result in a highly overcharged complex in phase R. The results for the overcharging degree, Γ, Eq. (3.5), are shown in Figure 3.10 (symbols with solid line) as a function of the rescaled inverse screening length $\tilde{\kappa}$ and for parameters corresponding to the configurations in Figure 3.9 ($\tilde{\ell}_{\mathrm{p}} = 0$, $\tilde{Z} = 1$ and $\tilde{L} = 22.4$). As seen, Γ linearly increases with κ as the chain becomes progressively more wrapped around the sphere, and saturates to a constant value in phase R. Strikingly, the complex is found to be overcharged with an effective charge up to twenty times larger than the bare charge of the sphere! Such a large overcharging is possible only in the presence of strong screening

---

[2]Note that for a mechanically flexible chain, ground-state approximation does not hold at very high salt as thermal fluctuations become relevant and may even cause dewrapping of the chain.
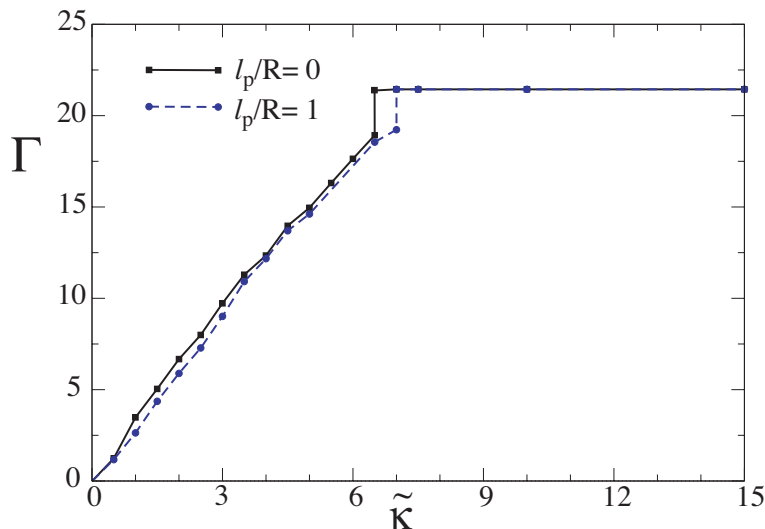
Figure 3.10: Overcharging degree Γ, Eq. (3.5), as a function of $\tilde{\kappa}$ for sphere charge $\tilde{Z} = 1$ and contour length $\tilde{L} = 22.4$. The results are shown both for a mechanically flexible PE chain and a PE chain of persistence length $\ell_{\mathrm{p}} = R_s$

effects, where electrostatic interactions are very short-ranged (compare with Figures 3.2 and 3.6). Note that the variation of $\tilde{L}$ only affects the saturation behavior of Γ (i.e. it occurs at smaller or larger salt for smaller or larger length respectively), while the slop of the linear increase and other features are not affected (data not shown). The slope of the linear increase decreases for chains with non-zero mechanical persistence length and the saturation regime for Γ occurs at higher salt concentration (Figure 3.10, dashed line).

It is interesting to examine how salt-induced transitions described above change with other parameters, such as the sphere charge, $\tilde{Z}$, and the chain contour length and its persistence length. The $\kappa - Z$ phase diagram was investigated for the DNA-histone system throughly in the past [39, 48, 49] (see Chapter 2). Here I concentrate on the features induced by changing the rescaled contour length and the chain stiffness.

3.3.1 salt concentration–chain length phase diagram

I investigate the conformational changes of a PE chain complexed with a macroion by changing the salt concentration for a wide range of chain contour lengths, $\tilde{L}$. The ground-state configurations are determined numerically and the transition points are located by considering symmetry changes of the complex. The results are summarized in a $\tilde{\kappa} - \tilde{L}$ phase diagram shown in Figure 3.11 for fixed rescaled sphere charge $\tilde{Z} = 1$ and vanishing mechanical persistence length $\ell_{\mathrm{p}} = 0$. Note that in actual units and assuming the DNA-histone parameters as $R_{\mathrm{s}} = 5$ nm and $\tau = 5.88$ nm^{-1}, the current graph covers the regime of chain lengths up to $L = 125$ nm, and the inverse screening lengths up to $\kappa = 1.4$ nm ($\tilde{Z} = 1$ corresponds to $Z = 29.4$).

As discussed in detail before, the short-chain regime $\tilde{L} < 5.57$ is dominated by the fully symmetric phase F for the full range of $\tilde{\kappa}$, while intermediate and large chain length regimes show more complex structures corresponding to symmetry phases R and A. As seen in Figure
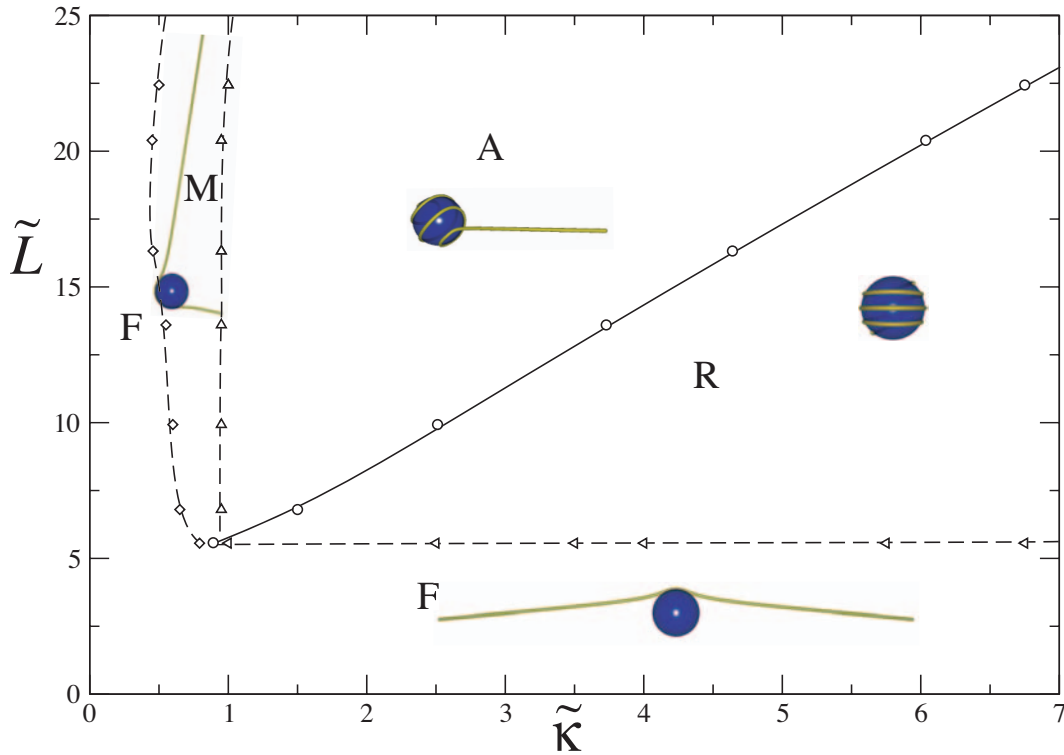
Figure 3.11: Phase diagram in terms of the rescaled inverse screening length $\tilde{\kappa}$ and the rescaled PE contour length $\tilde{L}$ for a mechanically flexible chain ($\ell_p = 0$). The rescaled charge of the sphere is taken to be unity ($\tilde{Z} = 1$).

3.11, the wrapped chain state is stable only for intermediate to large salt concentrations, i.e. inverse Debye screening length of $\tilde{\kappa} > 1$ and intermediate chain lengths. For larger chain lengths, the self-repulsion of the PE chain becomes considerable, deriving the dewrapping of the chain and leading to phase A and evetually, for very large $\tilde{L}$, to expanded phase F (not shown in the graph). Likewise, at small salt concentrations, the self-repulsion factor dominates as electrostatic interactions are long-ranged and one obtains the expanded complex phase F for the whole range of $\tilde{L}$. If the chain's mechanical persistence is finite, one would obtain an additional dewrapping transition to phase F at *high* salt as all electrostatic contributions diminish (see Section 3.4 below).

Unlike the zero-salt situation discussed before, here the two-fold rotational symmetry and the mirror symmetry are decoupled, and I obtain a narrow intermediate region with only mirror-symmetric ground-state configuration (phase M). Therefore, for a sufficiently long chain length $\tilde{L} > 5.57$ (corresponding to $L = 27.85$ nm or about the length of 82 base pairs of DNA), one can capture all four symmetry classes (for the present choice of $\tilde{Z}$ and ℓ_p) by changing the salt concentration (compare with Figure 3.7).

Note that the phase boundaries represent discontinuous (continuous) transitions as indicated by solid (dashed) lines. The transitions between phases F and M, that involves spontaneous breaking (restoring) of the two-fold rotational symmetry is found to be continuous. The same conclusion applies to the phase boundary between phase M and asymmetric
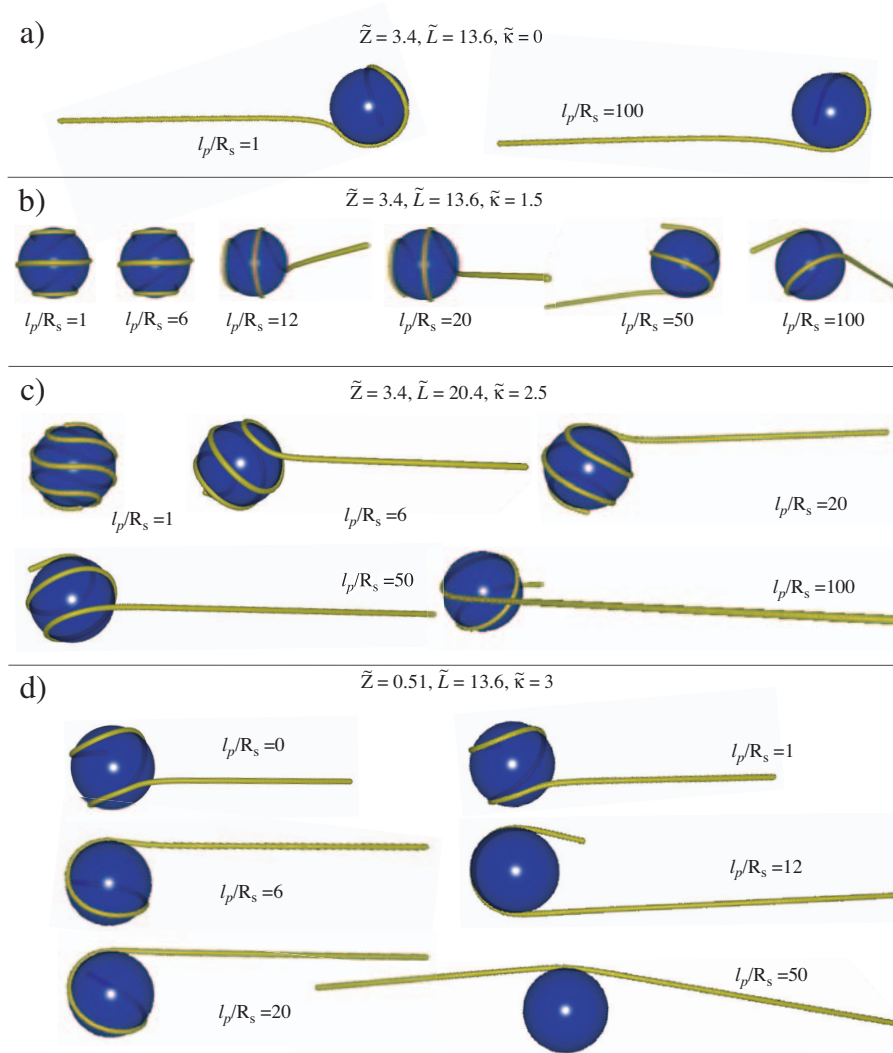
Figure 3.12: Optimal configurations obtained for various mechanical persistence lengths for the PE chain. Other parameters are explicitly indicated on the graph.

phase A, where the mirror symmetry is broken (restored). The interesting feature is that these phase boundaries, i.e. $\tilde{L}_{\mathrm{FM}} = \tilde{L}(\kappa)$ and $\tilde{L}_{\mathrm{MA}} = \tilde{L}(\kappa)$, show little dependence on the salt concentration. On the contrary, the phase boundary between phases F and R, as mentioned before (Section 3.2.4), shows no dependence on the chain length. While, a linear dependence on the salt concentration is found for the chain lengths which marks the transition between phases A and R.

3.4   Phase behavior: Mechanical stiffness effects

So far I considered only a complex formed by a single spherical macroion and a mechanically flexible PE chain (with mechanical persistence length $\ell_{\mathrm{p}} = 0$) in the strong coupling regime, where ground-state analysis is expected to be valid. As discussed in Chapter 2, the

effective bending stiffness of a PE chain results from both mechanical and electrostatic contributions. Therefore, for instance, in the low-salt regime, where electrostatic interactions are long-ranged, the PE chain behaves effectively as a semiflexible chain even if the mechanical bending rigidity of the chain is set to zero. In fact, it is only in a certain regime of parameters, where mechanical bending rigidity begins to play a role as I shall demonstrate below.

In Figure 3.12a, the optimal configuration of a complex is shown for two different regimes of mechanical persistence length ℓ_p and for zero salt concentration $\kappa = 0$. Clearly, the chain conformation is affected little when ℓ_p is increased by two orders of magnitude from $\ell_\mathrm{p}/R_\mathrm{s} = 1$ up to $\ell_\mathrm{p}/R_\mathrm{s} = 100$. Therefore, the results presented previously for sufficiently small κ, and in particular those with $\kappa = 0$, remain qualitatively unaffected by introducing a finite mechanical persistence lengths. In order to demonstrate the interplay between salt effects, I show in Figure 3.12 a selection of significant configurational changes in the presence of salt as the mechanical persistence length changes. In Figure 3.12b, the sphere charge is fixed at an intermediate value of $\tilde{Z} = 3.4$, the chain length is fixed at $\tilde{L} = 13.6$ and the inverse screening length at $\tilde{\kappa} = 1.5$ (corresponding to $Z = 100$, $L = 68$ nm and $\kappa = 0.3$ nm^{-1} for the DNA-histone system). At low ℓ_p, the complex configuration falls into the fully wrapped phase R, which remains intact even at $\ell_\mathrm{p}/R_\mathrm{s} = 6$, which is a large persistence length as compared with the sphere radius (choosing $R_\mathrm{s} = 5$ nm as suitable for histone proteins, one has here $\ell_\mathrm{p} = 30$ nm, which coincides with the bare mechanical persistence length of DNA). As the mechanical persistence length increases, a discontinuous transition to the asymmetric phase A occurs, which persists even up to $\ell_\mathrm{p}/R_\mathrm{s} = 100$ (very stiff chain), reflecting thus a large PE-macroion attraction. But as clearly seen, the chain turns open gradually as the mechanical persistence length increases. A similar behavior is shown in Figure 3.12c for a larger salt concentration ($\tilde{\kappa} = 2.5$) and chain contour length ($\tilde{L} = 20.4$), where at small persistence lengths, the chain shows a highly wrapped conformation. This figure clearly shows the process in which mechanical chain stiffening gradually opens up the wrapped chain by reducing the number of chain turns around the sphere.

To demonstrate the dewrapping transition, I choose a smaller macroion charge of $\tilde{Z} = 0.51$ and a larger salt concentration of $\tilde{\kappa} = 3$ (in actual units, $Z = 15$ and $\kappa = 0.6$ nm^{-1} for DNA-histone system) as shown in Figure 3.12d. In this case, at small persistence lengths, the chain adopts the asymmetric configuration A and thus upon increasing ℓ_p a sequence of transitions occur giving rise to phase M (see, e.g., $\ell_\mathrm{p}/R_\mathrm{s} = 20$) and the expanded phase F (see, e.g., $\ell_\mathrm{p}/R_\mathrm{s} = 50$).

3.5 Conclusion

In this chapter, I considered the structural phase behavior of complexes formed by one polyelectrolyte chain and an oppositely charged sphere within the chain-sphere model and on the ground-state level. I employed a rescaled representation in order to obtain generic results that can be applied to a large variety of systems by mapping the actual system parameters (such as chain persistence length, contour length and linear charge density, sphere charge and radius as well as the salt concentration) to a small set of dimensionless parameters.

As main results, I derived global phase diagrams that represent the effects due to variations in these rescaled parameters, in particular, those due to changes in rescaled chain length, rescaled macroion charge and rescaled inverse Debye screening length (salt concentration). It was shown that variations in these parameters can trigger a wrapping transition in a number of

different ways. For instance, increasing the sphere charge for an intermediate range of chain lengths leads to a fully wrapped state in which the macroion is overcharged by excessive adsorption of the PE chain. But this can occur for rescaled chain lengths $\tilde{L} = L/R_s > 5.57$, and a minimum rescaled sphere charge of $\tilde{Z} = Z/(\tau R_s) > 1.63$ is required as well for a mechanically flexible chain at zero salt. By increasing the salt concentration, however, the wrapped state appears to be stable in a wider range of chain lengths. Note that increasing the chain length in general does not favor wrapping because of the self-repulsion between charges on the chain. At elevated salt concentration, electrostatic interactions are screened and one reaches a highly compact wrapped state, where as shown, the PE chain may wrap around the sphere in several complete turns. This leads to a highly overcharged state, in which the net (absolute) complex charge may exceed the bare sphere charge by more than an order of magnitude. The wrapped state for fixed $\tilde{Z} = 1$ and a mechanically flexible chain can occur again for chain lengths $\tilde{L} = L/R_s > 5.57$, and a minimum rescaled inverse screening length of $\tilde{\kappa} = \kappa R_s > 1$ is required as well.

Note that the regimes of parameters considered in the present study do not cover the well-known *rosette* solutions, which consist of chain configurations with multiple point contacts with the sphere and large low-curvature loops connecting them. These structures are typically obtained for large persistence lengths (as compared with the sphere radius), large chain lengths, and for relatively small adsorption energy (note that the present strongly coupled PE-macroion complexes represent a very large adsorption energy). The rosette structures have been characterized in detail in the past [61, 62] and observed also within Monte-Carlo simulations [63].

Chapter 4

Complex Fibers

The structure and stability of complex fibers, formed by complexation of a single long poly-electrolyte chain and many oppositely charged spherical macroions, are investigated numerically and at the ground-state level using a chain-sphere cell model. The electrostatic and elastic contributions are taken into account in the same way as described in the preceding chapters. Two different models of constrained and unconstrained optimization are introduced, which differ in the way they account for conformational changes of the polyelectrolyte chain. The results indicate a variety of helical structures including zig-zag, solenoidal and beads-on-a-string patterns for the complex fiber depending on the parameters such as salt concentration, macroion charge and chain length per macroion. At about physiological salt concentration, zig-zag patterns are found as stable structures when DNA-histone parameters are adopted and the macroion charge is properly adjusted. The differences between the results obtained from the two optimization models and their possible application to the chromatin fiber structure will be discussed in detail.

Recent years have witnessed a growing interest in the structure and phase behavior of large polyelectrolyte-macroion clusters, in which, for instance, a single long PE chain is complexed with many oppositely charged spheres [20, 22, 28, 29, 41, 42, 47].Perhaps, the most striking example is realized in biology, where a huge fiber is formed by complexation of a long DNA chain with histone proteins, giving rise to the prominent *chromatin fiber*. The biological background for the chromatin fiber and its physical relevance were briefly reviewed in Chapter 1 (see also Ref. [50]). As pointed out therein, the fundamental unit of the chromatin is known as the *nucleosome* consisting of about 200 base pairs of DNA associated with a globular histone octamer. The nucleosome has two main parts: i) the *nucleosome core particle* (or the *core particle*) comprising 146 base pairs of DNA wrapped in a 1-and-3/4 left-handed helical turn around the histone octamer, and ii) the *linker DNA*, which connects adjacent core particles to one another. There is an additional component known as linker histone H1 (or its variant H5), which binds to the DNA and the histone octamer in such a way that it brings the entering and exiting strands of DNA together along a short distance forming a stem-like structure. The role of linker histone will be discussed further below (see also Chapter 1).

In vitro experiments have revealed striking salt-induced conformational changes for the chromatin fiber: at very small salt concentration, the fiber structure is swollen displaying an open *beads-on-a-string* pattern as individual core particles become highly separated from each other; the resultant fiber is known as the 10 nm fiber because of the nearly 10 nm diameter of the core particle. As the salt concentration increases, the fiber becomes more and more folded and finally within the physiologically relevant regime (around 100 mM NaCl), it exhibits a

thick and dense fiber of diameter about 30 nm, known as the 30 nm fiber, which is believed to be formed from a zig-zag arrangement of nucleosomes (in fact, even at salt concentrations as small as, e.g., 5 mM monovalent salt, the fiber is found to exhibit a zig-zag pattern, which is preserved and becomes more compact with increasing salt concentration–see Figures 4.1a, b and Chapter 1). This behavior indicates that predominant electrostatic mechanisms are involved and influence the organization of the chromatin fiber. This is further supported by the evidence that upon changing the charge of the core particle (e.g., by removing histone N-terminal tails that carry a large fraction of the octamer charge, or by removing the highly charged linker histone), the compact fiber structure is altered and, for instance, shows a loose expanded state in the absence of the linker histone.

This behavior has inspired various analytical and numerical studies, whose primary aim has been to explain the structure [116, 117, 122, 123, 125] and mechanical properties [108, 124] of the 30 nm chromatin fiber. These models incorporate a number of different approaches (including purely geometrical two-angle models [122, 137] and its improvements due, e.g., to short-ranged or electrostatic interactions within the fiber [138, 139]).They employ different levels of approximation, and yet their results emerge to be generally consistent with experimental findings and in terms of the structure, they seem to agree with the zig-zag model for the 30 nm chromatin fiber. From a fundamental point of view, this transpires that it is useful to examine the structural properties of charged polymer-sphere fibers based on simple models but on a more systematic level by incorporating generic interactions and geometrical constraints. Hence, one may be able to distinguish the *generic* aspects of the fiber formation from those associated with more specific structural details as found in realistic systems such as chromatin. This constitutes the main purpose of studies presented in this chapter.

I will thus address charged (infinite) *complex fibers* formed by a single long polyelectrolyte chain (PE) and many oppositely charged spheres (macroions) within a simple *chain-sphere cell model*. This model incorporates basic electrostatic and elastic bending contributions from conformational changes of the PE chain as well as interactions between individual PE-macroion complexes ("core particles") within the fiber in a systematic manner. (Note that as before electrostatic effects are accounted for using the linear Debye-Hückel theory.) I present a numerical method that allows to determine energetically optimal fiber structures using a minimization scheme that takes into account internal degrees of freedom associated with the conformation of the complexed PE chain and positions of macroions along the fiber. The organization of the PE chain on individual macroions are not thus externally imposed, but rather obtained as a result of the optimization procedure; hence this approach may be referred to as *unconstrained* or *full* optimization model. As a main result, I demonstrate that a large variety of helical structures arise within this generic model including, for instance, beads-on-a-string, zig-zag, and solenoidal patterns depending on a few basic system parameters such as salt concentration, macroion charge, and chain length per macroion. Other parameters (such as chain persistence length and its charge density as well as the sphere diameter) will be fixed according to the DNA-histone parameters throughout this study.

The ultimate goal of the present approach is to provide a detailed electrostatic model for the chromatin fiber, yet in the present study, no attempt is made as to explicitly incorporate specific structural details associated with realistic chromatin structure such as linker histone, core histone tails, specific binding effects or the precise shape of the histone octamer. Therefore, when comparing with chromatin, the present results should be used with caution, since they are primarily concerned with a generic complex fiber. Additional structural details associated with chromatin can be considered as improvements upon the present chain-sphere

cell model in future studies. Note, in particular, that within the unconstrained optimization model, the wrapping structure of the chain around individual macroions is not fixed and can vary so as to minimize the effective Hamiltonian of the fiber. This can be thought of as a simple model mimicking linker-histone-depleted chromatin. As explained above, the linker histone "glues" together the entering and exiting strands of the DNA and also stabilizes ("seals off") the internal structure of the DNA in the core particle. This latter effect can be mimicked in a simple way using a *constrained optimization* scheme, in which the core complex structure is fixed to the optimal structure of an isolated complex (with a chain length of 146 DNA base pairs), and only the relative orientation of core particle complexes can vary. This leads to a number of significant changes as will be discussed below.

The predicted optimal fiber structure shows a helical form, whose diameter and compactness (e.g., number of macroions per unit length along the fiber axis) are strongly influenced by the salt concentration. In particular, at low salt concentrations, the unconstrained fiber model shows a highly swollen beads-on-a-string pattern of diameter about 10 nm. Upon increasing the salt concentration, the degree of chain wrapping around the sphere increases resulting in more compact and thicker patterns and at the physiological concentration, the optimal fiber shows a zig-zag structure with diameter of 30 nm, which is consistent with experimental results. Further increase in salt concentration leads to highly wrapped individual chain-sphere complexes and thus very compact solenoidal structures for the fiber. The periodic structure of the fiber and dipolar distribution of core particle complexes will be examined afterwards and a two-angle phase diagram in the sense of the two-angle model [122, 137] will be constructed based on the numerically determined optimal structures.

The 30 nm fiber obtained within the unconstrained optimization model shows however a rather small density (number per unit length) of macroions along the fiber, i.e. about one macroion per 10 nm (see Figure 4.4 below), which is comparable with the nucleosome density at relatively small salt concentration where the chromatin still has a 30 nm diameter (Figure 4.1a) [123]. At physiological concentration, the histone density along the chromatin fiber is larger and appears to be about 6 histones per 10 nm. Such a large density of macroions within the fiber is in fact generated by the constrained optimization model, which predicts quite dense 30 nm fiber structures. Interestingly, in this case, the entering and exiting strands of the PE chain form a cross pattern (producing a small entry-exit angle as compared with the unconstrained model results), which resembles the stem-like pattern proposed in Refs. [116, 123, 122] (see Figures 4.1 and 1.9). This indicates that the present approach is indeed able to generate experimentally relevant structures by adding more features to the basic chain-sphere cell model, such as including linker histone H1, which will be modeled explicitly in the future.

4.1 Chain-sphere cell model for complex fibers

The model used here for the study of complex fibers is based upon the chain-sphere model, which was discussed in detail in Chapters 2 and 3. The single-complex chain-sphere model consists of a single semiflexible charged polymer (PE) complexed with a single oppositely charged sphere (macroion). Here I use this model to describe an infinite complex fiber, which is made from complexation of a *single* long PE chain with many macroions. As before, I restrict the discussion to strongly coupled complexes and thus employ the ground-state approximation corresponding to strong adsorption of PE chain on each sphere (Section 2.2).
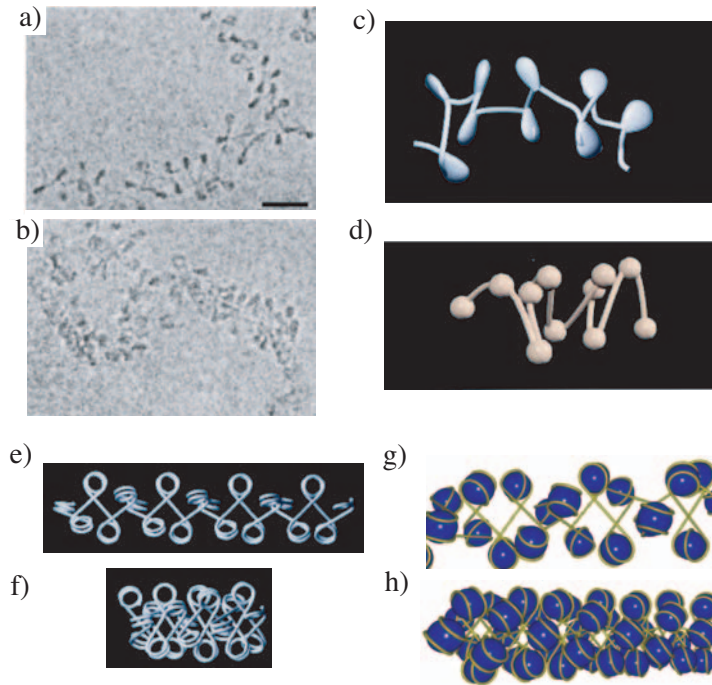
Figure 4.1: Salt induced behavior of an H1-intact chromatin fiber. a) and b) are structures obtained by electron cryomicroscopy (Bednar et al. [123]) of the chromatin extracted from chicken in monovalent salt concentration of about 5 mM and 15 mM respectively. c) and d) show a 3D constructed model of a 9-nucleosome segment of a chicken chromatin fiber imaged at about 5 mM and 80 mM respectively [123]. e) and f) are models of (uniform) chromatin fiber based on a two-angle description introduced by Woodcock et al. [122] using the mean linker entry-exit angle measured form micrographs [123, 122]; angles are 85° in e and 45° in f. g) and h) are fiber models obtained by constrained minimization of the effective Hamiltonian of the fiber, which includes electrostatic interactions explicitly (see Sections 4.1.4 and 4.5) with 200 base pairs of DNA associated with each macroion sphere along the fiber. The fiber in g is obtained for inverse Debye screening length $\kappa = 0.5$ nm^{-1} (corresponding to about 23 mM of monovalent salt) and sphere charge valency $Z = 40$ (see Section 4.5). The parameters in h are $\kappa = 1$ nm^{-1} (corresponding to 100 mM monovalent salt) and $Z = 100$.

The main idea here is to apply a *cell-model* approach by describing the complex fiber in terms of identical *unit cells*, each containing a piece of PE chain associated with a single macroion. The same PE strand links the adjacent unit cells to each other. One can think of each unit cell as two parts: i) the *core particle* complex comprising a single macroion sphere and the PE chain segment which is complexed with (or adsorbed on) the sphere, and ii) the linker chain connecting adjacent core particles to each other–see Figure 4.2. (Note that in the language of the chromatin fiber, the unit cell corresponds to the nucleosome comprising the nucleosome core particle connected to neighboring core particles via linker DNA.) The detailed structure of the PE-macroion complex is assumed to be the same within all unit cells. Using this scheme, the structure of the complex fiber may be deduced by focusing on a single unit cell as will be shown later. Although this cell model greatly simplifies the study of the complex fiber, its predictions for the optimal fiber structure (i.e. the way unit cells or core particles are arranged along the fiber) are non-trivial and display a diverse phase behavior depending

on the precise structure of the core particle complex as well as the inter-complex interactions and the geometrical constraints (see below). In what follows, I first introduce the geometry of the present model and the interaction potentials included, and then discuss the numerical minimization method used in the study of unconstrained complex fibers.

4.1.1 Main unit cell

The complex fiber is constructed within the cell-model approach by replicating a single unit cell, referred to as the *main unit cell*, infinitely many times such that the connectivity and smoothness of the PE chain is preserved and the overall Hamiltonian of the system is minimized. In order to demonstrate this procedure, I will first describe the main unit cell (Figure 4.2).

Each unit cell consists of a piece of PE chain of length L_c with linear charge density $-\tau$ (in units of the elementary charge e), bare mechanical persistence length ℓ_p, complexed with a uniformly charged sphere of radius R_s and charge valency Z within a salt solution of concentration C_s (the inverse Debye screening length is $\kappa = (8\pi\ell_B C_s)^{1/2}$ for monovalent salt). Although the present model is quite general, in making explicit calculations, I set the parameters appropriate for the DNA-histone system, i.e. by choosing $\tau = 5.88$ nm^{-1} (two elementary charges per DNA base pair of length 0.34 nm), $\ell_p = 30$ nm and $R_s = 5$ nm, while L_c, Z and κ can vary as system control parameters. The reason for choosing such numerical values for the DNA-histone system is discussed in Chapter 2. Likewise, to characterize the total length of the PE chain within each unit cell, I will use the language of DNA base pairs by representing the chain length per unit cell (or per macroion) in equivalent number of DNA base pairs (referred to simply as base pairs), i.e. $N_{\rm bp} = L_c/(0.34~nm)$. As before, I will employ a discretization scheme in order to parametrize the chain conformation, which is required for the purpose of numerical optimization methods introduced later.

The PE chain is discretized using $N+1$ discretization points or *beads* of charge valency $q = \tau L_c/(N+1)$ located at positions $\{\mathbf{r}_i^0\}$ with i running form 0 to N. (Note that the super-index 0 denotes the location of beads in the main unit cell.) This amounts to N rigid subunits for the PE chain within each unit cell described by *bond vectors* $\mathbf{u}_i^0 = \mathbf{r}_i^0 - \mathbf{r}_{i-1}^0$, each of a fixed length $|\mathbf{u}_i^0| = \Delta$. The bond vectors are specified by two polar and azimuthal angles, namely, θ_i and ϕ_i in the same way as described in Figure 2.4 for a single complex (see also Eq. (2.13)). The location of the macroion center in the main unit cell is given by $\mathbf{R}^0$, which is chosen as the *origin* of frame of coordinates, i.e. $\mathbf{R}^0 = \mathbf{0}$. I conventionally discretize each natural DNA base pair into two discrete subunits. Therefore, N (which in general has no connection with the number of actual monomers) is simply twice the number of the base pairs $N_{\rm bp}$, and for sufficiently large discretization degree, one has monovalent chain beads, $q = 1$, when DNA linear charge density is adopted.

4.1.2 Unit cell replication

Given the structure of the PE-macroion complex within the main unit cell (which may be obtained in turn from a minimization method as discussed later), one can construct a complex fiber by attaching a copy of the main unit cell (*image* unit cell) to it such that the linker chain tangentially connects the two unit cells and no kink is formed at the boundaries (see Figure 4.2). This means that the last bond vector, $\mathbf{u}_N^0$, of the chain in the main unit cell (labeled by super-index 0) is chosen the same as the first bond vector, $\mathbf{u}_1^1$, of the successive image unit
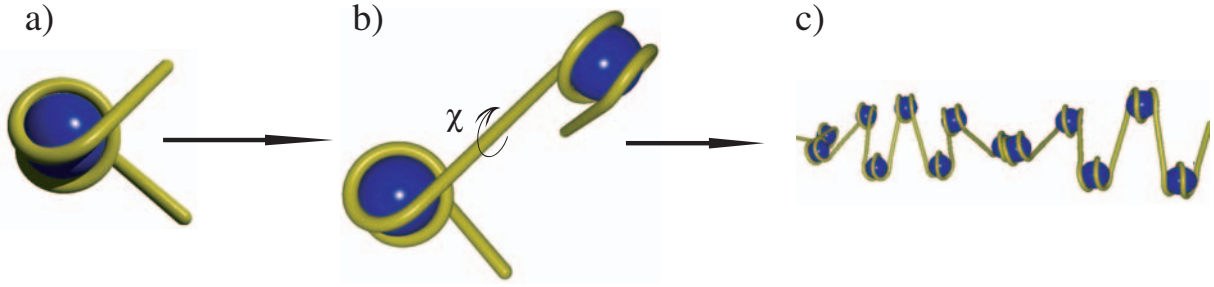
Figure 4.2: Cell model for a complex fiber: a) Each unit cell consists of a single PE-macroion complex the precise configuration of which may be obtained from a numerical minimization method. b) Two adjacent unit cells (which are identical in configuration) are linked together such that they share a common tangent (or bond) vector at the unit cell boundary. Formally, this is performed using a combined translation and rotation transformation (see the text). c) By repeating this procedure the whole complex fiber is constructed from a main unit cell. Within the full minimization scheme, all degrees of freedom associated with a single unit cell (that is chain beads location as well as the boundary rotational angle χ) are varied so as to find the optimal configuration minimizing the full effective Hamiltonian of the fiber.

cell (labeled by super-index 1).

Formally, this replication procedure is established using a translation and a rotation transformation. The translation vector is simply given by $\mathbf{T} = \mathbf{r}_{N-1}^0 - \mathbf{r}_0^0$. By translating all the points in the main unit cell by this vector, an image chain configuration is generated (specified by the image bead positions $\{\mathbf{r}_i^1\}$), which shares a common bead with the original chain configuration (specified by main bead positions $\{\mathbf{r}_i^0\}$), that is $\mathbf{r}_{N-1}^0 = \mathbf{r}_0^1$. The same translation is performed for the macroion sphere in the main unit cell. Next, I rotate the newly constructed (image) unit cell around this common bead such that the two vectors $\mathbf{u}_N^0$ and $\mathbf{u}_1^1$ coincide. Here I introduce a new angular degree of freedom, which is rotation around this common boundary bond vector, i.e. I let the image unit cell rotate around this bond vector by an angle χ (see Figure 4.2) so as to allow the system to energetically optimize its structure with respect to this degree of freedom as well (see Section 4.1.5 below). The full rotation matrix (around the common boundary bead $\mathbf{r}_{N-1}^0 = \mathbf{r}_0^1$ of the two unit cells, which brings the bond vectors $\mathbf{u}_N^0$ and $\mathbf{u}_1^1$ onto one another and then rotates the image unit cell around this common bond vector by an angle of χ) is denoted by $\mathbf{E}$.

The rotation matrix $\mathbf{E}$ is given by

$$\mathbf{E} = \mathbf{B}\,\mathbf{X}\,\mathbf{A} \tag{4.1}$$

with the matrices $\mathbf{A}$, $\mathbf{X}$ and $\mathbf{B}$ defined as follows

$$\mathbf{A} = \begin{pmatrix} -\sin\phi_1 & \cos\phi_1 & 0 \\ -\cos\phi_1\cos\theta_1 & -\sin\phi_1\cos\theta_1 & \sin\theta_1 \\ \sin\theta_1\cos\phi_1 & \sin\phi_1\sin\theta_1 & \cos\theta_1 \end{pmatrix}, \tag{4.2}$$

$$\mathbf{X} = \begin{pmatrix} \cos\chi & -\sin\chi & 0 \\ \sin\chi & \cos\chi & 0 \\ 0 & 0 & 1 \end{pmatrix}, \tag{4.3}$$

$$\mathbf{B} = \begin{pmatrix} -\sin\phi_N & -\cos\phi_N\cos\theta_N & \sin\theta_N\cos\phi_N \\ \cos\phi_N & -\sin\phi_N\cos\theta_N & \sin\phi_N\sin\theta_N \\ 0 & \sin\theta_N & \cos\theta_N \end{pmatrix}, \tag{4.4}$$

where θ_1 and ϕ_1 are the polar and azimuthal angles of $\mathbf{u}_1^0$ and θ_N and ϕ_N are the polar and azimuthal angles of $\mathbf{u}_N^0$. Note that the matrix $\mathbf{E}$ is only a function of the angles $\{\chi, \theta_1, \phi_1, \theta_N, \phi_N\}$.

The position of the i-th bead of the PE chain in the first image unit cell, $\mathbf{r}_i^1$, is obtained formally from the positions of the chain beads in the main unit cell as

$$\mathbf{r}_i^1 = \mathbf{E}\cdot(\mathbf{r}_i^0 - \mathbf{r}_0^0) + \mathbf{r}_{N-1}^0. \tag{4.5}$$

Thus, one needs the position of three beads (labeled by i, 0 and $N-1$) from the main unit cell to determine each bead position in the image unit cell. I perform the above translation/rotation procedure recursively for a given chain configuration in the main unit cell and for a given χ-angle, and thereby obtain the positions of the PE chain beads in the secondary image unit cell (labeled by super-index 2), $\{\mathbf{r}_i^2\}$, from those of the first image unit cell, $\{\mathbf{r}_i^1\}$, and so on. Similar transformation is used for the macroion position.

In general, the position of the i-th chain bead and the sphere center in the k-th unit cell (labeled by super-index k), that is $\mathbf{r}_i^k$ and $\mathbf{R}^k$ respectively, are obtained as

$$\mathbf{r}_i^k = \mathbf{E}\cdot(\mathbf{r}_i^{k-1} - \mathbf{r}_0^{k-1}) + \mathbf{r}_{N-1}^{k-1} \tag{4.6}$$

$$\mathbf{R}^k = \mathbf{E}\cdot(\mathbf{R}^{k-1} - \mathbf{r}_0^{k-1}) + \mathbf{r}_{N-1}^{k-1}, \tag{4.7}$$

which fully characterize the overall configuration of a complex fiber. This scheme for constructing a complex fiber is shown schematically in Figure 4.2. Note that this replication method can also be used within other numerical methods such as Monte-Carlo simulations.

The resultant fiber obtained from this replication procedure can exhibit a wide range of structures as dictated by both the structure of the unit cell, the angle χ, as well as all interactions involved. It may or may not show periodic helical structures (i.e. structures with discrete translational symmetry). In fact, as it will be shown later (Section 4.7), the optimal structure are *nearly* periodic, i.e. they do not show exact (rational) periodicity but may be described by a distribution of periodicities with a sharp peak around a mean value.

4.1.3 Two-angle description

Note that the arrangement of *macroions* along the fiber within the present model may also be described using a two-angle description in the spirit of the two-angle model presented in Ref. [122] for the chromatin fiber. For the sake of comparison, I define two independent angles, referred to as the entry-exit angle, ψ, and the dihedral angle, ξ, which are similar but not identical with the angles defined in Ref. [122].[1]

Let us assume that $\mathbf{a}_n = \mathbf{R}^n - \mathbf{R}^{n-1}$ is the connecting vector between two successive macroion spheres, where $\mathbf{R}^n$ is the position of the n-th sphere. The entry-exit angle, ψ, is

---

[1]In particular, the entry-exit angle in Ref. [122] is the angle formed between the entering and exiting DNA linkers, while in the present model, these two strands may be displaced due to the chain wrapping-dewrapping process, and a different definition is thus required. The situation is somewhat different when the wrapped chain structure is fixed on the macroion as will be discussed within the constrained optimization model in Section 4.5.
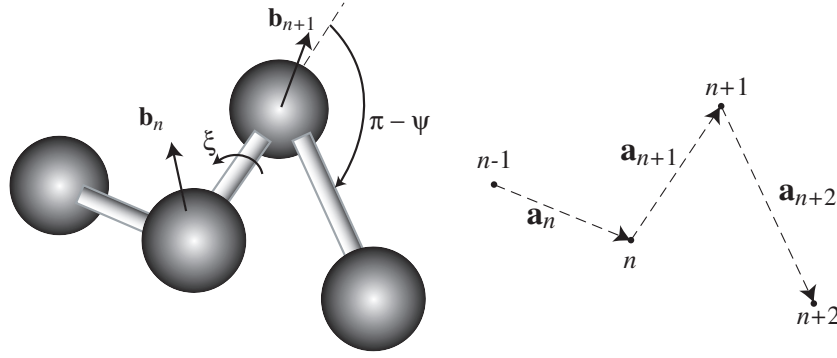
Figure 4.3: A schematic view of two-angle representation of macroion positions along the chromatin fiber. Each two successive spherical macroions, labeled by $n-1$ and n are connected to each other via the vector $\mathbf{a}_n$. The entry-exit angle ψ is defined as the complementary angle between vectors $\mathbf{a}_n$ and $\mathbf{a}_{n+1}$, as demonstrated in the graph. On the other hand, each three consecutive macroions, labeled by $n-1$, n and $n+1$, define a plate with normal vector $\mathbf{b}_n$. The dihedral angle ξ is defined as the angle between two such normal vectors $\mathbf{b}_n$ and $\mathbf{b}_{n+1}$ (see the formal definitions in the text).

defined from the angle between two such consecutive connecting vectors, $\mathbf{a}_n$ and $\mathbf{a}_{n+1}$, i.e. (see Figure 4.3)

$$\psi = \pi - \cos^{-1}\left(\frac{\mathbf{a}_n \cdot \mathbf{a}_{n+1}}{|\mathbf{a}_n||\mathbf{a}_{n+1}|}\right). \tag{4.8}$$

The dihedral angle, ξ, the angle by which four consecutive spheres are out-plane, is determined by calculating the angle between the normal vectors of two planes, one identified by spheres $\mathbf{R}^{n-1}$, $\mathbf{R}^n$, $\mathbf{R}^{n+1}$ and the other identified by $\mathbf{R}^n$, $\mathbf{R}^{n+1}$, $\mathbf{R}^{n+2}$, respectively. Explicitly, one has

$$\xi = \cos^{-1}\left(\frac{\mathbf{b}_n \cdot \mathbf{b}_{n+1}}{|\mathbf{b}_n||\mathbf{b}_{n+1}|}\right). \tag{4.9}$$

with $\mathbf{b}_n = \mathbf{a}_n \times \mathbf{a}_{n+1}$. For a perfect helical structure, which is the case in the present model, ψ and ξ are independent of n.

4.1.4 Intra-fiber interactions

The two-angle model is based on purely geometrical considerations [122, 137]. More elaborate chromatin fiber models have also been developed, which consider excluded-volume interactions as well as bending rigidity of the linker DNA combined with a short-ranged phenomenological interaction between nucleosomes [138, 139]. The core particle complex is often modeled effectively neglecting thus its precise structure. The simplicity of assembling PE-macroion fiber in the present chain-sphere cell model, however, enables one to consider the detailed structure of the PE chain on macroions and its bending energy cost, and incorporate electrostatic interactions (as well as excluded-volume interactions) between all charged components, i.e. chain beads and macroions within the fiber. These contributions are included in the same way as described for a single chain-sphere complex in Chapter 2, i.e. electrostatic interactions are considered on the linear Debye-Hückel level (thus effectively modeling salt screening), the mechanical bending rigidity and electrostatic self-energy of the PE chain are explicitly included, and macroions are modeled as semi-rigid spheres using a short-ranged soft potential. (The

approximations involved in this approach and their possible justification have been discussed in detail in Chapter 2.)

Because the infinite complex fiber is obtained by replicating identical unit cells, one can focus on the effective Hamiltonian per unit cell, which can be written as

$$\mathcal{H} = \mathcal{H}_{uc} + \sum_{k=1}^{M} \mathcal{H}_I^{0k}, \tag{4.10}$$

where $\mathcal{H}_{uc}$ gives the *self-energy* of the main unit cell, and $\mathcal{H}_I^{0k}$ accounts for the interactions between different unit cells. In the second term, I have used a cut-off M, i.e. account for the interaction between M consecutive unit cell, which is typically chosen as $M = 5$. (As explicitly checked, the results are not influenced by changing M, which in most cases is justified by the fact that electrostatic interaction are highly screened in the presence of salt. Note that for low salt, the highly expanded state of the unit cell, results in a large effective distance between two adjacent cells, therefore, the choice of $M = 5$ is still a good choice.)

The self-energy of main unit cell may be written in discretized form (Section 2.3.1) as

$$\mathcal{H}_{uc} = \frac{\ell_\mathrm{p}}{\Delta} \sum_{i=2}^{N} \left\{ 1 - \cos(\theta_i - \theta_{i-1}) + \sin\theta_i \sin\theta_{i-1} \Big(1 - \cos(\phi_i - \phi_{i-1}) \Big) \right\} \tag{4.11}$$

$$+ q^2 \ell_\mathrm{B} \sum_{i=0}^{N-1} \sum_{j=i+1}^{N} \frac{e^{-\kappa|\mathbf{r}_i^0 - \mathbf{r}_j^0|}}{|\mathbf{r}_i^0 - \mathbf{r}_j^0|} - \frac{Zq\ell_\mathrm{B}}{1 + \kappa R_\mathrm{s}} \sum_{i=0}^{N} \left[\frac{e^{-\kappa(|\mathbf{r}_i^0| - R_\mathrm{s})}}{|\mathbf{r}_i^0|} - A e^{-(|\mathbf{r}_i^0| - R_\mathrm{s})/\alpha} \right]$$

(in units of $k_\mathrm{B}T$), where the first term is the bare mechanical bending rigidity contribution, the second term gives the screened electrostatic repulsion between chain segments, the third term involves screened chain-sphere attraction as well as the soft-core repulsion (which is specified by a repulsion range, α, and strength A, which are fixed at typical values of $A = 0.014$ nm^{-1} and $\alpha = 0.02$ nm–see Section 2.1.3 and Appendix E).

The interaction between the main unit cell and the k-th image unit cell, $\mathcal{H}_I^{0k}$, may be written (in units of $k_\mathrm{B}T$) as

$$\mathcal{H}_I^{0k} = q^2 \ell_\mathrm{B} \sum_{i=0}^{N} \sum_{j=2}^{N} \frac{e^{-\kappa|\mathbf{r}_i^0 - \mathbf{r}_j^k|}}{|\mathbf{r}_i^0 - \mathbf{r}_j^k|} - \frac{Zq\ell_\mathrm{B}}{1 + \kappa R_\mathrm{s}} \left[\sum_{i=0}^{N} \left(\frac{e^{-\kappa(|\mathbf{r}_i^0 - \mathbf{R}^k| - R_\mathrm{s})}}{|\mathbf{r}_i^0 - \mathbf{R}^k|} - A e^{-(|\mathbf{r}_i^0 - \mathbf{R}^k| - R_\mathrm{s})/\alpha} \right) \right.$$

$$\left. + \sum_{i=2}^{N} \left(\frac{e^{-\kappa(|\mathbf{r}_i^k| - R_\mathrm{s})}}{|\mathbf{r}_i^k|} - A e^{-(|\mathbf{r}_i^k| - R_\mathrm{s})/\alpha} \right) \right] + \frac{Z^2 \ell_\mathrm{B} e^{2\kappa R_\mathrm{s}}}{(1 + \kappa R_\mathrm{s})^2} \frac{e^{-\kappa|\mathbf{R}^k|}}{|\mathbf{R}^k|}, \tag{4.12}$$

where, as explained before, $\mathbf{r}_i^k$ and $\mathbf{R}^k$ denote the position of the i-th chain bead and the sphere center in the k-th image unit cell, respectively (note that the first two beads $i = 0, 1$ for the k-th image unit cell are counted as the last beads of the $(k-1)$-th cell since they share a common boundary vector as explained before). In Eq. (4.12), the first term corresponds to repulsion between chain segments in the main unit cell and those in the k-th image unit cell, the second term involves screened electrostatic attraction and soft-repulsion between PE chain in the main unit cell and the sphere in the k-th image unit cell, where the third term indicates exactly the same interaction between PE chain in the k-th image unit cell and the sphere in the main unit call. The last term represents screened electrostatic repulsion between the spheres in the two unit cells.

4.1.5 Numerical method: Unconstrained (full) minimization model

In order to study the organization of the fiber for various system parameters, I employ the so-called ground-state-dominance approximation, which, as discussed in Chapter 2, is valid for strongly coupled PE-macroion complexes. One thus seeks the *optimal* or *ground-state* configuration of the fiber minimizing the effective Hamiltonian (4.10) with respect to all degrees of freedom, i.e. those specifying the overall PE conformation and the additional unit cell rotation angle, χ. This amounts to $2N + 1$ independent degrees of freedom. Recall from Chapter 2, that the chain configuration (within the main unit cell) is specified by the set of variables $\{\theta_i, \phi_{i \neq P}, r_P\}$, where θ_i and $\phi_{i \neq P}$ are bond vectors polar and azimuthal angles and r_P is the z component of the position of the middle bead of the chain $P = N/2$ (measured from the sphere center); ϕ_P (azimuthal angle of the subunit or bond vector $\mathbf{u}_P$) is fixed in order to remove Goldestone modes associated with a trivial rotational symmetry around the z axis connecting the sphere center to the middle bead P.

Due to a large number of free variables, this minimization clearly requires a numerical approach, which is implemented using the quasi-Newton minimization algorithm [3] (see Section 2.3). The quasi-Newton method finds the minimum of the Hamiltonian using its first-order derivatives; at the minimum the first-order variation of the Hamiltonian vanishes, i.e.

$$\delta\mathcal{H} = \sum_{i=1}^{N} \left(\frac{\mathrm{d}\mathcal{H}}{\mathrm{d}\theta_i}\delta\theta_i + \frac{\mathrm{d}\mathcal{H}}{\mathrm{d}\phi_i}\delta\phi_i \right) + \frac{\mathrm{d}\mathcal{H}}{\mathrm{d}\chi}\delta\chi + \frac{\mathrm{d}\mathcal{H}}{\mathrm{d}r_P}\delta r_P = 0, \tag{4.13}$$

where the azimuthal angle ϕ_P is excluded. In Appendix A.2, I present the details of calculations for derivatives of the Hamiltonian as used in the minimization algorithm.

4.2 Salt-induced structural changes of the fiber

In this section, I investigate the dependence of structural properties of the complex fiber on the salt concentration. Here I concentrate on a system with fixed macroion charge valency $Z = 15$ and *fixed* total length of the PE chain per unit cell (or per macroion), which is chosen to be $L_c = 68$ nm equivalent to the length of $N_{\mathrm{bp}} = 200$ base pairs of DNA. This value falls within the experimental range [116, 123]. The effects due to the chain length and macroion charge will be considered in the forthcoming sections. Recall that the salt concentration enters via the Debye inverse screening length, κ, which is varied here between $\kappa = 0$ (no salt) and 1.5 nm^{-1} and thus, in particular, spans the physiologically relevant range of about $\kappa = 1$ nm^{-1} (corresponding to 100 mM monovalent salt).

In this section, I will only consider the full (unconstrained) minimization scheme as explained before (Section 4.1.5). Therefore, the length of the chain wrapped around the sphere is not fixed and can change according to various intra-cell and inter-cell interactions. The results display a variety of optimal helical fibers visualized in Figures 4.4 and 4.5, which reflect drastic structural variations by changing the salt concentration in the system.

4.2.1 Overall behavior for various salt concentrations

The optimal (or ground-state) fiber configuration takes a number of different geometrical architectures, which can be distinguished as *beads-on-a-string* (Figures 4.4a, b, g), *zig-zag* or crossed-linker (Figures 4.4d, 4.5a-e), *loose solenoidal* (Figures 4.4c, e, f) and also *compact*
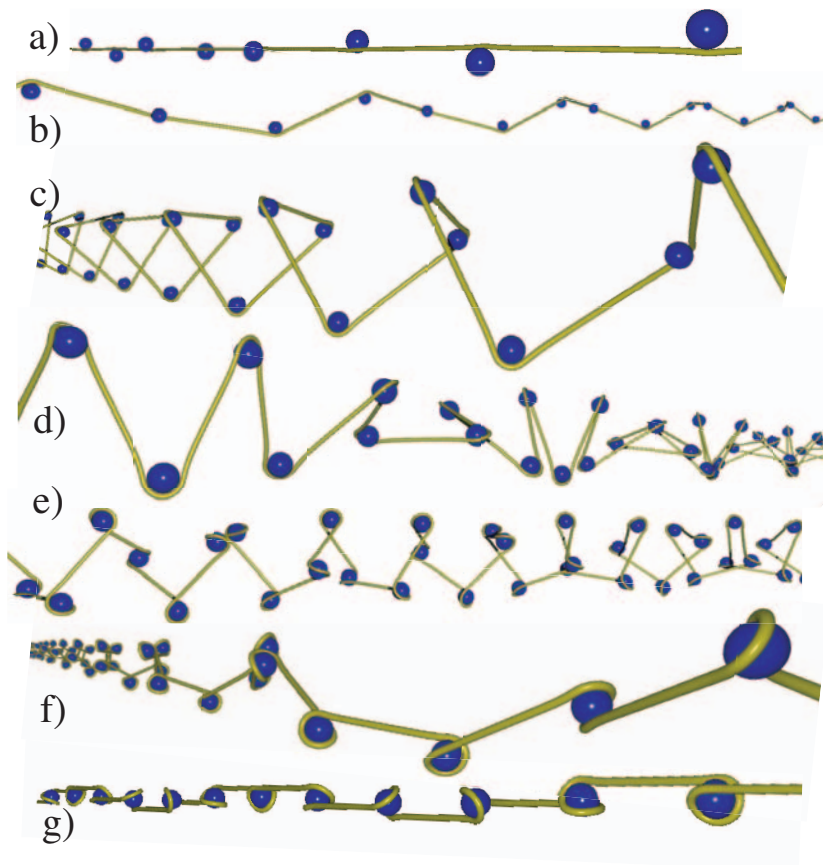
Figure 4.4: The optimal spatial configuration of the complex fiber as obtained from the full minimization of the Hamiltonian (4.10) for macroion (sphere) charge valency $Z = 15$, total chain length per unit cell (per sphere) of $L_c = 68$ nm (equivalent to 200 DNA base pairs) and for various Debye inverse screening lengths (from top to bottom): $\kappa = 0$ (a), 0.1 (b), 0.2 (c), 0.3 (d), 0.4 (e), 0.5 (f) and 0.6 nm^{-1} (g). Shown fiber structures are classified as: beads-on-a-string structure (a, b and g), loose solenoidal structure (c, e, and f) and zig-zag structure (d). In a-f, the PE chain wraps less than a complete turn around the sphere.

solenoidal structures (Figures 4.5f, g). These types of patterns have also been identified within other recent studies based on different models for the chromatin fiber [122, 137, 138].

As seen in the figures, the degree of complexation of the PE chain increases with increasing salt concentration as a larger length of the chain is wrapped around each sphere. As discussed in Chapter 3, the highly wrapped state occurs at intermediate salt concentration and results from the growing dominance of electrostatic chain-sphere attraction against the chain (electrostatic and bending) self-energy (as will be shown later, core particles are highly *overcharged* by the PE adsorption much in the same way as a single isolated complex is overcharged at intermediate salt regime.)

At vanishing salt concentration (Figure 4.4a), the PE chain takes a straight-line shape and macroions are merely attached to the chain. Such an extended (unwrapped) structure reflects the dominant electrostatic self-energy of the PE chain as charged units interact with long-ranged Coulomb interaction (Chapter 3). But interestingly, the distribution of spheres
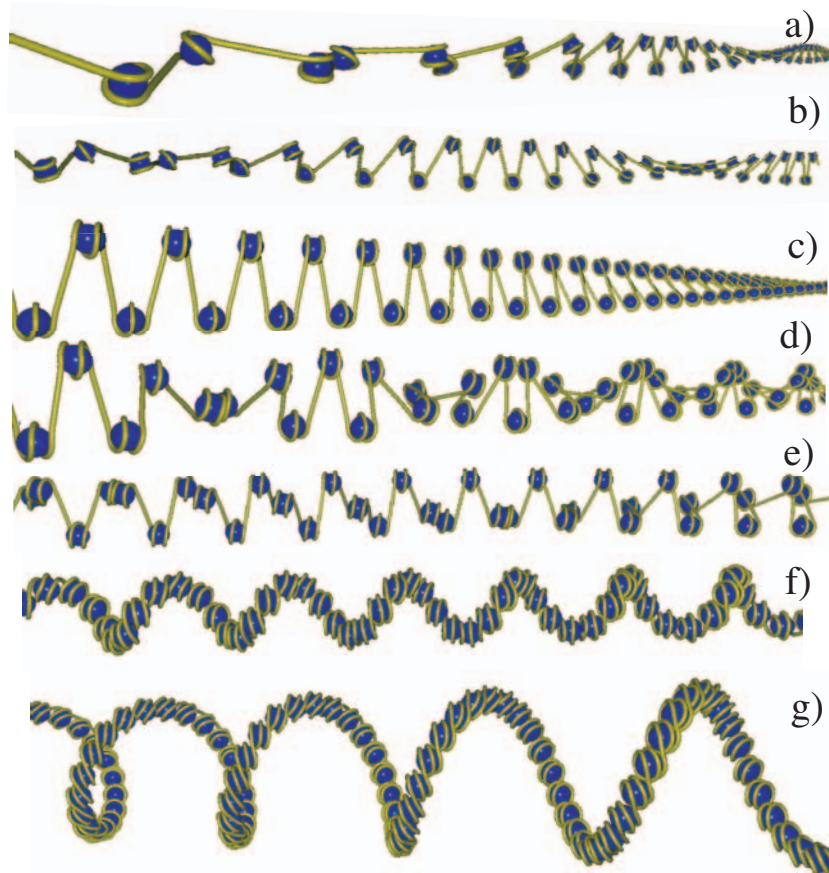
Figure 4.5: Same as Figure 4.4 but for Debye inverse screening lengths (from top to bottom): $\kappa = 0.7$ (a), 0.8 (b), 0.9 (c), 1 (d), 1.1 (e), 1.2 (f) and 1.5 nm^{-1} (g). The structures demonstrated here are zig-zag structure (a-e) and compact solenoidal structures (f and g). The PE-chain completes its second turn around each sphere for $\kappa = 1.2$ (f).

around the chain is periodic and their centers lie on different angular locations around the chain. The entry-exit angle (ψ-angle) here is $\psi \simeq \pi$ (Section 4.5). As the salt concentration and thereby, the chain complexation degree increases, the entry-exit angle of the chain on a sphere decreases. This triggers formation of more compact structures (or thicker fibers) as seen in Figure 4.4. For inverse screening length in the range of $\kappa = 0.3$ to 0.6 nm^{-1} (Figures 4.4d-g), the fiber structure shows an anomalous behavior, i.e. the diameter of the fiber decreases and the projected distance (along the fiber axis) between neighboring sphere centers increases, which is due to the fact that the chain completes its first turn around the sphere (as a result, the entry-exit angle becomes again close to $\psi \approx \pi$ for $\kappa = 0.6$ nm^{-1}). Upon further complexation of the chain (Figures 4.5a-e), the fiber thickness tends to increase and the spheres become more densely packed (the entry-exit angle decreases). These properties will be quantified in the following section.

Note that in the range of Debye screening lengths $\kappa = 0$ (zero salt) up to about $\kappa = 0.5$ nm^{-1} (25 mM monovalent salt), the PE wrapping around macroions is less than a complete turn and thus these configurations may be considered locally as beads-on-a-string structures,
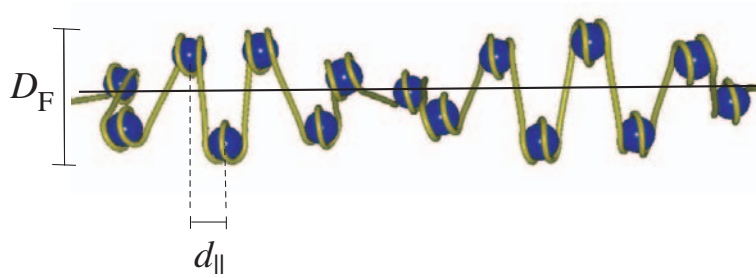
Figure 4.6: Schematic representation of the fiber diameter, $D_{\rm F}$, and the projected center-to-center distance, $d_{||}$, of consecutive spheres along the fiber axis. The central fiber axis is shown by a horizontal solid line.

although for non-vanishing salt, the fiber takes an overall zig-zag or loose solenoidal structure with rather large diameter as compared with the sphere size (see Figure 4.5 c, d and e). In fact, for higher sphere charge, the chain is wrapped more strongly around the macroion even for small κ, leading to different structures that will be discussed later in this chapter. The beads-on-a-string structure observed *in vitro* for chromatin at low ionic strength (the so-called 10 nm fiber) is more closer to the result obtained from the present model at $\kappa = 0.6$ nm^{-1}, where spheres are almost aligned and the angle between entering and exiting chain strands in each core particle is $\psi \simeq \pi$.

4.2.2 Structural analysis of the fiber: Summary of results

Beside the overall architecture of the complex fiber, one is interested in geometrical character-istics of the fiber and the way they vary with the salt concentration. Some of the characteristic parameters that are considered here are as follows (see Figure 4.6):

- The fiber diameter, $D_{\rm F}$, which refers to the diameter of the smallest *outer* cylinder co-axially enclosing the fiber.

- The projected center-to-center distance, $d_{||}$, of consecutive spheres along the central fiber axis, which gives a measure of *compactness* of the fiber when compared with the fiber diameter.

- The entry-exit angle, ψ, and the dihedral angle, ξ, as defined in Section 4.5.

At the end of this chapter (Section 4.7), I return to the periodic behavior of the fiber (i.e. whether the local structure of the fiber is repeated periodically along its axis), and also consider the local distribution of charges, which may be specified, for instance, by local dipole moments of the core particles. The latter gives insight into the internal interactions and orientational correlations between core particles within the fiber. For the moment, it is important to note that the optimal fiber structure obtained from the energy minimization method is not necessarily a simple helix with a single periodicity, but in general displays multiple periodicities depending on the way spheres are organized along the fiber backbone as will be made clear later on.

In what follows, I will focus on the diameter and compactness of the fiber and present a $\xi - \psi$ phase diagram as the salt concentration varies (the sphere charge and the total chain length per sphere are fixed as $Z = 15$ and $N_{bp}=200$).

Geometry

In Figure 4.7 a and b, I show the results for the projected distance between neighboring sphere centers, $d_{||}$, together with the outer fiber diameter, D_F, as a function of salt concentration.

As seen, the projected distance takes a maximum value of about $d_{||} = 70$ nm at zero salt concentration and then falls off in a non-monotonic fashion to quite small values of about sphere diameter $d_{||} \simeq R_s = 5$ nm, when inverse screening length (salt concentration) exceeds $\kappa = 1$ nm^{-1} (100 mM NaCl) reflecting a dense fiber with a *density* of about two spheres per 10 nm along the fiber axis. This regime, as seen from the optimal configurations in Figure 4.5, exhibits compact solenoidal structure. The non-monotonic behavior of projected distance with salt concentration displays a local minimum and a local maximum at inverse screening lengths of about $\kappa = 0.3$ nm^{-1} and $\kappa = 0.6$ nm^{-1}, respectively. These extrema in fact correspond to extrema in fiber diameter, D_F, which shows an almost opposite trend as compared with the projected distance when the salt concentration is varied (Figure 4.7b). At zero salt, the outer fiber diameter is roughly twice the sphere diameter, i.e. $D_F = 20$ nm. It changes rapidly at small salt concentration with κ, reaching a maximum and then a sharp minimum at an intermediate salt concentration of about $\kappa = 0.6$ nm^{-1}, where the projected distance exhibits a local maximum. The minimum fiber diameter at this point is about 10 nm (equal to the sphere diameter), hence at $\kappa = 0.6$ nm^{-1}, the complex fiber shows its largest projected distance to diameter ratio $d_{||}/D_F = 4$. As seen in Figure 4.4g, the fiber takes an almost one-dimensional beads-on-a-string structure in this region nearly resembling the so-called "10 nm fiber" pattern observed for chromatin fiber *in vitro* (see Figure 1.7) [1].

Interestingly, over the range of intermediate salt concentrations between $\kappa = 0.8$ and 1.3 nm^{-1} (corresponding to 60-160 mM monovalent salt), the fiber diameter remains almost unchanged at about $D_F = 30$ nm (reflected by a plateau-like region in Figure 4.7b), although the fiber structure changes from zig-zag to solenoidal pattern. The chain wrapping in this region amounts to about 1-and-3/4 turn, that is close to the structure of the nucleosome core particles in chromatin at intermediate salt concentration about the physiological range [123, 116, 122]. In fact, the experiments reveal that the chromatin fiber exhibits a dense structure in this regime with a diameter of about 30 nm, the so-called "30 nm fiber". The present results, which predict a stable 30 nm complex fiber at intermediate salt, thus represents a trend consistent with experiments. The resultant fiber however has a different local structure and a lower density of spheres (number of spheres per unit length along the fiber axis) as compared with the experimentally observed 30 nm fiber due to the fact that in the present model, the chain configuration within the core particle (and the conformation of entering and exiting chain) can change subject to interactions with other units; while in the experiments with H1-stabilized linker histone, the core particle configuration is almost fixed (and the entering and exiting strands form a stem-like pattern). As will be shown later, the constrained minimization model can improve these aspects of the modeled fiber to some extent.

For large salt concentrations (beyond $\kappa = 1.3$ nm^{-1}), the fiber diameter rapidly increases but the projected distance between spheres as well as the overall solenoidal form of the fiber (see, e.g., Figure 4.5f) remain intact. At $\kappa = 1.5$ nm^{-1}, the tightly packed arrangement of spheres along the fiber is reflected by a very small ratio $d_{||}/D_F = 0.077$.
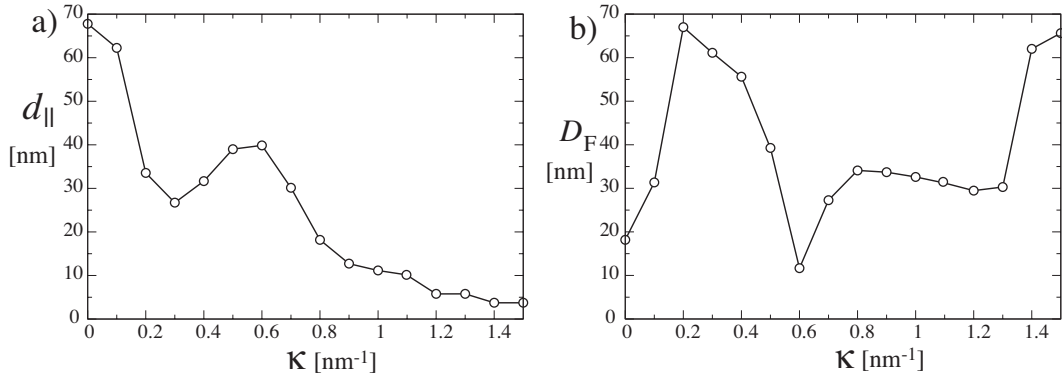
Figure 4.7: a) The projected distance of neighboring sphere centers along the fiber axis, $d_{||}$, and b) the fiber diameter, $D_{\rm F}$, as a function of inverse screening length. The macroion charge and chain length per unit cell are fixed as $Z = 15$ and $L_c = 68$ nm.

Overcharging

It is useful to consider the local structure of the core particles within the fiber in more detail. A closer view of the unit cell of the fiber is shown in Figure 4.8a for different salt concentrations. Here I introduce two quantities that measure the degree of PE chain wrapping around each macroion in the fiber, namely, the *adsorbed* PE charge, U (that includes only those chain beads that are within distances less than or equal to $1.02R_{\rm s}$ from the sphere center), and the net charge of the core particle defined as $U - Z$. Both quantities are shown in Figure 4.8b as a function of κ.

The unit cell configurations clearly show that the PE chain becomes gradually more wrapped around the sphere upon increasing the salt concentration amounting to more than two complete turns at high salt ($\kappa = 1.5$ nm^{-1}). As seen from Figure 4.8b, the adsorbed PE charge increases almost linearly with the salt concentration and reaches a plateau-like region at high salt in agreement with the behavior observed for a single isolated complex as shown in Figure 3.10. (The saturation at high salt is due to the finite and fixed length of the PE chain in each unit cell that is here 200 DNA base pairs.) Note that for the chosen parameters here (with sphere valency of $Z = 15$), the core particle is always overcharged, that is $U - Z > 0$. The overcharging degree $\Gamma = (U - Z)/Z$ becomes quite large at intermediate salt, such that the net complex charge becomes more than twenty times larger in magnitude than the bare sphere charge.

The figures here clearly display how the entry-exit angle, ψ, changes with salt concentrations as a result of the wrapping process, which in turn affects the overall structure of the fiber.

Energetics

Another important quantity which can provide more insight into the physical stability of the complex fiber is the *fiber binding energy*, $\Delta E = E_{\rm F} - E_0$, which is defined as the difference between the energy of a complex fiber per unit cell, $E_{\rm F}$, and that of an infinite free PE chain per unit cell (which in this case contains a straight PE chain of length L_c). Note that the
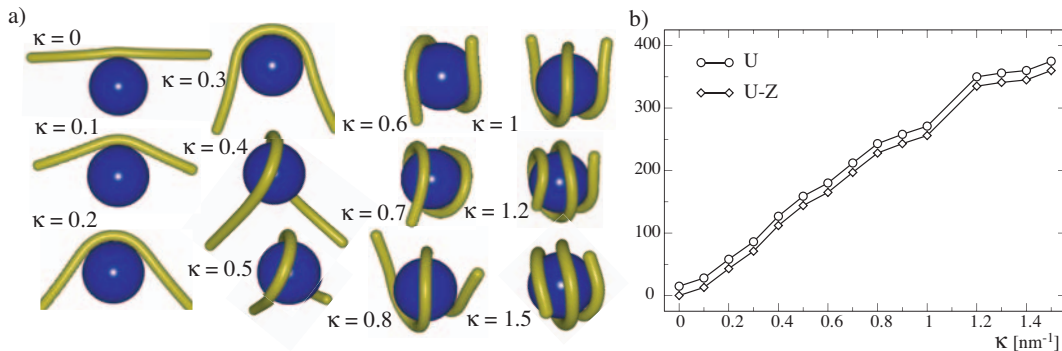
Figure 4.8: a) The local structure of the core particles within the numerically determined optimal fiber for sphere charge valency $Z = 15$ and various Debye screening length as indicated in the graph. The total length of the PE chain per unit cell is fixed as $L_c = 68$ nm ($N_{bp} = 200$). The increase in the number of PE chain turns around the macroion is clearly demonstrated. b) Number of chain beads (circles) that are attached to the sphere (i.e. within the distance $1.02R_s$ from the sphere center where $R_s = 5$ nm is the sphere radius) as a function of inverse screening length. Note that each bead is monovalent, thus this number equals the PE charge adsorbed on the sphere. Diamonds show the net charge of the complex, i.e. the sphere charge $-Z$ plus the PE charge adsorbed on the sphere. At vanishing salt, the sphere charge is already nearly compensated by the adsorbed PE segment and thus for larger salt, the sphere is strongly overcharged.

energies here refer to the ground-state energies, that is the minimum values of the complex fiber Hamiltonian (4.10), which are determined numerically. For an isolated PE chain, the optimal configuration is a straight line and the energy consists only of the mechanical and electrostatic self-energy contributions (see, e.g., Eq. (2.4)).

The results for ΔE, are shown in Figure 4.9 as a function of κ. Intuitively, one might expect that the binding energy decreases with increasing salt due to stronger screening of the electrostatic intercations. But as shown, the data indicate a non-monotonic behavior for ΔE: At small salt, the binding energy is positive and large indicating that fiber formation is not favored from an energetic point of view; recall that for vanishing salt, spheres are at minimum contact with the PE chain (Figure 4.4a), and strongly repel each other by long-range Coulomb interactions. At small finite salt concentrations (about $\kappa = 0.2\text{nm}^{-1}$), the binding energy vanishes and then becomes negative beyond this value.

The binding energy shows a rather flat minimum at intermediate salt regime (about $\kappa = 0.8\text{nm}^{-1}$), which indicates the highest energetic stability for the predicted zig-zag 30 nm complex fiber in the physiologically relevant salt regime. This is one of the main results for the unconstrained optimization model. Here, the model predicts $\Delta E \simeq -40$ (in units of $k_B T$), a large binding energy as compared with the thermal energy (see Ref. [50] and the Refs. therein). Recall that at intermediate salt the core particles are highly overcharged and there is a large repulsive interaction between them. But at the same time, electrostatic interactions become strongly screened, so that at high salt, core particles can be packed in a solenoidal fiber (Figure 4.5e and f). (In this regime, inter-particle correlations begin to play a role as negative charges on one core particle tend to face positive charges on the next core particle in some regions of the fiber that will be discussed later on.)
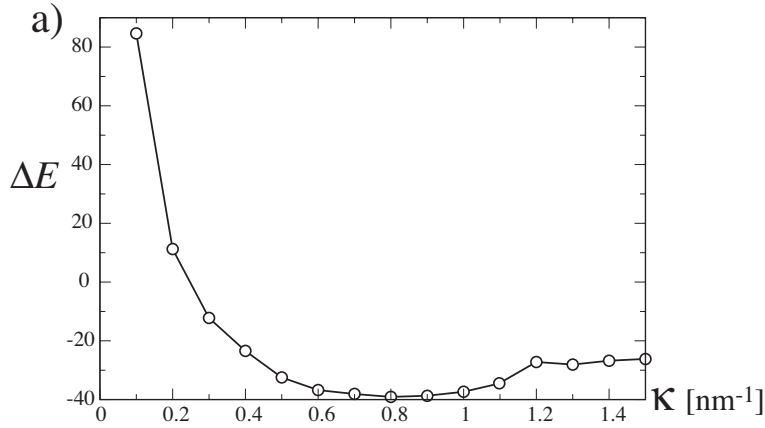
Figure 4.9: The binding energy of the fiber (defined as the difference between the optimal value of the Hamiltonian (4.10) per unit cell and the reference state of the system which is taken to be an infinite single isolated PE chain in the absence of spheres per unit cell, which in this case contains a straight PE chain of length L_c) is shown as a function of inverse screening length for fixed $Z = 15$ and $L_c = 68$ nm ($N_{\mathrm{bp}} = 200$).
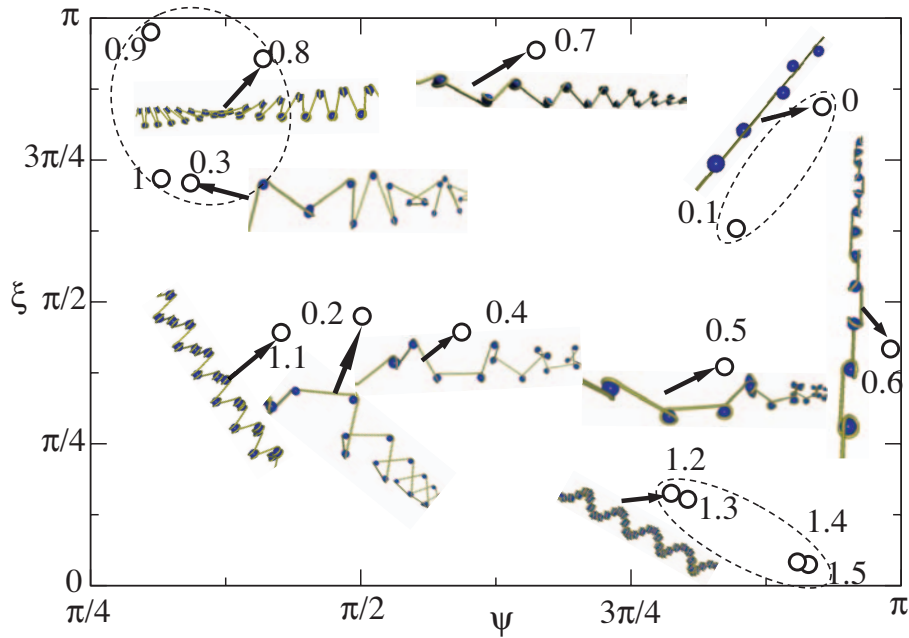
Figure 4.10: a) The two-angle phase diagram for various κ at fixed macroion charge valency $Z = 15$ and fixed chain length per unit cell $L_c = 68$ nm ($N_{\mathrm{bp}} = 200$). The values of κ associated with each point is indicated on the graph (in units of nm^{-1}). The zig-zag structures (upper left corner), beads-on-a-string structures (upper right region), and compact solenoids (lower right region) are specified by closed ellipses and for each case a characteristic structure is shown.

4.2.3   Two-angle phase diagram

As already mentioned in the section 4.1, the structure of the fiber can be described in terms of the entry-exit angle, ψ, and the dihedral angle, ξ [122]. By calculating these two angles for the fiber structure for various salt concentrations, one can sketch a two-parameter $\xi - \psi$ structural phase diagram. The result is shown in Figure 4.10 for fixed sphere charge $Z = 15$ and fixed chain length (per unit cell) of $N_{\mathrm{bp}} = 200$. Open circles give the two-angle coordinates associated with the numerically calculated optimal configuration at a given inverse screening length κ (indicated as numbers on the graph).

The phase diagram indicates that the angle ψ determines the compactness of the fiber, while ξ determines its structural class, e.g., being zig-zag or solenoidal. At small salt concentrations, these angles vary rapidly with the salt concentration, which, as mentioned above, is a consequence of the chain wrapping process. At high salt most of the free length of the chain available in a unit cell is already wrapped and thus the angles vary weakly. The parameter which varies more dramatically with κ is ψ. As seen, ψ-angle never becomes smaller than $\pi/4$, due to excluded-volume interactions [137], while ξ spans the whole $0 < \xi < \pi$ interval.

The beads-on-a-string patterns are found at the boundaries of the diagram with entry-exit angles roughly in the range $3\pi/4 < \psi < \pi$. While the compact solenoidal structures appear in the lower-left corner, that is with small dihedral angle $0 < \xi < \pi/4$ but large entry-exit angle $3\pi/4 < \psi < \pi$. One may thus distinguish a *compact solenoidal phase*, which is roughly indicated by a closed ellipse on the lower-right corner of the graph. The 30 nm zig-zag structures obtained at intermediate salt regime typically appear on the left part of the graph, that is for $\pi/4 < \psi < \pi/2$ and typically large $\xi > \pi/2$.

4.3   Effects of sphere charge on the fiber structure

As discussed in Chapter 2, the sphere charge within the present model is treated as an effective parameter, that is, it does not necessarily represent the bare charge of the macroion (or histone proteins in the case of chromatin). In realistic conditions, the macroion charge may be shifted from its bare value due to the non-linear effects such as charge renormalization and charge regulation. In fact, the optimal configurations obtained within the present model are most comparable with the *in vitro* chromatin structure [116, 122, 123, 125] when the sphere charge is about $Z = 15$ (as chosen in the preceding sections), and κ is chosen within the physiological range around $\kappa = 1.0$ nm^{-1}. In other words, Z may be used as a fitting parameter as will be discussed further below.

In order to bring out the structural changes induced by the sphere charge, I show in Figure 4.11a, the optimal fiber configurations for somewhat large value of the sphere charge $Z = 40$ and for several different salt concentrations. Chain length per unit cell is fixed as $N_{\mathrm{bp}} = 200$. The striking difference with the case of $Z = 15$ (Figures 4.4 and 4.5) is that at intermediate salt regime, the fiber shows compact solenoidal (e.g., for $\kappa = 0.6$ nm^{-1}) or compact beads-on-a-string (e.g., for $\kappa = 1.0$ nm^{-1}) patterns. While at lower ionic strength, the fiber typically displays loose solenoidal or swollen zig-zag patterns. The results for the fiber diameter (Figure 4.11c) and the projected sphere-sphere distance (Figure 4.11b) explicitly show that both quantities are about the sphere diameter $D_{\mathrm{F}} \simeq d_{\parallel} \simeq 10$ nm for large κ; while the zig-zag fiber for $\kappa = 0.4$ nm^{-1} shows a diameter of 30 nm. The global patterns obtained for $Z = 40$ are distinctly different from those obtained in experiments, which indicates a 30 nm diameter fiber with zig-zag form.
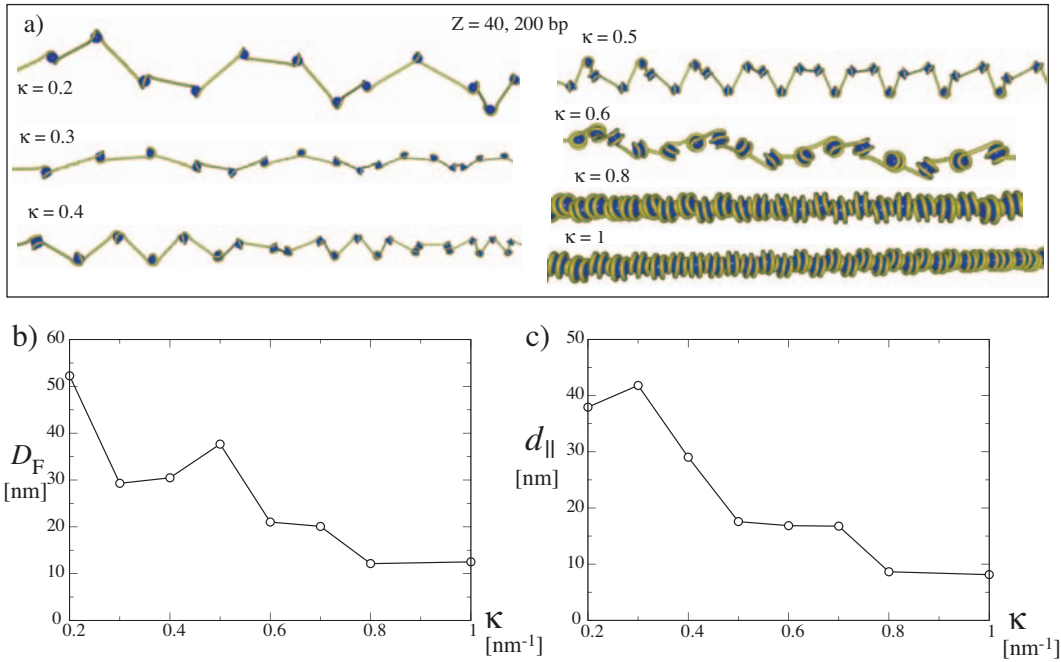
Figure 4.11: a) Optimal complex fiber structures for various inverse Debye screening length κ as indicated on the graph (for fixed $Z = 40$ and $N_{\mathrm{bp}} = 200$). The resultant structures are loose solenoidal and beads-on-a-string for $\kappa = 0.2$ and 0.3 nm^{-1} respectively, swollen zig-zag for $\kappa = 0.4$ and 0.5 nm^{-1}, compact solenoid for $\kappa = 0.6$ nm^{-1}, and compact beads-on-a-string for $\kappa = 0.8$ to 1 nm^{-1}. b) shows the diameter of the fiber D_{F} as a function of κ for the same parameters as in (a). c) demonstrates the projected distance $d_{\parallel}$ as a function of κ for the same parameters, i.e. $Z = 40$ and $N_{\mathrm{bp}} = 200$. It indicates that the zig-zag structure obtained at $\kappa = 0.4$ and 0.5 nm^{-1} is quite loose, with $d_{\parallel} \simeq 20$ nm. Maximum projected distance is obtained for the swollen beads-on-a-string structure at $\kappa = 0.3$ nm^{-1}, where $d_{\parallel} \simeq 40$ nm.

These differences are directly caused by difference of the local structure of the core particles between the two cases with $Z = 15$ and $Z = 40$. As shown in Chapter 3, by increasing the macroion charge at fixed salt concentration, the PE adsorption on the sphere becomes more enhanced resulting thus in a different structure for the entering and exiting strands of the PE chain in a core particle. For comparison note that for $Z = 40$, the PE chain already wraps at least a complete turn around the sphere for $\kappa > 0.1$ nm^{-1}, while for smaller sphere charge $Z = 15$, a complete turn occurs only beyond $\kappa = 0.5$ nm^{-1} (see Figure 4.8).

Now I set the salt concentration equal to the typical physiological concentration with $\kappa = 1$ nm^{-1} and the chain length as $N_{\mathrm{bp}} = 200$ and vary the sphere charge Z (Figure 4.12a). The global structure of the fiber drastically varies with small changes in the sphere charge and, as seen from the data in Figures 4.12b and 4.12c, it evolves from a 30 nm diameter zig-zag pattern to a thick solenoidal (with diameter of $D_{\mathrm{F}} = 55$ nm), and then to a compact 10 nm diameter beads-on-a-string structure.

These results indicate that in order to obtain structures most compatible with the experimentally observed zig-zag chromatin pattern at intermediate salt concentrations [116, 122, 123, 125], one must set the sphere charge at about $Z = 15$ within the present unconstrained-
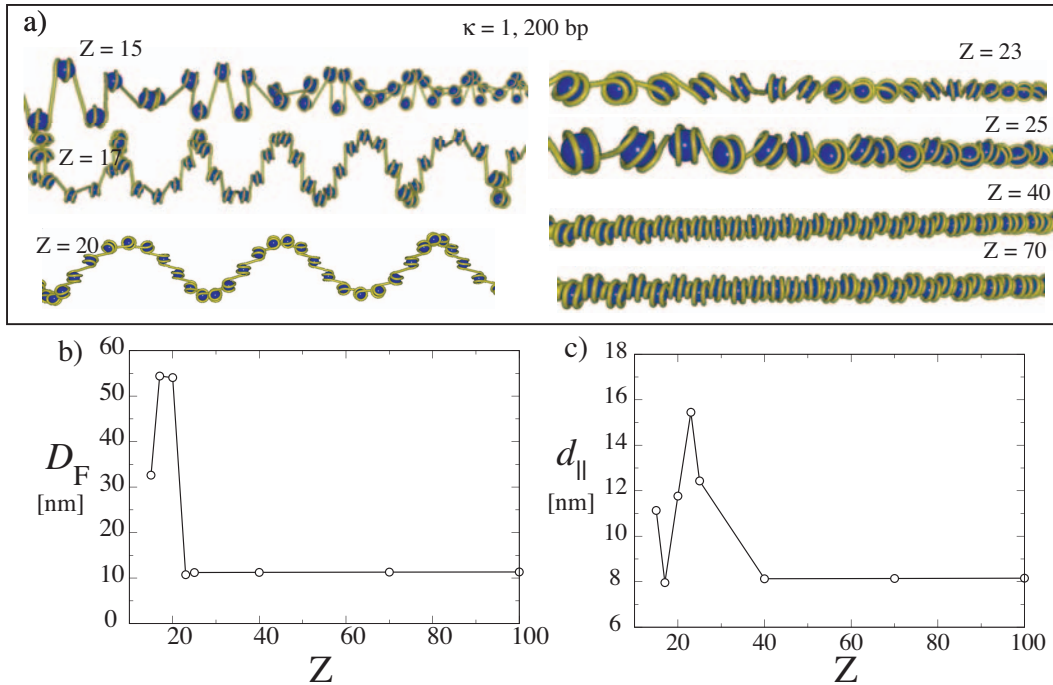
Figure 4.12: a) Optimal complex fiber structures obtained for various sphere charge valency at fixed $\kappa = 1\text{nm}^{-1}$ and fixed length per unit cell ($N_{\text{bp}} = 200$). The obtained structures show zig-zag pattern for $Z = 15$, thick solenoid for $Z = 17$ and 20, and a beads-on-a-string structure for $Z = 23$ and above. b) shows the diameter of the fiber D_{F} as a function of Z for the same parameters as in (a). For $Z > 23$ it falls into the 10 nm beads-on-a-string fiber. For $Z < 23$, large diameter indicates thick solenoidal structure. c) shows the projected distance $d_{||}$ as a function of Z, which drops to a small value of $d_{||} = 10$ for $Z > 40$. The rage of variation of $d_{||}$ is relatively small, i.e. between 10 and 16 nm.

optimization model. For larger Z, one obtains compact beads-on-a-string structure, while for smaller Z, the PE chain actually does not complete 1-and-3/4 turns around the sphere as expected for the nucleosome core particles within the chromatin.

In Figure 4.13, I show the two-angle phase diagram for $Z = 40$ and various κ (a) and for fixed $\kappa = 1$ nm^{-1} and various Z (b). In the former case (a), both the entry-exit angle and the dihedral angle typically span intermediate values at small salt concentration and at high concentrations, ξ tends to π as the spheres tend to align.

4.4   Effects of chain length on the fiber structure

So far I have considered the effects of salt concentration and sphere charge on the structure of the complex fiber at a fixed length of the chain per unit cell. In this section, I will address the effects due to changes in the length of the PE chain per unit cell of the fiber for a fixed sphere charge, $Z = 15$, and at fixed salt concentration. As before, I represent the chain length per unit cell, L_c, in terms of equivalent number of DNA base pairs, N_{bp}, each of length 0.34 nm.
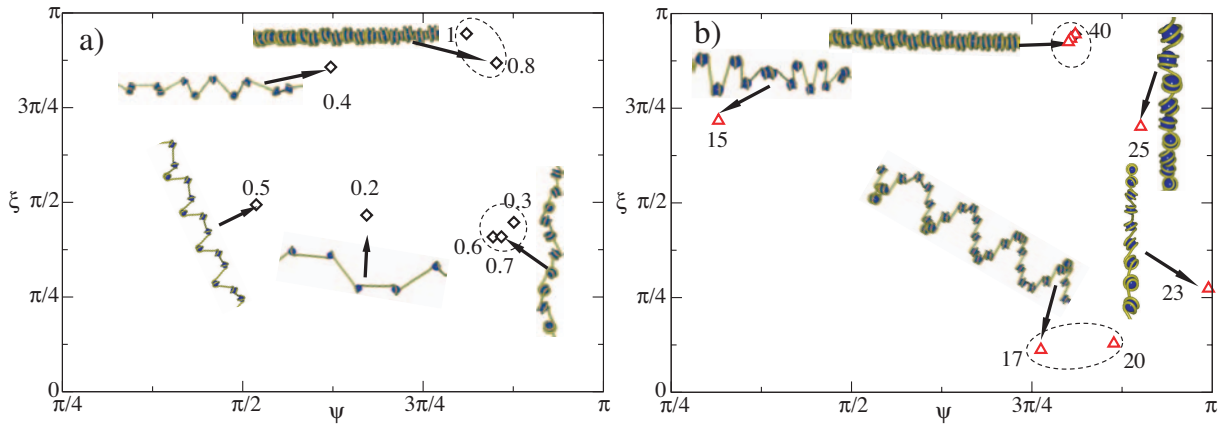
Figure 4.13: The ξ-ψ structural phase diagram for the study of the effects of sphere charge at fixed $N_{\rm bp} = 200$. a) shows the phase diagram for $Z = 40$, and various inverse Debye screening lengths κ. The corresponding values of κ are explicitly indicated on the graph (in units of $\rm nm^{-1}$). The compact beads-on-a-string (top right) and the solenoidal (middle right) regions are specified by closed loops and in each a characteristic structure is shown. The structures of other three isolated points are also given. b) The phase diagram for varying Z at fixed $\kappa = 1\rm nm^{-1}$. The corresponding values of Z are indicated on the graph. Thick, loose solenoidal region (bottom right) as well as compact beads-on-a-string region (top right) are shown by closed loops.

4.4.1 Overall behavior for various chain lengths

I change $N_{\rm bp}$ in the range of 50 to 240 base pairs and, for the moment, fix the inverse Debye screening length as $\kappa = 0.8$ nm^{-1} and the sphere charge valency as $Z = 15$. At this salt concentration, the fiber was shown to be most stable from an energetic point of view (Figure 4.9) and exhibits a 30 nm zig-zag fiber (Figure 4.5).

The numerically calculated optimal fiber structures for various $N_{\rm bp}$ are shown in Figure 4.14. For relatively large chain length per unit cell, the overall structure changes weakly with the length and exhibits, for the parameters chosen here, the zig-zag pattern. This is because the structure of the core particle (i.e. the conformation of the chain wrapped around each sphere) is nearly independent of the chain length in this regime. Note that for $N_{\rm bp} > 200$, almost 120 base pairs of the PE chain are adsorbed on each sphere, and the rest serves as the linker chain. As the chain length decreases down to the length adsorbed on the sphere, i.e. $N_{\rm bp} = 120$, the diameter of the zig-zag fiber reduces to that of the macroion sphere displaying a compact 10 nm fiber with a beads-on-a-string structure.

For smaller chain lengths, there is practically no linker chain present and the core particles will thus be located very close to each other. As seen in the figure, the fiber structure evolves to a compact solenoidal pattern with decreasing chain length, quite similar to the behavior obtained for large κ in the preceding sections. Meanwhile, the number of chain turns around the sphere decreases such that, for instance, for a total chain length of $N_{\rm bp} = 50$ base pairs per unit cell, only half a turn of the chain is on the sphere as shown in the figure.

The general behavior of the fiber configuration as a function of PE-chain length per unit cell remains qualitatively the same at different salt concentrations. I show a selected set of numerically determined optimal configurations in Figure 4.15 for the inverse Debye screening
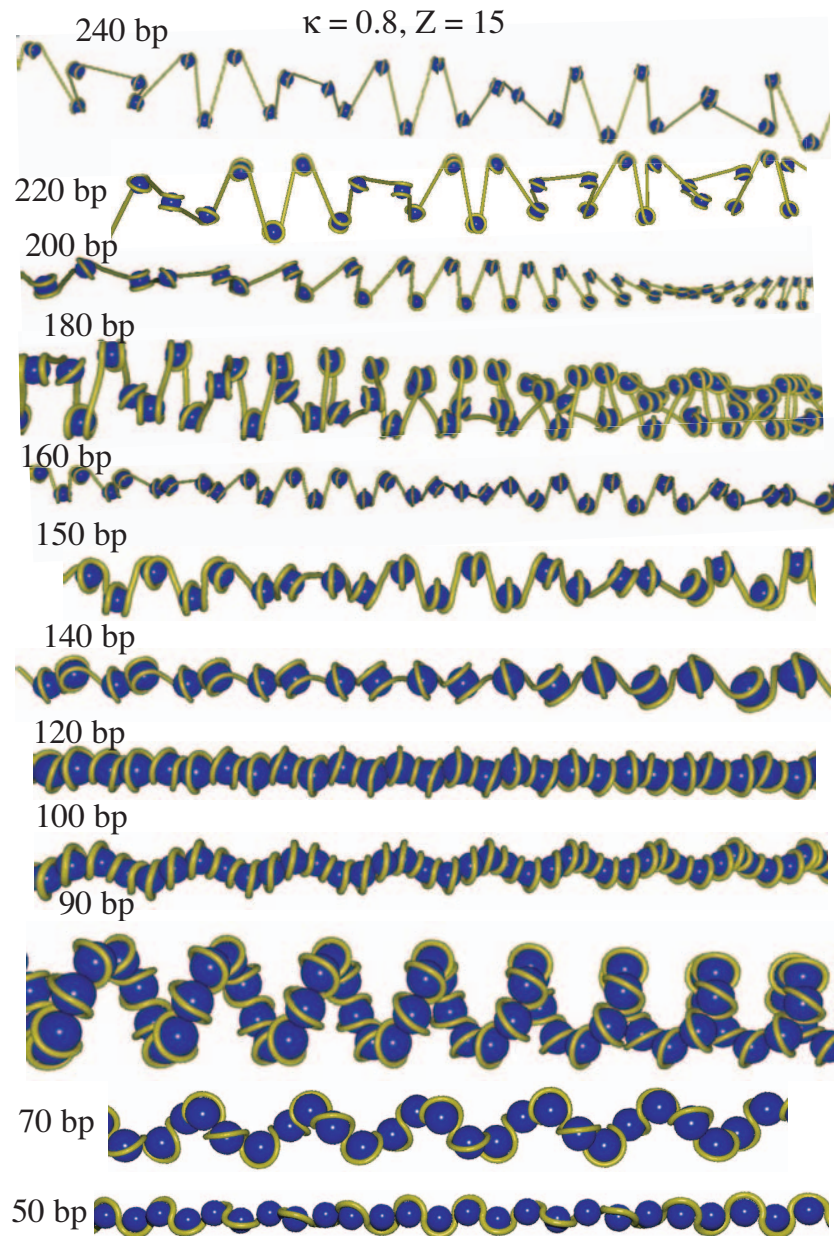
Figure 4.14: Optimal fiber configurations obtained from the full minimization of the Hamiltonian (4.10) for fixed inverse screening length $\kappa = 0.8$ nm^{-1}, fixed sphere charge valency $Z = 15$, and increasing total chain length per unit cell as indicated in the graph for each structure, in the units of DNA base pairs (bp). The resultant structures are zig-zag structure for $N_{\mathrm{bp}} = 240$ down to 150, compact beads-on-a-string for $N_{\mathrm{bp}} = 140$, 120 and 50, and compact solenoids for $N_{\mathrm{bp}} = 100$, 90 and 70.

length $\kappa = 0.4$, 1 and 2 nm^{-1}. As discussed in Chapter 3, the total length of wrapped chain around the sphere is predominantly determined by the sphere charge, Z, and κ. For a complex fiber with $Z = 15$, it amounts to 63, 136 and 185 base pairs for $\kappa = 0.4, 1$ and 2 nm^{-1} respectively, when a sufficiently large amount of base pairs are available. The chosen range

Figure 4.15: Same as Figure 4.14 but for a) $\kappa = 0.4$ nm^{-1}, b) $\kappa = 1.0$ nm^{-1} and c) $\kappa = 2.0$ nm^{-1}. The tot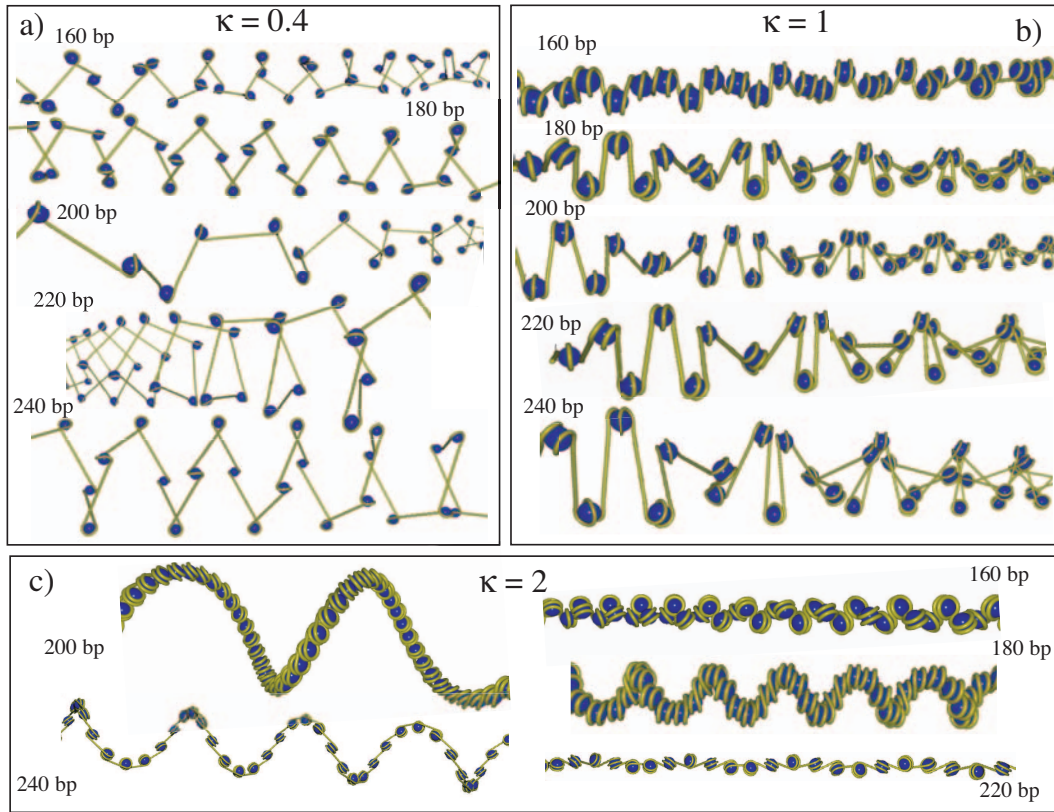al chain length per unit cell is indicated in the graph. Shown structures are loose solenoids in (a), zig-zag structures in (b), compact zig-zag for $N_{bp} = 160$ in (c), compact beads-on-a-string $N_{bp} = 220$ in (c), and compact solenoid for $N_{bp} = 180, 200$ and 240 in (c).

of total chain length per cell are reasonably larger than the wrapped length for $\kappa = 0.4$ and $\kappa = 1$ and thus one observes the loose solenoidal and the zig-zag patterns respectively (Figure 4.15a and b). For $\kappa = 2$nm^{-1}, however, some of the adsorbed base pairs have to dewrap for small chain lengths $N_{bp} < 185$. The zig-zag structure is no longer stable for this value of κ, and as shown also before (Section 4.2), compact solenoidal structures are obtained (Figure 4.15c). This is due to the fact that within the core particles, the PE chain wraps almost two complete turns around the sphere, and therefore, the entry-exit angle, ψ, is almost equal to π.

4.4.2 Summary of results for different chain lengths

Geometry

In Figure 4.16a and b, I show the results obtained for the fiber diameter, D_F, and the projected center-to-center distance between two consecutive spheres, $d_{||}$, as a function of the chain length per unit cell, N_{bp} (in units of DNA base pairs) for several different salt concentrations. As seen the fiber typically shows a small diameter of the order $D_F = 10$ to 20 nm for short chain length ($N_{bp} < 150$) and at intermediate salt concentrations. In this regime, the projected
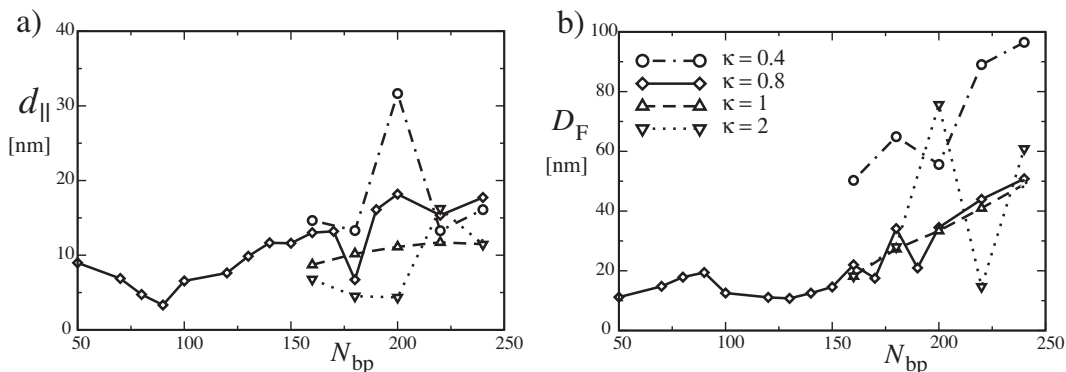
Figure 4.16:   a) The projected distance of neighboring histone centers along fiber axis, $d_{||}$, and b) the fiber diameter D_F as a function of chain length per unit cell, N_{bp}, for various salt concentrations: $\kappa = 0.4$ (circles), 0.8 (diamond), 1.0 (triangle-ups) and 2.0 nm^{-1} (triangle-downs). Both functions show an overall decreasing behavior with decreasing N_{bp}, although there are anomalous behaviors, e.g., for $\kappa = 0.4$ nm^{-1} (in $N_{bp} = 200$) and $\kappa = 0.8$ nm^{-1} (in $N_{bp} = 180$).
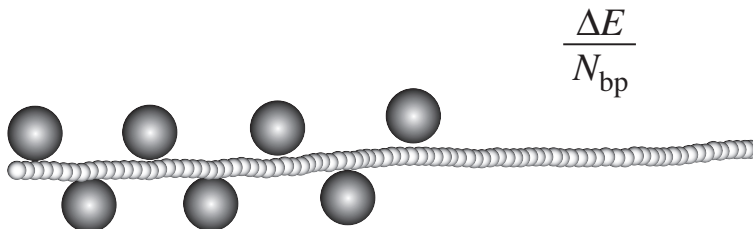
Figure 4.17:   Schematic view of the ensemble with fixed number of macroions adsorbed on a fixed length of PE chain. The relevant control parameter here is the linear density of adsorbed macroions on the PE chain $(1/N_{bp})$, and the energy function to be minimized (on the ground-state level) is the binding energy per unit length of the PE chain, $\Delta E/N_{bp}$.

distance, $d_{||}$, varies in the range $d_{||} = 5$ to 10 nm reflecting tightly packed spheres within the fiber.

Energetic behavior

So far, I have discussed the configurational changes associated with the length of PE segment per unit cell. But assume that we have a solution of long polyelectrolytes in equilibrium with a solution of spherical macroions. The question is: What would be the linear number density of macroions attached to the (infinitely) long polyelectrolyte chain, and what would be the structure of the resultant fiber? Clearly, a complete answer to this question requires a full thermodynamic study by considering the full free energy in an appropriate ensemble. But within the ground-state-dominance approximation, one can address this questions *on the energetic level*, i.e. strictly neglecting the entropic effects and approximating the free energy with the energy.

   In order to investigate the stability of the system, one should calculate the energy density. In an ensemble consisting of fixed number of macroions adsorbed on a fixed, large length of

Figure 4.18: a) Binding energy of the complex fiber per PE chain unit length as a function of the concentration of adsorbed macroions on the chain $1/N_{bp}$ for different values of κ indi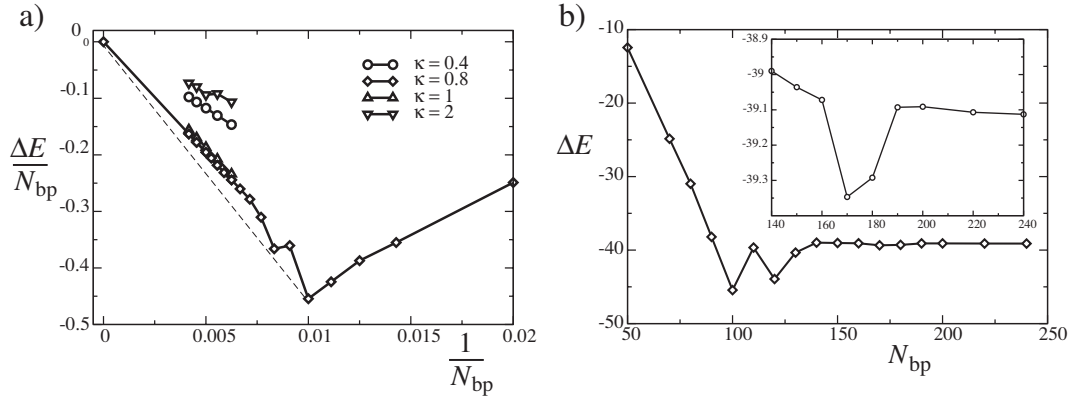cated in the graph. b) Binding energy of the fiber per unit cell as a function of N_{bp} for $\kappa = 0.8 \text{nm}^{-1}$ and $Z = 15$. The inset shows details of the same graph for the range of $140 \leq N_{bp} \leq 240$. Note that ΔE represents the optimal value of the Hamiltonian (4.10) per unit cell measured with respect to the reference state of the system which is taken to be the energy of a single isolated PE chain per unit cell, which contains a straight chain of length N_{bp}.

PE chain, I will consider the PE as the container and minimize the energy per unit length of PE chain. The relevant control parameter is the linear number density of attached spheres to the long PE chain, i.e. $1/N_{bp}$ (see the illustration in Figure 4.17). This ensemble refers to a system where the macroions are depleted from the solution and, e.g. the concentration of adsorbed macroions is larger than the concentration of macoions in the solution.

For this I consider the fiber binding energy per length, $\Delta E/N_{bp} = E_F/N_{bp} - E_0/N_{bp}$, where the first term is the energy of a complex fiber per unit length of the PE chain, and the second term is the energy of a free PE chain per unit length. Recall that ΔE is defined as the binding energy of a complex fiber per unit cell, which is the difference between the energy of a complex fiber per unit cell, E_F, and that of an infinite free PE chain per unit cell (which in this case contains a straight PE chain of length N_{bp}), E_0. $\Delta E/N_{bp}$ is shown in Figure 4.18a for $\kappa = 0.8 \text{ nm}^{-1}$ and $Z = 15$ as a function of adsorbed macroion density, $1/N_{bp}$, and ΔE is shown in Figure 4.18b for the same parameters as a function of N_{bp} (in this former graph, I also show the results for $\kappa = 0.4$, 1 and 2 nm^{-1} at large N_{bp}). Recall that the former case is suitable for a fiber with fixed number of adsorbed macoions on the PE chain.

As seen for $\kappa = 0.8 \text{ nm}^{-1}$, $\Delta E/N_{bp}$ appears to have two minima at intermediate values of macroion density, i.e. one at about $1/N_{bp} = 0.01$ ($N_{bp} = 100$), where the fiber exhibits a compact solenoidal structure, and the other minimum at about $1/N_{bp} = 0.008$ ($N_{bp} = 120$), where a compact beads-on-a-string structure is obtained as discussed before. Also $\Delta E/N_{bp}$ shows an overall convex behavior between $1/N_{bp} = 0.01$ and the limit of infinite dilute (no macroion adsorbed) PE chain $1/N_{bp} = 0$. In order to examine stable structures in the thermodynamic sense, one should consider a systematic common-tangent construction. Although the present results represent only energetic of the fiber formation process, a naive common-tangent construction (broken line in Figures 4.18a) suggests a phase separation between two phases of complex fibers: one phase rich in compact fibers with small chain length per unit cell ($1/N_{bp} > 0.01$) and the other phase rich in un-complexed PE, i.e. with $N_{bp} \to \infty$ (note

that for infinite chain length per unit cell, the optimal structure is fully expanded due to large self-repulsion of chain segments as discussed in Chapter 3). In between, the energy has a non-monotonic behavior with values higher than the the common-tangent line, which indicates a region with meta-stable structures within an ensemble of various optimal fiber structures. This indicates a "gas-liquid"type phase "coexistence"along the fiber, i.e. a part of the PE chain forms a dense complex fiber with macroions with linear number density of macroions $1/N_{\mathrm{bp}} \sim 0.01$ (the "liquid"phase) in "coexistence"with the rest it consisting of the un-complexed PE chain (the infinite dilute "gas"phase). One expects that adding the entropy of macroions would lead to a more dilute fiber ("liquid-phase"). A complete study of this phase separation type phenomenon will be considered in the future. Another interesting problem that one can study is the complex fiber in equilibrium with a solution of macroions, where one has to take into account the chemical potential of macorions, since the number of adsorbed macroions is no longer fixed. This may leads to a completely different phase diagram, where may be able to indicate the binding-unbinding phase transitions.

The binding energy per unit length of chain is also shown in Figure 4.18b for other values of salt concentration. Note that the data corresponding to $\kappa = 0.8\mathrm{nm}^{-1}$ lies below the other data, i.e. for this range of N_{bp}, the energy of optimal fiber is minimum for $\kappa = 0.8\mathrm{nm}^{-1}$.

In Figure 4.18b the binding energy per unit cell ΔE as a function of length of PE-chain is shown. Here also there appear two minima at intermediate values of chain length, i.e. one at about $N_{\mathrm{bp}} = 100$, with a compact solenoidal fiber, and the other minimum at about $N_{\mathrm{bp}} = 120$, where a compact beads-on-a-string structure is obtained as discussed before. The behavior of ΔE, however, needs a closer attention since it shows a shallow local minimum at $N_{\mathrm{bp}} \sim 170$ (see the inset). As discussed in the previous section, the optimal structure corresponding to this local minimum (e.g. for $N_{\mathrm{bp}} = 170$) exhibits a zig-zag pattern. Therefore, if a stabilizer transforms this shallow local minimum to a deeper minimum or a global minimum, this can affect the stable phase in the large chain-length regime favoring thus zig-zag fibers. The first suggestion for a stabilizer in the case of chromatin would be a linker histone, which will be considered in the future works.

4.4.3   Two-angle diagram for various lengths

In Figure 4.19, I have sketched a two-angle diagram summarizing structural changes of the fiber with chain length per unit cell in terms of the entry-exit angle, ψ, and the dihedral angle, ξ. Here $\kappa = 0.8$ nm^{-1} and $Z = 15$ are fixed.

Recall that in the case with varying salt concentration (Figure 4.10), the ψ-angle spans the range $\pi/4 < \psi < \pi$, while the dihedral angle covers the whole range of $0 < \xi < \pi$. But as seen in Figure 4.19, the optimal configurations are mostly gathered in the boundaries of the graph. The resultant zig-zag patterns for large chain lengths are concentrated on the upper-left corner of the graph, that is with large dihedral angles (typically $\xi > \pi/2$) and small to intermediate entry-exit angles ($\pi/4 < \psi < 5\pi/8$). While the beads-on-a-string structure are located in the upper-right corner displaying large entry-exit angles ($\psi > 3\pi/4$) and large dihedral angles ($\xi > 3\pi/4$). Note that the beads-on-a-string patterns are obtained both with very small chain length per unit cell (e.g., $N_{\mathrm{bp}} = 50$), where the chain is only partially wrapped around the sphere, and also with intermediate chain lengths $100 < N_{\mathrm{bp}} < 150$ (see also Figure 4.14). There is a narrow range of chain lengths $50 < N_{\mathrm{bp}} < 100$, where fiber adopts a compact solenoidal form, with $0 < \xi < \pi/2$ and ψ being distributed around $3\pi/4$.

Note that the transition between zig-zag and beads-on-a-string structures involves an
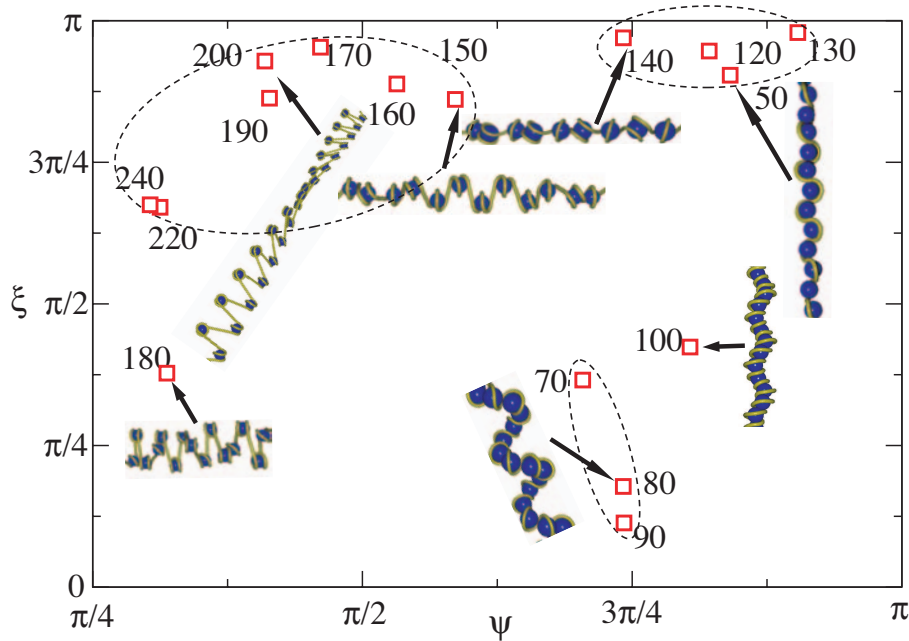
Figure 4.19: Entry-exit and dihedral angles diagram for various chain length per macroion. The corresponding values of N_{bp} is indicated on the graph. The zig-zag region (top left), beads-on-a-string region (top right) and compact solenoidal region (bottom right) are shown by closed loops.

increasing entry-exit angle ψ which maximizes the distance between adjacent spheres (minimizing their repulsion), while ξ changes only weakly. In contrast, the transition between beads-on-a-string and compact solenoidal structures involves large variations in ξ and small variations in ψ.

Another point to be noted is that the case with chain length $N_{bp} = 180$ that exhibits a zig-zag pattern is isolated from the zig-zag-dominated area in the graph. This anomalous behavior reflects the local minimum in the binding energy of the fiber as discussed above.

4.5 Constrained optimization model: a step toward chromatin

When applied to chromatin, the present chain-sphere cell model should be considered with caution. There are several components in actual chromatin structure with specific nature which are not captured within the present approach as discussed in detail in Chapter 1. One of the relevant factors that affects the chromatin structure is the so-called *linker histone* H1, a cationic protein which is believed to act near the entry-exit region of the DNA at the nucleosome. It brings together the two strands of the DNA that enter and exit the central core particle [116, 123] (see also Chapter 1). In *in vitro* experiments, H1 histone can be removed by exposing the system to high salt concentrations (about 0.6 M), and washing the solution in order to remove dissociated linker histone. In such H1-depleted cases, the chromatin fiber appears to be rather open and loose (i.e. with low number of histones per unit length along the fiber) [116]. While in the presence of H1, the fiber is relatively dense and moreover, the nucleosome structure is stabilized, that is no unwrapping or sliding of the DNA on the histone
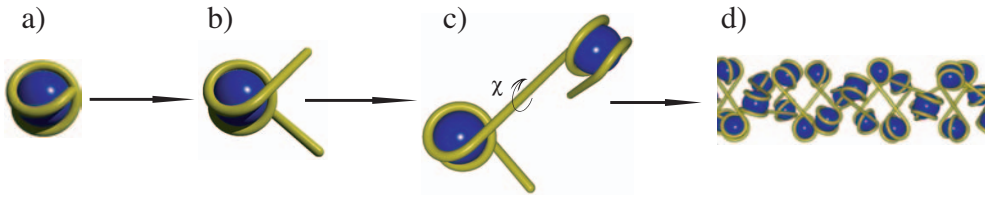
Figure 4.20: In constrained optimization model, the conformation of the chain in each unit cell is fixed and only the rotational angle χ can vary. The core particle complex (a) consists of a chain segment of length equivalent to 146 DNA base pairs, whose configuration is obtained from numerical minimization in the case of single isolated complex. The core particles are linked together with straight linker chain (b) of various length. The replication procedure (c and d) is the same as explained in Section 4.1.

octamer is possible [123]. As a result, the number of base pairs complexed with the histone octamer is fixed.

The full minimization scheme described in the preceding sections may thus serve as a naive model for chromatin without the linker histone effects as there is no constraint as to fix the amount of chain adsorbed on the sphere (which is determined by the minimization procedure and varies depending on system parameters). However, to construct a model closer to the chromatin fiber with linker histone, I also consider a variant of the preceding model, in which a *constrained* minimization scheme is employed.

For this purpose, I fix the structure of the chain complexed with the sphere within each unit cell according to the optimal (ground-state) configuration of the chain in an isolated complex, which is obtained separately from a minimization method as explained in previous chapters. For this I use a chain length equivalent to 146 base pairs of DNA (corresponding to the chain length in stabilized nucleosome core particle), and then connect the entering and exiting strands with straight linker chains of arbitrary length. This makes a single unit cell for the fiber which can be constructed by replicating this unit cell using the transformation method explained in Section 4.1.2–see Figure 4.20. In this case, there is only a single degree of freedom, that is χ, which can be varied in order to find the minimum of the effective Hamiltonian of the fiber as discussed before (see Sections 4.1.4 and 4.1.5).

It is however important to note that this *constrained model* for the fiber does not explicitly include the linker histones effects as, for instance, the PE chain strands are far apart at the entry and exit regions. Yet as it will be demonstrated below, this revised model indeed gives dense fibers that resemble the 30 nm chromatin fiber more closely both in the overall pattern and density of core particles along the fiber.

4.5.1 Optimal configurations for various sphere charge

In Figure 4.21, I show several structures obtained from constrained minimization for the inverse screening length $\kappa = 1$ nm^{-1} and for small to large sphere charge Z. The PE chain length per unit cell here is fixed at $N_{\mathrm{bp}} = 200$. Clearly, the compactness of the fiber is less sensitive to changes in the sphere charge, in main part due to the fact that the conformation of individual core particle complexes are fixed. As a result, the entry-exit angle of the PE strand changes weakly as compared with the unconstrained minimization case. Yet as seen, the fiber becomes denser for large sphere charge: for $Z = 15$ the number of sphere per 10 nm
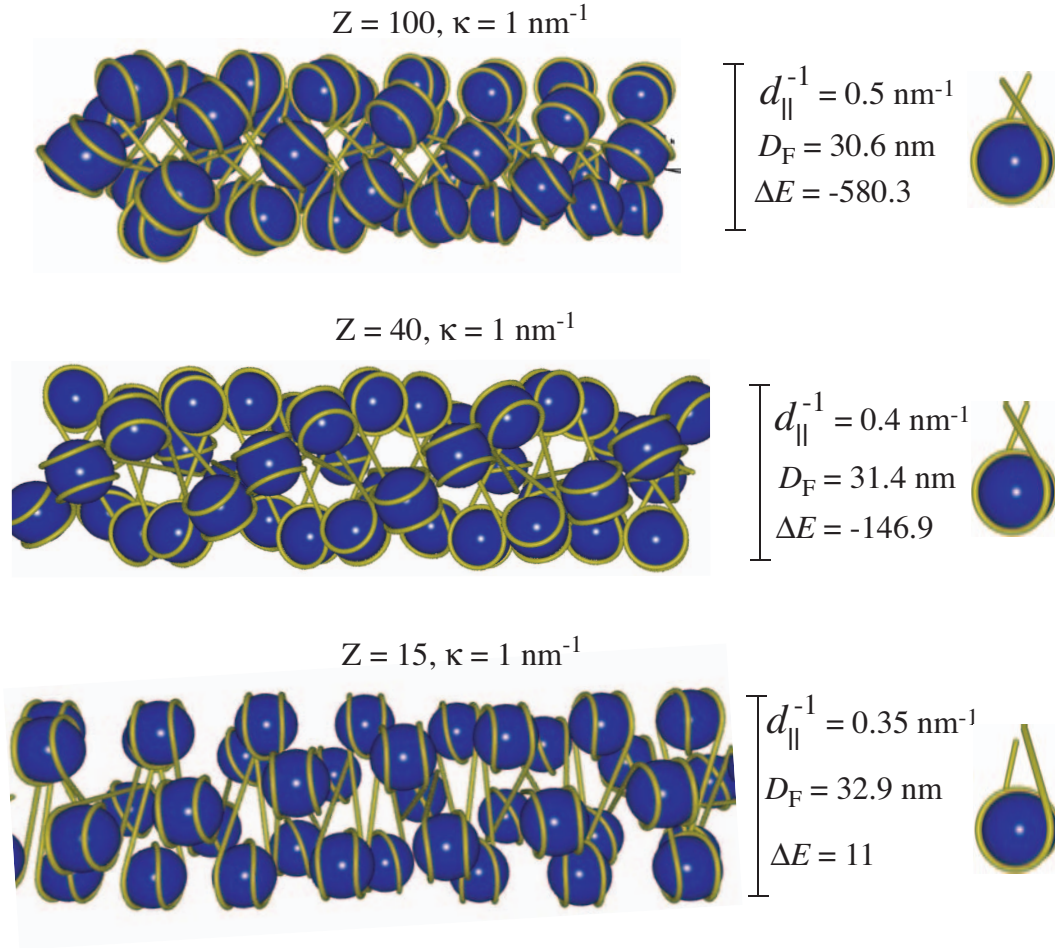
Figure 4.21: Optimal fiber configurations obtained from the constrained optimization model for various sphere charge Z as indicated on the graph but for fixed inverse screening length $\kappa = 1$ nm^{-1} and the PE chain length per unit cell $N_{bp} = 200$. The sphere density (number of macroions per unit length along the fiber axis), $d_{\parallel}^{-1}$, the binding energy, ΔE, and the fiber diameter D_F are given in the graph for each fiber. The corresponding local structure of the fiber unit cell is shown on the right.

length along the fiber axis is about three (sphere density is $d_{\parallel}^{-1} = 0.35$ nm^{-1}) and for $Z = 100$, there are five spheres per 10 nm (sphere density $d_{\parallel}^{-1} = 0.5$ nm^{-1}).

In order to understand the underlying mechanism behind the compaction of the fiber with the sphere charge, I consider the binding energy of the fiber, ΔE, i.e. the energy of the optimal configuration measured with respect to the reference state of a free straight PE chain. While for $Z = 15$, the binding energy is positive, it becomes highly negative for larger Z as indicated on the graph, i.e. $\Delta E = -580.3$. This in fact reflects effective attraction between core particle complexes within the fiber, which results from correlations between positive and negative patches on each core complex as may be seen already in the spatial configurations.

Note also that the diameter of the fiber is quite stable and is about 30 nm, that is about the diameter of the H1-intact 30 nm chromatin fiber in the physiological salt regime (i.e. $\kappa \sim 1$ nm^{-1}). In fact, the striking point here is that within this simple model the

$Z = 100$, $\kappa = 0.2$ nm^{-1}

$d_{\parallel}^{-1} = 0.105$ nm^{-1}

$D_{\mathrm{F}} = 40.6$ nm

$Z = 100$, $\kappa = 0.5$ nm^{-1}

$d_{\parallel}^{-1} = 0.16$ nm^{-1}

$D_{\mathrm{F}} = 38.3$ nm

$Z = 100$, $\kappa = 1$ nm^{-1}

$d_{\parallel}^{-1} = 0.5$ nm^{-1}

$D_{\mathrm{F}} = 30.6$ nm

- -

$Z = 40$, $\kappa = 0.5$ nm^{-1}

$d_{\parallel}^{-1} = 0.2$ nm^{-1}

$D_{\mathrm{F}} = 32.3$ nm

$Z = 40$, $\kappa = 1$ nm^{-1}

$d_{\parallel}^{-1} = 0.4$ nm^{-1}

$D_{\mathrm{F}} = 31.4$ nm
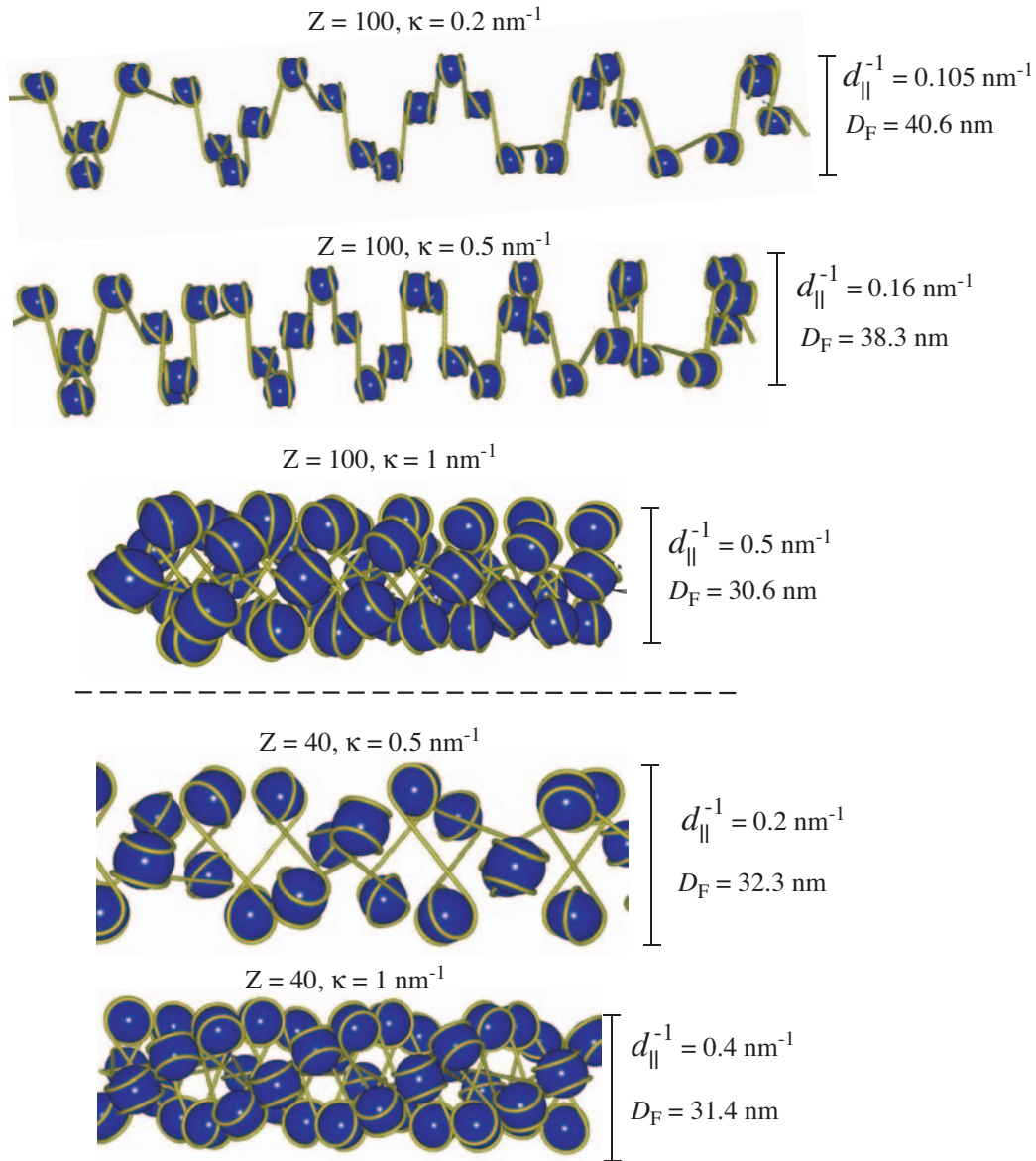
Figure 4.22: Same as Figure 4.21 but for fixed sphere charge $Z = 100$ and 40 and various salt concentrations as indicated on the graph.

entering and exiting strands of the PE chain form a cross pattern as explicitly shown by focusing on a single unit cell in Figure 4.21 (on the right). This situation (that resembles the experimentally stem-like pattern for the DNA in a nucleosome) is only obtained within the constrained minimization and leads to a small entry-exit angle[2], and thus a rather compact fiber. The fiber density at large Z is actually very close to the experimental chromatin value, i.e. about 5-6 histones per 11 nm.

---

[2]The entry-exit angle is a result of the PE-chain structure on the macroion core, which is by itself a function of Z and κ.

4.5.2   Optimal configurations for various salt concentration

In Figure 4.22, I show configurations with fixed Z and changing the salt concentration. As seen for $Z = 100$, the structure of the fiber becomes expanded for small κ, which is direct consequence of electrostatic repulsions between spheres, which become stronger at smaller salt concentration. The density of the fiber reduces to about one sphere per 10 nm and the fiber diameter increases to about 40 nm for smaller κ as indicated on the graph.

As explained before, the sphere charge should be taken as an effective (or fitting) parameter within the present model, because the true sphere charge may be regulated in experiments depending on the pH, or it may shift from the bare value due to charge renormalization effects in a salt solution. In fact, within the present model, the most relevant fiber configurations (that resemble the chromatin fiber best) are obtained by changing Z according to the salt concentrations. This may be thought of as a fitting procedure since the effective sphere charge is expected to depend on κ. To make this point clear, note that the fiber configurations for $Z = 100$ and low κ do not show zig-zag patterns as expected from chromatin experiments [116, 117, 123, 122, 125]. But zig-zag patterns at small κ may be recovered by taking a smaller value for sphere charge Z.

In Figure 4.22, I also show the optimal fiber structures for $Z = 40$ and two different values for κ. For instance, at $\kappa = 0.5$ nm^{-1}, the fiber shows a zig-zag form at this value of the sphere charge unlike the case with $Z = 100$.

4.6   Conclusion and discussion

In this chapter, I present a systematic numerical approach for investigating the structural properties and energetic stability of complex fibers, that are formed by complexation of a long polyelectrolyte chain with many oppositely charged spheres. The complex fiber is described using a chain-sphere cell model, in which the detailed structure of the PE chain (locally wrapped around individual spheres) as well as interactions between various components are taken into account. These interactions include screened electrostatic interactions (using linear Debye-Hückel potential) of charged units, the bending elasticity of the PE chain as well as the excluded-volume interactions between the PE chain and spheres. Here I choose parameters consistent with the DNA-histone system (e.g., using DNA charge and persistence length and a sphere diameter of 5 nm) as discussed in Chapter 2, but vary salt concentration, the sphere charge, and chain length per sphere as control parameters.

I focus on the optimal structure of the fiber, i.e. the structure which minimizes the effective Hamiltonian of the system. This amounts to a ground-state analysis, which, as explained in previous chapters, is expected to be valid for strongly coupled complexes. Two different schemes are used for the optimization (minimization) procedure: i) unconstrained (or full) optimization, and ii) constrained (or rotational) optimization. In the former case, I treat position of all chain beads within the fiber as degrees of freedom in addition to an independent degree of freedom that defines rotation of two adjacent unit cells (core particles) with respect to each other. This case therefore represents a many variable analysis. In the latter case, the conformation of the PE chain on each macroion sphere is fixed to that of an isolated PE-macroion complex. Two such complexes are then linked one by one to form a fiber with the help of straight linker chains and the only degree of freedom in this case is the relative rotation of unit cells (core particles) around the linker chain. In both cases, a variety of optimal structures are obtained for the fiber including, in particular, the zig-zag patterns.

There are however qualitative differences between the two models as explained below.

In unconstrained minimization, the PE conformation is free to change on the sphere, i.e. upon changing the salt concentration or the macroion charge, the PE chain in each core complex may become increasingly more wrapped or dewrapped. As a result, the entry-exit form of the PE strand varies accordingly leading to dramatic changes in the overall fiber structure. As shown, the optimal fiber structure shows beads-on-a-string pattern at low salt: At vanishing salt, the spheres touch the highly expanded PE strand over a short section, which increases with salt leading to thick loose (or open) solenoidal patterns. At about the inverse screening length $\kappa = 0.6$ nm^{-1}, the chain is already wrapped around the sphere for almost a complete turn. In this case, the spheres are aligned and form a fiber of diameter about 10 nm, which resembles the swollen 10 nm chromatin fiber. For salt concentrations within the physiological regime, zig-zag patterns are found as optimal structures and the fiber diameter is about 30 nm; this diameter and the fact that the fiber form is zig-zag in physiological regime agree with experimental trends on chromatin, although the unconstrained model predicts a qualitatively different core particle structure due to the lack of linker histone. In fact, the entering and exiting strands are displaced and divergent in this case and thus, the density of spheres appears to be typically small (i.e. about one sphere per 10 nm along the fiber axis). For higher salt concentrations, the chain wrapping degree still increases and the spheres become highly packed along the fiber backbone (for fixed chain length per sphere) leading to compact solenoidal structure. I have also studied the role of sphere charge and chain length per sphere and their influence on the fiber structure. As shown, by increasing the sphere charge at physiological salt concentration, fiber undergoes a series of dramatic structural changes (including transitions between zig-zag, solenoidal and beads-on-a-string patterns) as the PE chain becomes increasingly more wrapped around individual spheres, leading eventually to a 10 nm fiber consisting of highly packed and aligned core particles. As shown, zig-zag patterns are obtained as stable structures within the physiologically relevant regime, i.e. $\kappa \sim 1$ nm^{-1}, when the sphere charge valency is chosen close to $Z = 15$. This may be thought of as a fitting procedure in order to obtain structures closer to the experimentally observed zig-zag patterns for chromatin at intermediate salt concentration, because, as explained before (Chapter 2), macroion charge should indeed be taken as an effective (or fitting) parameter within the present model.

In the second approach (constrained optimization model), the core particle structure is fixed and only the relative rotation of core particles (unit cells) is allowed in order to minimize the fiber Hamiltonian. As shown, for large sphere charge and within the physiological salt regime, the fiber shows zig-zag pattern and sphere densities of about 5 spheres per 10 nm length along fiber axis. The structure as well as the fiber density and diameter in this case agree more closely with experiments on 30 nm chromatin [123, 122, 125] and also with the predictions of the two-angle model proposed by Woodcock et al. [122]. Yet it is important to note that the linker histone effects (or other factors such as histone tails) are not yet explicitly incorporated within the present model. Interestingly, the dense zig-zag pattern results from the fact that the entering and exiting strands form a cross pattern leading to a small entry-exit angle (the form of the entry-exit strands in this case becomes close to the stem-like form expected in the presence of the linker histone).

Note that, strictly speaking, the present results are obtained for a generic charged chain-sphere complex fiber and its direct comparison with the 30 nm chromatin fiber (which involves additional structural and specific details) should be considered with caution. Yet the approach presented in this chapter provides a systematic numerical method for investigation of complex

fibers in the limit of strong electrostatic coupling (i.e. where thermal fluctuations are rather small), which can be easily applied to more sophisticated models as well. In particular, it can be extended in the future studies so as to analyze the chromatin structure. The predictions of the constrained optimization model already indicates that further improvements upon the present model leads to more relevant results when applied to chromatin. Explicit incorporation of the linker histone constructs an interesting problem for future research.

Another interesting problem is to study the response of the fiber to an externally applied stress. Recent experiments have shown that the response of the chromatin to an external mechanical stress can provide more insight into the DNA-histone interactions and the detailed conformation of the fiber [50] (see Chapter 1). This problem has been considered in several recent theoretical studies [49, 97]. Finally, one may also consider an inhomogeneous fiber in which the linker length may vary from one unit cell to the other. In this case, as shown within the two-angle models for chromatin [122], the fiber may exhibit overall deformations and large-scale conformational fluctuations.

4.7 Supplementary information: Details of structural analysis of the complex fiber

In this section, I present a more detailed study of the local complex fiber structure, and in particular, discuss the periodic properties of the patterns obtained by unconstrained optimization model. I will also consider the distribution of local dipole along the fiber. Here I concentrate on a case with fixed sphere charge $Z = 15$ and fixed chain length per unit cell $N_{\mathrm{bp}} = 200$.

4.7.1 Fiber axis

In order to determine the geometrical properties of the fiber structure such as its diameter, projected sphere-sphere distance and periodicity, one needs first to determine the fiber axis, which can be calculated using the numerically determined (optimal) positions of spheres.

The position vectors of the sphere center along the fiber are denoted here by $\mathbf{R}_n = (x_n, y_n, z_n)$ with $n = -\infty, \ldots, \infty$ being the sphere numbering label (recall that within the present minimal cell model, the consecutive spheres are in equal center-to-center distances from each other). Although, the fiber takes in general a helical structure, the sphere positions R_n do not necessarily define a simple helix in space (described with a single periodicity). When the frame of the reference is chosen such that the *fiber axis* lies on z-axis (natural frame), the projected coordinates of sphere centers may be written as

$$x_n = f(n), \quad y_n = g(n), \quad z_n = h(n), \tag{4.14}$$

where $h(n)$ is a linear monotonically increasing function of n, and $f(n)$ and $g(n)$ are in general given in terms of superposing periodic functions of n. Note that, in present study, n is an integer number, therefore a single helix defined above is *exactly* periodic only when its frequency, ω, is a rational factor of π. However, here I give the analyses for a general case of real n.

Within the minimization procedure described in Section 4.1, the z-axis is initially fixed and thus the resultant optimal fiber axis may be in general displaced from the origin and elongated in a different direction as compared with the z axis. Thus the numerically obtained

components x_n, y_n and z_n have both periodic and linear components, which are combined linearly via a three-dimensional rotation matrix and possibly also a translation in space.

The axis of the fiber (which is defined to be a straight line of the same distance from all sphere centers) may be achieved simply from the x_n, y_n and z_n data by averaging out the periodic component over a long range of n. What remains, i.e. $\overline{x_n}$, $\overline{y_n}$ and $\overline{z_n}$, are nothing but the fiber axis coordinates parametrized by n. To illustrate this point, consider a *simple* helix $(\sin \omega n, \cos \omega n, n)$ of unit radius, periodicity ω^{-1} and unit pitch in its natural frame of reference. The helix axis is specified by the guide vector $(0, 0, 1)$. In a general coordinates frame, which may be related to the natural frame by a rotation matrix $\hat{R}$ and a translation (x^0, y^0, z^0), the helix is specified by

$$x_n = R_{11} \sin \omega n + R_{12} \cos \omega n + R_{13} n + x^0,$$
$$y_n = R_{21} \sin \omega n + R_{22} \cos \omega n + R_{23} n + y^0,$$
$$z_n = R_{31} \sin \omega n + R_{32} \cos \omega n + R_{33} n + z^0,$$

and the fiber axis in this frame reads

$$x_{\text{axis}} = R_{13} n + x^0,$$
$$y_{\text{axis}} = R_{23} n + y^0,$$
$$z_{\text{axis}} = R_{33} n + z^0,$$

where R_{ij} are different components of $\hat{R}$. Clearly, this axis can be obtained from (x_n, y_n, z_n) expressions above merely by averaging over or a sufficiently large range of n that yields

$$\overline{x_n} = R_{13} n + x^0,$$
$$\overline{y_n} = R_{23} n + y^0,$$
$$\overline{z_n} = R_{33} n + z^0. \tag{4.15}$$

I use this procedure to locate the fiber axis in a fixed frame of reference. Given the fiber axis, one can easily determine the fiber diameter, D_{F}, from the distance of spheres from the axis, and the projected center-to-center distance, $d_{\parallel}$, of spheres along the axis.

4.7.2 Periodicity

The periodic structure of the fiber is reflected in the behavior of the sphere center position $\mathbf{R}_n = (x_n, y_n, z_n)$ as a function of n. But as will be shown explicitly later, one typically observes a complex behavior that reflects a multiple-periodic structure (e.g., a "beating" periodic pattern). A close inspection (using Fourier analysis) reveals a discrete distribution of wavelengths centered sharply around a given wavelength. In general, therefore, the fiber can not be described by an *exact* periodicity (because first the ratio between various wavelengths involved is not a rational and moreover the sphere positions form a discrete set), but only an *approximate* (or apparent) periodicity may be found (see below).

To characterize the periodic structure of the fiber, I shall make use of the difference functions $\Delta x_n = x_n - x_{n-1}$, $\Delta y_n = y_n - y_{n-1}$, etc., because the linear component of position coordinates (as discussed in the preceding section) is cancelled out in these quantities.

I will then employ discrete Fourier transformation methods to identify the characteristic periodicities wavelengths of the fiber from these difference function (one can concentrate, e.g.,

on Δx_n since all different components lead to the same result). For this I choose a discrete set of data, say $\{\Delta x_n\}$ with $n = 1, \ldots, N_s$ for large number of spheres N_s. Fourier transform with respect to the numbering label n is defined as

$$\Delta \tilde{x}_s = \frac{1}{\sqrt{N_s}} \sum_{n=1}^{N_s} \Delta x_n \exp\left(\frac{2\pi i (n-1)s}{N_s}\right), \tag{4.16}$$

where s, the so-called *mode number*, is the Fourier conjugate of n and takes the discrete set of values $s = 0, \ldots, N_s - 1$. Note that

$$\lambda(s) = \frac{N_s}{s} \tag{4.17}$$

represents the *wavelength* associated with the mode number s defining the structural spectrum of the fiber. The squared Fourier amplitude,

$$I(s) = |\Delta \tilde{x}_s|^2, \tag{4.18}$$

plotted as a function of s, which will be referred to as the *spectral density*, reflects structural periodicity of the fiber of which explicit examples will be given later. If the fiber can be described by a single periodic function, one obtains a single peak in $I(s)$ at for instance s_* characterizing a unique periodicity (or wavelength) for the fiber $\lambda_* = N_s/s_*$. Due to the discrete nature of the data, this peak is accompanied by a symmetric Fourier peak located at $1 - (s_*/N_s)$.

An exact periodicity, λ_P, is defined as the number of spheres along the fiber after which Δx_n is repeated, i.e. upon translation $n \to n + \lambda_P$ we obtain the same data as

$$\Delta x_{n+\lambda_P} = \Delta x_n. \tag{4.19}$$

In general however this relation holds only approximately, i.e. an approximate periodic behavior may be found within a finite section of the fiber by including a sufficiently large number of spheres (I consider typically $N_s = 500$ spheres). The location of the peak in $I(s)$ does not directly yield this periodicity when several superimposing periodic functions are involved. To obtain λ_P, one in fact needs to *filter* the information regarding low-wavelength contributions to the spectral density $I(s)$. In position space, this procedure may be done by choosing a subset of original $\{\Delta x_n\}$ data, i.e. as $\{\Delta x_k\}$, where $k = [n/K]$. Here the bracket sign denotes the integer part of its argument and $K = 1, 2, 3 \ldots$ is a given integral number. Clearly, Δx_k only picks up every K-th data point, which in Fourier space corresponds to filtering out the wavelengths smaller than K. The filtered spectral density associated with $\{\Delta x_k\}$ reads

$$I_K(s) = \left| \frac{1}{\sqrt{[N_s/K]}} \sum_{k=1}^{[N_s/K]} \Delta x_k \exp\left(\frac{2\pi i (k-1)s}{[N_s/K]}\right) \right|^2 \qquad k = [\frac{n}{K}], \, n = 1, \ldots, N_s. \tag{4.20}$$

This procedure can be repeated for various K by choosing a sufficiently large number of original data points N_s. I use the following procedure to obtain λ_P: I first identify the mode number, s_*, where the original spectrum $I(s) = I_{K=1}(s)$ exhibits a peak. I shall then filter the spectrum using $K = [N_s/s_*]$ because this peak is typically dominated by the low-wavelength periodic structure of the fiber. The resultant spectrum shows a new peak at some mode number s_{**}, which yields the approximate (or apparent) periodicity of the fiber as $\lambda_P = N_s/s_{**}$. In most cases, the results can be checked explicitly by examining the actual fiber structure.

4.7.3   Orientational order of core particles

Another interesting point regarding the organization of the complex fiber is the orientation of core particles along the fiber. As shown before, the core particles are typically highly overcharged and have a finite local dipole moment due to their highly asymmetric charge distribution. This quantity can be used to determine the relative orientation of core particles along the fiber. For a core particle located at $\mathbf{R}_n$, the local dipole moment is defined as

$$\mathbf{P}_n = q \sum_i (\mathbf{r}_i - \mathbf{R}_n) \tag{4.21}$$

(with $q = 1$ in the present case), where the sum runs only over those PE beads (labeled by i) that are in contact with the sphere (conventionally defined as beads with distances $|\mathbf{r}_i - \mathbf{R}_n| < 1.02 R_\mathrm{s}$ from the center).

The orientation of each local dipole moment may be specified by the polar and azimuthal angles, θ_n^d and ϕ_n^d respectively, that are measured with respect to a fixed frame of reference in space (with the z-axis passing through the mid-point of the PE segment lying on a given sphere–see Section 4.1). The dipole orientations reflect the nature of interaction between various core particles on the dipolar level. As will be shown, the dipole moments (or a given component of them) may be oriented parallel to each other reflecting short-range correlations along the fiber or may be anti-parallel.

In the following sections, I discuss the periodic and dipolar structure of the fiber for a selected set of parameters in more detail.

4.7.4   Low salt regime $\kappa = 0.2 \mathrm{nm}^{-1}$

I begin with a rather small salt concentration corresponding to Debye screening length $\kappa = 0.2$ nm^{-1} (see Figures 4.4c and 4.23a), where the numerically calculated fiber shows a loose solenoidal structure.

In order to demonstrate the periodic behavior of the fiber for $\kappa = 0.2$ nm^{-1}, I show the difference sphere position projected along x axis, $\Delta x_n = x_n - x_{n-1}$, in Figure 4.23b. The Δx_n data show that the location of spheres in the fiber does not follow a simple helix structure as given by Eq. (4.15), but it rather indicates a triple-helix for the fiber structure, i.e. sphere centers lie on *three* intervening (discrete) helices of roughly the same periodicity. In other words, a given sphere labeled by n_0 defines a simple helix together with a series of spheres labeled by $n_0 + 3n$ for integral number n. There are three such helices. This may also be seen directly from the conformation of the fiber in Figure 4.23b.

In Figure 4.23c, I have shown $I(s)$, defined in Eq. (4.18), which is obtained from the data in Figure 4.23b using $N_\mathrm{s} = 500$ spheres along the fiber. As seen there is a peak (containing several mode numbers) centered at $s_*/N_\mathrm{s} = 0.33$, which is accompanied by a symmetric Fourier peak at $1 - (s_*/N_\mathrm{s})$. This peak yields a wavelength of about $\lambda(s_*) = N_\mathrm{s}/s_* = 3.0$ which in fact reflects the low-wavelength structure of the fiber, that is the existence of three intervening helices (note that there is also a peak corresponding to the zero mode $s = 0$). As may be seen from Figure 4.23b, there is an approximate periodicity, λ_P, which appears to be indeed much larger than the value given by the peak location s_*. Information due to small wavelengths may be filtered by choosing the cut-off $K = [s_*/N_\mathrm{s}] = 3$ that is equivalent to including only every third point. The spectrum $I_{K=3}(s)$ now reflects the high-wavelength structure of the fiber with a sharp peak centered at $3 s_{**}/N_\mathrm{s} = 0.024$ as shown in Figure 4.23c.
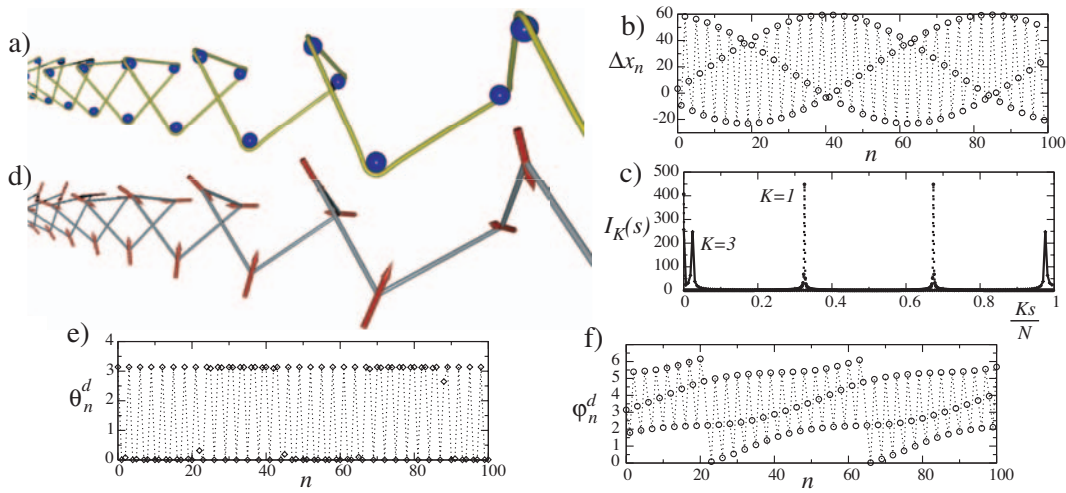
Figure 4.23: a) The optimal complex fiber configuration obtained from the unconstrained optimization model for $\kappa = 0.2$ nm^{-1} and with sphere charge $Z = 15$ and fixed chain length per unit cell $N_{\mathrm{bp}} = 200$. b) The difference sphere center location along x axis, $\Delta x_n = x_n - x_{n-1}$, as a function of the sphere site number n. c) The spectral density of the Δx_n data obtained with no mode-filtering, labeled with $K = 1$, and with filtering of wavelengths smaller than 3 (in units of the projected sphere-sphere distance), labeled with $K = 3$; see Eq. (4.20). The peak location in the former case specifies the multiplicity of the helical structure of the fiber (here composed of three helices) and the later case exhibits a peak at the value corresponding to the approximate (apparent) fiber periodicity. d) The schematic view of local dipole moments of the core particles distributed along the fiber backbone (see Eq. (4.21)). e) and f) show the polar and azimuthal dipole angles, θ_n^{d} and ϕ_n^{d}, respectively (with respect to a fixed frame in space).

I thus obtain the approximate periodicity of the fiber as $\lambda_{\mathrm{P}} = N_{\mathrm{s}}/s_{**} = 125$ in units of the projected distance, $d_{||}$, between centers of neighboring spheres. This amounts to a very large scale which can be resolved only when a sufficiently large number of spheres are taken into account.

In Figure 4.23d, I have schematically shown the orientation of local dipole moments of the core particles as defined via Eq. (4.21), and shown the orientation angles of each local dipole moment, θ_n^{d} and ϕ_n^{d}, in Figures 4.23e and f as a function of the sphere site label n. The periodic structure of the fiber shows up also within these graphs. The data for θ_n^{d} clearly show that among each three subsequent dipoles, two of them have z components in the same direction while the third dipole has a z component in the opposite direction, as may be seen also from Figure 4.23d.

The dipole orientations reflect *repulsive* dipolar interactions. One should also note that the sphere is already highly overcharged with the adsorbed PE segment (Section 4.2.2), and thus the monopole interactions between different core particles are also highly repulsive.

4.7.5 Intermediate salt regime $\kappa = 0.8$nm^{-1}

I now consider the regime of intermediate salt concentrations and focus on the fiber structure for inverse screening length $\kappa = 0.8$ nm^{-1} (see Figures 4.5b and Figure 4.24a), where the
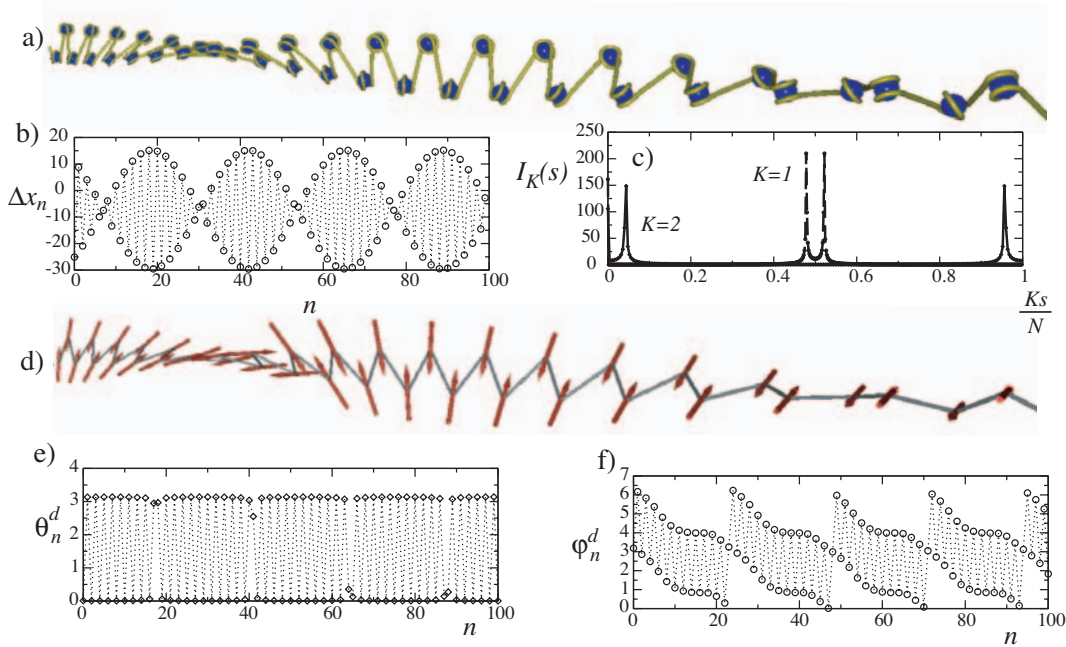
Figure 4.24: Same as Figure 4.23 but obtained for $\kappa = 0.8$ nm^{-1}.

optimal structure is found to display a zig-zag pattern.

In this case, the sphere centers positions in Figure 4.24b display *two* sub-helices, which may also be seen from the fiber configuration itself. Therefore the fiber represents a double-helical structure. The spectral density of Δx_n data reveals a peak centered at about $s_*/N_s = 0.48$ corresponding to a wavelength of $\lambda(s_*) = N_s/s_* = 2.08$, which reflects the double helical structure. Using the filtering procedure with a cutoff $K = 2$ (see Eq. (4.20)), a long-wavelength peak is found at $2s_{**}/N_s = 0.044$, which gives an approximate periodicity of $\lambda_P = 45$ in units of the projected sphere-sphere distance, $d_{||}$ (Figure 4.24c).

The local dipole moments in this case tend to take anti-parallel orientations (Figure 4.24d) as seen from the θ_n^d-angle of spheres in Figure 4.24e, which in fact shows that there are wide periodic regions in which the z component of the dipoles flip-flops in opposite directions as one moves from one sphere to its immediate neighbors. The polar angle changes almost by an amount equal to π (Figure 4.24f). The opposite orientation of dipole moments again reflects repulsive interactions on the dipolar level which adds up with the already repulsive monopole interactions between overcharged core particles.

4.7.6 Intermediate salt regime $\kappa = 1.0$nm^{-1}

For still larger values of the inverse Debye screening length, e.g., at $\kappa = 1.0$ nm^{-1}, the optimal fiber configuration shows a somewhat less ordered structure in terms of the sphere center locations along the PE chain (Figures 4.5d and 4.25a). This may be seen more clearly from the Δx_n data in Figure 4.25b, which still however reflects the appearance of a double-helical structure.

To establish this fact on a quantitative level, I consider the spectral density with no
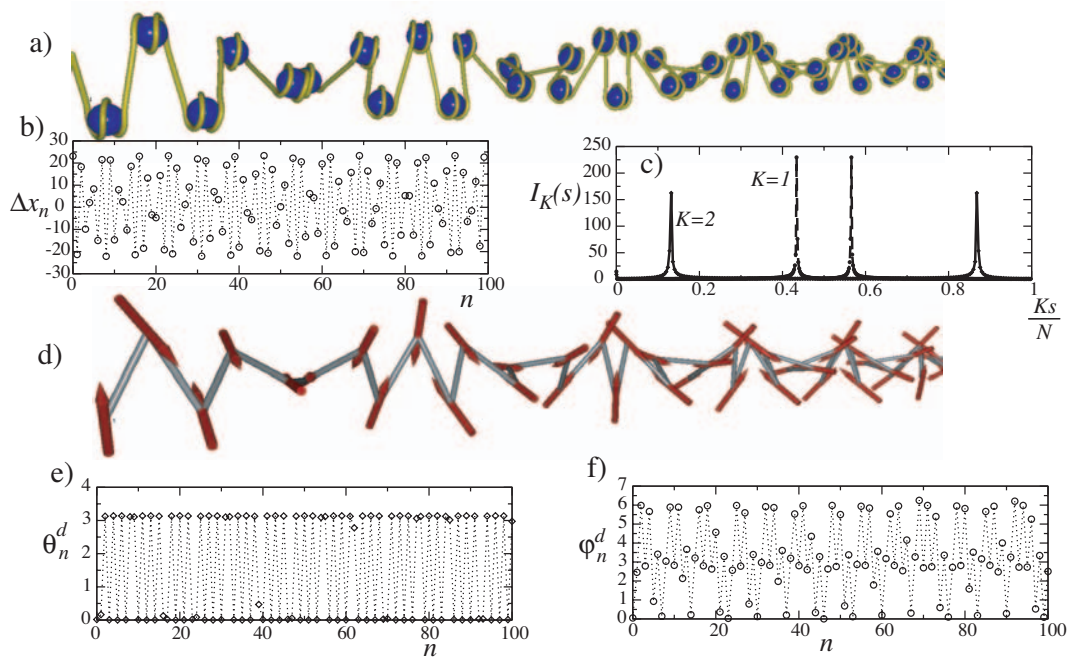
Figure 4.25: Same as Figure 4.23 but obtained for $\kappa = 1.0$ nm^{-1}.

filtering, i.e. $I(s)$ as shown in Figure 4.25c. It exhibits a peak in the high-mode-number
range at $s_*/N_s = 0.456$, corresponding to a small wavelength of $\lambda(s_*) = 2.19$, which indicates
the double-helicity of the fiber. I thus use a filtering procedure with $K = 2$, i.e. including only
every second sphere, to find the periodicity of the fiber at longer wavelengths, which shows
up in the form of a low-mode-number peak at $2s_{**}/N_s = 0.132$ (Figure 4.25c). This yields an
approximate periodicity length of $\lambda_P = N_s/s_{**} = 15$ in units of the projected distance. As
seen the periodicity of the fiber is markedly reduced for this salt concentration.

The z component of the local dipole moments flip-flops in opposite directions from one
sphere to its immediate neighbors while the azimuthal angle shows a periodic behavior be-
tween 0 and 2π with the average of π and in periodic ranges comparable to the periodicity of
the fiber (Figures 4.25d-f).

4.7.7 Moderate salt regime $\kappa = 1.2$nm^{-1}

I now consider a moderate salt concentration with inverse screening length of $\kappa = 1.2$ nm^{-1}. In
general in the large salt regime, the optimal fiber is found to fall within the compact solenoidal
structures (see Figure 4.5e, f and 4.26a), where the projected distance of neighboring sphere
centers is quite small as compared with the fiber diameter.

The location of spheres within the fiber in this case roughly follows a simple (single) helix
as it is evident from the configuration shown in Figure 4.26a. Equivalently, the difference
sphere location in x direction, that is $\Delta x_n = x_n - x_{n-1}$ plotted in Figure 4.26b, coincides
nearly with a simple periodic curve, which immediately gives the periodicity of the fiber.
The spectral density data show a peak located at $s_*/N_s = 0.132$ yielding the periodicity
$\lambda(s_*) = N_s/s_* = 7.57$ in units of the projected distance $d_{||}$.
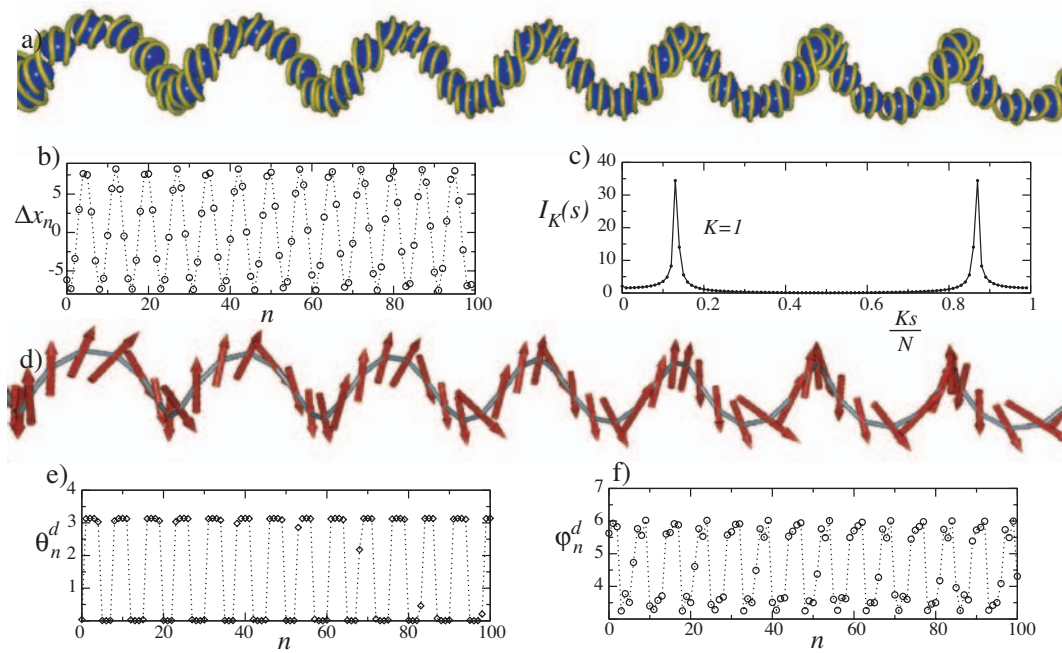
Figure 4.26: Same as Figure 4.23 but obtained for $\kappa = 1.2$ nm^{-1}.

Interestingly, the local dipole moments of core particles on the fiber exhibit a short-ranged *correlation*, i.e. they tend to orient parallel to each other and in the same direction in small periodic domains composed of a few core particles (Figure 4.26d). This is seen clearly from the polar angle of the dipoles shown in Figure 4.26e, which indicates the appearance of two distinct domains with opposite dipole orientation; but in each domain dipole moments have almost the same z component. The azimuthal angle is almost constant in each domain but varies by an amount equal to π from one domain to the other.

Chapter 5

Thermodynamic Stability of PE-Macroion Complexes

I investigate the thermodynamic stability of complexes formed by one semiflexible charged polymer wrapped around an oppositely charged sphere by incorporating thermal fluctuations around the ground-state configuration. Choosing parameters suitable for the DNA-histone system, I determine all conformational eigen-modes and the corresponding eigen-value spectrum of the complexed chain fluctuations on the sphere, from which the free energy of complexation is obtained. This free energy includes the adsorption energy of the chain as well as the entropy loss the chain suffers upon binding to the sphere. Using this I determine the so-called reaction constant corresponding to the complex formation process in a dilute solution of charged polymers and macroions. Hence a global complexation phase diagram as a function of salt and DNA/histone concentration is obtained, which exhibits qualitative agreement with experimental results.

In the preceding chapters, I focused on examining the structure and conformation of *strongly coupled* complexes consisting of a highly charged polyelectrolyte (PE) chain and oppositely charged spherical macroions. As demonstrated, these complexes exhibit a flat PE layer adsorbed on the sphere with pronounced lateral order due to mutual electrostatic repulsion of the PE segments. The strong PE adsorption energy and the large effective (electrostatic plus mechanical) bending rigidity of the PE chain allow one to employ ground-state analysis to investigate the structure of these complexes, neglecting thus the effects due to thermal fluctuations (Chapter 3). Fluctuation effects become large and dominant for weakly coupled complexes, that is at high-temperatures and for weakly charged chains and macroions, where the adsorption energy becomes comparable to the thermal energy giving rise to a diffuse adsorbed polymer layer on the sphere as investigated in several other studies [58, 59, 37]. For strongly coupled complexes, which are considered in the present work, fluctuation effects are relatively small but it becomes particularly important to examine these effects when the *thermodynamics* of the complexation process in a *solution* of macroions and PE chains is of concern. Here one has to incorporate chain fluctuation effects in order to obtain both chain adsorption (complexation) and desorption (de-complexation) behavior. Despite numerous studies on strongly coupled complexes on the ground-state level, the role of thermal fluctuations has not yet been analyzed in a systematic fashion.

Leaving aside kinetics of adsorption, the key issues here are: i) what is the reaction

constant of complex formation, and ii) what is the phase behavior of the mixed solution of PEs, spheres and complexes as a function of concentration of different species. Recent experiments on nucleosomal core particles (NCPs) have in fact addressed the DNA adsorption process on histone proteins in dilute NCP solutions [83, 113, 88, 89, 90, 103, 104]. An association (or complexation) equilibrium has been observed between free (unassociated) DNA chains and histones in solution with the complexed ones in the range of small to moderate salt concentrations [103, 104]. It is shown in particular that at higher salt, a larger concentration of histones is required to form complexes, reflecting the role of electrostatic interactions in this process. Understanding this behavior has received less attention in the previous theoretical works and in particular, the reaction constant of complexation is not known. Note that the reaction constant for a bimolecular reaction has units of an inverse volume: for simple reactants, this volume depends on the range of the binding potential (or, in the quantum limit, on the thermal wavelength) and arises from mutual vibrations of the binding partners in the product. When a flexible polymer binds to a sphere, the interpretation of this inverse volume factor is less obvious and requires determining the full entropy loss upon binding of the chain, as will be made clear later on. Note that simulations, which have been successfully used for the study of the complexation equilibrium between spheres and moderately charged polymers [51, 52, 44, 47], face a severe and fundamental problem for parameters corresponding to the strongly coupled complexes (such as DNA-histone complexes): Here the binding energies are much larger than $k_B T$, and the PE stiffness induces pronounced free energy barriers, so that astronomically large simulation times would be needed to observe spontaneous de-complexation. Similar problems occur in many other complex many-body systems; a solution is provided recently by the so-called metadynamics [53].

In this chapter, I will study the effects of thermal fluctuations on the structure of a strongly coupled PE-macroion complex within the chain-sphere model introduced before. As the main result, I will determine the thermodynamic stability and phase behavior of such complexes in solution as a function of salt and PE/macroion concentration. Here I will consider only complexes formed by one sphere and one charged semiflexible chain and do all explicit calculations for parameters corresponding to the well-studied nucleosomal core particles. But the methods presented here can in principle be used for any strongly complexed polymer-particle system.

Thermal fluctuations of the PE on the macroion will be examined using a normal-mode analysis and based on a saddle-point approximation that incorporates small-amplitude fluctuations around the optimal path (ground state conformation) of the chain. By identifying all normal modes of chain fluctuations and determining their corresponding eigen-values (the spectrum of fluctuations), the free energy of complexation is determined, which incorporates the energy gain as well as the entropy loss associated with the complexation of the PE chain. I will then derive the relation between this free energy and the reaction constant, which introduces the law of mass action for the PE-macroion complexation. This allows to sketch the complexation diagram as a function of salt and PE/macroion (or DNA/histone) concentration which shows qualitative agreement with the experimental phase diagram [103, 104]. Here I will focus on dilute solutions of macroion and PEs and thus neglect interactions between different complexes, which will be studied separately in the forthcoming Chapter 6.

As discussed in Chapter 2, the present model accounts for the electrostatics effects on the linear Debye-Hückel (DH) level and thus neglects non-linear effects due to charge regulation and charge renormalization [56] (neglecting, as a result, also counterion release effects [54, 55]). These factors shift the effective charge of macroions and the effective linear charge density of

PEs from their bare values. The influence of non-linear effects on the resulting phase diagram can be examined within the present model by considering the macroion charge and the chain linear charge density as effective parameters within the DH theory. I will thus vary macroion charge and consider both bare and fully renormalized PE charge as predicted by Manning for an infinite chain as the upper- and lower-bound values for the actual PE charge (see Chapter 2). As will be shown, a reduced macroion or PE charge leads to a more enhanced de-complexed phase since the chain adsorption energy decreases but qualitative features remain the same.

The organization of this chapter is as follows: In Sections 5.1, I briefly recall the details of the model used in the present work and the results for the ground-state conformational phases of a complex that were discussed in detail in Chapters 2 and 3. In Section 5.2, I obtain a general free energy expression for a dilute solution of PEs and macroions and derive the law of mass action governing the complexation process. The complexation free energy is calculated explicitly in Section 5.3 using a normal-mode analysis of chain fluctuations that are analyzed in detail for various ground-state phases. In Section 5.4, I present the predicted complexation phase diagram of PEs and macroions.

5.1   Ground-state of a single complex

Review of the model

As discussed before (Chapter 2), the polyelectrolyte chain is modeled as a semiflexible chain of length L, linear charge density $-\tau e$ and persistence length ℓ_{p}. The macroion is a semi-rigid sphere of radius R_{s} and opposite charge Ze. The Hamiltonian for the PE chain in units of $k_{\mathrm{B}}T$ consists of electrostatic and bending contributions

$$\mathcal{H}_p[\mathbf{r}(s)] = \frac{\ell_{\mathrm{p}}}{2} \int_0^L \ddot{\mathbf{r}}^2(s)\,ds + \tau^2 \ell_{\mathrm{B}} \int_0^L ds \int_s^L ds' \frac{e^{-\kappa|\mathbf{r}(s)-\mathbf{r}(s')|}}{|\mathbf{r}(s)-\mathbf{r}(s')|}, \tag{5.1}$$

where $\mathbf{r}(s)$ specifies the chain configuration and s its contour. The Bjerrum length $\ell_{\mathrm{B}} = e^2/(4\pi\varepsilon\varepsilon_0 k_{\mathrm{B}}T)$ is about $\ell_{\mathrm{B}} \approx 0.7$ nm in water and at room temperature, and $\kappa = \sqrt{8\pi\ell_{\mathrm{B}}C_s}$ is the inverse screening length associated with monovalent salt concentration C_s. The PE-macroion interaction reads

$$\mathcal{H}_{pm}[\mathbf{r}(s)] = -\frac{Z\tau\ell_{\mathrm{B}}}{1+\kappa R_{\mathrm{s}}} \int_0^L ds \left[\frac{e^{-\kappa(|\mathbf{r}(s)|-R_{\mathrm{s}})}}{|\mathbf{r}(s)|} - Ae^{-(|\mathbf{r}(s)|-R_{\mathrm{s}})/\alpha} \right] \tag{5.2}$$

contains the electrostatic contribution (first term) and a soft repulsion term (second term), which is characterized by strength A and range α (chosen as $A \ll 1/R_{\mathrm{s}}$ and $\alpha < \kappa^{-1}$–see Section 2.1.3 and Appendix E for details). The Hamiltonian of a chain-sphere complex is obtained by combining the above two expressions, i.e.

$$\mathcal{H}_c = \mathcal{H}_p + \mathcal{H}_{pm}. \tag{5.3}$$

In this chapter, I choose parameters suitable for DNA-histone complexes, i.e. $L = 49.64$ nm corresponding to 146 base pairs of DNA, $\ell_{\mathrm{p}} = 30$ nm as the mechanical persistence length of DNA (obtained in the limit of high salt and not including electrostatic stiffening effects, which are incorporated explicitly in the present model), $R_{\mathrm{s}} = 5$ nm as the effective
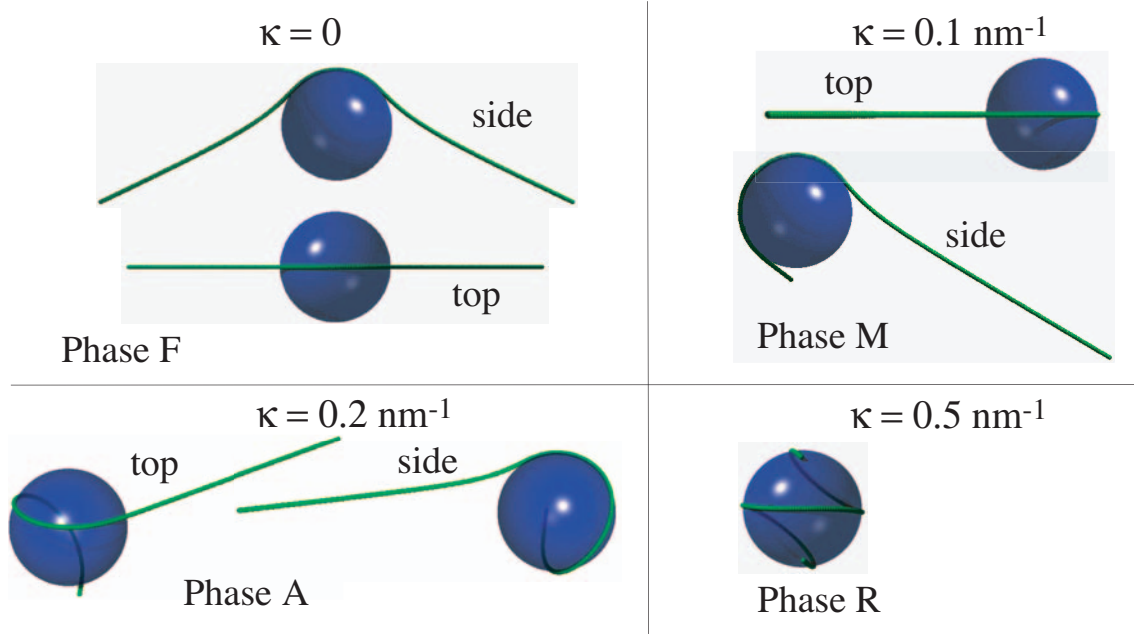
Figure 5.1: Numerically calculated ground-state configurations of a complex fall into four symmetry classes: fully symmetric or expanded phase F, mirror symmetry phase M, asymmetric phase A and rotational symmetry or wrapped phase R. Here they are obtained for $Z = 40$ and inverse Debye screening lengths $\kappa = 0$, 0.1, 0.2 and 0.5nm^{-1} respectively.

histone radius (which also includes the radius of DNA–see Section 2.1.2), and in most calculations $\tau = 5.88$ nm^{-1} corresponding to the maximum dissociation of phosphate groups in the case of DNA. The true histone charge is regulated depending on the pH, and charge renormalization shifts the effective sphere and PE charges from their bare values [55]. Hence Z and τ are parameters that approximately include both charge regulation and renormalization. I will return to this point later in Section 5.4.

In order to proceed the continuum chain model is discretized into N rigid subunits $\mathbf{u}_i$ (bond vectors) of fixed length $\Delta = L/N$, each characterized by a polar and an azimuthal angle θ_i and ϕ_i as explained in detail in Chapter 2 (see Figure 2.4). The minimization of $\mathcal{H}_c$ is performed numerically in the configurational space of all subunit angels by taking typically $N = 250$ discretization subunits.

Ground-state phases

Ground-state conformations of the chain fall into four symmetry classes, see Figure 5.1b, where typical structures are shown for different salt concentrations and fixed sphere charge $Z = 40$. The fully symmetric phase F (for $\kappa = 0$) exhibits *two-fold rotational* symmetry around the axis connecting the mid-point of the chain to the sphere center and also *mirror* symmetry, i.e. the chain has a planar two-dimensional structure. Phase M (for $\kappa = 0.1$ nm^{-1}) only has mirror symmetry; in the asymmetric phase A (for $\kappa = 0.2$ nm^{-1}) both symmetries are broken, and in phase R (for $\kappa = 0.5$ nm^{-1}), the chain only exhibits rotational symmetry. In agreement with experiments, the highly condensed phase R is only stable for intermediate salt concentrations, which can be traced back to a subtle interplay between electrostatic

repulsion between PE segments (which is most pronounced at low salt concentrations) and the mechanical bending rigidity (which becomes stronger than the electrostatic attraction between sphere and PE at high salt concentration) [48, 49]. For both low and high salt concentration, the PE exhibits a rather elongated conformation.

5.2 Complexes in solution: Complexation free energy

I now consider a solution of PEs, charged spheres and complexes formed by *one* PE and *one* sphere (generalization to complexes formed by more than one sphere or PE is straight-forward). I assume that these three components are in equilibrium and with *total* concentrations of C_m, C_p and C_c for macroions, PEs, and complexes respectively (I assume $C_p = C_m = C_0$ is constant). The complexation of PEs and macroions is driven by strong electrostatic attraction between them, while entropic gain due to both conformational and translational degrees of freedom of the PE chain favors desorption or de-complexation. In order to describe the equilibrium maintained by these two competing contributions, I will consider the total free energy density (that is the free energy per *unit volume*) of the solution, $\mathcal{F}_{\text{tot}}$. In the *dilute limit*, one can write this latter quantity (in units of $k_{\text{B}}T$) as

$$\mathcal{F}_{\text{tot}} = -\mathcal{S}_m - \mathcal{S}_p - \mathcal{S}_c + C_p\mathcal{F}_p + C_c\Delta\mathcal{F}, \tag{5.4}$$

where the ideal translational entropy density for free PE chains (of concentration $C_p - C_c$) is

$$\mathcal{S}_p = -(C_p - C_c)\ln(C_p - C_c) + (C_p - C_c) \tag{5.5}$$

with similar expressions for the translational entropy density of free macroions, i.e.

$$\mathcal{S}_m = -(C_m - C_c)\ln(C_m - C_c) + (C_m - C_c), \tag{5.6}$$

and for complexes as

$$\mathcal{S}_c = -C_c\ln C_c + C_c. \tag{5.7}$$

Here $\Delta\mathcal{F}$ represents the chemical potential of a complex (see below), which will be referred to in what follows as the *binding free energy* or *complexation free energy*. $\mathcal{F}_p$ represent chemical potential of a single PE chain, which in the dilute limit is dominated by the internal free energy of the chain. Note that the above approximate expressions are valid as long as the typical distance between complexes is larger than the Debye screening length.

Minimizing the free energy $\mathcal{F}_{\text{tot}}$ with respect to the concentration of complexes, C_c, gives the law of mass action for the complexation "reaction" as

$$K \equiv \frac{C_c}{(C_p - C_c)(C_m - C_c)} = e^{-\Delta\mathcal{F}}, \tag{5.8}$$

where K is the so-called equilibrium constant. Assuming equal total concentration of macroions and polymers, $C_m = C_p = C_0$, I obtain

$$C_c \simeq C_0^2\, e^{-\Delta\mathcal{F}} \tag{5.9}$$

from Eq. (5.8) in the low concentration limit $C_0\exp(-\Delta\mathcal{F}) \ll 1$. Inserting this back into the free energy expression (5.4), I find

$$\mathcal{F}_{\text{tot}} \simeq 2C_0(\ln C_0 - 1) + C_0^2\exp(-\Delta\mathcal{F}). \tag{5.10}$$

This equation is indeed equivalent to the first terms of a standard virial expansion for the PE-macroion solution, where the coefficient of the last term represents the second virial coefficient associated with different species and depends on effective pair interactions between PEs and macroions (see Appendix C.2 for details). The contribution due to PE-PE and macroion-macroion interactions are however negligible as compared with the PE-macroion interaction, since the latter amounts to a strongly attractive interaction. Hence, one can associate the term $e^{-\Delta\mathcal{F}}$ approximately with the second-virial of PE-macroion interaction. The explicit second-virial expression in Appendix C.2 shows that

$$\Delta\mathcal{F} = \mathcal{F}_c - \mathcal{F}_p, \tag{5.11}$$

where $\mathcal{F}_p$ and $\mathcal{F}_c$ are defined as

$$\mathcal{F}_p = -\ln\left[4\pi \int_{-1}^{1} \prod_{i=1}^{N-1} \mathrm{d}\cos\theta_i \int_0^{2\pi} \prod_{i=1}^{N-1} \mathrm{d}\phi_i \; e^{-\mathcal{H}_p}\right], \tag{5.12}$$

$$\mathcal{F}_c = -\ln\left\{4\pi \int_0^{\infty} r_P^2 \,\mathrm{d}r_P\left[\left(2\pi \int_{-1}^{1} \prod_{i=1}^{N} \mathrm{d}\cos\theta_i \int_0^{2\pi} \prod_{i=1}^{N-1} \mathrm{d}\phi_i \; e^{-\mathcal{H}_c}\right) - e^{-\mathcal{F}_p}\right]\right\}, \tag{5.13}$$

with $\mathcal{H}_c = \mathcal{H}_p + \mathcal{H}_{pm}$ being the complex Hamiltonian, and $\mathcal{H}_p$ and $\mathcal{H}_{pm}$ being single PE Hamiltonian and the PE-macroion interaction as given in Eqs. (5.1) and (5.2) respectively.

Note that $\mathcal{F}_c$ and thus $\Delta\mathcal{F}$ as defined above have logarithmic volume units, $\sim \ln V$, as required by dimensional analysis of the law of mass action Eq. (5.8). In order to proceed with a dimensionless representation of free energies, I rescale the integrand in Eq. (5.13) by the volume of a sphere,

$$V_0 = \frac{4}{3}\pi R_s^3, \tag{5.14}$$

and thus redefine $\mathcal{F}_c$ as

$$\tilde{\mathcal{F}}_c = -\ln\left\{\frac{3}{R_s^3} \int_0^{\infty} r_P^2 \,\mathrm{d}r_P\left[\left(2\pi \int_{-1}^{1} \prod_{i=1}^{N} \mathrm{d}\cos\theta_i \int_0^{2\pi} \prod_{i=1}^{N-1} \mathrm{d}\phi_i \; e^{-\mathcal{H}_c}\right) - e^{-\mathcal{F}_p}\right]\right\}. \tag{5.15}$$

As a result, the law of mass action (5.8) is rewritten as

$$K \equiv \frac{C_c}{(C_p - C_c)(C_m - C_c)} = V_0 \, e^{-\Delta\tilde{\mathcal{F}}}, \tag{5.16}$$

where now $\Delta\tilde{\mathcal{F}} = \tilde{\mathcal{F}}_c - \mathcal{F}_p$ is obtained from Eqs. (5.12) and (5.15). In what follows, I will use this dimensionless representation to calculate $\tilde{\mathcal{F}}_c$ and $\Delta\tilde{\mathcal{F}}$.

5.3   Nomal-mode analysis of chain fluctuations

The integrals in (5.12) and (5.15) are taken over degrees of freedom associated with a free and a complexed chain respectively. For the free chain, I arbitrarily fix the direction of one bond vector and the remaining $2N - 2$ degrees of freedom are represented by a vector $\mathbf{x}_p = \{\theta_i, \phi_i\}$. For the complex, the $2N$ degrees of freedom are $\mathbf{x}_c = \{\theta_i, \phi_{j\neq P}, r_P\}$, where r_P is the distance of the chain middle bead ($P = N/2$) from the sphere center and I have eliminated the azimuthal angle of this bead since it constitutes a Goldstone mode (see Chapter 2).

Since the mechanical persistence length of the DNA (~ 30 nm) is comparable with its length (~ 50 nm), thermal fluctuations of the chain around the ground state are small. Thus the integrals in Eqs. (5.12) and (5.15) can be approximated by a saddle-point expansion around the ground state as explained in Section 2.2. To this end, I expand the Hamiltonians $\mathcal{H}_p$ and $\mathcal{H}_c$ up to second order around the ground-state configuration of a single free chain, which is a straight line and will be denoted by $\mathbf{x}_p^*$, and that of a complex $\mathbf{x}_c^*$ respectively. Note that for a complex, the optimal or ground-state configuration, $\mathbf{x}_c^*$, is calculated numerically as before. For a complex, I write

$$\mathcal{H}_c(\mathbf{x}_c) = \mathcal{H}_c^* + \frac{1}{2}(\mathbf{x}_c - \mathbf{x}_c^*)^t \, \mathbf{H}_c'' \, (\mathbf{x}_c - \mathbf{x}_c^*), \tag{5.17}$$

where $\mathcal{H}_c^* = \mathcal{H}_c(\mathbf{x}_c^*)$ is the ground-state energy with $\partial \mathcal{H}_c / \partial \mathbf{x}_c^* = 0$, and

$$\mathbf{H}_c'' = \frac{\partial^2 \mathcal{H}_c}{\partial \mathbf{x}_c^* \partial \mathbf{x}_c^*} \tag{5.18}$$

is the Hessian matrix. A similar expansion is used for the single PE fluctuations. The elements of the Hessian matrix are calculated explicitly in Appendix A.

Using these expressions, the integrals in Eqs. (5.12) and (5.15) reduce to coupled Gaussian integrals, which can then be calculated by diagonalizing the Hessian matrix according to

$$\mathbf{y} = \mathbf{A}^t \mathbf{x}, \tag{5.19}$$

where $\mathbf{A}$ is the unitary matrix containing the orthonormal eigen-vectors of the Hessian. I obtain the eigen-vectors numerically [3] by solving the eigen-value problem

$$\mathbf{H}'' \mathbf{A} = \mathbf{A} \Lambda, \tag{5.20}$$

where Λ is a diagonal matrix containing the corresponding eigen-values λ_n of the Hessian matrix. In the space of new variables $\mathbf{y}$, the Gaussian integrals in Eqs. (5.12) and (5.15) factorize. Since the width of the Gaussian integrands, given by the inverse eigen-values $\sim \lambda_n^{-1}$, is narrow, one can extend the integration boundaries to infinity. Within the saddle-point expansion, the complex and the single-PE free energies are obtained as

$$\tilde{\mathcal{F}}_c = \mathcal{H}_c^* + \mathcal{F}_c^{(1)}, \tag{5.21}$$
$$\mathcal{F}_p = \mathcal{H}_p^* + \mathcal{F}_p^{(1)}, \tag{5.22}$$

where the Gaussian-fluctuations corrections to the ground-state energy of an individual complex, $\mathcal{H}_c^*$, and that of a single PE chain, $\mathcal{H}_p^*$, are then obtained as

$$\mathcal{F}_c^{(1)} = -\sum_{n=1}^{2N} \ln\left(\sqrt{\frac{2\pi}{\lambda_n^c}}\right) - \ln\left(8\pi^2 \sum_{n=1}^{2N} \frac{(A_{2N,n}^c)^2}{\lambda_n^c}\right) \tag{5.23}$$

$$\mathcal{F}_p^{(1)} = -\sum_{n=2}^{2N-1} \ln\left(\sqrt{\frac{2\pi}{\lambda_n^p}}\right) - \ln(4\pi), \tag{5.24}$$

respectively, where λ_n^c and λ_n^p denote the corresponding eigen-values (see below). These terms incorporate the entropy due to internal degrees of freedom of free PE chains and individual complexes. Note that the translational entropy of free PE chains, free macroions and that of
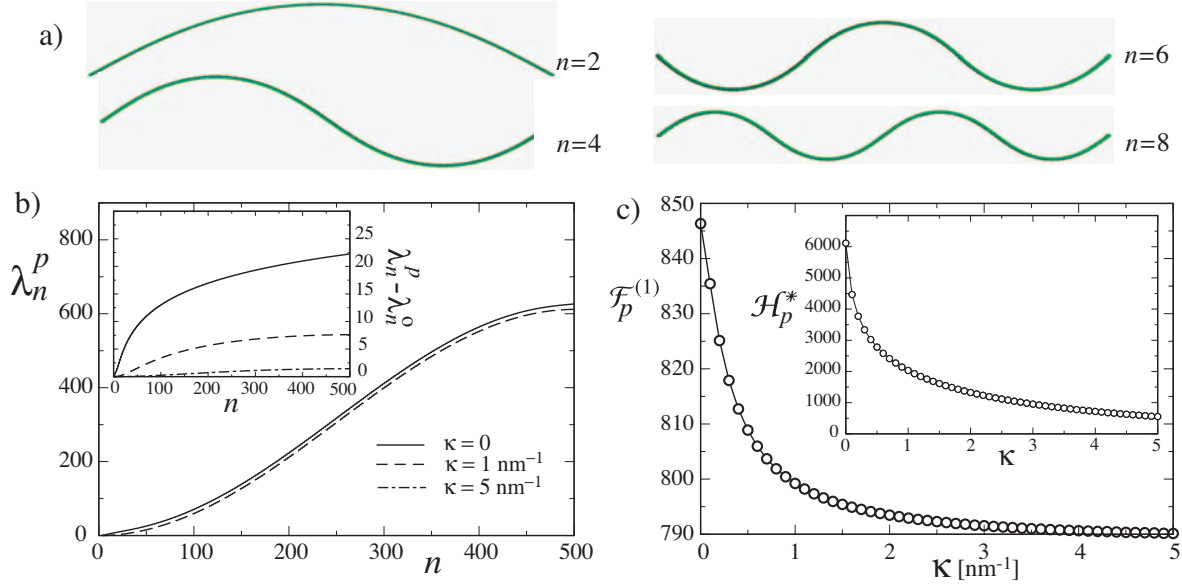
Figure 5.2: a) The first four distinct eigen-modes of free PE chain fluctuations for $\kappa = 5$ nm^{-1}. b) Eigen-value spectrum, λ_n^p, of a single PE chain of length $L = 49.6$ nm for three different salt concentrations. The inset shows the electrostatic contribution, $\lambda_n^p - \lambda_n^0$, without the mechanical part, λ_n^0. c) Different contributions to the free energy of a free PE chain as a function of κ. The main set shows the fluctuations correction term, $\mathcal{F}_p^{(1)}$, as a function of κ. The inset shows the ground-state energy term, $\mathcal{H}_p^*$, corresponding to the minimum of the Hamiltonian (a straight chain), as a function of κ.

complexes (from center-of-mass coordinates) are separately accounted for in the free energy density expression (5.4).

Before proceeding further with the calculation of the free energy, it is useful to examine the normal modes and fluctuation spectrum of a PE chain around its ground-state both when it is free in the solution and when it is complexed with a macroion.

5.3.1   Normal modes of a free PE chain

In Figures 5.2a and b, I show the eigen-value spectrum of a free (uncomplexed) PE chain, that is λ_n^p, as a function of the mode number n, for three different salt concentrations, and visualize the first four distinct eigen-modes.

Note that the spectrum of a *neutral* semiflexible chain reads

$$\lambda_n^0 = 4(N\ell_{\mathrm{p}}/L)\sin^2((n-1)\pi/4N) \tag{5.25}$$

for odd and

$$\lambda_n^0 = 4(N\ell_{\mathrm{p}}/L)\sin^2(n\pi/4N) \tag{5.26}$$

for even values of the mode number $n = 2,\ldots,2N-1$, reflecting the two-fold degeneracy of the spectrum (I discard the trivial zero-modes $n = 0$ and 1 for the free chain). λ_n^0 represents only the mechanical contribution to the spectrum. The *electrostatic* contribution to the spectrum is given by $\lambda_n^p - \lambda_n^0$, which is shown in the inset of Figure 5.2a. It depends logarithmically
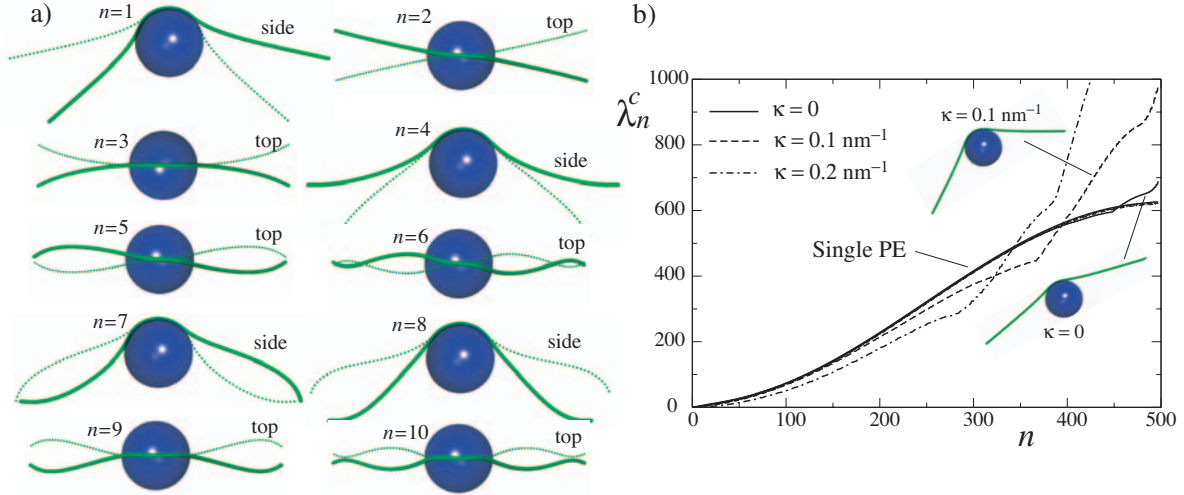
Figure 5.3: a) The first ten eigen-modes of fluctuations around the ground-state phase F (for $Z = 40$ and $\kappa = 0$ nm^{-1}) shown from the side or top views as indicated on the graph. Chain vibrations are shown with both positive (thick curve) and negative (thin curve) amplitudes, which are enhanced for the sake of representation. b) The spectrum of chain fluctuations in phase F for $Z = 20$ compared with that of a free PE chain for different inverse screening lengths $\kappa = 0$ (full line), 0.1 nm^{-1} (dashed line) and 0.2 nm^{-1} (dot-dashed line).

on n [178, 179, 180, 181, 182, 183, 184], but exhibits a rather small correction to the neutral limit due to the high mechanical rigidity of the PE chain $\ell_p = 30$ nm.

In Figure 5.2c, I consider the contributions to the internal free energy of a single PE chain, namely, the leading ground-state energy term, $\mathcal{H}_p^*$, and the fluctuations correction term $\mathcal{F}_p^{(1)}$ as defined in Eqs. (5.22) and (5.24). Recall that this latter quantity represents the (negative) entropy of fluctuations associated with internal degrees of freedom of the PE chain. The comparison between these two quantities will also give us a measure for the regime of validity of the saddle-point approximation.

As seen, both contribution decrease for increasing κ. The ground state energy tends to zero in the neutral limit $\kappa \to \infty$, while fluctuations contribution tends to a constant corresponding to the *entropy* of fluctuations of a *neutral* semi-flexible chain. The behavior of $\mathcal{F}_p^{(1)}$ therefore indicates that with growing electrostatic screening, the chain fluctuations and thus the chain conformational entropy increases. In fact, $\mathcal{H}_p^*$ and $\mathcal{F}_p^{(1)}$ curves cross each other at about $\kappa = 4$ nm^{-1} (for the chosen set of parameters here, i.e., $\ell_p = 30$ nm, $\tau = 5.88$ nm^{-1} and discretization degree $N = 250$). The saddle-point approximation thus breaks down for a *single chain* beyond this value as chain fluctuations dominate and higher-order corrections (beyond Gaussian fluctuations) become relevant.

5.3.2 Normal modes of a complexed PE chain

In the complex phases, the eigen-value spectrum of chain fluctuations, λ_n^c, exhibits more features. In general, the two-fold degeneracy present in the spectrum of an isolated chain is broken in the case of a complex due to the spatial inhomogeneity introduced by the presence of the sphere's central attractive potential.
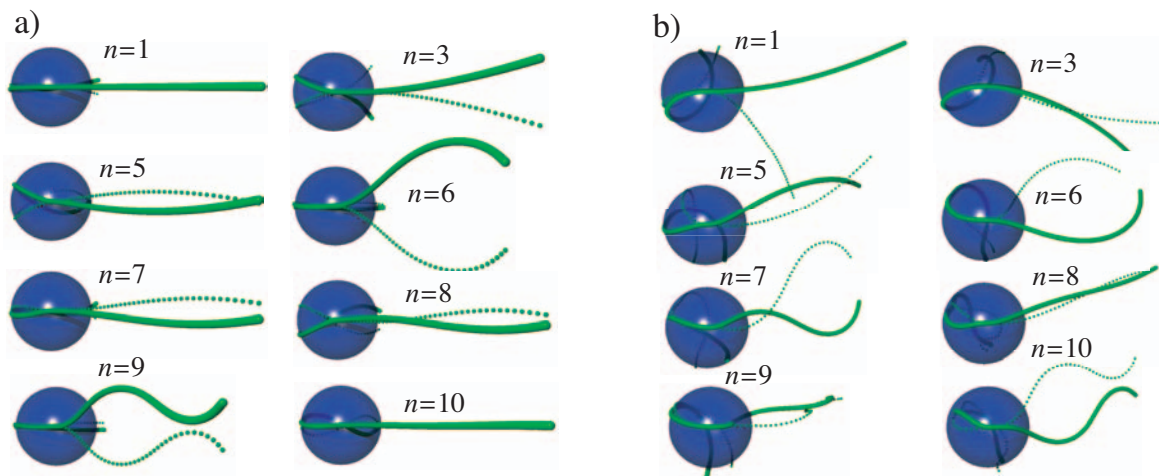
Figure 5.4:   a) Several eigen-modes of fluctuations around the ground-state phase M (for $Z = 40$ and $\kappa = 0.1$ nm^{-1}). The corresponding mode number n is indicated on the graph. b) The same as a) but for phase A (for $Z = 40$ and $\kappa = 0.2$ nm^{-1}). Chain vibrations are shown with both positive (thick curve) and negative (thin curve) amplitudes, which are enhanced for the sake of representation.

Extended phase F

In Figure 5.3a, the first ten eigen-modes of fluctuations around the expanded phase F are visualized (for $Z = 40$ and $\kappa = 0$) which explore all possible symmetries: modes $n = 4$ and 8 preserve the full symmetry of the ground state, that is both mirror symmetry (amounting to a planar configuration) and the two-fold rotational symmetry, while modes $n = 3$, 7, 9 and 10 break both symmetries. The modes $n = 2$, 5 and 6 are non-planar but keep the rotational symmetry. Note that these modes show either in-plane (in the plane of the ground-state configuration) or normal-to-plane (normal to the plane of the ground-state configuration) vibrations. In the former case, fluctuations may cause vibrations normal to the sphere surface (also penetration or detachment of beads from the sphere), which are energetically costly. These fluctuations thus typically constitute higher order modes (large n). It is interesting to note that the excited states for $n = 3$, 9 and 10 exhibit a three-dimensional chain conformation but still possess mirror symmetry with respect to the plane perpendicular to the ground-state configuration plane. This situation is not found for the ground-state configurations (see Chapters 2 and 3) but it is observed also among meta-stable states [44, 43].

In Figure 5.3b, the spectrum of phase F for $Z = 20$ and different values of κ, that is $\kappa = 0$, 0.1 and 0.2 nm^{-1}, is shown and compared with the spectrum of a single PE-chain with the same values chosen for κ (note that the chain spectra are not distinguishable in the scale of the graph–see also figure 5.2b). For $\kappa = 0$, the spectrum of the complex roughly coincides with the spectrum of the free PE chain, reflecting the fact that the complex ground state in this case has a shape quite close to a straight line. As κ becomes larger, complexation degree increases and deviations from the free chain spectrum become larger. Interestingly for smaller mode numbers, the complex eigen-values are smaller and thus fluctuations are more enhanced as compared with a free PE chain, while at high mode numbers the complex eigen-values are typically larger.
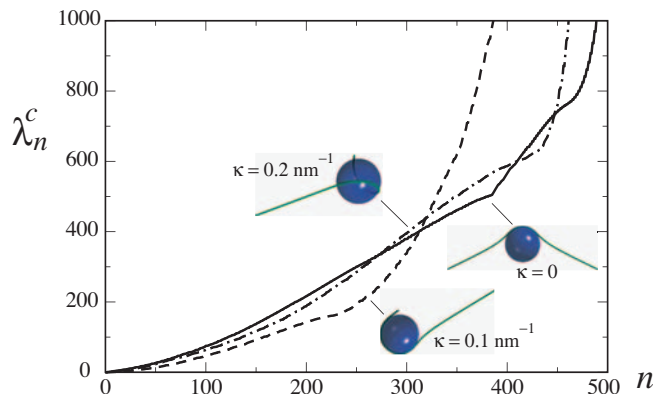
Figure 5.5: Spectrum of chain fluctuations for $Z = 40$ and in different configurational phases for the ground state, that is phase F ($\kappa = 0$, solid curve), phase M ($\kappa = 0.1$ nm^{-1}, dash curve) and phase A ($\kappa = 0.2$ nm^{-1}, dot-dashed curve).

Asymmetric phases M and A

In Figure 5.4a, I show several eigen-modes of chain fluctuations for $Z = 40$, $\kappa = 0.1$ nm^{-1}, where the ground state exhibits the conformational phase M, that is the rotational symmetry of chain configuration is broken, but the mirror symmetry still holds. Note that the low energy fluctuations, as shown in the figure, display mainly vibrations tangential to the sphere surface; there is also a fixed node on the sphere surface, which separates the "tail" and the "head" part fluctuations. Figure 5.4b shows the eigen-modes around a ground state configuration for $Z = 40$ and $\kappa = 0.2$ nm^{-1}, which exhibits the asymmetric phase A. This case displays more complex eigen-modes due to the non-planar form of the ground state conformation.

In Figure 5.5, I compare the spectra of Gaussian-fluctuations around the symmetry classes F, M and A that are obtained for $Z = 40$ and $\kappa = 0$, 0.1 and 0.2nm^{-1} respectively. As seen, low-energy modes are more easily excited in phase M as compared with other phases because it has smaller eigen-values typically for $n < 300$. This is related to the fact that phase M occurs for higher salt concentrations as compared with phase F. In general, one expects that chain fluctuations become stronger at higher salt, but on the other hand, the wrapping process as will be shown later suppresses the fluctuations at intermediate salt concentrations, e.g., within phase A. As a result, the intermediate phase M appears to be more favorable from an entropic (or fluctuations) point of view as compared with all other phases displaying typically larger entropic contribution (smaller free energy contribution) from fluctuations around the ground state (Figure 5.7a below).

For higher-order modes ($n > 300$), eigen-values rapidly increase with the mode number n due to energetically costly vibrations in the direction normal to the sphere surface. This effect appears to be more dramatic in phase M, while, for instance, in phase A, the structure of the head part (segments in contact with the sphere) is three-dimensional and allows stronger tangential vibrations.
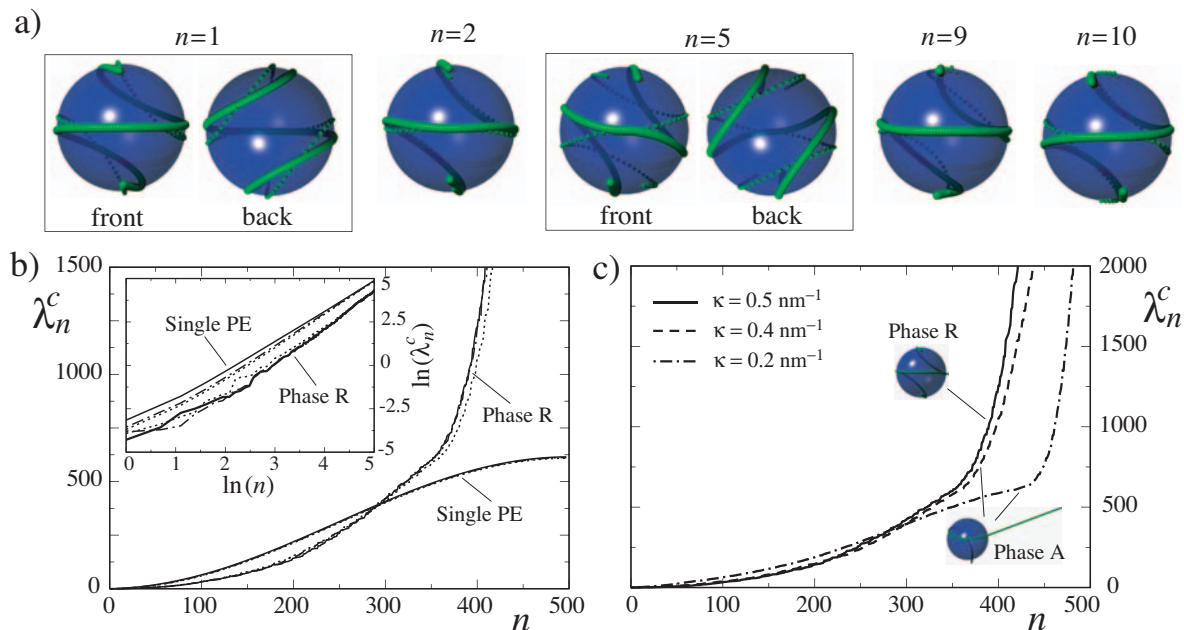
a)

b)

c)

Figure 5.6: a) Eigen-modes of chain fluctuations around the ground-state phase R (for $Z = 40$ and $\kappa = 0.5$ nm^{-1}). b) The fluctuations spectrum of phase R (with $Z = 40$) compared with that of an isolated PE chain for different inverse screening lengths $\kappa = 0.5$ (solid curve), 1 (dot-dashed curve) and 2 nm^{-1} (dotted curve). The inset shows the same graph for mode numbers $n < 150$ in logarithmic scale. c) The spectra for $\kappa = 0.2$ (dot-dashed curve) and 0.4 nm^{-1} (dashed curve), which belong to the symmetry class A, and for $\kappa = 0.5$ nm^{-1} (solid curve), which belongs to the symmetry class R. All spectra are obtained for $Z = 40$.

Fully wrapped phase R

In the fully wrapped phase R, the eigen-modes typically correspond to tangential vibrations for small n as shown in Figure 5.6a. Figure 5.6b shows the spectrum of fluctuations in phase R for $Z = 40$ and three different values of $\kappa = 0.5$, 1 and 2 nm^{-1}, which are compared with the spectrum of a single isolated PE chain in the same salt concentrations. The eigen-value spectrum differs drastically from the isolated PE chain and is quite insensitive to changes in salt concentration, which reflects the fact that the ground-state conformation varies weakly with the salt concentration.

In order to examine the general dependence of the eigen-values, λ_n^c, on the mode number, n, I compare the spectrum with that of a PE chain in the inset of Figure 5.6b, where all spectra are plotted on logarithmic scales for small n ($n < 150$). It is seen that for small n, the slopes of the complex and the isolated chain curves are almost the same, but they have different intercepts. Thus the surprising result is that for small n, the dependence of the spectrum of a complex in phase R to n is nearly the same as the dependence on n of the spectrum of a PE chain.

In Figure 5.6c, I show the spectrum for $\kappa = 0.2$ nm^{-1} and $\kappa = 0.4$ nm^{-1} with $Z = 40$, which both have the symmetry class of A, and for $\kappa = 0.5$ nm^{-1} with the same Z, which has the symmetry class of R. By increasing κ, the wrapping transition occurs between phase A and phase R; therefore the spectrum of phase A tends to that of phase R.

5.3.3 Fluctuations contribution

Now I will consider the fluctuations contribution to the complexation free energy. Recall that fluctuations contribute to the free energy via the second-order correction terms $\mathcal{F}_c^{(1)}$ and $\mathcal{F}_p^{(1)}$ as defined in Eqs. (5.23) and (5.24) for a free PE chain and a complex respectively. Note that the binding free energy $\Delta\tilde{\mathcal{F}} = \tilde{\mathcal{F}}_c - \mathcal{F}_p$, Eq. (5.11), is only due to internal degrees of freedom and may be written as

$$\Delta\tilde{\mathcal{F}} = \Delta\mathcal{H}^* + \Delta\mathcal{F}^{(1)}, \tag{5.27}$$

comprising adsorption energy due to the difference in ground-state energy of a complexed chain and a free PE chain,

$$\Delta\mathcal{H}^* = \mathcal{H}_c^* - \mathcal{H}_p^*, \tag{5.28}$$

and the fluctuations correction term,

$$\Delta\mathcal{F}^{(1)} = \mathcal{F}_c^{(1)} - \mathcal{F}_p^{(1)}, \tag{5.29}$$

which is a measure of the chain entropy loss upon complexation with the macroion. In what follows, I shall compare various contributions to the binding free energy as a function of salt concentration.

Figure 5.7a shows the ground-state energy contribution, $\mathcal{H}_c^*$, and the fluctuations contribution, $\mathcal{F}_c^{(1)}$, of a complex as a function of κ for fixed $Z = 40$. The inset shows the detailed behavior of $\mathcal{F}_c^{(1)}$ on logarithmic κ scales, where boundaries between different symmetry phases are included. The phase sequence is determined by minimizing the free energy $\mathcal{F}_c$ in the complexed phase. The shift of these phase boundaries as the Gaussian-fluctuations correction $\mathcal{F}_c^{(1)}$ is added is quite small.

As seen, for small to moderate salt concentrations, the fluctuations correction is smaller than the ground-state energy, but it becomes larger beyond a typically large value of $\kappa \simeq 3\,\text{nm}^{-1}$, meaning that the present saddle-point approximation, which considers small-amplitude fluctuations around the ground state, breaks down at very high salt concentration. The experimentally relevant regime of salt concentrations (corresponding to $\kappa \sim 0.5 - 1.5\ \text{nm}^{-1}$) is, however, within the regime of validity of the saddle-point approximation. The results in the inset indicate that $\mathcal{F}_c^{(1)}$ exhibits non-monotonic and quite complicated behavior with salt concentration. This behavior results from an interplay between the screening of electrostatic interactions for growing salt (which enhances chain fluctuations as discussed for a free PE chain in Figure 5.2c) and the structural changes of the complex due to the chain wrapping process (which suppresses chain fluctuations).

In the expanded chain phase F, the fluctuations contribution to the free energy monotonically decreases with increasing salt concentration until it undergoes a discontinuous transition to the planar asymmetric phase M at about $\kappa = 0.08\ \text{nm}^{-1}$. $\mathcal{F}_c^{(1)}$ takes its global minimum close to the continuous-transition boundary with the asymmetric phase A at about $\kappa = 0.12\ \text{nm}^{-1}$ (it also has a local maximum close to the boundary with phase F). Therefore, the asymmetric phases A and M at about $\kappa = 0.12\ \text{nm}^{-1}$ exhibit larger *entropic* contribution as compared with other ranges of the salt concentration. In other words, fluctuations are more enhanced in this region. Note that as salt concentration increases, the ground state energy monotonically decreases with κ (main plot in Figure 5.7a) as more chain segments become adsorbed on the macroion. But the decreasing behavior of $\mathcal{F}_c^{(1)}$ with κ indicates that the entropy of fluctuations *increases* until the complex undergoes a transition to phase
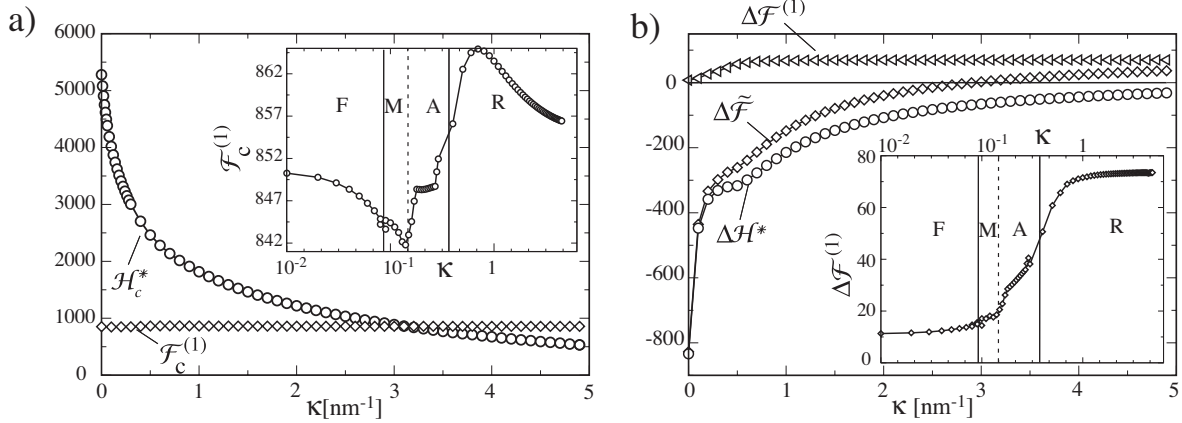
Figure 5.7:   a) Ground-state and fluctuations contribution $\mathcal{H}_c^*$ and $\mathcal{F}_c^{(1)}$ to the complex free energy as a function of κ for $Z = 40$. The inset shows $\mathcal{F}_c^{(1)}$ on a logarithmic κ scale. b) Binding free energy $\Delta\mathcal{F} = \Delta\mathcal{H}^* + \Delta\mathcal{F}^{(1)}$ together with the separate ground-state and fluctuations contributions, $\Delta\mathcal{H}^*$ and $\Delta\mathcal{F}^{(1)}$, as a function of κ for $Z = 40$. The inset shows $\Delta\mathcal{F}^{(1)}$ on a logarithmic κ scale. Solid (dashed) vertical lines show discontinuous (continuous) transitions between different complex symmetry phases.

A. However, as κ increases within phases A and R, the free energy of fluctuations, $\mathcal{F}_c^{(1)}$, increases and reaches a global maximum around $\kappa \simeq 0.7$ nm^{-1} in phase R.[1] This reflects a *decreasing* fluctuations entropy in this regime, since the structural changes of the chain lead here to a tightly wrapped conformation around the sphere. By further increasing the salt concentration in phase R, the chain structure remains almost unchanged (until very large values $\kappa \simeq 10$ nm^{-1} where it again undergoes a dewrapping transition [48, 49]). The growing salt screening leads to stronger entropic effects (smaller free energy) from fluctuations that explains the decreasing behavior of $\mathcal{F}_c^{(1)}$ in phase R.

Now I turn to the binding free energy, $\Delta\tilde{\mathcal{F}} = \tilde{\mathcal{F}}_c - \mathcal{F}_p = \Delta\mathcal{H}^* + \Delta\mathcal{F}^{(1)}$, which can be calculated numerically using Eqs. (5.28) and (5.29) as a function of the salt concentration. The contribution from the ground-state energy differences between complex and free chain, $\Delta\mathcal{H}^* = \mathcal{H}_c^* - \mathcal{H}_p^*$, and the difference in fluctuations correction, $\Delta\mathcal{F}^{(1)} = \mathcal{F}_c^{(1)} - \mathcal{F}_p^{(1)}$, are separately shown in Figure 5.7b as a function of κ together with the total binding free energy $\Delta\tilde{\mathcal{F}}$ for a fixed sphere charge $Z = 40$. The ground-state contribution $\Delta\mathcal{H}^*$ is dominant and highly negative at small to moderate salt, thus favoring the complexation due to electrostatic attraction between the sphere and the PE chain. The fluctuations contribution $\Delta\mathcal{F}^{(1)}$ on the other hand is positive, reflecting the conformational entropy loss as the PE binds and wraps around the sphere. Note that the binding or adsorption *energy* decreases in magnitude for increasing salt screening, while the fluctuations contribution, $\Delta\mathcal{F}^{(1)}$, tends to a finite constant value (in the *neutral* limit $\kappa \to \infty$, the PE chain dewraps to a straight line conformation and thus both contributions tend to zero). For larger κ, fluctuations dominate and render the saddle-point approach an invalid approximation.

The results for $\Delta\mathcal{F}^{(1)}$ in the inset of Figure 5.7b indicate that the entropy loss upon complexation of a free PE chain with macroion remains almost *constant* with increasing

---

[1]It is noteworthy that the plateau region observed in phase A (Figure 5.7, inset) corresponds to the values where the PE chain makes its second turn around the sphere.
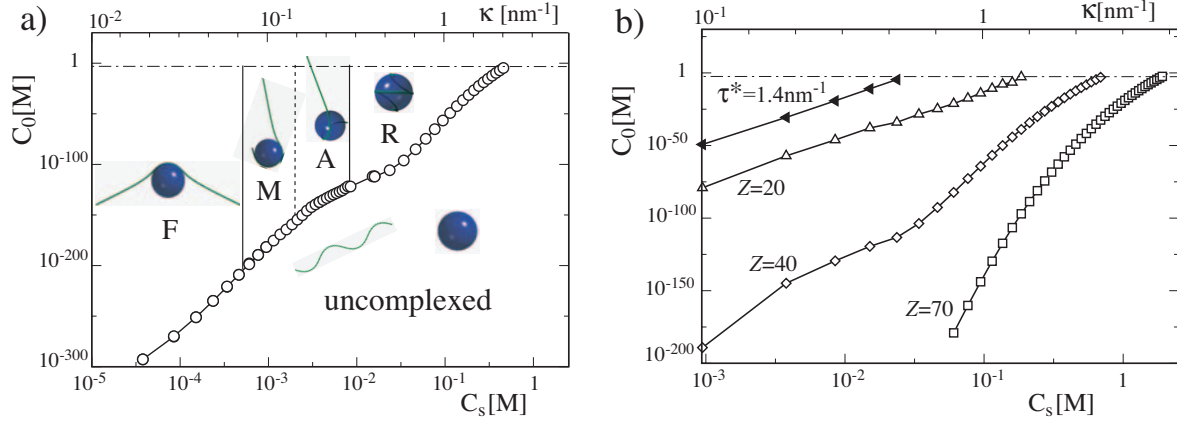
Figure 5.8: a) Diagram exhibiting complexed and uncomplexed regimes as a function of salt concentration C_s and PE/macroion concentration C_0 (in molar units M=mol/l) for sphere charge $Z = 40$. b) Complexation diagram for various Z (open symbols) at fixed $\tau = 5.88$ nm^{-1}, and for renormalized PE charge density $\tau^* = 1.4$ nm^{-1} (filled symbols) with fixed $Z = 40$. The horizontal dot-dashed line represents the maximum macroion concentration $C_0^{\text{max}} = 1/V_0$, where $V_0 = 4\pi R_s^3/3$ is the sphere volume; for $R_s = 5$ nm, one has $C_0^{\text{max}} \simeq 3.2$ mM.

salt concentration in the expanded-conformation phase F and in the fully wrapped phase R (note that $\Delta\mathcal{F}^{(1)}$ is obviously larger in the latter case). This is expected since the shape of the ground state in phase F is quite close to that of a free chain for small κ, and that in phase R the ground state configuration is quite insensitive to changes in salt concentration. Roughly speaking, the saturated value for large $\kappa > 1$nm^{-1} in phase R may be regarded as the conformational entropy difference of a *neutral* semi-flexible chain when it is free and when it is constrained in a wrapped state around a sphere.

5.4   Complexation phase diagram

Given the binding free $\Delta\tilde{\mathcal{F}}$ calculated in the preceding section, one can use the law of mass action derived in Section 5.2 to determine the PE-macroion "reaction"equilibrium and the overall phase behavior of a solution of PEs and macroions within the present model.

The reaction equilibrium between complexed and uncomplexed chains and spheres does of course not give rise to a true phase transition in the system. I heuristically define the boundary between complexed and uncomplexed regimes to occur when half of the spheres have reacted to complexes. From the law of mass action Eq. (5.16) this complexation boundary follows as

$$C_0 = \frac{2\,e^{\Delta\tilde{\mathcal{F}}}}{V_0}, \tag{5.30}$$

where $\Delta\tilde{\mathcal{F}}$ is obtained using Eqs. (5.23) and (5.24). In Figure 5.8a, I show this line for fixed sphere charge $Z = 40$, which separates the regime dominated by uncomplexed spheres and PEs (lower region) from the complexation regime (upper region). The complex regime itself consists of the four different symmetry phases, including the expanded phase F at low salt and the fully wrapped phase R at elevated salt, in qualitative agreement with experiments

[103, 104] and previous calculations [48, 49]. In particular, the transition between the fully and partially wrapped R and A phases occurs at a salt concentration of about $C_s = 10$ mM, which is close to the experimental value [103, 104].

The calculated complexation line agrees with the experimental trend obtained for NCP solutions [103, 104], that is for higher salt, a larger sphere concentration is required to form complexes. The slope of this line is however larger than the experimental value. In fact, the complexation boundary varies with the effective parameters of the present model, that is the sphere charge valency and the PE linear charge density, which vary depending on the surrounding condition (e.g., charge-regulation and charge-renormalization effects). So far I have chosen the linear charge density of the PE chain consistent with maximum linear charge density of DNA, i.e. $\tau = 5.88$ nm^{-1}, and typically used $Z = 40$ for the macroion (histone) charge valency. As discussed before, the maximum charge renormalization occurs for a free infinite rod-like PE chain in the zero-salt limit, where the standard Manning result gives the effective PE charge of $\tau^* = 1/\ell_B \simeq 1.4$ nm^{-1} [55] for monovalent counterions as considered here.

In Figure 5.8b, I show the results of the present model for $\tau = 5.88$ and various Z, and also for the maximally renormalized PE charge density, $\tau = 1/\ell_B$, and $Z = 40$. As seen, the complexation boundary becomes flatter for decreasing sphere charge Z (open symbols). In fact, the appropriate value of Z could be fitted by matching the experimental complexation boundary. The filled symbols in Figure 5.8b obtained for sphere charge $Z = 40$ and the PE linear charge density $\tau^* = 1.4$ nm^{-1} also show a reduced slope when compared with curves obtained using the bare PE charge (Figure 5.8a). Since the renormalized PE charge is for finite salt in between τ and τ^* [56], the resulting complexation line constitutes an upper limit of the effects expected in the presence of non-linear charge-renormalization.

5.5   Conclusion and discussion

In this chapter, I present an extensive analysis of fluctuations effects on the structure and phase behavior of strongly coupled polyelectrolyte-macroion complexes. For these complexes, the adsorption energy is large and fluctuations around the ground-state path of the PE chain on the macroion are relatively weak, such that a normal-mode analysis based on a saddle-point approximation can be used to characterize the chain fluctuations. These results therefore extend the ground-state analysis considered in Chapter 3 and also in previous works [48, 49].

As a main result, I have determined the global thermodynamic phase behavior of a solution of PEs and macroions that includes both the complexation- and decomplexation-dominated phases. This is accomplished by evaluating entropic effects due to chain fluctuations. As shown, the association (or complexation) equilibrium constant of a PE-macroion solution can be determined from a law of mass action in terms of the binding (or complexation) free energy of a PE-macroion complex, which comprises the adsorption energy of the chain on the sphere as well as the chain entropy loss upon complexation. This quantity can be obtained in terms of the spectrum (eigen-values) of fluctuations of a free chain and a complexed chain, which are determined here explicitly for parameters corresponding to a DNA-histone system (in nucleosomal core particles).

The behavior of chain fluctuation spectrum is analyzed for different salt concentrations spanning various symmetry classes of a PE-macroion complex. At low salt, the complex ground state adopts an expanded conformation with two open arms for the PE chain, which

thus exhibits an eigen-value spectrum close to that of a free PE chain. As the salt concentration increases, fluctuations become enhanced due to stronger screening of electrostatic interactions (between chain segments and chain with the sphere). Meanwhile, the conformational symmetries of a complex vary and affect the fluctuations in different ways: for increasing salt, first phase F undergoes a discontinuous transition to the planar asymmetric phase M, which then undergoes a continuous transition to the non-planar asymmetric phase A and eventually to the fully wrapped phase R. This wrapping process suppresses chain fluctuations and therefore competes with the screening effects. As a result, strongest fluctuation effects (largest complex entropy due to chain fluctuations) are obtained at the boundary between phases M and A. The wrapping process dominates at larger values of salt concentration leading to a reduced fluctuations entropy in phase R. In both phases R and F, the PE chain displays an almost constant entropy loss upon complexation with the sphere.

The present results for the complexation reaction equilibrium agree qualitatively with recent experiments on NCP solutions [103, 104] indicating larger macroion concentration to form complexes at higher salt concentration. In agreement with previous results, PEs and macroions react to tightly wrapped complexes at moderate salt concentration (about 10 mM monovalent salt), while at low salt, they form expanded complex states. However, as I show, the effective parameters within the present model, namely, the macroion and the PE charge can influence the values of the equilibrium constant, or in other words, the slope of the complexation equilibrium line, although the general trend remains still the same, suggesting that non-linear effects (such as counterion condensation [186, 187, 189, 71]) do not induce qualitative changes. Non-linear effects however, become small at moderate to high salt (e.g., at about the inverse screening length $\kappa \sim 1$ nm^{-1}), where the Debye-Hückel approximation used here is expected to become accurate. Examining non-linear effects such as counterion-release [54, 55] on a more systematic level forms an interesting direction for future research.

The analysis of reaction equilibria in terms of a normal-mode analysis holds potential for all strongly bound and kinetically trapped complexes, where direct simulation methods are hampered. It can also be performed in the framework of Molecular Dynamics or *ab-initio* simulation techniques and thus be modified to include solvent effects and more realistic force-fields as well.

Chapter 6

Inter-complex Interactions

I investigate the effective interaction between two polyelectrolyte-macroion complexes within the ground-state approximation. It will be shown that at small distances, the complexes become highly correlated due to structural changes of the polyelectrolyte chains which leads to an asymmetric binding state (where positively charged patches on one complex match up with negatively charged patches on the other complex) or a bridging state (where one polyelectrolyte chain bridges between the two complexes). This gives rise to a strong attraction between complexes and thus a negative virial coefficient associated with the inter-complex interaction at intermediate salt concentrations within the range where stable complexes are formed. These findings agree qualitatively with recent experiments on nucleosome core particles. I shall demonstrate that a simple screened monopole-dipole model reproduces these results.

The adsorption of polyelectrolytes (PEs) on oppositely charged spherical macroions is of interest for such diverse applications as fabrication of polymeric hollow shells [19] and calcium-incrustation-inhibition during the washing process [21]. An interesting feature is that adsorbed PEs can act both as stabilizing and destabilizing agents in charged colloidal suspensions depending on the effective interactions mediated by the adsorbed PE layer between the resulting PE-colloid complexes. A number of experimental studies [23, 29, 24, 25, 36, 30] investigated the structure and stability of these complexes and elucidated the conditions (in terms of salt concentration, polymer length and its charge fraction) under which complexes form, but also demonstrated the importance of controlling the interactions between complexes. One important question is whether it is possible to have stable complexes which repel each other and how to control the inter-complex interaction without loosing the stability of the complexes themselves. In the preceding chapter, I showed that highly charged macroions and PEs can associate into complexes that form a thermodynamically stable phase in the *low* concentration regime. In this chapter, I will use the chain-sphere model to address the interactions between these complexes which come into play at *high* concentrations of macroions.

The interaction between complexes has also been considered in previous works using analytical methods for the case of many spheres bound to a single PE [45, 68] and for a single PE bridging two spheres [206]. A system of two spheres and two PEs was recently investigated using simulations [207] and field theoretic methods [208], while large-scale simulations tackled the problem of many spheres with a number of PEs in the presence of salt ions [41, 42, 47]. (Recent simulations have also considered the role of semi-flexible charged chains modeled as histone tails bridging between two oppositely charged spheres [157].) An interesting result

is that for strongly coupled PE-macroion complexes, the inter-complex interactions may become attractive due to structural correlations induced by the highly ordered polymer layer on macroion surfaces [66, 69, 64, 67]. Given that such complexes are typically highly overcharged by the adsorbed PE, this result thus indicates an effective correlation-induced attraction between two *like-charged* objects which constitutes a general field of high interest in current investigation of charged systems [197, 198, 199, 200, 201]. Another related mechanism, which has been observed in the simulation of highly charged PEs and macroions [47, 41, 42, 208], is the PE bridging between two or more macroions that results in an effective attraction between complexes as well. Both these mechanisms evidently occur at sufficiently high concentration of complexes, where a phase instability has been predicted to occur indicating a phase separation in the system due to the formation of a large aggregate of complexes [41, 42, 66, 69, 64, 67].

On the other hand, the interaction between strongly coupled PE-macroion complexes has been considered experimentally in the biologically relevant context of nucleosome core particles (NCPs) [212, 213]. It has been shown that the effective interaction between NCPs can become attractive giving rise to a negative second virial coefficient for the NCP solution. In this case, however, the underlying mechanism for attraction between two NCPs is not yet completely understood and the role of electrostatic interactions and specific effects such as histone tails is yet to be elucidated [157].

Motivated by these observations, I shall study two PE-macroion complexes using the chain-sphere model and within the ground-state approximation, where fluctuations around the optimal PE configurations are neglected. Using parameters relevant for DNA-histone complexes, I determine the interaction between complexes for the full range of sphere distances and salt concentrations taking into account PE configurational changes and thereby, I calculate the second-virial coefficient associated with the complex-complex interaction. It will be demonstrated that *attractive* inter-complex forces can result from an interplay between electrostatic contributions and configurational changes of the polyelectrolyte chain, which leads to structural correlations between two complexes at sufficiently small separations. As will be shown, the attraction (or correlation) mechanism includes *asymmetric binding* of the two complexes or *chain bridging* between the complexes depending on system parameters such as macroion charge and the salt concentration. As a result, the second virial coefficient becomes negative at intermediate salt concentrations (displaying also a minimum at about physiological salt concentration), which qualitatively agrees with recent experiments on NCPs [213].

The present results thus predict precipitation of PE-macroion complexes for intermediate salt concentrations and at sufficiently high complex concentrations. I will also determine the repulsion-dominated regime, where complexes are formed and stay solubilized in solution. Note that these two regimes occur in different salt concentrations and have similar features to the salting in and salting out phenomena [203]. I shall then present a simplified phenomenological model in terms of the complex net charge and its dipole moment, which reproduces these findings and can be used for predicting the phase behavior of more general systems.

6.1   The two-complex model

I shall employ a chain-sphere model similar to what was introduced in Chapter 2, in which the PEs are modeled as semi-flexible chains of length $L = 49.64$ nm (corresponding to 146 base

pairs of DNA) with a bare mechanical persistence length of $\ell_{\mathrm{p}} = 30$ nm (which corresponds to the persistence length in the absence of electrostatic interactions as realized at very high salt concentrations [48, 49]). The spheres are semi-rigid with an effective radius $R_{\mathrm{s}} = 5$ nm (roughly equal to the sum of the histone and DNA radii) and valency Z. The PE line charge density is fixed here at $\tau = 2/0.34$ nm^{-1} corresponding to maximal dissociation of two charges per DNA base pair. I use for all electrostatic interactions the linearized Debye-Hückel theory as explained in Chapter 2. The neglect of nonlinear effects connected with counter-ion condensation makes quantitative comparison with experiments questionable at low salt concentrations; however, charge renormalization was shown to leave the qualitative features of the complexation phase diagram unchanged [48, 49] (see also Chapters 2 and 5).

I consider two polyelectrolyte-macroion complexes at a centre-to-centre distance of D from each other. The effective Hamiltonian of this system may be written as

$$\mathcal{H}_{\mathrm{tot}} = \sum_{i=1}^{2} \mathcal{H}_p[\mathbf{r}_i] + \sum_{i,j=1}^{2} \mathcal{H}_{pm}[\mathbf{r}_i, \mathbf{R}_j] + \mathcal{H}_{mm}(\mathbf{R}_1, \mathbf{R}_2) + \mathcal{H}_{pp}[\mathbf{r}_1, \mathbf{r}_2], \qquad (6.1)$$

where $\mathcal{H}_p$ is the (electrostatic and mechanical bending) self-energy of the PE chain (in units of $k_{\mathrm{B}}T$) in both complexes (labeled by $i, j = 1, 2$),

$$\mathcal{H}_p[\mathbf{r}_i] = \frac{\ell_{\mathrm{p}}}{2} \int_0^L \mathrm{d}s\, [\ddot{\mathbf{r}}_i(s)]^2 + \tau^2 \ell_{\mathrm{B}} \int_0^L \mathrm{d}s \int_s^L \mathrm{d}s' \frac{e^{-\kappa|\mathbf{r}_i(s) - \mathbf{r}_i(s')|}}{|\mathbf{r}_i(s) - \mathbf{r}_i(s')|}, \qquad (6.2)$$

and $\mathcal{H}_{pm}$ includes the interaction between the PE chains and the spheres, i.e.

$$\mathcal{H}_{pm}[\mathbf{r}_i, \mathbf{R}_j] = -\frac{Z\tau\ell_{\mathrm{B}}}{1 + \kappa R_{\mathrm{s}}} \int_0^L \mathrm{d}s \left[\frac{e^{-\kappa(|\mathbf{r}_i(s) - \mathbf{R}_j| - R_{\mathrm{s}})}}{|\mathbf{r}_i(s) - \mathbf{R}_j|} - A e^{-(|\mathbf{r}_i(s) - \mathbf{R}_j| - R_{\mathrm{s}})/\alpha} \right], \qquad (6.3)$$

where $\mathbf{r}_i(s)$ specifies the configuration of the PE chain in complex i and $\mathbf{R}_j$ gives the position of the sphere center in complex j. The first term in Eq. (6.3) describes the electrostatic PE-sphere attraction, the second term is a soft short-ranged PE-sphere repulsion with $\alpha = 0.02$ nm and $A = 0.012$ nm^{-1} (see Chapter 2 and Appendix E for details). Finally the electrostatic repulsion between the two PEs is given by

$$\mathcal{H}_{pp}[\mathbf{r}_1, \mathbf{r}_2] = \tau^2 \ell_{\mathrm{B}} \int_0^L \mathrm{d}s \int_0^L \mathrm{d}s' \frac{e^{-\kappa|\mathbf{r}_1(s) - \mathbf{r}_2(s')|}}{|\mathbf{r}_1(s) - \mathbf{r}_2(s')|} \qquad (6.4)$$

and between the two spheres at a separation $D = |\mathbf{R}_1 - \mathbf{R}_2|$ by (Appendix B)

$$\mathcal{H}_{mm}(\mathbf{R}_1, \mathbf{R}_2) = \left(\frac{Z e^{\kappa R_{\mathrm{s}}}}{1 + \kappa R_{\mathrm{s}}} \right)^2 \ell_{\mathrm{B}} \frac{e^{-\kappa D}}{D}. \qquad (6.5)$$

Similar to the calculation made for a single complex, I focus on the ground-state properties of this system, which is expected to be valid for chain lengths not much longer than the persistence length as is the case in the present study. For a given set of parameters, I numerically determine the ground-state (or optimal) PE configurations that minimize the total energy $\mathcal{H}_{\mathrm{tot}}$ using numerical minimization methods on a discretized model of the chains (the number of discretization points for each of the PE chains is taken here as $N = 250$). The details of the numerical minimization method is explained in Chapter 2 and Appendix A.3. Hence, the configurational changes of the chain as well as the effective interaction between the optimal complex configurations are determined as a function of the distance between spheres, D, and for given sphere charge Z and inverse Debye screening length κ.
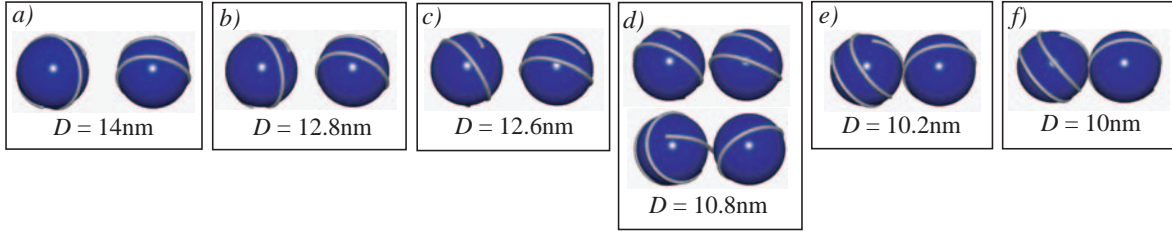
Figure 6.1:   Ground-state configurations for sphere charge $Z = 100$ and inverse screening length $\kappa = 2$ nm^{-1} for various sphere distances D. At $D = 12.8$ nm the symmetry between the two PEs is continuously broken, at $D = 10.8$ nm a discontinuous bridging transition takes place (d), where the two shown configurations coexist.

6.2   Configurations and symmetries

In Figure 6.1, I show a few ground-state configurations for fixed sphere charge ($Z = 100$) and fixed salt concentration (with $\kappa = 2$ nm^{-1}) for varying sphere-sphere distance. For large distances, the complexes exhibit the same chain configuration as in the case of a single isolated complex (Chapter 2), since the surface separation between spheres is much larger than the screening length ($\kappa^{-1} = 0.5$ nm in the Figure). At $D = 12.8$ nm, the symmetry between the conformation of the chains on both spheres is broken (i.e. the two PE conformations are dissimilar) and for even smaller distances $D < 10.8$ nm, a bridging conformation is found in which one PE is bound to both spheres. Note that at $D = 10.8$ nm, the non-bridging and bridging states coexist, i.e. they are both obtained as the optimal configuration of the system with the same energy.

The configurational changes of the chains in fact indicate a series of configurational phase transitions induced by mutual interactions between complexes, which can be characterized by considering suitable order parameters as will be discussed below. In general, one can distinguish a *symmetric phase*, where both complexes show the same structure, from an *asymmetric phase* with dissimilar structures for the two complexes. An extreme example of such symmetry breaking is the *bridging phase*.

6.2.1   Order Parameters

To categorize the conformational changes upon approach of the complexes, I define the order parameter

$$\Delta P_i = |\mathbf{P}_i| - |\mathbf{P}_0| \tag{6.6}$$

for each complex $i = 1, 2$, which is the difference between the (in general D-dependent) dipole moment of one complex,

$$\mathbf{P}_i = \tau \int_0^L \mathrm{d}s\, (\mathbf{r}_i(s) - \mathbf{R}_i), \tag{6.7}$$

and that of an *isolated* complex, $\mathbf{P}_0$. By construction, ΔP_i is zero when D is infinity. In Figure 6.2a-c I show ΔP_1 and ΔP_2 for fixed sphere charge $Z = 100$ and various salt concentrations as a function of the sphere distance D. One observes two symmetric phases denoted by S and S$'$, where $\Delta P_1 = \Delta P_2$, and an asymmetric phase denoted by A, where $\Delta P_1 \neq \Delta P_2$. Note that in the symmetric phase S, one has $\Delta P_1 = \Delta P_2 = 0$ because the structure of each complex is the
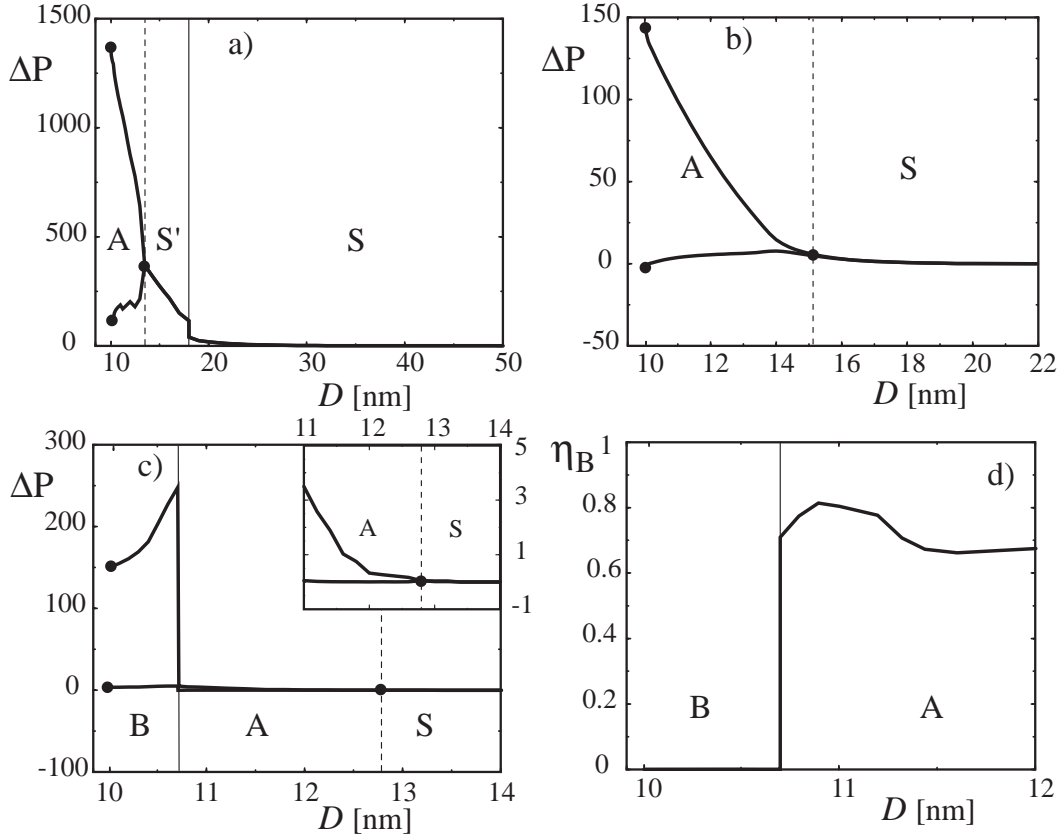
Figure 6.2: Dipole moments ΔP_i, Eq. (6.6), of both complexes for fixed sphere charge $Z = 100$ as a function of the sphere separation D for inverse screening lengths a) $\kappa = 0.16$ nm^{-1}, b) $\kappa = 0.40$ nm^{-1}, and c) $\kappa = 2.0$ nm^{-1}. d) Bridging order parameter η_B for $Z = 100$ and $\kappa = 2.0$ nm^{-1}.

same as the structure of a single isolated complex, but in phase S′, one has $\Delta P_1 = \Delta P_2 \neq 0$ since the inter-complex interaction is sufficiently large to perturb their internal structure.

In order to quantify the amount of bridging, I define the bridging order parameter as

$$\eta_B = \prod_{i=1}^{2} K_i(\mathbf{R}_1, \mathbf{R}_2) K_i(\mathbf{R}_2, \mathbf{R}_1), \tag{6.8}$$

with $K_i(\mathbf{R}_\alpha, \mathbf{R}_\beta)$ being defined as

$$K_i(\mathbf{R}_\alpha, \mathbf{R}_\beta) = |(\mathbf{r}_i(0) - \mathbf{R}_\alpha)^2 - (\mathbf{r}_i(L) - \mathbf{R}_\beta)^2|/D^2. \tag{6.9}$$

This quantity will be zero only if one end of a given PE chain lies on one sphere while the other end is located on the other sphere, thus forming a bridge. In all other cases η_B is finite, and it thus allows to identify the bridging phase B. In Figure 6.2d, I show η_B as a function of the center-to-center distance D for $Z = 100$ and $\kappa = 2$ nm^{-1}. The discontinuous bridging transition at $D = 10.8$ nm is clearly recognized.

Note that the transitions between different phases may be continuous or discontinuous (as indicated in the figure with dashed and solid vertical lines respectively), which reflect
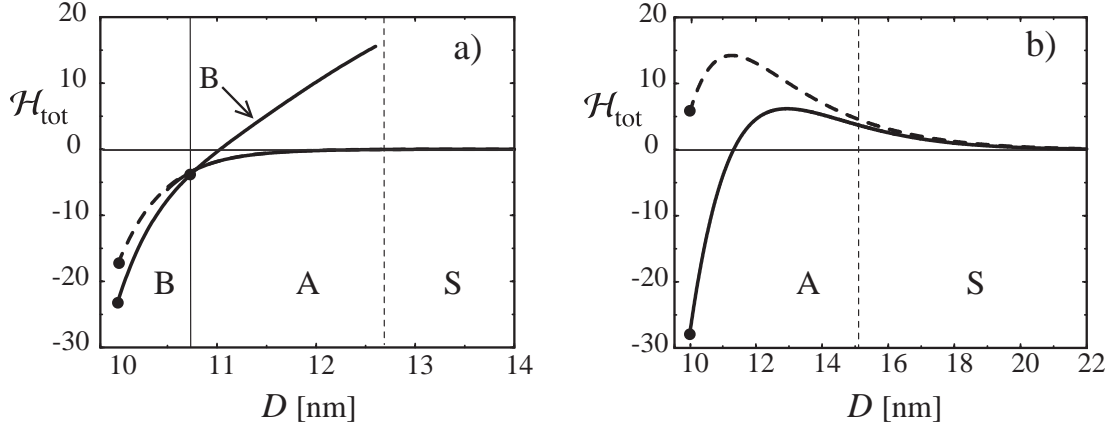
Figure 6.3: Energy of the two-complex system (in units of $k_{\mathrm{B}}T$) within full optimization (solid line) and constrained, rotational minimization [210] (broken line) for $Z = 100$ and a) $\kappa = 2$ nm^{-1} and b) $\kappa = 0.40$ nm^{-1}. In a) the transition between phases B and A at $D = 10.8$ nm is discontinuous, while the transition between phases S and A is continuous. In b) the transition between the symmetric S and asymmetric A states is continuous and the bridging phase is not present.

continuous or discontinuous changes in the order parameters. A discontinuous transition can be identified also from the effective Hamiltonian of the system, Eq. (6.1), which exhibits two stable minima corresponding to *coexistence* of two different optimal structures (see below).

6.2.2   Interaction energies

The interaction energy as a function of distance D for $Z = 100$ and $\kappa = 2$ nm^{-1} is shown in Figure 6.3a and for $\kappa = 0.4$ nm^{-1} in Figure 6.3b. Here the values at $D = \infty$ (two isolated complexes) have been subtracted as the reference state energy. Note that the energies refer to the minimal value of the two-complex Hamiltonian (6.1) as obtained from the numerical minimization method. The solid lines denote results from a *full optimization* of the PE configurations, while the broken lines denote the results from *constrained optimizations* where the PE conformation on each sphere is fixed to the one in the isolated complex case ($D = \infty$) and only the orientation of the complex may vary.

Figure 6.3a corresponds to configurations at large salt concentration that are visualized in Figure 6.1. The discontinuous bridging transition at $D = 10.8$ nm is clearly identified by the crossing of the energy of the bridging and asymmetric phases. The bridging phase is stable for smaller separation and becomes meta-stable for larger separation. The meta-stable solution of the asymmetric phase disappears at separations smaller than $D = 10.6$ nm. Note also that here the difference between the rotationally constrained minimization (broken line) and the unconstrained unbridged energy is small and unresolved at the resolution of the figure. Both methods give a strongly attractive interaction at small distances, although different mechanisms are involved, that is bridging within the full minimization scheme and asymmetric binding within the constrained minimization.

For small salt concentration (Figure 6.3b), it is seen that the bridging phase B disappears, but an attractive inter-complex interaction still occurs within the asymmetric phase A at small separations. The transition between the symmetric (S) and asymmetric (A) phase
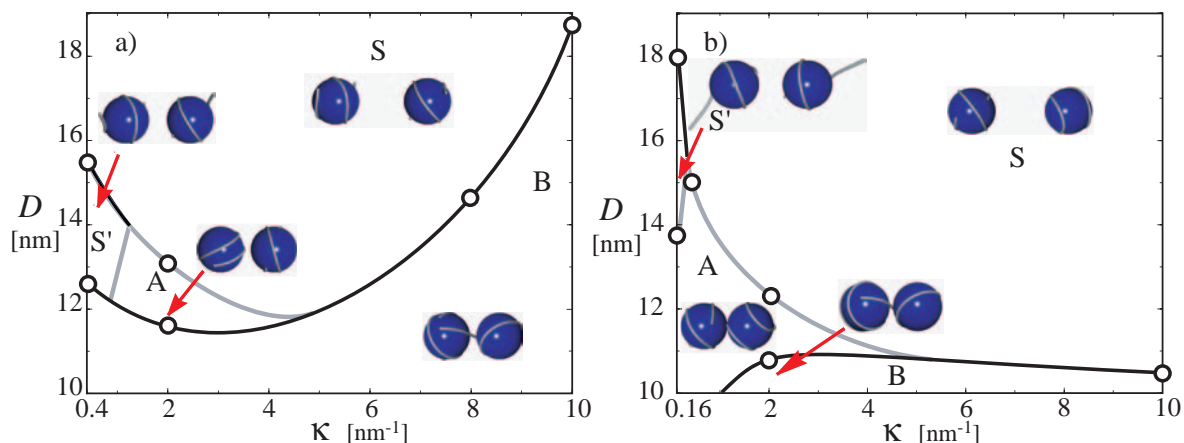
Figure 6.4: Phase diagram for two PE-sphere complexes as a function of the inverse Debye screening length κ and spheres center-to-center distance D for a) sphere charge $Z = 40$ and b) $Z = 100$, featuring symmetric, S and S′, asymmetric, A, and bridging phases, B. Black (gray) lines denote discontinuous (continuous) phase boundaries. Shown are actual configurations calculated in the respective phases.

at $D = 16$ nm is continuous. Here both full optimization and constrained optimization lead to an attractive force between two complexes, though only the former case (solid line) gives a negative effective interaction energy contribution which at contact is of the order of $\mathcal{H}_{\text{tot}} = -29$. The attraction in this case is merely due to changes (structural correlations) in the relative orientation of the chains, representing an asymmetric binding mechanism (see also Figure 6.1).

I also considered the possibility of complexes consisting of two spheres and one PE or two spheres with more than two PEs. Since the binding energy of a single PE-sphere complex is $\mathcal{H} = -319$ in Figure 6.3a and $\mathcal{H} = -1112$ in Figure 6.3b, it is clear that unbinding of a PE from the complex is not favored. Likewise, adsorption of an additional PE is unfavorable due to the high negative net charges of the complexes. The present results should therefore be relevant to mixtures of spheres and PEs of not too different and not too low concentrations.

6.3 Phase diagram

I summarize the structural results in the $D - \kappa$ phase diagrams shown in Figure 6.4 for two sphere charges $Z = 40$ (a) and $Z = 100$ (b). Results from constant-κ scans are denoted by open circles, the lines are guides to the eyes. The continuous (discontinuous) transitions between different phases is indicated in the figure by gray (black) lines. The general trends that emerge are as follows: i) at large sphere separations the symmetric phase S prevails, ii) at small distances the bridging phase B is stable at intermediate to large salt concentration, and iii) at intermediate distances and predominantly at intermediate to small salt concentrations, small κ, the asymmetric phase A is found. For very small salt concentration, i.e. for long-ranged Coulomb interactions, the second symmetric phase S′ appears, in which the conformation of PE chains are similar, but each complex exhibits a configuration different from that of an isolated complex with a large relative dipole moment (caused by extending PE tails) as shown in Figure 6.4. It is important to keep in mind that individual complexes are stably
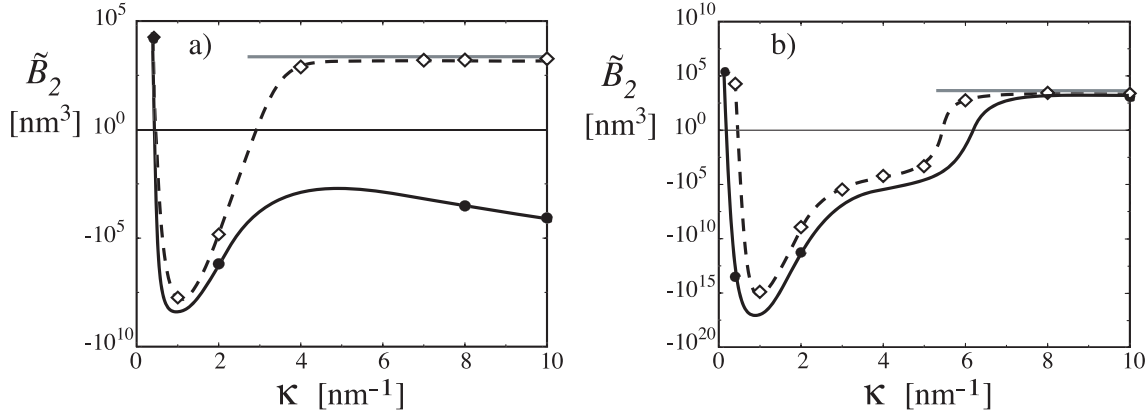
Figure 6.5: The rescaled second virial coefficient $\tilde{B}_2 = B_2(1 + |B_2|)/|B_2|$ as a function of κ a) for $Z = 40$, b) for $Z = 100$. Shown are results for the full optimization (solid lines) and rotational constrained optimization (broken lines). Horizontal gray lines denote the hard-core limit.

wrapped in the salt range 0.42 nm$^{-1} < \kappa < 10.0$ nm^{-1} (0.16 nm$^{-1} < \kappa < 25.2$ nm^{-1}) for $Z = 40$ ($Z = 100$) and also show a complex evolution of morphology as the salt concentration is changed (Chapters 2 and 3) [48, 49].

6.4   Second virial coefficient

As already seen from the optimal configurations in Figures 6.1 and 6.4, two chain-sphere complexes can become highly coupled at small separations in the bridging and asymmetric phases. In these regimes, PE chains on different spheres adapt their orientation and conformation in such a way that opposite charges from different complexes face each other. This reflects structural correlations between complexes at small distances, which emerge as a result of the inter-relation between electrostatic and bending contributions as the system finds its optimal (ground-state) configuration. These effects lead to an effective *attraction* between the two complexes at small distances as seen from the interaction energy curves in Figure 6.3. Note that both complexes are typically highly overcharged (e.g., with a total negative charge of up to $200e$ for $Z = 100$ given the DNA charge density $\tau = 5.88$ nm^{-1}). The present results therefore resemble the attraction mechanism obtained for like-charged macroions in the strong-coupling limit, which arises from structural correlations in the counterionic layers on opposite macroion surfaces [198, 199, 69]. These effects can induce phase instability in solutions of PE-macroion complexes at sufficiently high concentration [41, 42, 66, 69, 64, 67] and may lead to a negative second virial coefficient for the solution [212, 213].

Thus, in the final step, I calculate the second virial coefficient B_2 associated with the inter-complex interaction, which is defined as

$$B_2 = \frac{2}{3}\pi(2R_s)^3 + 2\pi \int_{2R_s}^{\infty} dD\, D^2(1 - e^{-\mathcal{H}_{\text{tot}}(D)}). \tag{6.10}$$

The first term in Eq.(6.10) is the hard-core contribution. The second term is due to inter-complex electrostatic interaction, $\mathcal{H}_{\text{tot}}(D)$, which is obtained by numerical optimization of the chain configuration at a given D as discussed before. The connection with the osmotic

pressure P of a solution of PE-macroion complexes (such as nucleosome core particle [213]) of concentration C_c is furnished by the relation (see Appendix C.1)

$$\frac{P}{k_{\mathrm{B}}T} = C_c + B_2 C_c^2 + \mathcal{O}(C_c^3). \tag{6.11}$$

In the limit of large salt concentration, the electrostatic contribution disappears and B_2 tends to the purely hard-core result. On the other hand, for vanishing salt concentration, the integral in Eq. (6.10) diverges. Therefore, since B_2 takes very large negative and positive values, I present the rescaled quantity $\tilde{B}_2 = B_2(1 + |B_2|)/|B_2|$ (on a logarithmic scale for the function in the parentheses) in Figure 6.5 for a) $Z = 40$ and b) $Z = 100$. The solid lines are obtained by full minimization of the energy functional (where thus the internal PE conformation changes as the sphere separation decreases), and the broken lines show the results from the constrained minimization (where the PEs are fixed to the conformation of an isolated complex and only mutual rotation is allowed). As expected, the unconstrained optimization always gives a lower value for B_2. The pronounced difference between the two curves in Figure 6.5a is caused by PE bridging, which is quite prominent for $Z = 40$ (see Figure 6.4a) because here the PE-sphere binding energy is smaller in magnitude. The main feature is that B_2 has a minimum at intermediate salt concentrations, which is consistent with the general experimental trend [212].

It is worth-mentioning that the high negative value of the second virial coefficient is not due to the bridging phenomena, since constrained optimization also gives a negative second virial coefficient, but it is due to the correlations of negative and positive charges on opposite complexes. Nonetheless, bridging gives also a highly negative B_2 when the correlation effects fade at high salt concentration (see Figure 6.5a).

The minimum value for B_2, for both values of Z, happens at $\kappa^{-1} \simeq 1$ nm, which is of the order of the wave length of charge modulation on the surface of the complex. This also corresponds to the salt concentration at which a minimal sphere charge is needed to obtain a wrapped state [48, 49]. In experiments also the minimum of the second virial coefficient occurs at about this salt concentration, although the value of B_2 is smaller. Within the present model, smaller absolute values for B_2 may be recovered by taking a smaller sphere charge in the range $10 < Z < 20$.

6.5 Monopole-dipole model

The results so far were obtained for a very specific choice of parameters, namely 146 base pairs of DNA wrapped around histone proteins. The qualitative behavior of the second virial coefficient in Figure 6.5 is however more general, as follows from considering a much simplified *monopole-dipole model*. For this I replace the PE-sphere complexes by spheres of diameter $2R_\mathrm{s}$, with one charge $Q = Z - \tau L$ in the middle and two opposite charges q and $-q$ along a straight line through the center and at a distance b from the sphere surface, as shown in Figure 6.6d. The net charge Q is fixed such as to match the net charge of the complexes studied before. The parameters q and b are fitted to reproduce the dipole moment P of an isolated complex and the interaction energy between two complexes at contact, $\mathcal{H}(2R_\mathrm{s})$. This way the simplified model will correctly reproduce the interaction between complexes both at large and small separations. I use the fitting of q and b at an intermediate salt concentration $\kappa = 1$ nm^{-1} because in this range the attraction is most pronounced. I obtain for $Z = 100$
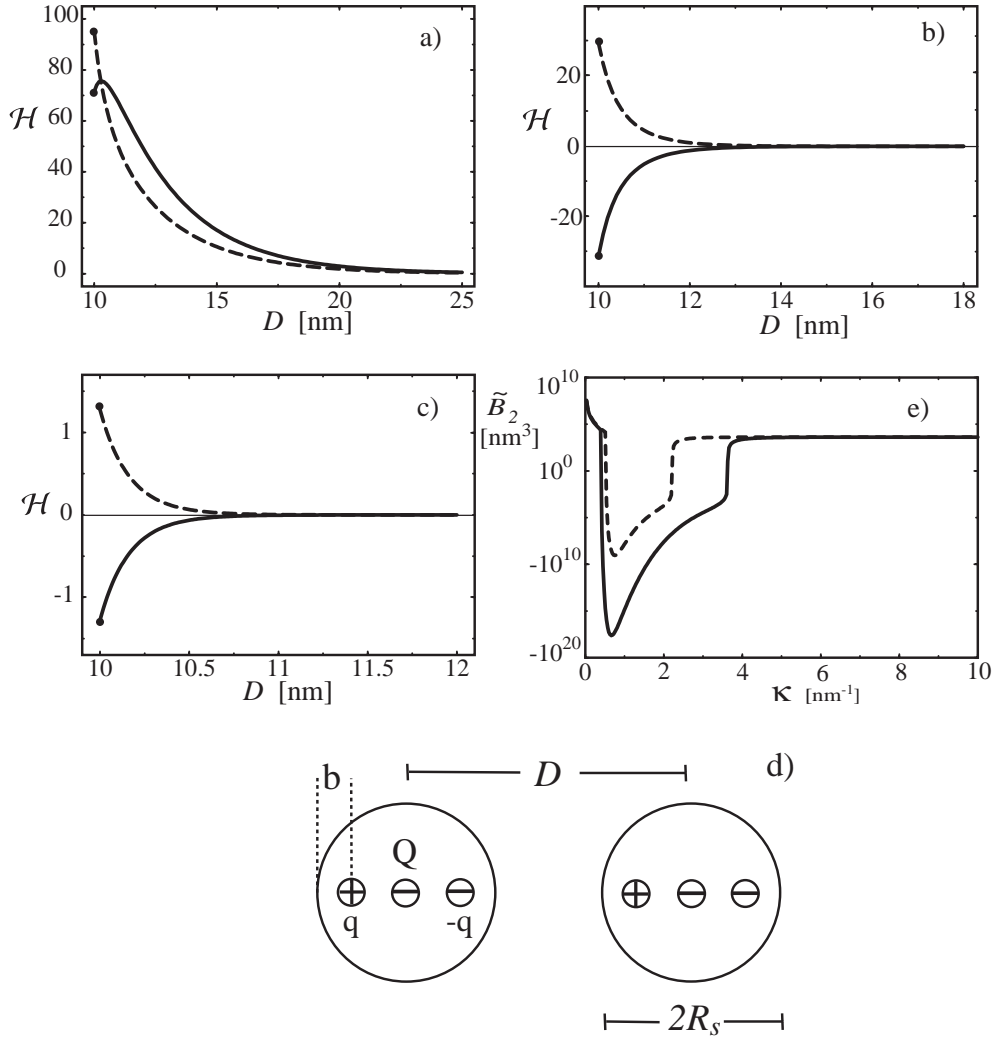
Figure 6.6:   Results obtained for the simplified monopole-dipole model which consists of hard spheres with a central charge Q and two charges q and $-q$ at a certain distance b from the sphere surface, see d). Interaction energies for $Q = -190, q = 8.9, b = 0.4$ nm (fitted to mimick a DNA-histone system with $Z = 100$ as explained in the text) for a) $\kappa = 0.3$ nm^{-1}, b) $\kappa = 1.0$ nm^{-1}, and c) $\kappa = 5.0$ nm^{-1}. The parallel and antiparallel dipolar configurations (solid and broken lines, respectively) compete for stability. e) Shown is the rescaled second virial coefficient $\tilde{B}_2 = B_2(1 + |B_2|)/|B_2|$ as a function of κ for $Q = -190, q = 8.9, b = 0.4$ nm (corresponding to the case of PE-sphere complex with $Z = 100$, solid line) and $Q = -250, q = 9.3, b = 0.62$ nm (corresponding to $Z = 40$, broken line).

(with a contact energy $\mathcal{H}(D = 2R_\mathrm{s}) = -31.25$ at $\kappa = 1$ nm^{-1}) the values $Q = -190, q = 8.9$, $b = 0.4$ nm, and for $Z = 40$ (with $\mathcal{H}(D = 2R_\mathrm{s}) = -14.02$) the values $Q = -250, q = 9.3$, $b = 0.62$ nm.

   In Figure 6.6, I show energies from this simplified model as a function of the distance, D, for $Z = 100$ and a) $\kappa = 0.3$ nm^{-1}, b) $\kappa = 1$ nm^{-1}, c) $\kappa = 5$ nm^{-1} using screened Debye-Hückel (DH) potentials between all charges. Two competing dipole configurations are found, namely

one where the dipoles are colinear and *parallel* (solid lines), which is stabilized by attraction between charges q and $-q$, and one where the dipoles are colinear and *antiparallel* (broken lines), which is stabilized by attractions between charges q and Q. In the range of small to intermediate salt concentrations (0.245 nm$^{-1} < \kappa < 1$ nm^{-1} for $Z = 100$), the parallel configuration is preferred at small separations and the anti-parallel configuration is dominant at large separations as follows from the interaction energies shown in Figure 6.6a. For large salt concentrations (Figure 6.6b and c), the parallel dipolar configuration is preferred, while at very small salt concentrations (not shown), anti-parallel configuration is dominant. Note that by construction the energy at contact in Figure 6.6b agrees with the result from the previous sections.

Using again Eq.(6.10) for calculating the second virial coefficient B_2, I obtain the results in Figure 6.6e for $Z = 40$ (broken line) and $Z = 100$ (solid line). By construction, they fit the results in Figure 6.5 accurately at the salt concentration $\kappa = 1$ nm^{-1} where the model parameters q and b were fitted. But besides that, the shape of the curves are quite similar, showing that at least the constrained minimization is well represented by the monopole-dipole model. For small salt concentrations (small κ), the monopole-monopole repulsion dominates and leads to a positive and diverging coefficient B_2. For large salt concentration, all electrostatics are screened and one is left with the usual hard-core second virial coefficient. At intermediate salt concentrations, the quite large attraction at contact, $\mathcal{H} = -14.02$ for $Z = 40$ and $\mathcal{H} = -31.25$ for $Z = 100$, leads to an enormous contribution to the second-virial coefficient and explains its large and negative values. The almost kinked functional form of the curves in Figure 6.6e is caused by the non-linear relation between $\tilde{B}_2$ and B_2. In principle, the monopole-dipole model could be generalized to include higher-order multipole moments and also polarization effects (which would be a way of including the bridging effects seen in Figure 6.5), but it seems clear that it has the minimal complexity to reproduce the non-monotonic behavior of the second-virial coefficient obtained within the more complicated PE-sphere complexation.

6.6   Conclusion and discussion

Within the ground-state analysis of a chain-sphere model that takes the conformational changes of PEs complexed with oppositely charged spheres into account, I have examined the effective interaction between two PE-macroion complexes. As shown, the second-virial coefficient B_2 associated with the complex-complex interaction becomes negative at intermediate salt concentration, while it remains positive both for small and large salt concentrations. This holds even when the complexes have a rather large net charge. The negative values can be traced back to an asymmetric (or mosaic) binding of the two complexes, in which positively charged patches on the first complex surface match up with negatively charged patches on the second complex and thus give rise to a short-ranged but strong attraction[1]. The typical salt concentration where this binding is expected to be maximal occurs when the screening length is of the order of the charge-modulation wavelength on the complex surface. In this regime, the second virial coefficient has a minimum, which for the parameters chosen for the DNA-histone system roughly coincides with the physiological monovalent salt concentration of 100 mM. Bridging of PE from one sphere to the other further increases the inter-complex

---

[1]Similar effects are observed for the interaction between two proteins with discrete charge patterns[197, 198, 202, 204, 205].

attraction, but is not needed for obtaining negative values for B_2.

A simplified monopole-dipole model can reproduce these findings. To first order in a virial expansion in terms of the concentration of complexes, C_c, the low-concentration branch of the demixing spinodal is given by $C_c = -1/B_2$ which signals a local instability towards precipitation. It is shown that this spinodal can be crossed by changing the salt concentration, while complexes themselves are stable in a much wider range of salt concentration.

The present results are in qualitative agreement with experiments on nucleosome core particles although experiments indicate that histone-tail rearrangements at different salt concentrations may be considerable and play a role as well [212] [2]. These effects have recently been studied using numerical simulation [157].

The present results should also be relevant to mixtures of spheres and PEs as long as the concentrations are not too different. The concentrations also should not be too low, otherwise the mean distance of complexes becomes far more than the screening length and therefore more than the range of the effective interaction.

---

[2]Experiments done in high concentrations of nucleoesome core particles reveal a variety of structures such as bilayers and hexagonal phases[172, 173, 214, 215, 216]. In order to have a theoretical understanding of such systems, one has to use a liquid crystal approach [217, 218].

Appendix A

Numerical Minimization: Derivatives of effective Hamiltonian

As explained in the text, the ground-state configuration of PE-macroion complexes is obtained using a numerical minimization scheme based on a discretized model (see Chapter 2). The minimization method makes use of the so-called quasi-Newton algorithm [3], which requires evaluation of the first derivatives of the effective Hamiltonian of the system in order to locate the minimum of the Hamiltonian in the multi-dimensional space of variables.

In this appendix, I will derive these derivatives for all different systems that are studied in this thesis, i.e. a single PE-macroion complex (Chapters 2, 3 and 5), two interacting complexes (Chapter 6) and many complexes forming a fiber (Chapter 4). I will consider both full minimization schemes (in which the optimal state is obtained by minimization with respect to all degrees of freedom of the chain-sphere system) as well as constrained (or rotational) minimization as introduced in the study of complex fibers (Chapter 4). In the constrained minimization, the chain configuration on the sphere is fixed to the configuration in an isolated complex, and as specified in the text, only the relevant angular (rotational) degrees of freedom of the system are changed in order to find the optimal configuration.

For the calculation of chain fluctuations in Chapter 5, one needs the second derivatives or the so-called Hessian matrix of an isolated complex, which will be derived at the end of this appendix.

A.1   Isolated complex

The discretized effective Hamiltonian (in units of $k_{\mathrm{B}}T$) of an isolated complex is given by Eqs. (2.14), (2.15) and (2.16), i.e.

$$
\begin{aligned}
\mathcal{H} \;=\;& \frac{\ell_{\mathrm{p}}}{\Delta} \sum_{i=2}^{N} \left\{ 1 - \cos(\theta_i - \theta_{i-1}) + \sin\theta_i \sin\theta_{i-1} \Big(1 - \cos(\phi_i - \phi_{i-1}) \Big) \right\} \\
& + q^2 \ell_{\mathrm{B}} \sum_{i=0}^{N-1} \sum_{j=i+1}^{N} \frac{e^{-\kappa|\mathbf{r}_i - \mathbf{r}_j|}}{|\mathbf{r}_i - \mathbf{r}_j|} - \frac{Zq\ell_{\mathrm{B}}}{1 + \kappa R_{\mathrm{s}}} \sum_{i=0}^{N} \left[\frac{e^{-\kappa(|\mathbf{r}_i| - R_{\mathrm{s}})}}{|\mathbf{r}_i|} - A e^{-(|\mathbf{r}_i| - R_{\mathrm{s}})/\alpha} \right], \; \text{(A.1)}
\end{aligned}
$$

where the first two terms refer to the mechanical and electrostatic self-energy of the charged polymer, and the third term is the combined electrostatic attraction and the soft-repulsion

between the macroion and the charged polymer. As discussed in Chapter 2, the above Hamiltonian depends of a minimal set of $2N$ independent variables (with N being the dicretization degree), namely, the polar and azimuthal angles, $\{\theta_i, \phi_{i \neq P}\}$, of the bond vectors $\{\mathbf{u}_i\}$ used to discretize the chain conformation (Section 2.3.1), and r_P which is the z component of the vector, $\mathbf{r}_P$, connecting the sphere center (origin O) to the mid-point of the polymer, P (the middle bead labeled $P = N/2$). Recall that the z-axis lies on the O-P line and that the azimuthal angle of the middle subunit $\mathbf{u}_P$ is fixed in order to remove Goldeston modes. Also, the position vector of each dicretization bead, $\mathbf{r}_i$, is calculated form $\{\mathbf{u}_j\}$ and $\mathbf{r}_P$ as

$$
\mathbf{r}_k = \begin{cases} \mathbf{r}_P - \sum_{i=1}^{P-k} \mathbf{u}_{P-i+1} & k < P, \\[2mm] \mathbf{r}_P + \sum_{i=P+1}^{k} \mathbf{u}_i & k > P. \end{cases} \tag{A.2}
$$

Thus the first-order variation of the above Hamiltonian can be written as

$$
\delta \mathcal{H} = \sum_{i=1}^{N} \frac{\mathrm{d}\mathcal{H}}{\mathrm{d}\theta_i} \delta\theta_i + \sum_{i=1, i \neq P}^{N} \frac{\mathrm{d}\mathcal{H}}{\mathrm{d}\phi_i} \delta\phi_i + \frac{\mathrm{d}\mathcal{H}}{\mathrm{d}r_P} \delta r_P. \tag{A.3}
$$

Each of the derivatives in the above equation can be formally written as

$$
\frac{\mathrm{d}\mathcal{H}}{\mathrm{d}\gamma} = \frac{\partial \mathcal{H}}{\partial \gamma} + \sum_{l=0, l \neq P}^{N} \sum_{\nu=1}^{3} \frac{\partial \mathcal{H}}{\partial r_{l,\nu}} \frac{\partial r_{l,\nu}}{\partial \gamma}, \tag{A.4}
$$

where $r_{l,\nu}$ is the ν-th Cartesian component of the vector $\mathbf{r}_l$ and γ can be any of the independent variables $\{\theta_i, \phi_{i \neq P}, r_P\}$. In what follows, I determine $\mathrm{d}\mathcal{H}/\mathrm{d}\gamma$ for all these variables. Note that everywhere in this section, the azimuthal angles $\{\phi_i\}$ are considered always for $i \neq P$, which, for the sake of simplicity of notation, is not explicitly mentioned.

Using the effective Hamiltonian (A.1), the partial derivatives $\partial \mathcal{H}/\partial r_{l,\nu}$ is obtained as

$$
\frac{\partial \mathcal{H}}{\partial r_{l,\nu}} = -q^2 \ell_B \sum_{i=1}^{N-1} \sum_{j=i+1}^{N} g_{ij} \, (r_{i,\nu} - r_{j,\nu})(\delta_{i,l} - \delta_{j,l}) + \frac{Zq\ell_B}{1 + \kappa R_s} \sum_{i=0}^{N} (f_i - k_i) \, r_{i,\nu} \delta_{i,l} \tag{A.5}
$$

where g_{ij}, f_i and k_i are defined as

$$
g_{ij} = \frac{(1 + \kappa|\mathbf{r}_i - \mathbf{r}_j|)e^{-\kappa|\mathbf{r}_i - \mathbf{r}_j|}}{|\mathbf{r}_i - \mathbf{r}_j|^3}, \tag{A.6}
$$

$$
f_i = \frac{(1 + \kappa|\mathbf{r}_i|)e^{-\kappa(|\mathbf{r}_i| - R_s)}}{|\mathbf{r}_i|^3}, \tag{A.7}
$$

$$
k_i = \frac{A}{\alpha} \frac{e^{-(|\mathbf{r}_i| - R_s)/\alpha}}{|\mathbf{r}_i|}. \tag{A.8}
$$

Derivative with respect to r_P

The derivative of effective Hamiltonian (A.1) with respect to $\gamma = r_P$, that is $\mathrm{d}\mathcal{H}/\mathrm{d}r_P$, simply equals the partial derivative with respect to r_P. Thus using Eq. (A.5), I obtain

$$
\frac{\mathrm{d}\mathcal{H}}{\mathrm{d}r_P} = \frac{Zq\ell_B}{1 + \kappa R_s} \sum_{l=0}^{N} (f_l - k_l) \, r_{l,3}. \tag{A.9}
$$

Derivatives with respect to θ_m and ϕ_m

The total derivatives with respect to θ_m and ϕ_m in Eq. (A.4) (obtained by setting $\gamma = \theta_m$ and ϕ_m) can be calculated as follows.

First note that the partial derivative of the Hamiltonian (A.1) with respect to the polar angle θ_m and the azimuthal angle ϕ_m are given by

$$\frac{\Delta}{\ell_{\mathrm{B}}}\frac{\partial \mathcal{H}}{\partial \theta_m} = \sum_{i=2}^{N}\left\{ \sin(\theta_i - \theta_{i-1})\left(\delta_{i,m} - \delta_{i-1,m}\right) + \left(1 - \cos(\phi_i - \phi_{i-1})\right) \right.$$

$$\left. \times (\cos\theta_i \sin\theta_{i-1}\delta_{i,m} + \sin\theta_i \cos\theta_{i-1}\delta_{i-1,m}) \right\} \tag{A.10}$$

$$\frac{\Delta}{\ell_{\mathrm{B}}}\frac{\partial \mathcal{H}}{\partial \phi_m} = \sum_{i=2}^{N}\left\{ \sin\theta_i \sin\theta_{i-1}\sin(\phi_i - \phi_{i-1})(\delta_{i,m} - \delta_{i-1,m}) \right\}. \tag{A.11}$$

On the other hand, the partial derivative of $r_{i,\nu}$ with respect to θ_m and ϕ_m can be written using the chain rule as

$$\frac{\partial r_{l,\nu}}{\partial \theta_m} = \frac{\partial r_{l,\nu}}{\partial u_{m,\nu}}\frac{\partial u_{m,\nu}}{\partial \theta_m} \tag{A.12}$$

(with a similar expression for ϕ_m), where $u_{m,\nu}$ denotes Cartesian components of $\mathbf{u}_m$. Using Eq. (A.2), one obtains

$$\frac{\partial r_{l,\nu}}{\partial u_{m,\nu}} = \begin{cases} -\Theta(m - l - 1)\Theta(P - m) & l < P, \\[2mm] \Theta(l - m)\Theta(m - P - 1) & l > P, \end{cases} \tag{A.13}$$

where $\Theta(x)$ denotes the step function, i.e. $\Theta(x) = 1$ for $x \geq 0$ and zero otherwise. The derivatives of $\mathbf{u}_m$ with respect to θ_m and ϕ_m are obtained (using the definition of the discretized model in Chapter 2) as

$$\frac{\partial \mathbf{u}_m}{\partial \theta_m} = \Delta \begin{pmatrix} \cos\theta_m \cos\phi_m \\ \cos\theta_m \sin\phi_m \\ -\sin\theta_m \end{pmatrix}, \tag{A.14}$$

$$\frac{\partial \mathbf{u}_m}{\partial \phi_m} = \Delta \begin{pmatrix} -\sin\theta_m \sin\phi_m \\ \sin\theta_m \cos\phi_m \\ 0 \end{pmatrix}. \tag{A.15}$$

For the sake of convenience, in what follows, I use the notation $\mathcal{C}^{\nu}_{m,\theta} = \partial u_{m,\nu}/\partial \theta_m$ and $\mathcal{C}^{\nu}_{m,\phi} = \partial u_{m,\nu}/\partial \phi_m$. Combining Eqs. (A.13), (A.14) and (A.15) with Eq. (A.5), I obtain

$$\sum_{l=0}^{P-1}\sum_{\nu=1}^{3}\frac{\partial \mathcal{H}}{\partial r_{l,\nu}}\frac{\partial r_{l,\nu}}{\partial u_{m,\nu}}\mathcal{C}^{\nu}_{m,\theta} = -\Theta(P - m)\left\{ \sum_{l=0}^{m-1}\sum_{\nu=1}^{3}\left[-q^2\ell_{\mathrm{B}}\sum_{i=0,i\neq l}^{N}g_{li}\left(r_{l,\nu} - r_{i,\nu}\right) + \right.\right.$$

$$\left.\left. +\frac{Zq\ell_{\mathrm{B}}}{1 + \kappa R_{\mathrm{s}}}(f_l - k_l)\,r_{l,\nu} \right]\mathcal{C}^{\nu}_{m,\theta} \right\}, \tag{A.16}$$

$$\sum_{l=P}^{N}\sum_{\nu=1}^{3}\frac{\partial \mathcal{H}}{\partial r_{l,\nu}}\frac{\partial r_{l,\nu}}{\partial u_{m,\nu}}\mathcal{C}^{\nu}_{m,\theta} = \Theta(m - P - 1)\left\{ \sum_{l=m}^{N}\sum_{\nu=1}^{3}\left[-q^2\ell_{\mathrm{B}}\sum_{i=0,i\neq l}^{N}g_{li}\left(r_{l,\nu} - r_{i,\nu}\right) + \right.\right.$$

$$\left.\left. +\frac{Zq\ell_{\mathrm{B}}}{1 + \kappa R_{\mathrm{s}}}(f_l - k_l)\,r_{l,\nu} \right]\mathcal{C}^{\nu}_{m,\theta} \right\}. \tag{A.17}$$

The same relations hold for derivatives with respect to ϕ_m by replacing $\mathcal{C}^{\nu}_{m,\theta}$ with $\mathcal{C}^{\nu}_{m,\phi}$ in the above equations. Combining Eqs. (A.10) and (A.11) with Eqs. (A.16) and (A.17), one can obtain the total derivatives with respect to θ_m and ϕ_m to be used in Eq. (A.4).

A.2   Complex fiber

Generalizing the formalism introduced in the previous section to a complex fiber as defined in Chapter 4 is straight forward. The discretized Hamiltonian of the complex fiber (in units of $k_{\mathrm{B}}T$) reads

$$\mathcal{H} = \mathcal{H}_{uc} + \sum_{k=1}^{M} \mathcal{H}_{I}^{0k}, \tag{A.18}$$

where $\mathcal{H}_{uc}$ is the self-energy of the main unit cell,

$$
\begin{aligned}
\mathcal{H}_{uc} = {} & \frac{\ell_{\mathrm{p}}}{\Delta} \sum_{i=2}^{N} \left\{ 1 - \cos(\theta_i - \theta_{i-1}) + \sin\theta_i \sin\theta_{i-1}\Big(1 - \cos(\phi_i - \phi_{i-1}) \Big) \right\} \\
& + q^2 \ell_{\mathrm{B}} \sum_{i=0}^{N-1} \sum_{j=i+1}^{N} \frac{e^{-\kappa|\mathbf{r}_i^0 - \mathbf{r}_j^0|}}{|\mathbf{r}_i^0 - \mathbf{r}_j^0|} - \frac{Zq\ell_{\mathrm{B}}}{1+\kappa R_{\mathrm{s}}} \sum_{i=0}^{N} \left[\frac{e^{-\kappa(|\mathbf{r}_i^0|-R_{\mathrm{s}})}}{|\mathbf{r}_i^0|} - Ae^{-(|\mathbf{r}_i^0|-R_{\mathrm{s}})/\alpha} \right],
\end{aligned}
\tag{A.19}
$$

with $\{\mathbf{r}_i^0\}$ being the position of polymer beads (with $i = 0, \dots, N$) in the main unit cell (recall that the center of the sphere in the main unit cell is taken as the origin). $\mathcal{H}_I^{0k}$ gives the interaction energy between the main unit cell and the k-th image unit cell, i.e.

$$
\begin{aligned}
\mathcal{H}_I^{0k} = {} & q^2 \ell_{\mathrm{B}} \sum_{i=0}^{N} \sum_{j=2}^{N} \frac{e^{-\kappa|\mathbf{r}_i^0 - \mathbf{r}_j^k|}}{|\mathbf{r}_i^0 - \mathbf{r}_j^k|} - \frac{Zq\ell_{\mathrm{B}}}{1+\kappa R_{\mathrm{s}}} \sum_{i=0}^{N} \left[\left(\frac{e^{-\kappa(|\mathbf{r}_i^0 - \mathbf{R}^k|-R_{\mathrm{s}})}}{|\mathbf{r}_i^0 - \mathbf{R}^k|} + \frac{e^{-\kappa(|\mathbf{r}_i^k|-R_{\mathrm{s}})}}{|\mathbf{r}_i^k|} \right) \right. \\
& \left. - A\Big(e^{-(|\mathbf{r}_i^0 - \mathbf{R}^k|-R_{\mathrm{s}})/\alpha} + e^{-(|\mathbf{r}_i^k|-R_{\mathrm{s}})/\alpha} \Big) \right] + \frac{Z^2\ell_{\mathrm{B}}e^{2\kappa R_{\mathrm{s}}}}{(1+\kappa R_{\mathrm{s}})^2} \frac{e^{-\kappa|\mathbf{R}^k|}}{|\mathbf{R}^k|},
\end{aligned}
\tag{A.20}
$$

where $\{\mathbf{r}_i^k\}$ and $\mathbf{R}^k$ denote the position of the polymer beads and the sphere center in the k-th unit cell respectively, that is

$$\mathbf{r}_i^k = \mathbf{E} \cdot (\mathbf{r}_i^{k-1} - \mathbf{r}_0^{k-1}) + \mathbf{r}_{N-1}^{k-1}, \tag{A.21}$$

$$\mathbf{R}^k = \mathbf{E} \cdot (\mathbf{R}^{k-1} - \mathbf{r}_0^{k-1}) + \mathbf{r}_{N-1}^{k-1}, \tag{A.22}$$

with the rotation matrix $\mathbf{E}$ being defined in Chapter 4. The independent variables are the same as introduced in the previous section for an isolated complex but with the addition of an angular degree of freedom, χ, representing the rotation angle of each unit cell. The first-order variation of Eq. (A.18) is

$$\delta\mathcal{H} = \delta\mathcal{H}_{uc} + \sum_{k=1}^{M} \delta\mathcal{H}_I^{0k}. \tag{A.23}$$

The first term is not a function of χ, as the self-energy of each unit cell is similar to that of an isolate polymer-macroion complex (comapre Eqs. (A.1) and (A.19)). This term has been calculated in the previous section. The second term is calculated as follows

$$\sum_{k=1}^{M} \delta\mathcal{H}_I^{0k} = \sum_{k=1}^{M} \left[\sum_{i=1}^{N} \left(\frac{\mathrm{d}\mathcal{H}_I^{0k}}{\mathrm{d}\theta_i} \delta\theta_i + \frac{\mathrm{d}\mathcal{H}_I^{0k}}{\mathrm{d}\phi_i} \delta\phi_i \right) + \frac{\mathrm{d}\mathcal{H}_I^{0k}}{\mathrm{d}\chi} \delta\chi + \frac{\mathrm{d}\mathcal{H}_I^{0k}}{\mathrm{d}r_P} \delta r_P \right], \tag{A.24}$$

where as before the azimuthal angle of the middle discretization subunit of the chain (labeled by $P = N/2$) is fixed and thus excluded in the series above (not indicated explicitly). In general, the total derivative $\mathrm{d}\mathcal{H}_I^{0k}/\mathrm{d}\gamma$ (where γ may be chosen either of θ_i, $\phi_{i \neq P}$, χ or r_P) can be written as

$$\frac{\mathrm{d}\mathcal{H}_I^{0k}}{\mathrm{d}\gamma} = \frac{\partial \mathcal{H}_I^{0k}}{\partial \gamma} + \sum_{l=0}^{N} \sum_{\nu=1}^{3} \left(\frac{\partial \mathcal{H}_I^{0k}}{\partial r_{l,\nu}^0} \frac{\partial r_{l,\nu}^0}{\partial \gamma} + \frac{\partial \mathcal{H}_I^{0k}}{\partial r_{l,\nu}^k} \frac{\partial r_{l,\nu}^k}{\partial \gamma} \right) + \sum_{\nu=1}^{3} \frac{\partial \mathcal{H}_I^{0k}}{\partial R_\nu^k} \frac{\partial R_\nu^k}{\partial \gamma}. \tag{A.25}$$

Note that in the first term in parentheses, one must exclud the term with $l = P = N/2$. In what follows, I give the results for all partial derivatives present in the above equation.

Partial derivatives of $r_{l,\nu}^k$ and R_ν^k with respect to γ

I will first consider the term $\partial r_{l,\nu}^k / \partial \gamma$. For $k = 0$, full calculation of this term is given in previous section (Eqs. (A.12) and (A.13)). For $k \neq 0$, however, the results can be obtained from the recursive relation

$$\frac{\partial r_{l,\nu}^k}{\partial \gamma} = \sum_{\mu=1}^{3} \left[\frac{\partial E_{\nu\mu}}{\partial \gamma} (r_{l,\mu}^{k-1} - r_{0,\mu}^{k-1}) + E_{\nu\mu} \left(\frac{\partial r_{l,\mu}^{k-1}}{\partial \gamma} - \frac{\partial r_{0,\mu}^{k-1}}{\partial \gamma} \right) \right] + \frac{\partial r_{N-1,\nu}^{k-1}}{\partial \gamma}. \tag{A.26}$$

Using the above relation, one can numerically calculate the derivatives of $\mathbf{r}_i^k$ with respect to θ_i, $\phi_{i \neq P}$, r_P and χ. For this purpose, one only needs the derivatives of $\mathbf{r}_i^0$ with respect to these parameters, which have been calculated previously, as well as the relevant derivatives of the matrix $\mathbf{E}$ (see below).

Note that term $\partial R_\nu^k / \partial \gamma$ is also calculated via the same recursive relation, i.e.

$$\frac{\partial R_\nu^k}{\partial \gamma} = \sum_{\mu=1}^{3} \left[\frac{\partial E_{\nu\mu}}{\partial \gamma} (R_\mu^{k-1} - r_{0,\mu}^{k-1}) + E_{\nu\mu} \left(\frac{\partial R_\mu^{k-1}}{\partial \gamma} - \frac{\partial r_{0,\mu}^{k-1}}{\partial \gamma} \right) \right] + \frac{\partial r_{N-1,\nu}^{k-1}}{\partial \gamma} \tag{A.27}$$

with $R_1^0 = R_2^0 = R_3^0 = 0$, since the center of the sphere in the main unit cell is chosen as the origin of the Cartesian system.

Partial derivatives of the rotation matrix E

The rotation matrix $\mathbf{E}$ is given by (see Chapter 4)

$$\mathbf{E} = \mathbf{B} \, \mathbf{X} \, \mathbf{A} \tag{A.28}$$

with $\mathbf{A}$, $\mathbf{X}$ and $\mathbf{B}$ defined as follows

$$\mathbf{A} = \begin{pmatrix} -\sin\phi_1 & \cos\phi_1 & 0 \\ -\cos\phi_1 \cos\theta_1 & -\sin\phi_1 \cos\theta_1 & \sin\theta_1 \\ \sin\theta_1 \cos\phi_1 & \sin\phi_1 \sin\theta_1 & \cos\theta_1 \end{pmatrix}, \tag{A.29}$$

$$\mathbf{X} = \begin{pmatrix} \cos\chi & -\sin\chi & 0 \\ \sin\chi & \cos\chi & 0 \\ 0 & 0 & 1 \end{pmatrix}, \tag{A.30}$$

$$\mathbf{B} = \begin{pmatrix} -\sin\phi_N & -\cos\phi_N \cos\theta_N & \sin\theta_N \cos\phi_N \\ \cos\phi_N & -\sin\phi_N \cos\theta_N & \sin\phi_N \sin\theta_N \\ 0 & \sin\theta_N & \cos\theta_N \end{pmatrix}. \tag{A.31}$$

This shows that $\mathbf{E}$ is a function of χ, θ_1, θ_N, ϕ_1 and ϕ_N only. Therefore, only the derivatives of $\mathbf{E}$ with respect to these parameters are non-zero, which are obtained as

$$\frac{\partial \mathbf{E}}{\partial \chi} = \mathbf{B}\,\frac{\partial \mathbf{X}}{\partial \chi}\,\mathbf{A}, \qquad \frac{\partial \mathbf{E}}{\partial \theta_1} = \mathbf{B}\,\mathbf{X}\,\frac{\partial \mathbf{A}}{\partial \theta_1}, \qquad \frac{\partial \mathbf{E}}{\partial \phi_1} = \mathbf{B}\,\mathbf{X}\,\frac{\partial \mathbf{A}}{\partial \phi_1},$$

$$\frac{\partial \mathbf{E}}{\partial \theta_N} = \frac{\partial \mathbf{B}}{\partial \theta_N}\,\mathbf{X}\,\mathbf{A}, \qquad \frac{\partial \mathbf{E}}{\partial \phi_N} = \frac{\partial \mathbf{B}}{\partial \phi_N}\,\mathbf{X}\,\mathbf{A}, \tag{A.32}$$

where

$$\frac{\partial \mathbf{X}}{\partial \chi} = \begin{pmatrix} -\sin\chi & -\cos\chi & 0 \\ \cos\chi & -\sin\chi & 0 \\ 0 & 0 & 1 \end{pmatrix}, \tag{A.33}$$

$$\frac{\partial \mathbf{A}}{\partial \theta_1} = \begin{pmatrix} 0 & 0 & 0 \\ \cos\phi_1\sin\theta_1 & \sin\phi_1\sin\theta_1 & \cos\theta_1 \\ \cos\theta_1\cos\phi_1 & \sin\phi_1\cos\theta_1 & -\sin\theta_1 \end{pmatrix}, \tag{A.34}$$

$$\frac{\partial \mathbf{A}}{\partial \phi_1} = \begin{pmatrix} -\cos\phi_1 & -\sin\phi_1 & 0 \\ \sin\phi_1\cos\theta_1 & -\cos\phi_1\cos\theta_1 & 0 \\ -\sin\theta_1\sin\phi_1 & \cos\phi_1\sin\theta_1 & \cos\theta_1 \end{pmatrix}, \tag{A.35}$$

$$\frac{\partial \mathbf{B}}{\partial \theta_N} = \begin{pmatrix} 0 & \cos\phi_N\sin\theta_N & \cos\theta_N\cos\phi_N \\ 0 & \sin\phi_N\sin\theta_N & \sin\phi_N\cos\theta_N \\ 0 & \cos\theta_N & -\sin\theta_N \end{pmatrix}, \tag{A.36}$$

$$\frac{\partial \mathbf{B}}{\partial \phi_N} = \begin{pmatrix} -\cos\phi_N & \sin\phi_N\cos\theta_N & -\sin\theta_N\sin\phi_N \\ -\sin\phi_N & -\cos\phi_N\cos\theta_N & \cos\phi_N\sin\theta_N \\ 0 & 0 & 0 \end{pmatrix}. \tag{A.37}$$

Partial derivatives of the interaction Hamiltonian $\mathcal{H}_I^{0k}$

Finally, partial derivatives of the interaction Hamiltonian in Eq. (A.25) can be calculated in a straight forward manner and in the same way as the partial derivatives of an isolated-complex Hamiltonian were calculated. The derivatives with respect to $r_{l,\nu}^0$ and $r_{l,\nu}^k$ are

$$\frac{\partial \mathcal{H}_I^{0k}}{\partial r_{l,\nu}^0} = -q^2\ell_\mathrm{B}\sum_{j=2}^N G(\mathbf{r}_l^0,\mathbf{r}_j^k)\,(r_{l,\nu}^0-r_{j,\nu}^k) + \frac{Zq\ell_\mathrm{B}}{1+\kappa R_\mathrm{s}}\left[F(\mathbf{r}_l^0,\mathbf{R}^k)-K(\mathbf{r}_l^0,\mathbf{R}^k)\right](r_{l,\nu}^0-R_\nu^k), \tag{A.38}$$

$$\frac{\partial \mathcal{H}_I^{0k}}{\partial r_{l,\nu}^k} = -q^2\ell_\mathrm{B}\sum_{i=0}^N G(\mathbf{r}_i^0,\mathbf{r}_l^k)\,(r_{i,\nu}^0-r_{l,\nu}^k) + \frac{Zq\ell_\mathrm{B}}{1+\kappa R_\mathrm{s}}\left[F(\mathbf{r}_l^k,\mathbf{0})-K(\mathbf{r}_l^0,\mathbf{0})\right]r_{l,\nu}^k, \tag{A.39}$$

where $\mathbf{0}$ denotes the origin and

$$G(\mathbf{r}_i,\mathbf{r}_j) \equiv \frac{(1+\kappa|\mathbf{r}_i-\mathbf{r}_j|)e^{-\kappa|\mathbf{r}_i-\mathbf{r}_j|}}{|\mathbf{r}_i-\mathbf{r}_j|^3}, \tag{A.40}$$

$$F(\mathbf{r}_i,\mathbf{R}) \equiv \frac{(1+\kappa|\mathbf{r}_i-\mathbf{R}|)e^{-\kappa(|\mathbf{r}_i-\mathbf{R}|-R_\mathrm{s})}}{|\mathbf{r}_i-\mathbf{R}|^3}, \tag{A.41}$$

$$K(\mathbf{r}_i,\mathbf{R}) \equiv \frac{A}{\alpha}\frac{e^{-(|\mathbf{r}_i-\mathbf{R}|-R_\mathrm{s})/\alpha}}{|\mathbf{r}_i-\mathbf{R}|}, \tag{A.42}$$

are the generalized forms of g_{ij}, f_i and k_i given in Eqs. (A.6)-(A.8). The derivative of $\mathcal{H}_I^{0k}$ with respect to R_ν^k is given as

$$\frac{\partial \mathcal{H}_I^{0k}}{\partial R_\nu^k} = \frac{Zq\ell_{\mathrm{B}}}{1+\kappa R_{\mathrm{s}}} \sum_{i=0}^{N} \left[F(\mathbf{r}_i^0, \mathbf{R}^k) - K(\mathbf{r}_i^0, \mathbf{R}^k)(r_{i,\nu}^0 - R_\nu^k) \right] - \frac{Z^2 \ell_{\mathrm{B}} e^{2\kappa R_{\mathrm{s}}}}{(1+\kappa R_{\mathrm{s}}^2)} \frac{(1+\kappa|\mathbf{R}|)e^{-\kappa|\mathbf{R}|}}{|\mathbf{R}|^3}.$$
(A.43)

The only remaining partial derivative, i.e. the first term in Eq. (A.25), is zero ($\partial \mathcal{H}_I^{0k}/\partial \gamma = 0$) except for $\gamma = r_P$, which can be obtained from Eq. (A.38) by setting $r_{l,\nu}^0 = r_P$.

A.3   Two interacting complexes

The Hamiltonian of two interacting complexes (Chapter 6) consists of two parts: i) the self-energy of each complex (containing the interaction between each of the polymers with the sphere that is associated with it), and ii) the interaction between polymers and spheres in different complexes. It can be rewritten in discretized form (and in units of $k_{\mathrm{B}}T$) as

$$\mathcal{H} = \sum_{l=1}^{2} \mathcal{H}_s^l + \mathcal{H}_I^{(1,2)}$$
(A.44)

with $\mathcal{H}_s^l$ (for $l = 1, 2$) being the same as Eq. (A.1), i.e.

$$\begin{aligned}
\mathcal{H}_s^l &= \frac{\ell_{\mathrm{p}}}{\Delta} \sum_{i=2}^{N} \left\{ 1 - \cos(\theta_i^l - \theta_{i-1}^l) + \sin\theta_i^l \sin\theta_{i-1}^l \left(1 - \cos(\phi_i^l - \phi_{i-1}^l)\right) \right\} \\
&\quad + q^2 \ell_{\mathrm{B}} \sum_{i=0}^{N-1} \sum_{j=i+1}^{N} \frac{e^{-\kappa|\mathbf{r}_i^l - \mathbf{r}_j^l|}}{|\mathbf{r}_i^l - \mathbf{r}_j^l|} - \frac{Zq\ell_{\mathrm{B}}}{1+\kappa R_{\mathrm{s}}} \sum_{i=0}^{N} \left[\frac{e^{-\kappa(|\mathbf{r}_i^l - \mathbf{R}_l| - R_{\mathrm{s}})}}{|\mathbf{r}_i^l - \mathbf{R}_l|} - A e^{-(|\mathbf{r}_i^l - \mathbf{R}_l| - R_{\mathrm{s}})/\alpha} \right],
\end{aligned}$$
(A.45)

and the interaction part, $\mathcal{H}_l^{(1,2)}$, as

$$\begin{aligned}
\mathcal{H}_I^{(1,2)} &= q^2 \ell_{\mathrm{B}} \sum_{i=0}^{N-1} \sum_{j=0}^{N} \frac{e^{-\kappa|\mathbf{r}_i^1 - \mathbf{r}_j^2|}}{|\mathbf{r}_i^1 - \mathbf{r}_j^2|} - \frac{Zq\ell_{\mathrm{B}}}{1+\kappa R_{\mathrm{s}}} \sum_{i=0}^{N} \left[e^{\kappa R_{\mathrm{s}}} \left(\frac{e^{-\kappa|\mathbf{r}_i^1 - \mathbf{R}_2|}}{|\mathbf{r}_i^1 - \mathbf{R}_2|} + \frac{e^{-\kappa|\mathbf{r}_i^2 - \mathbf{R}_1|}}{|\mathbf{r}_i^2 - \mathbf{R}_1|} \right) \right. \\
&\quad \left. - A e^{R_{\mathrm{s}}/\alpha} \left(e^{-(|\mathbf{r}_i^1 - \mathbf{R}_2|)/\alpha} + e^{-(|\mathbf{r}_i^2 - \mathbf{R}_1|)/\alpha} \right) \right] + \frac{Z^2 \ell_{\mathrm{B}} e^{2\kappa R_{\mathrm{s}}}}{(1+\kappa R_{\mathrm{s}})^2} \frac{e^{-\kappa|\mathbf{R}_1 - \mathbf{R}_2|}}{|\mathbf{R}_1 - \mathbf{R}_2|}, \quad (\text{A.46})
\end{aligned}$$

where sub- and super-indices 1 and 2 refer to the polymer/sphere belonging to complexes 1 and 2 respectively. The independent variables of the two-complex system are $\{\theta_i^l, \phi_i^l\}$ (the set of polar and azimuthal angles of the two polymers) as well as the the mid-point coordinates of each polymer, $\mathbf{r}_P^l$ (with $P = N/2$), which specify the location of polymers with respect to macroions. The distance between two charged spheres is fixed. Therefore, the system is described by $4N + 6$ independent variables with respect to which one has to minimize the effective Hamiltonian (A.44). One thus needs the derivatives of the Hamiltonian with respect to these variables to be used within the quasi-Newton minimization algorithm. Derivatives of $\mathcal{H}_s$ are the same as those already presented for an isolated complex (Section A.1). Derivatives of the term $\mathcal{H}_I$ are similar to the results given in the preceding section for $\mathcal{H}_I^{0k}$. Note that one can write the first-order variation of the Hamiltonian as

$$\delta \mathcal{H}_I = \sum_{l=1}^{2} \left\{ \sum_{i=1}^{N} \left(\frac{\mathrm{d}\mathcal{H}_I}{\mathrm{d}\theta_i^l} \delta\theta_i^l + \frac{\mathrm{d}\mathcal{H}_I}{\mathrm{d}\phi_i^l} \delta\phi_i^l \right) + \sum_{\nu=1}^{3} \frac{\mathrm{d}\mathcal{H}_I}{\mathrm{d}r_{P,\nu}^l} \delta r_{P,\nu}^l \right\},$$
(A.47)

where, in general, the Hamiltonian's total derivative with respect to a given variable γ^l reads

$$\frac{\mathrm{d}\mathcal{H}_I}{\mathrm{d}\gamma^l} = \frac{\partial\mathcal{H}_I}{\partial\gamma^l} + \sum_{i=0,i\neq P}^{N}\sum_{\nu=1}^{3}\frac{\partial\mathcal{H}_I}{\partial r_{i,\nu}^l}\frac{\partial r_{i,\nu}^l}{\partial\gamma^l}. \tag{A.48}$$

The term $\partial r_{i,\nu}^l/\partial\gamma^l$ has been calculated previously (see, e.g., Eq. (A.13)), and the derivatives of $\mathcal{H}_I$ with respect to γ^l are zero except when γ^l is chosen as $\mathbf{r}_P^l$. This derivative can be calculated from the following relation, i.e.

$$\frac{\partial\mathcal{H}_I}{\partial r_{m,\nu}^l} = -q^2\ell_{\mathrm{B}}\sum_{j=1}^{N}G(\mathbf{r}_m^l,\mathbf{r}_j^{l'})\,(r_{m,\nu}^l - r_{j,\nu}^{l'}) + \frac{Zq\ell_{\mathrm{B}}}{1+\kappa R_{\mathrm{s}}}\left[F(\mathbf{r}_m^l,\mathbf{R}^l) - K(\mathbf{r}_m^l,\mathbf{R}^l)\right]\,(r_{m,\nu}^l - R_\nu^l), \tag{A.49}$$

where the functions G, F and K are defined in Eqs. (A.40)-(A.42).

A.4   Hessian matrix

In this section, I calculate the Hessian matrix of the effective Hamiltonian of an isolated PE-macroion complex, which is used in Chapter 5 to evaluate the entropic contribution from small-amplitude fluctuations of a complexed chain around its ground-state configuration. The Hessian matrix contains second-order derivatives with respect to degrees of freedom of an isolated complex. This requires more involved calculations (using the expressions obtained in Section A.1 for the first-order derivatives) and thus I present here only the final formulae for the elements of the Hessian matrix. Using the symbol γ_m for the angular degrees of freedom of a chain θ_m and ϕ_m, the elements of the Hessian matrix have the following form

$$\frac{\mathrm{d}^2\mathcal{H}}{\mathrm{d}\gamma_m\mathrm{d}\gamma_n}, \qquad \frac{\mathrm{d}^2\mathcal{H}}{\mathrm{d}\gamma_m\mathrm{d}r_P}, \qquad \frac{\mathrm{d}^2\mathcal{H}}{\mathrm{d}^2r_P}, \tag{A.50}$$

where

$$\frac{\mathrm{d}^2\mathcal{H}}{\mathrm{d}\gamma_m\mathrm{d}\gamma_n} = \frac{\partial^2\mathcal{H}}{\partial\gamma_m\partial\gamma_n} + \sum_{\nu=1}^{3}\sum_{l=0,l\neq P}^{N}\left[\frac{\partial\mathcal{H}}{\partial r_{l,\nu}}\frac{\partial^2 r_{l,\nu}}{\partial\gamma_m\partial\gamma_n} + \sum_{\mu=1}^{3}\sum_{h=0,h\neq P}^{N}\frac{\partial^2\mathcal{H}}{\partial r_{l,\nu}\partial r_{h,\mu}}\frac{\partial r_{l,\nu}}{\partial\gamma_m}\frac{\partial r_{h,\mu}}{\partial\gamma_n}\right], \tag{A.51}$$

$$\frac{\mathrm{d}^2\mathcal{H}}{\mathrm{d}\gamma_m\mathrm{d}r_P} = \sum_{h=0}^{N}\sum_{l=0}^{N}\sum_{\nu=1}^{3}\frac{\partial^2\mathcal{H}}{\partial r_{l,\nu}\partial r_{h,3}}\frac{\partial r_{l,\nu}}{\partial\gamma_m}, \tag{A.52}$$

$$\frac{\mathrm{d}^2\mathcal{H}}{\mathrm{d}^2r_P} = \sum_{h=0}^{N}\sum_{l=0}^{N}\frac{\partial^2\mathcal{H}}{\partial r_{l,3}\partial r_{h,3}}. \tag{A.53}$$

The partial derivatives of the Hamiltonian are explicitly written as

$$\begin{aligned}\frac{\partial^2\mathcal{H}}{\partial\theta_m\partial\theta_n} =\ & \frac{\ell_{\mathrm{p}}}{\Delta}\sum_{i=2}^{N}\bigg[\cos(\theta_i - \theta_{i-1})(\delta_{i,m} - \delta_{i-1,m})(\delta_{i,n} - \delta_{i-1,n}) + \\ & + \bigg(\cos\theta_i\cos\theta_{i-1}\delta_{i,m}\delta_{i-1,n} - \sin\theta_i\sin\theta_{i-1}\delta_{i,m}\delta_{i-1,n} + \cos\theta_i\cos\theta_{i-1}\delta_{i,n}\delta_{i-1,m} \\ & - \sin\theta_i\sin\theta_{i-1}\delta_{i,n}\delta_{i-1,n}\bigg)\bigg(1 - \cos(\phi_i - \phi_{i-1})\bigg)\bigg],\end{aligned} \tag{A.54}$$

$$\frac{\partial^2 \mathcal{H}}{\partial \theta_m \partial \phi_n} = \frac{\ell_{\mathrm{p}}}{\Delta} \sum_{i=2}^{N} \left[\cos \theta_i \sin \theta_{i-1} \sin(\phi_i - \phi_{i-1}) \delta_{i,m} (\delta_{i,n} - \delta_{i-1,n}) \right.$$

$$\left. + \sin \theta_i \cos \theta_{i-1} \sin(\phi_i - \phi_{i-1}) \delta_{i-1,m} (\delta_{i,n} - \delta_{i-1,n}) \right], \tag{A.55}$$

$$\frac{\partial^2 \mathcal{H}}{\partial \phi_m \partial \phi_n} = \frac{\ell_{\mathrm{p}}}{\Delta} \sum_{i=2}^{N} \left[\sin \theta_i \sin \phi_{i-1} \cos(\phi_i - \phi_{i-1}) (\delta_{i,m} - \delta_{i-1,m})(\delta_{i,n} - \delta_{i-1,n}) \right]. \tag{A.56}$$

The terms $\partial r_{l,\nu} / \partial \gamma_m$ and $\partial \mathcal{H} / \partial r_{m,\nu}$ have been evaluated before. Here I first consider the term $\partial^2 r_{l,\nu} / \partial \gamma_m \partial \gamma_n$, which is obtained as

$$\frac{\partial^2 r_{l,\nu}}{\partial \gamma_m \partial \gamma_n} = 0 \qquad \text{for } m \neq n, \tag{A.57}$$

but for $m = n$, one has

$$\frac{\partial^2 r_{l,\nu}}{\partial \gamma_m \partial \gamma_m'} = \begin{cases} \mathcal{S}^\nu_{m,\gamma,\gamma'} \, \Theta(m - l - 1)\Theta(P - m) & l < P, \\[2mm] \mathcal{S}^\nu_{m,\gamma,\gamma'} \, \Theta(l - m)\Theta(m - P - 1) & l > P, \end{cases} \tag{A.58}$$

where $\mathcal{S}^\nu_{m,\gamma,\gamma'}$ is the second derivative of the ν-th component of $\mathbf{u}_m$ with respect to γ and γ', which may be θ_m or ϕ_m, that is explicitly,

$$\mathcal{S}_{m,\theta,\theta} = \frac{\partial^2 \mathbf{u}_m}{\partial \theta_m^2} = \Delta \begin{pmatrix} -\sin \theta_m \cos \phi_m \\ -\sin \theta_m \sin \phi_m \\ -\cos \theta_m \end{pmatrix},$$

$$\mathcal{S}_{m,\theta,\phi} = \frac{\partial^2 \mathbf{u}_m}{\partial \theta_m \partial \phi_m} = \Delta \begin{pmatrix} -\cos \theta_m \sin \phi_m \\ \cos \theta_m \cos \phi_m \\ 0 \end{pmatrix},$$

$$\mathcal{S}_{m,\phi,\phi} = \frac{\partial^2 \mathbf{u}_m}{\partial \phi_m^2} = \Delta \begin{pmatrix} -\sin \theta_m \cos \phi_m \\ -\sin \theta_m \sin \phi_m \\ 0 \end{pmatrix}.$$

I consider now the term $\partial^2 \mathcal{H} / \partial r_{l,\nu} \partial r_{h,\mu}$, which is obtained as

$$\frac{\partial^2 \mathcal{H}}{\partial r_{l,\nu} \partial r_{h,\mu}} = -q^2 \ell_{\mathrm{B}} \sum_{i=0}^{N-1} \sum_{j=i+1}^{N} \left[\mathcal{G}_{hj} \, (r_{i,\nu} - r_{j,\nu})(r_{i,\mu} - r_{j,\mu})(\delta_{i,l} - \delta_{j,l})(\delta_{i,h} - \delta_{j,h}) \right.$$

$$\left. + g_{ij} \, (\delta_{i,l} - \delta_{j,l})(\delta_{i,h} - \delta_{j,h}) \delta_{\nu,\mu} \right]$$

$$+ \frac{Zq\ell_{\mathrm{B}}}{1 + \kappa R_{\mathrm{s}}} \left[(\mathcal{F}_h + \mathcal{K}_h) \, r_{h,\nu} r_{h,\mu} + (f_h + k_h) \, \delta_{\nu,\mu} \right] \delta_{l,h}. \tag{A.59}$$

where the functions $\mathcal{G}_{ij}$, $\mathcal{F}_i$ and $\mathcal{K}_i$ are defined as

$$\mathcal{G}_{ij} \equiv -\frac{e^{-\kappa|\mathbf{r}_i - \mathbf{r}_j|}}{|\mathbf{r}_i - \mathbf{r}_j|^5} \left\{ 3(1 + \kappa|\mathbf{r}_i - \mathbf{r}_j|) + \kappa^2 |\mathbf{r}_i - \mathbf{r}_j|^2 \right\} \tag{A.60}$$

$$\mathcal{F}_i \equiv -\frac{e^{-\kappa(|\mathbf{r}_i| - R_{\mathrm{s}})}}{|\mathbf{r}_i|^5} \left\{ 3(1 + \kappa|\mathbf{r}_i|) + \kappa^2 |\mathbf{r}_i|^2 \right\} \tag{A.61}$$

$$\mathcal{K}_i \equiv -\frac{A}{\alpha} \frac{e^{-(|\mathbf{r}_i| - R_{\mathrm{s}})/\alpha}}{|\mathbf{r}_i|^3} \left\{ \frac{|\mathbf{r}_i|}{\alpha} + 1 \right\}, \tag{A.62}$$

and the functions g_{ij}, f_i and k_i have already been introduced in Eqs. (A.6)-(A.8). The last component which needs to be calculated in order to complete the evaluation of the Hessian matrix is the following derivative (see Eq. (A.51))

$$\frac{\partial r_{l,\nu}}{\partial \gamma_m}\frac{\partial r_{h,\mu}}{\partial \gamma_n} = \begin{cases} \Theta(m-l-1)\Theta(P-m)\Theta(n-h-1)\Theta(P-n)\mathcal{C}_{m,\gamma}^{\nu}\mathcal{C}_{n,\gamma}^{\mu} & l,h < P, \\[2mm] -\Theta(m-l-1)\Theta(P-m)\Theta(h-n)\Theta(n-P-1)\mathcal{C}_{m,\gamma}^{\nu}\mathcal{C}_{n,\gamma}^{\mu} & l < P < h, \\[2mm] -\Theta(n-h-1)\Theta(P-n)\Theta(l-m)\Theta(m-P-1)\mathcal{C}_{m,\gamma}^{\nu}\mathcal{C}_{n,\gamma}^{\mu} & h < P < l, \\[2mm] \Theta(l-m)\Theta(m-P-1)\Theta(h-n)\Theta(n-P-1)\mathcal{C}_{m,\gamma}^{\nu}\mathcal{C}_{n,\gamma}^{\mu} & l,h > P, \end{cases}$$

$$(A.63)$$

where $\mathcal{C}_{m,\gamma}^{\nu}$ has the same definition as, for instance, in Eq. (A.16) (see also Eqs. (A.14) and (A.15)).

Appendix B

Electrostatic Interactions in an Ionic Mixture

In vacuum, fixed charged objects (macroions) interact via Coulomb electrostatic interactions. In an ionic mixture, the interaction between macroions is modified due to the presence of small mobile ions, known as counterions (of the opposite charge) and coions (of the same charge as macroions). These microscopic ions may result from dissociation of surface chemical groups of macroions in an aqueous solution, or may come form dissociation of additional electrolyte or salt molecules in the solution. They form loosely bound ionic clouds around macroions and tend to screen their charges. In particular, counterions, that are attracted towards macroion surfaces, predominantly determine static or dynamic properties of macroionic solutions in many instances [7]. Understanding the *effective* interaction between macroions across an ionic medium requires an understanding of the ionic clouds first. This however appears to be a challenging task from a theoretical point of view, since the long-range nature of Coulomb interaction typically leads to a complex many-body problem, which can be treated only within certain approximations.

A common theoretical approximation to study electrostatic interactions in an ionic mixture is to employ *mean-field approximation*. This amounts to neglecting fluctuations (and correlation effects) in the ionic atmosphere, that is focusing only on the mean resultant electrostatic potential from small ions and macroions. The mean-field theory, known also as Poisson-Boltzmann (PB) theory [11], can be established on a systematic level by means of a saddle-point approximation [11, 200]. In the following section, I derive the PB theory using a simple heuristic argument. The PB theory involves a non-linear equation (the so-called PB equation) for mean electrostatic potential, which can be solved analytically only for a few special cases. In certain conditions, the non-linear PB equation can be approximated by a linear equation, the so-called Debye-Hückel (DH) equation [7, 12], which makes it possible to develop analytical methods for more complex systems such as polymer-sphere interactions as considered in the present work. The DH approximation and its non-linear improvement for the case of charged polymers will be discussed later in this appendix.

While the mean-field theory proves to be a quite useful approximation, it breaks down in the situation where electrostatic correlations among mobile ions become important. This occurs particularly when multivalent counterions are introduced, which are strongly attracted towards macroions and form highly correlated layers on their surfaces. Counterion-induced correlation effects go beyond the scope of the present work and further details can be found,

e.g., in Refs. [199, 200, 201].

B.1 Mean-field theory

Consider a classical charged system consisting of fixed macroions of charge distribution $\sigma(\mathbf{r})e$ in an ionic mixture (electrolyte) of n different ionic species. The solvent is treated as a continuum medium of dielectric constant ε at temperature T, and small ions are taken as point-like particles. This amounts to neglecting the solvent structure, image charges due to dielectric mismatch on the boundaries, and excluded-volume effects due to finite size of small ions. The ionic species i (with $i = 1, \ldots, n$) is present with bulk concentration of c_i and charge valency z_i. In equilibrium, the mean-field theory may be deduced simply by combining two basic relations, namely, the Poisson equation governing the mean electrostatic potential field, $\Psi(\mathbf{r})$, in space and the Boltzmann distribution that determines the number density profile of ions, $\rho_i(\mathbf{r})$, in the presence of macroions.

The Poisson equation reads

$$\nabla^2 \Psi(\mathbf{r}) = -\frac{\sigma(\mathbf{r})e}{\varepsilon\varepsilon_0} - \sum_{i=1}^{n} \frac{z_i e \rho_i(\mathbf{r})}{\varepsilon\varepsilon_0}, \tag{B.1}$$

which is supplemented by the Boltzmann distribution for ionic species i as

$$\rho_i(\mathbf{r}) = c_i\, \Omega_i(\mathbf{r})\, \exp(-z_i e \Psi / k_{\mathrm{B}} T). \tag{B.2}$$

Here $\Omega(\mathbf{r})$ is a geometry function that takes into account the presence of hard walls and specifies the space accessible to mobile ions. The prefactor c_i may be related to the bulk concentration of ions assuming that at large distances from macroions the electrostatic potential vanishes. The Poisson-Boltzmann (PB) equation thus reads

$$\nabla^2 \Psi(\mathbf{r}) = -\frac{\sigma(\mathbf{r})e}{\varepsilon\varepsilon_0} - \sum_{i=1}^{n} \frac{z_i e}{\varepsilon\varepsilon_0}\, c_i\Omega_i(\mathbf{r})\, \exp(-z_i e \Psi / k_{\mathrm{B}} T), \tag{B.3}$$

which involves a non-linear term (second term on the right hand side) that accommodates many-body features: local density of ions which determines the local electrostatic potential is adjusted itself by the electrostatic potential via the exponential Boltzmann factor.

B.2 Debye-Hückel theory: linearization approximation

For small electrostatic potentials, namely, $|z_i e \Psi / k_{\mathrm{B}} T| < 1$, the PB equation may be linearized by expanding the non-linear term up to first order in Ψ as

$$\sum_{i=1}^{n} z_i c_i\, \Omega_i(\mathbf{r})\, e^{-z_i e \Psi / k_{\mathrm{B}} T} \simeq \sum_{i=1}^{n} z_i c_i\, \Omega_i(\mathbf{r}) - \sum_{i=1}^{n} z_i^2 c_i\, \Omega_i(\mathbf{r})\left(\frac{e\Psi(\mathbf{r})}{k_{\mathrm{B}} T}\right). \tag{B.4}$$

Assuming that ions are present everywhere in space, i.e. $\Omega_i(\mathbf{r}) = 1$, and defining the rescaled electrostatic potential $\tilde{\Psi} = e\Psi / k_{\mathrm{B}} T$, one finds the Debye-Hückel (DH) equation as

$$\nabla^2 \tilde{\Psi}(\mathbf{r}) = -4\pi \ell_{\mathrm{B}} \sigma(\mathbf{r}) + \kappa^2 \tilde{\Psi}(\mathbf{r}). \tag{B.5}$$

Note that here I have assumed electroneutrality condition in the bulk, i.e. $\sum_{i=1}^{n} z_i c_i = 0$. The inverse Debye screening length, κ, is defined via

$$\kappa^2 = 4\pi\ell_B \sum_{i=1}^{n} z_i^2 c_i. \tag{B.6}$$

The DH approximation is expected to be valid for not too high electrostatic potentials, which is typically the case for moderate to high salt concentration and not too high surface charges on macroions. For highly charged macroions such as DNA and at low salt, the DH theory is not valid in the vicinity of the macroion surface, where there will be an excessive accumulation of counterions. For charged polymers, these non-linear effects can be accounted for within the DH frame work using a phenomenological approach (see below).

It is useful to consider the solution of the DH equation for a few standard cases.

Point charge

For a fixed elementary point charge located at the origin with the distribution $\sigma(\mathbf{r}) = \delta(\mathbf{r})$, the DH equation may be written as

$$\nabla^2\tilde{\Psi}(\mathbf{r}) - \kappa^2\tilde{\Psi}(\mathbf{r}) = -4\pi\ell_B\delta(\mathbf{r}), \tag{B.7}$$

which can readily be solved using the standard Fourier transformation techniques yielding the so-called Green's function of the DH equation as

$$\tilde{\Psi}(\mathbf{r}) = v_{DH}(\mathbf{r}) \equiv \ell_B\frac{e^{-\kappa|\mathbf{r}|}}{|\mathbf{r}|}. \tag{B.8}$$

This is nothing but the screened Coulomb potential of a fixed charge in the presence of screening salt ions in the medium. At distances smaller than the Debye screening length κ^{-1}, the electrostatic potential is Coulomb-like, but beyond this range, it falls off exponentially with distance from the central charge.

Charged sphere

For a single charged sphere with charge valency Z and radius R (centered at origin), the DH equation may be written as

$$\nabla^2\tilde{\Psi}(\mathbf{r}) - \kappa^2\tilde{\Psi}(\mathbf{r}) = -\frac{Z\ell_B}{R^2}\delta(|\mathbf{r}| - R). \tag{B.9}$$

This equation can be solved easily in polar coordinates assuming that no salt is present inside the sphere (i.e. including the second term on the left hand side only for $|\mathbf{r}| > R$) and that the electrostatic potential vanishes at infinity.[1] The result for the mean electrostatic potential may be cast into a point-charge form as

$$\tilde{\Psi}(\mathbf{r}) = Z_*\ell_B\frac{e^{-\kappa|\mathbf{r}|}}{|\mathbf{r}|}, \tag{B.10}$$

---

[1]Effects due to the discontinuity in salt concentration across the macroion surafce are neglected here.

where the prefactor, Z_* (DH effective charge), reads

$$Z_* = \frac{Z e^{\kappa R}}{1 + \kappa R},\tag{B.11}$$

as used in the chain-sphere interaction potential in the text (see, e.g., Chapter 2).

For a sphere radius of $R = 5$ nm and charge $Z = 15$, the DH approximation (valid for $\tilde{\Psi} < 1$) is expected to become accurate for $\kappa > 0.22$ nm^{-1}. For higher sphere charge, a larger salt screening is required.

Charged cylinder

For a single infinite charged cylinder with linear charge density $-\tau e$ and radius R, the DH equation may be written as

$$\nabla^2 \tilde{\Psi}(\mathbf{r}) - \kappa^2 \tilde{\Psi}(\mathbf{r}) = \frac{2\tau \ell_B}{R} \delta(r - R),\tag{B.12}$$

where r denotes the radial distance from the central cylinder axis. Assuming that the salt is present only outside the cylinder ($r > R$), one can solve the above DH equation [7, 12] obtaining

$$\tilde{\Psi}(\mathbf{r}) = -\frac{2\tau \ell_B}{\kappa R\, K_1(\kappa R)}\, K_0(\kappa r),\tag{B.13}$$

where K_0 and K_1 are modified Bessel functions.

In the zero-salt limit $\kappa \to 0$, one can recover the standard (unscreened) potential $\tilde{\Psi}(\mathbf{r}) = 2\tau \ell_B \ln(r/R)$ (assuming also that the potential is zero at the cylinder surface, i.e. $\tilde{\Psi}(R) = 0$). Note that this result approximately holds within distances smaller than the screening length, i.e. for $R < r < \kappa^{-1}$. For larger separations, the potential decays exponentially with distance since the Bessel functions behave as $K_0(x) \sim K_1(x) \sim \exp(-x)/\sqrt{x}$.

B.3   Counterion condensation at charged cylinders

At equilibrium, counterions tend to diffuse away from macroions in order to maximize the entropy of the system, while at the same time, they are attracted energetically toward the macroion surfaces.

In the presence of a charged cylinder (or line), both competing mechanisms (that is the counterion energetic attraction and the "entropic repulsion") scale like $\sim \ln r$ with the radial distance from the cylinder axis, r. This leads to a threshold binding-unbinding process, which is known as the *counterion-condensation transition* at charged cylinders. On a single-particle level, this threshold behavior can be characterized using the single-counterion interaction energy, $U/(k_B T) = 2(z\ell_B \tau)\ln(r/R) = 2\xi \ln(r/R)$, with an *infinitely long* cylinder in an outer confining cylindrical box of radius $D > R$. Here $\xi = z\ell_B \tau$ is the Manning parameter with $+z$ being the counterion valency and $-\tau$ the cylinder linear charge density. The single-particle partition function may be written as

$$\mathcal{Z}_1 = 2\pi \int_R^D r\, dr\, e^{-2\xi \ln(r/R)} \sim \int_0^\epsilon dy\, e^{-2(\xi-1)y},\tag{B.14}$$

where I have used a logarithmic transformation for the radial coordinate as $y = \ln(r/R)$, and defined $\epsilon = \ln(D/R)$ [187]. The relevant infinite-volume limit (infinite-dilution limit)

for cylinders is determined by this factor as $\epsilon \to \infty$, where $\mathcal{Z}_1$ may remain finite or diverge depending on the Manning parameter ξ: For $\xi < 1$, $\mathcal{Z}_1$ diverges and the single-particle distribution function, $\rho_1(r) \sim \exp(-2\xi \ln r)/\mathcal{Z}_1$, tends to zero reflecting *complete de-condensation* of counterions. For $\xi > 1$, on the contrary, $\mathcal{Z}_1$ remains finite indicating *condensation* of counterions, which adopt a finite density profile at the cylinder (the condensation is not complete in the sense that a fraction of (neutralizing) counterions always escapes to infinity [71]). The above argument suggests a critical threshold of $\xi_* = 1$ for the counterion-condensation transition, which has been confirmed by more systematic approaches including mean-field theory (see e.g. Ref. [188]) and extensive Monte-Carlo simulations [187]. The critical Manning parameter corresponds to a critical linear charge density of

$$\tau_* = \frac{1}{z\ell_{\mathrm{B}}}. \tag{B.15}$$

Note that a similar divergency occurs at $\xi_* = 1$ for a thin charged *line*, i.e. when the cylinder radius tends to $R \to 0$ (even in a finite confining box). But clearly, in this case, the single-particle partition function is divergent *above* the critical Manning parameter ($\xi > \xi_* = 1$). Manning interpreted this divergency as a counterion condensation process onto the charged line, which reduces the effective linear charge density of the line to its critical value [71]. Assuming that the total number of counterions in the system is given by the global electroneutrality condition as $N_{\mathrm{ci}}/L = \tau/z$ (with L being the cylinder or line length), it follows that a fraction $\alpha_{\mathrm{M}} = 1 - 1/\xi$ of counterions (Manning fraction) has to condense on a highly charged line ($\tau > \tau_*$) in order to bring its *effective* (or net) linear charge density down to the critical value τ_*. This process is generally known as *charge renormalization*. A more accurate derivation of the Manning's phenomenological theory for counterion condensation can be found in Ref. [71], where a two-fluid model (based on a mean-field approach that accounts for many-body effects as well) has been developed by partitioning counterions into two population, namely, condensed counterions (within a thin layer on the cylinder surface or on the charged line) and de-condensed counterions (forming a diffuse cloud in the bulk and in equilibrium with the former layer). Within the frame work of the PB theory, a similar conclusion can be reached for a cylinder of finite radius as discussed in Ref. [188], although in this case, the so-called condensed counterions form a smooth and extended density profile in the vicinity of the charged cylinder.

Strictly speaking, the critical counterion condensation behavior emerges only at an infinitely long cylinder or line. For finite cylinders of length L, one can distinguish two regimes of radial distances, namely, $r < L$, where the cylindrical symmetry assumed above (and the results for the threshold behavior) approximately holds, and $r > L$, where counterions experience an almost-spherically-symmetric potential, and thus tend to diffuse away.[2]

As discussed before, in the presence of salt, the counterion-cylinder attraction decays exponentially at large distances beyond the Debye screening length, $r > \kappa^{-1}$, while it is almost logarithmic at smaller distances from the cylinder axis. Therefore, the threshold counterion condensation, that emerges as a result of the interplay between entropic and energetic factors, can occur at a charged cylinder only in the zero-salt limit $\kappa^{-1} \to \infty$ (or equivalently $\kappa \to 0$). The limiting nature of the counterion condensation has been discussed by Manning [71], which reveals that for finite salt concentration, the condensed fraction is always smaller than

---

[2]Note that in the presence of a charged sphere, the entropic factor (that grows as $\sim \ln r$) is much stronger than the counterion-sphere attraction ($\sim 1/r$), and thus counterions always de-condense in the absence of confining boundaries or salt screening effects.

the limiting (zero-salt) value $\alpha_M = 1 - 1/\xi$ and moreover, the convergency to this value is logarithmically weak as κ tends to zero. (Such a weak logarithmic convergency to the critical limit is already indicated by Eq. (B.14) above since the upper limit of the integral depends on the logarithmic size factor $\epsilon = \ln(D/R)$.)

It is therefore important to keep in mind that for finite salt concentrations and for short PE chains (as considered in the present work), the effective (renormalized) charge of the PE chain lies somewhere between the two limits: the upper limit which is set by the bare linear charge density τ (no charge renormalization), and the lower limit which is set by the Manning limiting value $\tau_* = 1/(z\ell_B)$ (maximum charge renormalization).

Appendix C

Virial Expansion

In this appendix, I discuss the standard virial expansion for a simple fluid, and then generalize the same method to obtain a low-concentration expansion for a complex fluid consisting of charged polymers and macroions as used in Chapter 5. (Here I use a simple method to derive the virial expansion. Rigorous derivation of these results can be found in literature [5].)

C.1 Simple fluids

Consider a system of N identical spherical particles that interact via pair potential $v(\mathbf{r})$ (in the units of $k_{\mathrm{B}}T$). The partition function of this system reads

$$\mathcal{Z}_N = \frac{1}{N!}\left[\prod_i \int \frac{\mathrm{d}\mathbf{r}_i}{\lambda_t^3}\right] e^{-\frac{1}{2}\sum_{i\neq j} v_{ij}}, \tag{C.1}$$

where $v_{ij} = v(\mathbf{r}_i - \mathbf{r}_j)$ and λ_t is the thermal wavelength. To proceed further, I make use of Mayer functions as

$$f_{ij} = e^{-v_{ij}} - 1. \tag{C.2}$$

The partition function may thus be rewritten as

$$\mathcal{Z}_N = \frac{1}{N!}\left[\prod_i \int \frac{\mathrm{d}\mathbf{r}_i}{\lambda_t^3}\right] \prod_{j=1}^{N}\prod_{k=j+1}^{N}(1 + f_{jk}). \tag{C.3}$$

Because the particles are indistinguishable, one can expand the integrand in powers of f as

$$\mathcal{Z}_N = \frac{1}{N!}\left[\prod_i \int \frac{\mathrm{d}\mathbf{r}_i}{\lambda_t^3}\right]\left(1 + \frac{N(N-1)}{2}f_{12} + \dots\right), \tag{C.4}$$

which can be simplified further as

$$\mathcal{Z}_N = \frac{1}{N!}\frac{V^N}{\lambda_t^{3N}}\left(1 + \frac{N(N-1)}{2V}\int \mathrm{d}\mathbf{r}\,[e^{-v(\mathbf{r})} - 1] + \dots\right) \tag{C.5}$$

where $\mathbf{r} = \mathbf{r}_i - \mathbf{r}_j$ represents the distance of any two particles. Finally the free energy density of the system (in units of $k_{\mathrm{B}}T$) can be written as

$$\frac{\mathcal{F}_N}{V} = -\frac{1}{V}\ln \mathcal{Z}_N = c\ln(c\lambda_t^3) - c - \ln\left[1 + \frac{N(N-1)}{2V}\int \mathrm{d}\mathbf{r}\,(e^{-v(\mathbf{r})} - 1) + \dots\right]^{1/V}, \tag{C.6}$$

where $c = N/V$ is the particle concentration. Here I have used $\ln N! \simeq N \ln N - N$ in the thermodynamic limit $N \to \infty$. The last term of the above equation can be expanded as

$$-\ln\left[1 + \frac{N(N-1)}{2V}\int d\mathbf{r}\,(e^{-v(\mathbf{r})}-1)+\dots\right]^{1/V} \simeq -\ln\left[1 + \frac{N(N-1)}{2V^2}\int d\mathbf{r}\,(e^{-v(\mathbf{r})}-1)+\dots\right].$$
(C.7)

Using this relation, the free energy density of the system in the low concentration limit is obtained as

$$\frac{\mathcal{F}_N}{V} = c\ln(c\,\lambda_t^3) - c + B_2\,c^2 + \dots,$$
(C.8)

where

$$B_2 = -\frac{1}{2}\int d\mathbf{r}\,[e^{-v(\mathbf{r})}-1]$$
(C.9)

is referred to as the second virial coefficient of the system, which incorporates the inter-particle interactions on the leading order.

C.2   Complex fluids: Mixture of polymers and macroions

In Chapter 5, I employed a virial expansion in order to investigate the reaction equilibrium between charged polymers and macroions in the low-concentration limit. The virial expansion for this system can be obtained as follows.

Consider a solution of N_2 charged spherical colloidal particles (macroions) and N_1 charged polymers, each consisting of $N+1$ monomers, that are confined in a volume of V. The solvent is considered to be a continuum medium, containing small mobile ions (additional salt) as well, which are accounted for only through the *effective* interaction between two fixed elementary charges in this ionic medium, $v(\mathbf{r})$. Likewise, the effective interaction between two monomers is denoted by v_{mm}, and between two spheres by v_{ss}, and between a sphere and a monomer by v_{sm}. The position of the first monomer of the polymer i is given by vector $\mathbf{R}_i$ (with $i = 1, \dots, N_1$). The relative position vector of the other N monomers with respect to the first monomer are given by $\mathbf{r}_{i\nu}$ (denoted by Greek indices, e.g., as $\nu = 1, \dots, N$). The position of the center of macroion j is given by $\mathbf{D}_j$ (with $i = 1, \dots, N_2$) confined in the volume V. The solvent is considered to be a continuum medium.

The effective Hamiltonian of such a system can be written (in units of $k_{\mathrm{B}}T$) as

$$
\begin{aligned}
\mathcal{H}_{\mathrm{tot}} &= \sum_{i=1}^{N_1}\sum_{\nu<\mu}^{N} v_{\mathrm{mm}}(\mathbf{r}_{i\nu}-\mathbf{r}_{i\mu}) + \sum_{i<i'}^{N_1}\sum_{\nu,\mu=1}^{N} v_{\mathrm{mm}}(\mathbf{r}_{i\nu}-\mathbf{r}_{i'\mu}+\mathbf{R}_i-\mathbf{R}_{i'}) \\
&+ \sum_{i=1}^{N_1}\sum_{j=1}^{N_2}\sum_{\nu=1}^{N} v_{\mathrm{sm}}(\mathbf{r}_{i\nu}+\mathbf{R}_i-\mathbf{D}_j) + \sum_{j<j'}^{N_2} v_{\mathrm{ss}}(\mathbf{D}_j-\mathbf{D}_{j'}).
\end{aligned}
$$
(C.10)

Using the above Hamiltonian, the partition function of the solution is written as

$$
\begin{aligned}
\mathcal{Z}_{\mathrm{tot}} &= \frac{1}{N_1!N_2!}\int\prod_{i=1}^{N_1}d\mathbf{R}_i\int\prod_{i=1}^{N_1}\{d\mathbf{r}\}_i\int\prod_{j=1}^{N_2}d\mathbf{D}_j\left[\prod_{i=1}^{N_1}e^{-\sum_{\nu<\mu}^{N} v_{\mathrm{mm}}(\mathbf{r}_{i\nu}-\mathbf{r}_{i\mu})}\right] \\
&\times \left[\prod_{i<i'}^{N_1}e^{-\sum_{\nu,\mu}^{N} v_{\mathrm{mm}}(\mathbf{r}_{i\nu}-\mathbf{r}_{i'\mu}+\mathbf{R}_i-\mathbf{R}_{i'})}\right]\left[\prod_{i,j}^{N_1,N_2}e^{-\sum_{\nu}^{N} v_{\mathrm{sm}}(\mathbf{r}_{i\nu}+\mathbf{R}_i-\mathbf{D}_j)}\right]
\end{aligned}
$$

$$\times \ \left[\prod_{j<j'}^{N_2} e^{-v_{\mathrm{ss}}(\mathbf{D}_j-\mathbf{D}_{j'})} \right], \tag{C.11}$$

where the integrals are taken over all degrees of freedom of macroions and polymers. In particular, $\{\mathrm{d}\mathbf{r}\}_i$ refers to all internal degrees of freedom of polymer i, which can expressed in terms of internal polar and azimuthal angles as will be specified later (Chapter 5).

I now introduce Mayer functions associated with monomer-monomer, monomer-sphere and sphere-sphere system as follows

$$f_{ii'}^{\mathrm{mm}} \ = \ e^{-\sum_{\nu,\mu} v_{\mathrm{mm}}(\mathbf{r}_{i\nu}-\mathbf{r}_{i'\mu}+\mathbf{R}_i-\mathbf{R}_{i'})} - 1, \tag{C.12}$$

$$f_{ij}^{\mathrm{sm}} \ = \ e^{-\sum_{\nu} v_{\mathrm{sm}}(\mathbf{r}_{i\nu}+\mathbf{R}_i-\mathbf{D}_j)} - 1, \tag{C.13}$$

$$f_{jj'}^{\mathrm{ss}} \ = \ e^{-\sum_{\nu} v_{\mathrm{sm}}(\mathbf{D}_j-\mathbf{D}_{j'})} - 1. \tag{C.14}$$

The partition function can be expanded up to the first order in f as

$$\mathcal{Z}_{\mathrm{tot}} = \frac{1}{N_1!N_2!}\mathcal{Z}_1^{N_1} \int \prod_{i=1}^{N_1} \mathrm{d}\mathbf{R}_i \prod_{j=1}^{N_2} \mathrm{d}\mathbf{D}_j \left[1 + \sum_{i<i'}^{N_1} f_{ii'}^{\mathrm{mm}} + \sum_{i,j}^{N_1,N_2} f_{ij}^{\mathrm{sm}} + \sum_{j<j'}^{N_2} f_{jj'}^{\mathrm{ss}} + \mathcal{O}(f^2) \right], \tag{C.15}$$

where $\mathcal{Z}_1$ is the (internal) partition function of a single polymer labeled by i, i.e.

$$\mathcal{Z}_1 = \int \{\mathrm{d}\mathbf{r}\}\ e^{-\sum_{\nu<\mu} v(\mathbf{r}_\nu-\mathbf{r}_\mu)}, \tag{C.16}$$

where I have dropped the polymer label i. By inserting the definition of Mayer functions and performing the necessary integrations and taking into account the fact that macroions and polymers are indistinguishable, the partition function can be written in the low concentration regime as

$$
\begin{aligned}
\mathcal{Z}_{\mathrm{tot}} \ \simeq \ & \frac{1}{N_1!N_2!} V^{N_1+N_2} \mathcal{Z}_1^{N_1} \Big[1 + \\
+ \ & \frac{N_1(N_1-1)}{2V}\mathcal{Z}_1^{-1} \int \mathrm{d}\mathbf{R} \int \{\mathrm{d}\mathbf{r}\} \left(e^{-\sum_{\nu,\mu} v_{\mathrm{mm}}(\mathbf{r}_\nu-\mathbf{r}_\mu+\mathbf{R})} - 1 \right) e^{-\sum_{\nu<\mu} v_{\mathrm{mm}}(\mathbf{r}_\nu-\mathbf{r}_\mu)} \\
+ \ & \frac{N_1 N_2}{V}\mathcal{Z}_1^{-1} \int \mathrm{d}\mathbf{R} \int \{\mathrm{d}\mathbf{r}\} \left(e^{-\sum_{\nu} v_{\mathrm{sm}}(\mathbf{r}_\nu+\mathbf{R})} - 1 \right) e^{-\sum_{\nu<\mu} v_{\mathrm{mm}}(\mathbf{r}_\nu-\mathbf{r}_\mu)} \\
+ \ & \frac{N_2(N_2-1)}{2V} \int \mathrm{d}\mathbf{R} \left(e^{-v_{\mathrm{ss}}(\mathbf{R})} - 1 \right) \Big].
\end{aligned} \tag{C.17}
$$

By introducing the following second virial coefficients for the three different types of interaction potentials present in the above partition function

$$B_2^{\mathrm{pp}} \ = \ -\frac{1}{2} \int \mathrm{d}\mathbf{R} \left[\frac{1}{\mathcal{Z}_1} \left(\int \{\mathrm{d}\mathbf{r}\}\, e^{-\sum_{\nu,\mu} v_{\mathrm{mm}}(\mathbf{r}_\nu-\mathbf{r}_\mu+\mathbf{R})} \right) - 1 \right], \tag{C.18}$$

$$B_2^{\mathrm{sp}} \ = \ -\frac{1}{2} \int \mathrm{d}\mathbf{R} \left[\frac{1}{\mathcal{Z}_1} \left(\int \{\mathrm{d}\mathbf{r}\}\, e^{-\sum_{\nu} v_{\mathrm{sm}}(\mathbf{r}_\nu+\mathbf{R})} \right) - 1 \right], \tag{C.19}$$

$$B_2^{\mathrm{ss}} \ = \ -\frac{1}{2} \int \mathrm{d}\mathbf{R} \left[e^{-v_{\mathrm{ss}}(\mathbf{R})} - 1 \right], \tag{C.20}$$

corresponding with polymer-polymer, polymer-sphere and sphere-sphere respectively, one obtains

$$\mathcal{Z}_{\mathrm{tot}} = \frac{V^{N_1+N_2}}{N_1!N_2!}\mathcal{Z}_1 \left[1 - \frac{N_1(N_1-1)}{V}B_2^{\mathrm{pp}} - \frac{2N_1 N_2}{V}B_2^{\mathrm{sp}} - \frac{N_2(N_2-1)}{V}B_2^{\mathrm{ss}} \right]. \tag{C.21}$$

Finally the free energy, $\mathcal{F}_{\text{tot}} = -\ln \mathcal{Z}_{\text{tot}}$, is calculated from the above expression as

$$\frac{\mathcal{F}_{\text{tot}}}{V} = (C_p \ln C_p - C_p) + (C_m \ln C_m - C_m) + B_2^{\text{pp}} C_p^2 + B_2^{\text{ss}} C_m^2 + 2B_2^{\text{sp}} C_p C_m - C_p \ln \mathcal{Z}_1 \quad (\text{C.22})$$

where $C_p = N_1/V$ is the concentration of polymers and $C_m = N_2/V$ is the concentration of macroions.

In the present study, I primarily focus on a system with like-charged polymers and liked-charged macroions, while charged polymers and macroions are oppositely charged. In this case, the second virial coefficient associated with the polymer-macroion interaction, which is attractive, is much larger that the second virial coefficient associated with macroion-macroion and polymer-polymer interaction. This justifies neglecting B_2^{mm} and B_2^{ss} against B_2^{sm} in the low-concentration regime. For a system of equal concentration for polymers and macroions, $C_p = C_m = C_0$, one thus finds

$$\frac{\mathcal{F}_{\text{tot}}}{V} = 2C_0(\ln C_0 - 1) + C_0 \mathcal{F}_p + 2B_2^{\text{sp}} C_0^2. \quad (\text{C.23})$$

in which $\mathcal{F}_p = -\ln \mathcal{Z}_1$ is the internal free energy of one polymer chain.

As explained in Chapter 5, the complexation reaction in the *dilute limit* can be studied by treating the charged polymer and macroion solution as a mixture of two (ideal) species that can interact with each other and associate into a third species (product), i.e. the complexes of concentration C_c. The free energy of a dilute solution may thus be written as

$$\begin{aligned}
\frac{\mathcal{F}_{\text{tot}}}{V} &= (C_p - C_c)\ln(C_p - C_c) - (C_p - C_c) + (C_m - C_c)\ln(C_m - C_c) \\
&\quad -(C_m - C_c) + C_c \ln C_c - C_c + C_p \mathcal{F}_p + C_c \Delta\mathcal{F},
\end{aligned} \quad (\text{C.24})$$

where the last term represents the chemical potential of a complex and $\mathcal{F}_p$ is that of a polymer. Minimizing the above free energy expression with respect to the concentration of complexes, C_c, gives the law of mass action for $C_p = C_m = C_0$ as

$$\frac{C_c}{(C_0 - C_c)^2} = e^{-\Delta\mathcal{F}}, \quad (\text{C.25})$$

which can be solved for C_c yielding $C_c = C_0^2 \exp(-\Delta\mathcal{F})$ in the limit of low concentrations $C_0 \exp(-\Delta\mathcal{F}) \ll 1$. Inserting this result into the preceding free energy, one obtains

$$\frac{\mathcal{F}_{\text{tot}}}{V} = 2C_0(\ln C_0 - 1) + C_0 \mathcal{F}_p + C_0^2 e^{-\Delta\mathcal{F}}. \quad (\text{C.26})$$

Comparison between Eqs. (C.23) and (C.26) shows that $\Delta\mathcal{F}$ can be associated with the second virial coefficient of the polymer-macroion interaction as

$$e^{-\Delta\mathcal{F}} = 2B_2^{\text{sp}} = -\int d\mathbf{R} \left[\frac{1}{\mathcal{Z}_1} \left(\int \{d\mathbf{r}\} e^{-\sum_\nu v_{\text{sm}}(\mathbf{r}_\nu + \mathbf{R})} \right) - 1 \right], \quad (\text{C.27})$$

which reproduces Eq. (5.11) in the text.

Appendix D

Notes on Discretization Effects

In the numerical studies used in this thesis, I have employed a discretization method by representing a continuous polyelectrolyte (PE) chain with a discrete set of N rigid subunits of fixed length Δ, where the contour length of the chain $L = N\Delta$ is fixed (see, e.g., Chapter 2). Clearly, in the limit $N \to \infty$, one recovers the continuum limit. The results obtained with a finite number of dicretization points depend on N. The goal is to take a large value for N such that the discretization effects are minimized. This is however limited in practice since large N renders a large computational time.

Here I use two quantities to examine discretization effects: i) the energy difference between an isolated complex and an isolated PE chain as reference system, i.e. $\Delta\mathcal{H}^* = \mathcal{H}_c^* - \mathcal{H}_p^*$, and ii) the difference between the Gaussian-fluctuations entropic contribution, $\Delta\mathcal{F}^{(1)} = \mathcal{F}_c^{(1)} - \mathcal{F}_p^{(1)}$ (due to chain fluctuations around the ground-state), of a complex and that of a free PE chain (see Chapter 5). These quantities are calculated for various number of discretization degree, N, and shown in Figure D.1 as a function of N for a typical set of parameters used in the present study (corresponding to 146-base-pair DNA complexed with histone proteins), i.e. chain persistence length $\ell_\mathrm{p} = 30$ nm, chain contour length $L = 49.64$ nm, chain linear
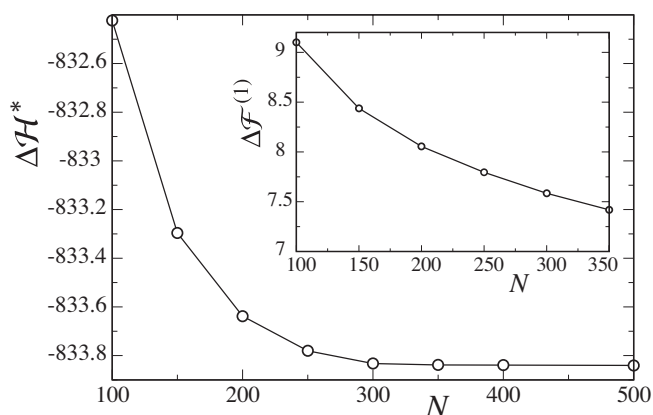
Figure D.1: The binding energy of a chain to a macroion, $\Delta\mathcal{H}^*$, shown as a function of the discretization degree, N (see the text for parameters). The inset shows the difference in the Gaussian-fluctuations correction term, $\Delta\mathcal{F}^{(1)}$.

charge density $\tau = 5.88$ nm^{-1}, sphere radius $R_\mathrm{s} = 5$ nm, sphere charge $Z = 40$. The salt concentration is set to zero, i.e. $\kappa = 0$.

For large enough N, one expects that both quantities tend to a saturated constant value corresponding to the continuum-limit results. In fact, as seen in the graph, variations of $\Delta \mathcal{H}^{(0)}$ with N is quite small, e.g., when N increases from $N = 100$ up to $N = 500$, there is only about 0.1% relative change in $\Delta \mathcal{H}^{(0)}$. For $\Delta \mathcal{F}^{(1)}$ the saturation appears to be weaker, but the dependence on N is still quite weak (a change of about 10%). Note that larger N means a more complicated energy landscape and as a result, a slower minimization routine. Therefore as a compromise between numerical accuracy and reasonable computational time, I have chosen $N = 250$.

Appendix E

Notes on Soft-Core Potential

In the chain-sphere model, I use a repulsive short-ranged potential in order to exclude the polyelectrolyte chain from the spherical region introduced by the macroion. This soft-core potential is taken in the form of an exponentially decaying function, i.e. as $\sim A \exp[-(r - R_\mathrm{s})/\alpha]$, where r is the distance from the sphere center of radius R_s, and A and α represent the strength and the range of this potential respectively (note that α represents the thickness of the penetration layer and, hence, the *softness* of the sphere). These two latter quantities are chosen such that the penetration of the chain into the sphere remains small as compared with the sphere radius, mimicking thus a rigid sphere. The chain penetration is influenced by other parameters such as salt concentration and one needs to specify an appropriate regime for the strength and range of the soft potential in terms of charge parameters. Before proceeding further, I emphasize that taking a soft sphere is advantageous as compared with a hard-core sphere used in previous studies [48, 49] in that i) one can account for the chain fluctuations on the sphere because small chain penetrations into the sphere are allowed, and ii) one can relax the hard-core constraint and thus the use of a constrained minimization method.

Consider a single chain bead (or particle) of charge valency q in the vicinity of an oppositely charged sphere of valency Z. The bead-sphere interaction (in units of $k_\mathrm{B}T$) is written as

$$V_1 = -\frac{qZ\ell_\mathrm{B}}{1 + \kappa R_\mathrm{s}} \left[\frac{e^{-\kappa(r - R_\mathrm{s})}}{r} - A e^{-(r - R_\mathrm{s})/\alpha} \right], \tag{E.1}$$

where the first term corresponds to the screened electrostatic attraction and the second term is the soft repulsive potential. The competition between these two terms lead to an equilibrium position for the bead (energy minimum location), r_*, which determines the effective radius of the sphere. Note that I have chosen the strength of the soft potential to be proportional with the charge parameters, q, Z and ℓ_B in such a way that the location of this minimum is independent of these parameters. I choose $A \ll 1/R_\mathrm{s}$ (e.g., typically $A \simeq 0.01$ nm^{-1} for $R_\mathrm{s} = 5$ nm) such that the soft-repulsion is not dominant at the contact with the sphere. But, on the other hand, take α within the range $\alpha < 1/\kappa$ such that the chain penetration remains small (see below).

In inset of Figure E.1, I plot V_1 as a function of r, for $Z = 70$, $q = 1.16$, $R_\mathrm{s} = 5$ nm, $A = 0.012$ nm^{-1} and varius values of α and two different values of κ. The three curves related to $\kappa = 1$ nm^{-1} show very little shift in the position and the value of the interaction energy minimum. But for $\kappa = 5$ nm^{-1}, both the value and the position of the minimum of energy is dramatically changed, therefore for $\kappa = 5$ nm^{-1}, $\alpha = 0.1$ nm is not a good choice. Acceptable
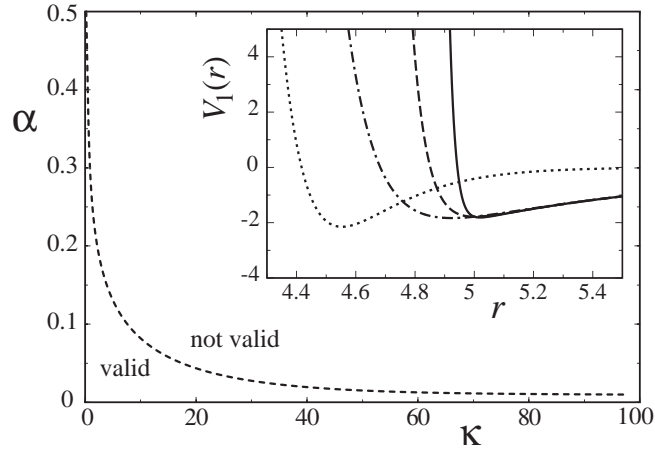
Figure E.1: The range of acceptable values of α for different κ. The inset shows the interaction energy of one bead with a sphere of charge valency $Z = 70$ (Eq. (E.1)) for different values of κ and α. The full line, dashed line and dot-dashed line are obtained for $\kappa = 1$ nm^{-1} but with different $\alpha = 0.02, 0.05$ and 0.1 nm respectively. The dotted curve is the interaction energy for $\kappa = 5$ nm^{-1} and $\alpha = 0.1$ nm.

values of α are conventionally chosen such that the distance of the potential minimum from the sphere center lies within the range $|r_* - R_{\mathrm{s}}| < 0.02R_{\mathrm{s}}$. The results are shown in the main set of figure indicating acceptable (valid) and unacceptable (not valid) ranges of α in terms of κ. The threshold value for α (dashed curve) is roughly proportional with κ^{-1}. In most of cases considered in this thesis, I have chosen the value of α as $\alpha = 0.02$ nm, which as seen from the graph, lies in the acceptable range for small to quite large values of κ.

Bibliography

[1] B. Alberts, A. Johnson, J. Lewis, M. Raff, K. Roberts and P. Walter, *Molecular Biology of The Cell* (Garland Science (Taylor and Francis Group), New York, 2002)

[2] B. M. Turner, *Chromatin and Gene Regulation* (Blackwell Science Ltd, Oxford, 2001)

[3] W. H. Press, B. P. Flanney, S. A. Teukolsky and W. T. Vetterling, *Numerical Recipes In C* (Cambridge University Press, Cambridge, 1998)

[4] J. Israelachvili, *Intermolecular and Surface Forces* (Academic Press, London, 1991).

[5] L. E. Reichl, *A Modern Course in Statistical Physics* (Edward Arnold Ltd, 1980)

[6] A.Y. Grosberg, A.R. Khokhlov, *Statistical Physics of Macromolecules* (American Institute of Physics, New York, 1994).

[7] P.M.V. Résibois, *Electrolyte Theory* (Harper and Row, New York, 1968).

[8] F. Oosawa, *Polyelectrolytes* (Marcel Dekker, New York, 1971).

[9] C. Holm, P. Kékicheff and R. Podgornik, *Electrostatic Effects in Soft Matter and Biophysics* (Kluwer Academic Publisher, Dordrecht, 2001).

[10] H. Dautzenberg, W. Jaeger, B.P.J. Kötz, C. Seidel, D. Stscherbina, *Polyelectrolytes: Formation, characterization and application* (Hanser Publishers, New York, 1994).

[11] E.J. Verwey, J.T.G. Overbeek, *Theory of the Stability of Lyophobic Colloids* (Elsevier, Amsterdam, 1948).

[12] P. Debye, E. Hückel, Physik. Z. **24**, 185 (1923).

[13] N. Bjerrum, Kgl. Danske Videnskab. Selskab. Mat.-fys. Medd. **7**, 1 (1926).

[14] H. Boroudjerdi, R.R. Netz, Europhys. Lett. **64**, 413 (2003); J. Phys.: Condens. Matter **17**, S1137 (2005).

[15] C. Fleck and R. R. Netz Phys. Rev. Lett. (2005) in press.

[16] H. Boroudjerdi, Y.-W. Kim, A. Naji, R.R. Netz , X. Schlagberger, A. Serr, Physics Reports (2005)–in press.

[17] J. K. Strauss and L. J. Maher, Science **266**, 1829 (1994).

[18] P. Haronska, T. A. Vilgis, R. Grottenmüller, and M. Schmidt, Macromol. Theor. Simul. **7**, 241 (1998).

[19] G. B. Sukhorukov, E. Donath, S. Davis, H. Lichtenfeld, F. Cauruso, V. I. Popov, and H. Möhwald, Polym. Adv. Technol. **89**, 759 (1998).

[20] A. U. Bielinska, J. F. Kukowska-Latallo, J. R. Baker Jr. Biochim. Biophys. Acta **1353**, 180 (1997).

[21] J. Rieger, E. Hädicke, I. U. Rau, and D. Boeckh, Tenside Surf. Det. **34**, 430 (1997).

[22] P. L. Dubin, D.R. Rigsbee, L.-M. Gan and M. A. Fallon Macromolecules **21**, 2555 (1988)

[23] D. W. McQuigg, J. I. Kaplan, and P. L. Dubin, J. Phys. Chem. **96**, 1973 (1992)

[24] P. L. Dubin, M. E. Curran, and J. Hua, Langmuir **6**, 707 (1990).

[25] P. L. Dubin, M. E. Curran, and J. Hua, J. Phys. Chem. **96**, 1973 (1992).

[26] J. Xia, P. L. Dubin and H. Dautzenberg Langmuir **9**, 2015 (1993).

[27] Y. Li, P. L. Dubin, H. A. Havel, S. L. Edwards and H. Dautzenberg Langmuir **11**, 2486 (1995).

[28] A. Tsuboi, T. Izumi, M. Hirata. J. Xia, P. L. Dubin and E. Kokufta Langmuir **12**, 6295 (1996).

[29] F. Ganachaud, A. Elaissari, C. Pichot, A. Laayoun, and P. Cros, Langmuir **13**, 701 (1997).

[30] D. I. Gittins and F. Caruso, J. Phys. Chem. B **105**, 6846 (2001).

[31] D. I. Gittins and F. Caruso, Adv. Mater. **12**, 1947 (2000).

[32] J. D. McGhee and G. Felsenfeld, Annu. Rev. Biochem **49**, 1115 (1980).

[33] J. Widom, Annu. Rev. Biophys. Biophys. Chem. **18**, 365 (1989).

[34] F. Caruso, R. Caruso, and H. Möhwald, Science **282**, 1111 (1998).

[35] E. Helfer, S. Harlepp, L. Bourdieu, J. Robert, F. C MacKintosh and D. Chatenay, Phys. Rev. Lett. **85**, 457 (2000).

[36] H. Zhang, P. L. Dubin, J. Ray, G. S. Manning, C. N. Moorefield and G. R. Newkome, J. Phys. Chem. B **103**. 2347 (1999).

[37] E. M. Mateescu, C. Jeppesen, and P. Pincus, Europhys. Lett. **46**, 493 (1999).

[38] R. R. Netz and J.-F. Joanny, Macromolecules **31**, 5123(1998).

[39] R. R. Netz and J.-F. Joanny, Macromolecules **32** , 9013 (1999).

[40] R. R. Netz and J.-F. Joanny, Macromolecules **32**, 9026(1999).

[41] M. Jonsson and P. Linse, J. Chem. Phys. **115**, 3406 (2001).

[42] M. Jonsson and P. Linse, J. Chem. Phys. **115**, 10975 (2001).

[43] P. Chodanowski and S. Stoll, J. Chem. Phys. **115**, 4951 (2001).

[44] S. Stoll and P. Chodanowski, Macromolecules **35**, 9556 (2002).

[45] H. Schiessel, R.F. Bruinsma, and W.M. Gelbart, J. Chem. Phys. **115**, 7245 (2001).

[46] P. Sens and J.-F. Joanny, Phys. Rev. Lett. **84**, 4862 (2000).

[47] M. Skepö and P. Linse, Macromolecules **36**, 508 (2003).

[48] K. K. Kunze and R. R. Netz, Phys. Rev. Lett. **85**, 4389 (2000);

[49] K. K. Kunze and R. R. Netz, Phys. Rev. E **66**, 011918 (2002).

[50] H. Schiessel, J. Phys.: Condensed Matter **15**, R699 (2003).

[51] T. Wallin and P. Linse, Langmuir **12**, 395 (1996)

[52] T. Wallin and P. Linse, J. Chem. Phys. **109**, 5089 (1998)

[53] A. Laio and M. Parrinello, Proc. Natl. Acad. Sci. **99**, 12562 (2002).

[54] M. T. Record jr. , C. F. Anderson and T. M. Lohman, Q. Rev. Biophys. **11**, 103 (1978).

[55] S. Alexander, P. M. Chaikin, P. Grant, G. J. Morales, D. Hone and P. Pincus, J. Chem. Phys. **80**, 11 (1984)

[56] R. R. Netz and H. Orland, Eur. Phys. J. E **11**, 301 (2003).

[57] F. von Goeler and M. Muthukumar, J. Chem. Phys. **100**, 7796 (1994).

[58] E. Gurovitch and P. Sens, Phys. Rev. Lett. **82**, 339 (1999).

[59] R. Golestanian, Phys. Rev. Lett. **83**, 2473 (1999).

[60] N. L. Marky and G. S. Manning, J. Mol. Biol. **254**, 50 (1995).

[61] H. Schiessel, J. Rudnick, R. F. Bruinsma, and W. M. Gelbart, Europhys. Lett. **51**, 237 (2000).

[62] H. Schiessel Macromolecules **36**, 3424 (2003).

[63] A. Akinchina and P. Linse Macromolecules **35**, 5183 (2002).

[64] T. T. Nguyen and B.I. Shklovskii, Physica A **293**, 324 (2001).

[65] S. Y. Park, R. F. Bruinsma, and W. M. Gelbart, Europhys. Lett. **46**, 454 (1999).

[66] T. T. Nguyen A. Y. Grosberg and B. I. Shklovskii, J. Chem. Phys. **113**, 1110 (2000).

[67] T. T. Nguyen and B. I. Shklovskii, J. Chem. Phys. **114**, 5905 (2001).

[68] T. T. Nguyen and B. I. Shklovskii, J. Chem. Phys. **115**, 7298 (2001).

[69] A. Yu. Grosberg, T. T. Nguyen, B. I. Shklovskii, Rev. Mod. Phys. **74**, 329 (2002).

[70] K. K. Kunze and R. R. Netz, Europhys. Lett. **58**, 299 (2002).

[71] G. S. Manning, J. Chem. Phys. **51**, 924 (1969).

[72] H. Boroudjerdi and R. R. Netz, Europhys. Lett. **71**, 1022 (2005)

[73] G. S. Manning, K. K. Ebralidse, A. D. Mirzabekov and A. Rich, J. Biomol. Struct. Dyn. **6**, 877 (1989).

[74] K. J. Polach, and J. Widom, J. Mol. Biol. **254**, 130 (1995).

[75] K. J. Polach, and J. Widom, J. Mol. Biol. **258**, 800 (1996).

[76] J. D Anderson, and J. Widom, J. Mol. Biol. **296**, 979 (2000).

[77] N. L. Marky and G. S. Manning, Biopolymers **31**, 1543 (1991).

[78] J. J. Hayes and J. C. Hansen, Curr. Opin. Gene. Dev. **11**, 124 (2001).

[79] D. J. Clark and G. Felsenfeld, The EMBO J. **10**, 387 (1991).

[80] J. J. Hayes, T. D. Tullius and A. P. Wolffe Proc. Natl. Acad. Sci. **87**, 7405 (1990).

[81] J. Ausio, D. Seger and H. Eisenberg J. Mol. Biol. **176**, 77 (1984).

[82] R. E. Harrington, Biopolymers **20**, 719 (1981).

[83] R. E. Harrington, Biochemistry **21**, 1177 (1982).

[84] G. Russev, L. Vassilev and R. Tsanev Molec. Biol. Rep. **6**, 45 (1980).

[85] S. N. Khrapunov, A. I. Dragan, A. V. Sivolob and A. M. Zagariya Biochim. Biophys. Acta **1351**, 213 (1997).

[86] A. E. Dieterich, R. Axel and C. R. Cantor J. Mol. Biol. **120**, 587 (1979).

[87] D. W. Brown, L. J. Libertini and E. W. Small Biochemistry **30**, 5293 (1991).

[88] L. J. Libertini and E. W. Small, Nucleic Acids Res. **8**, 3517 (1980).

[89] L. J. Libertini and E. W. Small, Biochemistry **21**, 3327 (1982).

[90] L. J. Libertini and E. W. Small, Nucleic Acids Res. **15**, 6655 (1987).

[91] I. Oohara and A. Wada J. Mol. Biol. **196**, 399 (1987).

[92] P. T. Lowary, and J. Widom, Proc. Natl. Acad. Sci. **94**, 1183 (1997).

[93] P. T. Lowary, and J. Widom, J. Mol. Biol. **276**, 19 (1998).

[94] A. Flaus and T. J. Richmond, J. Mol. Biol. **275**, 427 (1998).

[95] I. M. Kulić and H. Schiessel, Biophys. J. **84**, 3197 (2003).

[96] I. M. Kulić and H. Schiessel, Phys. Rev. Lett.**91**, 148103 (2003).

[97] I. M. Kulić and H. Schiessel, Phys. Rev. Lett.**92**, 228101 (2004).

[98] F. Mohammad-Rafiee, I. M. Kulić and H. Schiessel J. Mol. Biol. **344**, 47 (2004).

[99] V. G. Gordon, V. N. Schumaker, D. E. Olins, C. M. Knobler and J. Hoeowitz Nucl. Acids Res. **6**, 3845 (1979).

[100] A. Prunell Biophys. J. **74**, 2531 (1998).

[101] R. T. Simpson J. Biol. Chem. **254**, 10123 (1979).

[102] W. O. Weischet, K. Tatchell K. E. van Holde and H. Klump, Nucleic Acids Res. **5**, 139 (1978).

[103] T. D. Yager and K. E. van Holde, J. Biol. Chem. **259**, 4212 (1984);

[104] T. D. Yager, C. T. McMurray, and K. E. van Holde, Biochemistry **28**, 2271 (1989).

[105] R. D. Kornberg and A. Klug, Sci. Am. **244**, 48 (1981).

[106] K. Luger and T. J. Richmond, Curr. Opin. Struct. Biol. **8**, 33 (1998).

[107] M. Bennink, S. H. Leuba and G. Leno, Biophy. J. **78(1)**, 395A (2000).

[108] Y. Cui and C. Bustamente, Proc. Natl. Acad. Sci. USA **97**, 127 (2000).

[109] G. Felsenfeld, Nature **355**, 219 (1992).

[110] G. Felsenfeld, Cell **86**, 13 (1996).

[111] J. D. McGhee and G. Felsenfeld, Nucleic Acids Res. **8**, 2751 (1980).

[112] L. Stryer, *Biochemistry*, (W. H. Freeman, New York, 1995).

[113] E. C. Uberbacher, V. Ramakrishnan, D. E. Olins, and G. J. Bunick, Biochemistry **22**, 4916 (1983).

[114] M. L. Bennink et al., Nature Struct. Biol. **5**, 139 (1978).

[115] J. F. Marko and E. D. Siggia, Biophys. J. **73**, 2173 (1997).

[116] F. Thoma, TH. Koller and A. Klug, J. Cell Biol. **83**, 403 (1979).

[117] J. Allan, T. Mitchell, N. Harborne, L. Boehm and C. Crane-Robinson, J. Mol. Biol. **187**, 591 (1986).

[118] K. P. Nightingale, D. Pruss and A. P. Wolffe, J. Biol. Chem. **271**, 403 (1996).

[119] D. J. Clark and T. Kimura, J. Mol. Biol. **211**, 883 (1990).

[120] J. Widom, J. Mol. Biol. **190**, 411 (1986).

[121] J. Yao, P. T. Lowary and J. Widom, Proc. Natl. Acad. Sci. **87**, 7603 (1990).

[122] C. L. Woodcock, S. A. Grigoryev, R. A. Horowitz and N. Whitaker, Proc. Natl. Acad. Sci. **90**, 7603 (1993).

[123] J. Bednar, R. A. Horowitz, S. A. Grigoryev, L. M. Carruthers, J. C. Hansen, A. J. Koster and C. L. Woodcock, Proc. Natl. Acad. Sci. **95**, 14173 (1998).

[124] V. Katritch, C. Bustamante and W. K. Olson, J. Mol. Biol. **295**, 29 (2000).

[125] R. A. Horowitz, D. A. Agard, J. W. Sedat and C. L. Woodcock, J. Cell Biol. **125**, 1 (1994).

[126] J. A. Martino, V. Katritch and W. K. Olson Structure **7**, 1009 (1999).

[127] J. Zlatanova, S. H. Leuba, G. Yang, C. Bustamante and K. van Holde, Proc. Natl. Acad. Sci. **91**, 5277 (1994).

[128] S. H. Leuba, G. Yang, C. Robert, B. Samori, K. van Holde, J. Zlatanova and C. Bustamante, Proc. Natl. Acad. Sci. **91**, 11621 (1994).

Zlatanova J, Leuba S H and van Holde K 1998 Biophys. J. 74 2554

[129] J. Zlatanova, S. H. Leuba and K. van Holde, Biophys. J. **74**, 2554 (1998).

[130] B. Rydberg, W. R. Holley, I. S. Mian, and A. Chatterjee, J. Mol. Biol. **284**, 71 (1998).

[131] M. G. Poirier, A. Nemani, P. Gupta, S. Eroglu and J. F. Marko Phys. Rev. Lett. **86**, 360 (2001).

[132] F. Gill-Ortiz, I. Fita, S. Ramon-Maiques, A. Marina and V. Rubio, Acta. Cryst. D**58**, 1892 (2002).

[133] K. van Holde and J. Zlatanova J. Mol. Biol. **93**, 8373 (1995).

[134] P. J. Horn and C. L. Peterson, Science **297**, 1824 (2002).

[135] M. Hammermann, K. Toth, C. Rodemer, W. Waldeck, R. P. May and J. Langowski, Biophys. J. **79**, 584 (2000).

[136] D. A. Beard and T. Schlick, Structure **9**, 105 (2001).

[137] H. Schiessel, W. M. Gelbart and R. Bruinsma, Biophys. J. **80**, 1940 (2001).

[138] G. Wedemann and J. Langowski, Biophys. J. **82**, 2847 (2002).

[139] H. Schiessel, Europhys. Lett. **58**, 140 (2002).

[140] B. Mergell, R. Everaers and H. Schiessel, Phys. Rev. E **70**, 011915 (2004).

[141] E. M. Bradbury, J. Cell. Biochem. Suppl. **30/31**, 177 (1998).

[142] J. B. E. Burch and H. G. Martinson, Nucleic Acids Res. **8**, 4969 (1980).

[143] L. J. M. Jason, S. C. Moore, J. D. Lewis, G. Lindsey and J. Ausio, BioEssays **24**, 166 (2002).

[144] J. Allan, N. Harborne, D. C. Rau and H. Gould J. Cell Biol. **93**, 285 (1982).

[145] B. M. Turner, BioEssays **22**, 836 (2002).

[146] A. J. McNairn and D. M. Gilbert, BioEssays **25**, 647 (2003).

[147] F. Weissmann and F. Lyko, BioEssays **25**, 792 (2003).

[148] K. Luger, A. W. Mäder, P. K. Richmond, D. F. Sargent and T. J. Richmond, Nature (London) **389**, 251 (1997)

[149] C. A. Davey, D. F. Sargent, K. Luger, A. W. Mäder and T. J. Richmond, Nature (London) **389**, 251 (1997)

[150] C. Zhang and J. J. Hayes, Biopolymers **68**, 539 (2003).

[151] K. van Holde, Nature **362**, 111 (1993).

[152] J. R. Davie and V. A. Spencer, J. Cell. Biochem. Suppl. **32/33**, 141 (1999).

[153] B. D. Strahl and C. D. Allis, Nature **403**, 41 (2000).

[154] G. Arents and E. N. Moudrianakis, Proc. Natl. Acad. Sci. **90**, 10489 (1993).

[155] L. Louters and R. Chalkley, Biochemistry **23**, 547 (1984).

[156] K. P. Nightingale, D. Pruss and A. P. Wolffe, J. Biol. Chem. **271**, 7090 (1996).

[157] F. Mühlbacher, C. Holm and H. Schiessel, Submitted to PRL (2005)

[158] E. S. Sobel and J. A. Harpst, Biopolymers **31**, 1559 (1991).

[159] G. S. Manning, Biopolymers **20**, 1751 (1981)

[160] N. Borochov H. Eisenberg and Z. Kam, Biolopymers **20**, 231 (1981)

[161] D. Shore and R. L. Baldwin J. Mol. Biol. **170**, 983 (1983).

[162] P. Cluzel, A. Lebrun, C. Heller, R. Lavery, J.-L Viovy, D. Chatenay and F. Caron Science **271**, 792 (1996).

[163] S. B. Smith, Y. Cui and C. Bustamante Science **258**, 1122 (1992).

[164] S. B. Smith, L. Finzi and C. Bustamante Science **271**, 795 (1996).

[165] C. Bustamante, J. F. Marko, E. D Seggia and S. Smith Science **265**, 1599 (1994).

[166] C. Frontali, E. Dore, A. Ferrauto and E. Gratton Biopolymers **18**, 1353 (1979).

[167] M. Rief, H. Clausen-Schaumann and H. Gaub Nat. Struct. Biol. **6**, 346 (1999).

[168] P. J. Haggerman Ann. Rev. Biophys. Biophys. Chem, **17**, 265 (1988).

[169] J. F. Marko and E. D. Seggia Phys. Rev. E, **52**, 2912 (1995).

[170] T. R. Strick, J.-F Allemand, V. Croquette and D. Bensimon J. Stat. Phys., **93**, 647 (1998).

[171] D. Harries, S. May, W. M. Gelbart and A. Ben-Shaul Biophy. J., **75**, 159 (1998).

[172] J. O. Rädler, I. Koltover, T. Salditt and C. R. Safinya, Science **275**, 810 (1997).

[173] C. S. O'Hern and T. C. Lubensky, Phys. Rev. Lett. **80**, 4345 (1998).

[174] J. Skolnick and M. Fixman, Macromolecules **10**, 944 (1977).

[175] T. Odijk, J. Polym. Sci. **15**, 477 (1977).

[176] M. Fixman J. Chem. Phys. **76**, 6346 (1982).

[177] T. Odijk, Macromolecules **28**, 7016 (1995).

[178] J.-L. Barrat and J.-F. Joanny, Europhys. Lett. **24**, 333 (1993);

[179] J.-L. Barrat and J.-F. Joanny, J. Phys. II France **4**, 1089 (1994);

[180] R. Golestanina, M. Kardar and T.B. Liverpool Phys. Rev. Lett. **82**, 4456 (1999).

[181] R. Zandi, J. Rudnick and R. Golestanian, Eur. Phys. J. E **9**, 41 (2002).

[182] R. Zandi, J. Rudnick and R. Golestanian, Phys. Rev. E **67**, 021803 (2003).

[183] R. Zandi, J. Rudnick and R. Golestanian, Phys. Rev. E **67**, 061805 (2003).

[184] R. Zandi, R. Golestanian and J. Rudnick, App. Phys. Lett. **84**, 5467 (2003).

[185] A. R. Khokhlov, J. Phys. A: Math. Gen. **13**, 979 (1980).

[186] J. Ray and G. S. Manning Macromolecules **32**, 4588 (1999).

[187] A. Naji, R.R. Netz, Phys. Rev. Lett. (2005), in press; e-print: cond-mat/0504447.

[188] B.H. Zimm, M. Le Bret, J. Biomol. Struct. Dyn. **1**, 461 (1983); M. Le Bret, B.H. Zimm, Biopolymers **23**, 287 (1984).

[189] G. S Manning Cell Biophysics **7**, 57 (1985).

[190] C. P. Woodbury Jr. and G. V. Ramanathan Macromolecules **15**, 82 (1982).

[191] J. Skolnick and E. K. Grimmelmann, Macromolecules **13**, 335 (1980).

[192] J. Wilhelm and E. Frey, Phys. Rev. Lett. **77**, 2581 (1996).

[193] M. S. Z. Kellermayer, S. B. Smith, H. L. Granzier and C. Bustamante, Science **276**, 1112 (1997).

[194] M. Rief, M. Gautel, F. Oesterhelt, J. M. Fernandez and H. E. Gaub, Science **276**, 1109 (1997).

[195] M. Rief, J. M. Fernandez and H. E. Gaub, Phys. Rev. Lett. **81**, 4764 (1998).

[196] J. P. Kemp and Z. H. Chen, Phys. Rev. Lett. **81**, 3880 (1998).

[197] E. Allahyarov, H. Löwen, A. A. Louis, and J. P. Hansen, Europhys. Lett. **57**, (2002) 730.

[198] I. Rouzina, V. A. Bloomfield, J. Phys. Chem. **100**, 9977 (1996).

[199] A. Naji, S. Jungblut, A.G. Moreira, R.R. Netz, Physica A **352**, 131 (2005).

[200] R.R. Netz, Eur. Phys. J. E **5**, 557 (2001).

[201] R.R. Netz, H. Orland, Eur. Phys. J. E **1**, 203 (2000).

[202] C. N. Likos, N. Hoffmann, H. Löwen and A. A. Louis J. Phys.: Condens. Matter **14**, 7681 (2002).

[203] T. Arakawa and S. N. Timasheff Biochemistry **25**, 5912 (1984).

[204] A. A. Louis, E. Allahyarov, H. Löwen and R. Roth Phys. Rev. E **65**, 061407 (2002).

[205] E. Allahyarov, H. Löwen, J. P. Hansen and A. A. Louis Phys. Rev. E **65**, 061407 (2002).

[206] R. Podgornik and B. Jönsson, Europhys. Lett. **24**, 501 (1993).

[207] J. Dzubiella, A. G. Moreira and P. Pincus, Macromolecules, **36**, 1741(2003).

[208] R. Podgornik, J. Polym. Sci. Part B: Polym. Phys. **42**, 3539 (2004).

[209] R. Podgornik, T. Åkesson and B. Jönsson, J. Chem. Phys. **102**, 9423 (1995).

[210] H. Boroudjerdi and R. R. Netz, Europhys. Lett. **64**, 413 (2003).

[211] E. Raspaud, I. Chaperon, A. Leforestier and F. Livolant Biophys. J. **77**, 1547 (1999).

[212] S. Mangenot, A. Leforestier, P. Vachette, D. Durant, and F. Livolant, Biophys. J. **82**, 345 (2002).

[213] S. Mangenot, E. Raspaud, C. Tribet, L. Belloni and F. Livolant, Eur. Phys. J. E **7**, 221 (2002).

[214] F. Artzner, R. Zantl, G. Rapp and J. O. Rädler, Phys. Rev. Lett. **81**, 5015 (1998).

[215] A. Leforestier, J. Dubochet and F. Livolant, Biophys. J. **81**, 2414 (2001).

[216] S. Mangenot, A. Leforestier, D. Durand and F. Livolant, Biophys. J. **84**, 2570 (2003).

[217] V. Lorman, R. Podgornik and B. Žekš, Phys. Rev. Lett. **87**, 218101-1 (2002).

[218] V. Lorman, R. Podgornik and B. Žekš, Europhys. Lett. **69**, 1017 (2005).

List of Publications

1. H. Boroudjerdi, R.R. Netz, Interactions between polyelectrolyte-macroion complexes, *Europhysics Letters* **64**, 413 (2003).

2. H. Boroudjerdi, R.R. Netz, Stability of strong polyelectrolyte-macroion complexes, *Europhysics Letters* **71**, 1022 (2005).

3. H. Boroudjerdi, R.R. Netz, Strongly coupled polyelectrolyte-macroion complexes, *Journal of Physics: Condensed Matter* **17**, S1137 (2005).

4. H. Boroudjerdi, Y.-W. Kim, A. Naji, R.R. Netz, X. Schlagberger, A. Serr, Statics and dynamics of strongly charged soft matter, *Physics Reports* **416**, 129 (2005).

5. H. Boroudjerdi, R.R. Netz, Global structural phase diagram of strongly coupled polyelectrolyte-macroion complexes, preprint (2005); to be submitted.

6. H. Boroudjerdi, R.R. Netz, Conformation and stability of polyelectrolyte-macroion complex fibers, preprint (2005); to be submitted.

Acknowledgment

without whom this work was simply impossible. Not only his warmth and wit have helped me to maintain a high spirit, but in particular, I benefit from his sharp and critical scientific view as a colleague in numerous instances of constructive discussions. More than anybody else I owe him encouragements and useful consults.

Curriculum Vitae

Name:	Hoda Boroudjerdi
Date of birth:	3 April 1978
Place of birth:	Tehran, Iran

School:

1984 - 1989	Elementary school (Narges, Issar), Tehran, Iran
1989 - 1992	Guidance school (Tolou), Tehran
1992 - 1996	High school studies (Tolou High School), Tehran Subject: Mathematics and Physics

Higher education:

10/1996 - 09/2000	Bachelor of Science (BSc) in Physics, Sharif University of Technology, Tehran, Iran
10/2000 - 08/2001	Diploma Degree in Modeling and Simulation of Complex Realities, International Centre for Theoretical Physics (ICTP), Trieste, Italy Thesis title: Numerical Studies of Directed Polymers in Random Media (Supervisor: Prof. Matteo Marsili)
01/2002 - 11/2005	Ph.D. in Physics, University of Potsdam, Potsdam, Germany Thesis title: Charged Polymer-Macroion Complexes (Magna cum laude; supervisors: Prof. Dr. Roland R. Netz and Prof. Dr. Reinhard Lipowsky)